Imperial College
London

Nano-Engineered Materials to Probe and Affect Natural Killer Cell Function

Thesis submitted for the degree of Doctor of Philosophy

Christian Loftus

Sept 26th, 2017

Advisors: Prof. Daniel M. Davis and Dr. Iain E. Dunlop

Department of Chemistry, Imperial College London

Declarations

Publications

Chapters 1 and 2 of this work have been accepted for publication and can be found in the manuscript:

Christian Loftus, Mezida Saeed, Daniel M. Davis and Iain E. Dunlop. Activation of Human Natural Killer Cells by Graphene Oxide-Templated Antibody Nanoclusters. *Nano Letters*, April 2018. DOI: 10.1021/acs.nanolett.8b01089

Originality

I declare that the work presented in this thesis is my own and where work is taken from others it is clearly cited as such.

Copyright

Abstract

The nanoscale biological structures and dynamics that occur within cells have slowly been recognized as important features that determine cellular function. In the field of Immunology the receptors which determine a cell's response have recently been observed to organize on the nanoscale, forming clusters which vary in size, shape, and density. While these supramolecular structures have been observed, their function is still unknown, and current methods used to discern their function could be improved. Here, biomaterials with spatially controlled nanoscale features have been produced and developed with this goal in mind. Engineered nanomaterials have advantages over many biological techniques, especially in nanoscale manipulation and reduced experimental complexity.

In this thesis two new nanoscale biomaterial approaches are developed, focusing on controlling the nanoscale spatial presentation of ligands to Natural Killer (NK) cells. The first is the fabrication of a supramolecular reagent which clusters Monoclonal Antibodies (mAbs) using a Nanoscale Graphene Oxide (NGO) framework. These clusters are on the same scale and density as receptor nanoclusters and exhibit properties that better mimic natural receptor ligation—such as interconnected ligands and local ligand density. Nanoscale Graphene Oxide-Monoclonal Antibody (NGO-mAb) species were found to augment degranulation and cytokine secretion of primary (human) NK (pNK) cells in comparison to equivalent concentrations of unclustered mAbs.

Secondly, gold nanoparticle arrays, a nanotechnology used to create mimetic cell surfaces with nanometer control of ligand spacing, were imaged with Stochastic Optical Reconstruction Microscopy (STORM), a single molecule localization technique, to characterize their biological functionalization. This characterization step is necessary to confirm the nanoscale patterning, but remains difficult, and new methods for its accurate measurement are needed. Results obtained indicate that in spite of measured underoccupation, regions could be discerned as

having spatial properties and patterning that would be expected of a functionalized array by three independent analytical methods.

Acknowledgments

In the time it has taken to me to produce the work within this thesis, and then to write the thesis itself, I have been very fortunate, previously knowing and newly meeting a great number of people that have left an impression upon me; be it colleagues, supervisors, friends and family, each have contributed, and while not my inclination to list names, I would like to nevertheless express my gratitude. For the time taken to teach me something, support me, contribute to this work, make me laugh or tolerate my faults—Thank you.

Contents

List of Figures

List of Tables

Abbreviations

βME β-Mercaptoethanol

2-MEA 2-Mercaptoethylamine

ADCC Antibody Dependant Cell Cytotoxicity

AF546 Alexa Fluor 546

AF647 Alexa Fluor 647

AFM Atomic Force Microscopy

BCE Before Common Era

BCP Block Copolymer

CD Cluster of Differentiation

Ce6 Chlorin e6

CNT Carbon Nanotubes

CPT Camptothecin

DCC Dicyclohexyl Carbodiimide

DDAT *S*-1-Dodecyl-*S*′-(α,α′-Dimethyl-α″-Acetic acid) Trithiocarbonate

DLS Dynamic Light Scattering

DLVO Derjaguin–Landau–Verwey–Overbeek

DMAP N,N-Dimethylaminopyridine

DMDA N,N-Dimethylacetamide Dimethyl Acetal

DNA Deoxyribonucleic acid

DOL Degree of Labeling

DOX Doxorubicin

DPL Dip Pen Lithography

DTT Dithiothreitol

EBL Electron Beam Lithography

ECM Extra Cellular Matrix

EDC N-(3-dimethylaminopropyl-N′-ethylcarbodiimide) hydrochloride

EDTA Ethylenediaminetetraacetic acid

ELISA Enzyme-Linked Immunosorbent Assay

EM Electron Multiplying

EMCCD Electron Multiplying Charge Coupled Device

EosFP Eos Fluorescent Protein

ER Endoplasmic Reticulum

FEG-SEM Field Emission Gun Scanning Electron Microscope

FIB Focused Ion Beam

FOM Freedom of Movement

FRET Forster Resonance Energy Transfer

FTIR Fourier Transform Infrared Spectroscopy

GCE Glassy Carbon Electrode

GO Graphene Oxide

GOx Glucose Oxidase

HA Hyaluronic acid

HATU 2-(7-Aza-1*H* -Benzotriazole-1-yl)-1,1,3,3-Tetramethyluronium Hexafluorophosphate

hMSC human Mesenchymal Stem Cells

HRP Horseradish Peroxidase

IFN Interferon

Ig Immunoglobulin

IgG Immunoglobulin G

IL Interleukin

IQR Interquartile Range

KikGR Kaede, Kikume Green-Red

KIR Killer Immunoglobulin-like Receptor

LAMP1 Lysosomal Associated Membrane Protein 1

LSCM Laser Scanning Confocal Microscopy

mAb Monoclonal Antibody

MEM Minimum Essential Medium

MHC Major Histocompatibility Complex

MRI Magnetic Resonance Imaging

mRNA Messenger Ribonucleic Acid

MSC Mesenchymal Stem Cells

MTOC Microtubule-Organising Centre

MW Molecular Weight

MWCO Molecular Weight Cut-off

NA Numerical Aperture

NGO Nanoscale Graphene Oxide

NHS N-Hydroxysuccinimide

NIL Nano Imprint Lithography

NIR Near Infrared

NK Natural Killer

NN Nearest Neighbor

NSC Neural Stem Cell

OD Oxidative Debris

P2VP Poly(2-vinyl pyridine)

PA-GFP Photoactivatable Green Fluorescent Protein

PALM Photoactivated Localization Microscopy

PBS Dulbecco's Phosphate Buffered Saline

PDMS Poly(dimethylsiloxane)

pDNA plasmid DNA

PEG Poly(ethylene glycol)

PEI Poly(ethylene imine)

PET Positron Emission Tomography

PLL Poly-L-Lysine

pNK primary (human) Natural Killer

PS Poly(styrene)

PSF Point Spread Function

PSS Poly(sodium 4-styrenesulfonate)

PVA Poly(vinyl alcohol)

REF Rat Embryonic Fibroblasts

RGD Arginylglycylaspartic acid

rGO Reduced Graphene Oxide

ROI Region of Interest

ROS Reactive Oxygen Species

RPMI Roswell Park Memorial Institute

RTP Room Temperature and Pressure

SBL Scanning Beam Lithography

SDS-PAGE Sodium Dodecyl Sulfate-Poly(acrylamide) Gel Electrophoresis

SIM Structures Illumination Microscopy

SML Single Molecule Localization

SMLM Single Molecule Localization Microscopy

SPANI Sulfontated Poly(aniline)

SPL Scanning Probe Lithography

SSIM Saturated Structured Illumination Microscopy

STED Stimulated-Emission-Depletion Microscopy

STM Scanning Tunneling Microscope

STORM Stochastic Optical Reconstruction Microscopy

TCEP Tris(2-carboxyethyl)phosphine

TCNQ 7,7,8,8-Tetracyanoquinodimethane

TCR T cell Receptor

TGA Thermal Gravimetric Analysis

TIRF Total Internal Reflection Fluorescence

TMB 3,3′,5,5′-Tetramethylbenzidine

TNF-α Tumor Necrosis Factor alpha

UV-vis Ultraviolet-Visible Spectroscopy

VP Vinyl Pyridine

Chapter 1

Motivation and Outline

1.1 Motivation

Cells sense their environment through receptors which bind external ligands.[1] Once bound receptors induce signaling within the cell that lead to a broad array of cellular functions, including differentiation,[2] migration,[3] and cell death[4]. The interaction of a receptor binding its ligand is, however, not the only important factor, instead there are many others which further modulate and determine a cell's function. These factors can include the affinity of the ligand for the receptor,[5] the mechanical force transmitted to the receptor[6] or whether costimulation from other ligands has occured.[7, 8] Other factors are also beginning to be considered influential; one of these for instance is the nanoscale organization of receptors and their ligands.

Recently cell surface receptors and proteins have been observed[9, 10, 11] with organization on the nanoscale, forming supramolecular nanoclusters of 10–400 nm.[12] To date this has been noted across a number of cell types[12] and particularly with surface receptors of cells within the immune system, for instance T cells,[13, 14, 15] B cells,[16, 17] and Natural Killer (NK) cells.[18, 19] As a direct result, understanding whether receptor clustering is

important for their function is an area of present interest.

The function of NK cells within the immune system is broad, they are a key part of our innate response to tumorogenesis and viral infection with their responses enabled thanks to the surface receptors they express.[20, 21, 22, 23, 24] Signaling initiated from a broad range of activatory or inhibitory receptors are carefully balanced and determine the NK cell's response through cytotoxicity of a target cell and or cytokine and chemokine secretion.[25, 26, 27] Recent evidence suggests that the nanoclustering of these surface receptors enables their function, for instance the density of receptors in a T cell receptor (TCR) nanocluster is essential for effective signaling.[14] Oszmiana et al. have also shown that phosphorylation of specific kinases and phosphotases are favored in large nanoclusters of the Killer Immunoglobulin-like Receptor (KIR) family.[19]

More generally a number of hypothesis have been proposed to explain receptor nanoclustering. A leading example is the signaling from receptors in nanoclusters, due to their close proximity, are amplified, and therefore more capable of overcoming the threshold necessary for a functional response.[28, 29] Another hypothesis is that interconnected ligands (for instance those connected by a network of actin) form nanoclusters and generate additional resistance once they are bound by their receptor. The additional force generated as a receptor pulls against the cluster then enhances activation by fully actuating mechanosensitive receptors.[30] In the case of the T Cell Receptor (TCR) for instance the greater force transferred in comparison to unconnected ligands has been shown to be more effective at leading to its activation.[31]

Some of the most modern methods to investigate nanoclustering are through imaging them with superresolution microscopic techniques such as Photoactivated Localization Microscopy (PALM)[32] and Stochastic Optical Recon-

struction Microscopy (STORM).[33] These techniques provide the unique nanoscale resolution to observe nanoclusters but remain passive and do not physically manipulate or interact with the structures. Superresolution imaging of the PALM, STORM variety is also presently limited to providing data from a small proportion of the total cell population due to its complexity and long image acquisition times.[34, 35]

Other technologies have been developed to reproduce, interact with and affect nanoscale features, including nanoclusters, particularly in the field of Biomaterials. Materials have been produced which for example can control the nanometer spacing between ligands[36, 37] or form clusters after initial receptor-ligand binding[38] and have provided interesting insights. Methods such as these have, however, reproduced only a subset of the characteristics found in the nanoscale organization of the cell membrane. Areas which could be improved include, the nanoscale size, ligand density and planar geometry, which would be necessary to, for instance, fully imitate receptor nanoclustering.

One candidate material capable of emulating the aforementioned properties is Graphene Oxide (GO). GO is a 2D material formed by exfoliation of oxidized graphite to produce single sheets[39, 40, 41, 42, 43]. Its structure is related to graphene, with additional oxygen containing functional groups that help provide aqueous solubility at detriment to the otherwise hexagonal lattice of aromatic carbon.[44, 45] Of GOs physical and chemical properties its 2D planar geometry is unique compared to commonly used spherical nanoparticles where varying the lateral size also affects the curvature. The hydroxyl, carbonyl and epoxide surface chemistry enable it to be functionalized with biological ligands and importantly the nanoscale sheet sizes can be controlled,[46, 47, 48] together making it a viable candidate to synthetically produce ligand nanoclusters.

Nanoscale Graphene Oxide (NGO) sheets have previously been utilized as a biomaterial in a number of applications such as gene transfection, targeted drug delivery and theranostics.[49, 50, 51, 52, 46, 53, 54] In each case the properties of NGO have however only been used to enhance the targeting qualities or delivery characteristics of well established drugs. To date there have been no publications that utilize NGOs properties as a framework, with the goal of recreating a biological structure as theorized here.

Another area where nanoscale organization could be important is in the design of immunotherapeutic reagents. Monoclonal antibodies are currently in vogue as treatments for number of diseases, arthritis,[55] breast cancer,[56] and certain lymphomas.[57, 58] Rituximab for example is a treatment for treatment of Non-Hodgkin lymphoma, binding the CD20 receptor of B cells and stimulating Antibody Dependent Cell Cytoxicity (ADCC) with excellent success.[58, 59] Despite these successes biological reagents for better or worse have not been created with properties that mimic the supramolecular structures they often interact with including the nanoclustering of ligands and receptors. The prospect of enhanced therapeutic efficacy by using NGO as a framework for the clustering of biologically active species is therefore unexplored.

A second interesting Material Science technology which has enabled nanoscale organization of receptors to be investigated is nanolithography[60, 61, 62] and particularly nanoparticle arrays produced by BCP micellar lithography.[63] Nanoparticle arrays can have a multitude of interesting and controllable nanoscale features such as honeycomb particle patterning, inter-nanoparticle spacings (usually between 10 and 500 nm) and controllable nanoparticle size.[64, 65, 66] Later functionalization steps are then able to impart these materials with biomimetic properties, for instance the ability to present biologically relevant proteins and molecules with the same lithographic features. Nanoparticle arrays have therefore been used to mimic the

cell membrane via functionalization with ligands to common cell surface receptors.[67, 68, 37, 60, 69, 70]

Where functionalized nanoparticle arrays have met the greatest challenge is in the accurate characterization of the biofunctionalization step.[71, 72] Ensuring that the precise nanoscale control is transferred to the biologic is essential and the same techniques used to characterize the inorganic array are generally unsuccessful when applied to the biofunctionalization. The success of this step is critical to the successful application of mimetic arrays and the ability for conclusions to be drawn using them.

Superresolution microscopy can be applied, in theory, to overcome these limitations and accurately characterize functionalized nanoparticle arrays so that they can be confidently used in cell biology applications, however, they have not been widely tested or utilized. Importantly superresolution techniques have both the nanometer lateral resolution and broad operating conditions required to measure the location of fluorochrome labeled biological molecules conjugated to arrays[73] and two color imaging also enables the direct measurement of a cell's interaction with an array, for example by imaging the ligand attached to the array and labeled receptors on the cell at the same time. If achieved, producing nanoparticle arrays with controlled nanoscale features, later functionalized and characterized by superresolution techniques, and further imagined interacting with cells, would be an exceedingly powerful combination to understand the nanoscale organization of the cell membrane while overcoming the individual faults of each technology.

Having outlined both the important biological context of receptor-ligand interactions, and the state-of-the-art technologies available in nanotechnology and microscopy, there is clear potential for application of the latter to problems of the former. This work aims to do just that, within the scope of

creating new, or improving established materials, that can then be applied to understand and augment NK cell biology.

The spatially-controlled presentation of ligands to NK cells is the primary aim of the material syntheses presented here. In doing so control of the immediate ligand-receptor environment i.e. the ligand density and ligand clustering (shape and size), and the mechanical properties of the ligand assembly (by structurally associating ligands through a common scaffold) are achieved. Immune cell and NK cell activation has been shown to be affected by these receptor factors,[31, 74, 14, 19, 37, 68] and producing nanoscale materials with control of one or more of these attributes is the first step in realizing the potential of this insight.

The development of NGO-mAb supramolecular nanoclusters is thus carried out with two aims in mind. First, control of the receptor-ligand geometry by the pre-formed clustering of ligands—thereby controlling the shape and size of ligand-receptor interaction. Secondly, to enhance the force transduced to the receptor by tethering cognate ligands to each other and a comparatively massive (1–2 orders of magnitude) NGO scaffold.

Here, it is hypothesized that the ligation of activatory receptors by pre-clustered ligands will lead to enhanced activation of NK cells through multiple mechanisms—the enhanced mechanotransduction afforded by the size of the nanocluster which will transmit additional resistance to the NK cell after receptor-ligand interaction—or through maintaining large receptor-ligand cluster sizes by restricting diffusion away from the cluster and or enabling coalescing of receptor clusters. Both of these properties are reported to be important in augmenting receptor signaling, while also being difficult to achieve with conventional methods such as soluble mAbs, crosslinked mAbs, and mAb tetramers.

The development of nanoparticle arrays is accomplished to control the den-

sity of ligand presented to NK cells. Previous findings have directly illustrated the effectiveness of this technology for understanding thresholds of NK (and T cell) activation.[37, 68] This technology would, however, be enhanced by co-development with superresolution microscopy. The combination of nanoparticle arrays and superresolution microscopy would allow for the receptor-ligand interaction to be manipulated, and at the same time observed.

1.2 Thesis Outline

The thesis presented here consists of three main results chapters, numbered 3–5. Chapters 3 and 4 concern themselves with the synthesis of a Nanoscale Graphene Oxide-Monoclonal Antibody (NGO-mAb) supramolecular material, used to create synthetic nanoclusters that are subsequently tested for their affect on primary (human) Natural Killer (pNK) cells. Chapter 5 deals with the topic of using STORM superresolution microscopy to characterize the biological functionalization of Au nanoparticle arrays as an initial step towards their use in future cell experiments.

Chapter 3 as a synthesis chapter describes the stabilization of graphene oxide in salts by steric repulsion through covalent conjugation of a PEG star polymer, characterization of the optical properties by UV-vis spectroscopy and then confirmation of the biotin-streptavidin linking strategy used to conjugate Monoclonal Antibodies (mAbs) to the stabilized NGO—largely by spectroscopic methods. This is followed by separation of NGO-mAb species by sheet size using centrifugation and characterization of the NGO-mAb products by AFM. A combination of the physical properties measured by AFM and bulk mAb concentrations are then used to determine the number of antibodies attached to the NGO sheet in the NGO-mAb product.

Chapter 4 begins by assessing the functionality of the NGO-mAb species

by testing if the conjugated mAbs are presented such that they can bind their antigen, and then if the NGO-α-hCD16 can specifically bind the CD16 receptor found on pNK cells as well as the kinetics of this binding. The assays used to assess the activation of the pNK cell in response to the NGO-α-hCD16 species are selected: CD107a upregulation and IFN-γ secretion. Both the degranulation response and cytokine secretion are assayed and directly compared to unconjugated and hence unclustered α-hCD16. Additionally biocompatibility is demonstrated after 6 hrs.

Chapter 5 in a departure from the previous two chapters, focuses instead on the use of STORM superresolution microscopy to characterize the biological functionalization of Au nanoparticle arrays. As such the reproducible production of Au nanoparticle arrays by diblock copolymer lithography is demonstrated and the relevant characterization by SEM shown. A proposed functionalization by reduction of IgG antibodies at the hinge to produce a free thiol which can form a bond with Au is then presented. STORM imaging of the functionalized array surfaces (using fluorochrome labeled antibodies) and a number of control surfaces is carried out and results are shown for comparison.

From the STORM dataset the position of detected antibodies is extracted, and data analysis carried out to observe if they are positioned such that they are specifically bound to the underlying array. Firstly the observed occupancy i.e. number of nanoparticles which appear to have a antibody attached is calculated, followed by more complex analysis of spatial characteristics such as the spatial dispersion (by Nearest Neighbor (NN) analysis) and spatial homogeneity (by Ripley's *K*-Function Analysis). These results are directly compared to the same properties measured from 'ideal' nanoparticle arrays as well as 'ideal' arrays with faults introduced, such as underoccupancy and uncertainty in the antibody position as a result of the many possible binding orientations (here termed Freedom of Movement (FOM))

and lastly an array made of points randomly distributed.

Together Chapters 3 and 4 together show how to synthesize a new biomaterial with excellent characterization, and then demonstrate its potential to affect cellular function through the measurement of a novel NK cell response. Chapter 5 improves upon the current work used to combine two powerful technologies, so that in the future they can be utilized for applications within cell biology.

Chapter 2

Literature Review

2.1 Immune System

2.1.1 Overview

The mammalian vertebrate immune system is a collection of cells and molecules that prevent damage to a host and enhance its likelihood of continued existence. Pathogens found throughout the environment and imperfections in cellular replication, leading to neoplasm, all threaten a hosts survival. The most abundant pathogens include bacteria, viruses, fungi, single and multicellular parasites and their toxins which the immune system in response can mount protective mechanisms such as, cytotoxicity of infected cells, phagocytosis and secretion of antibodies.[75]

Given this diversity of pathogens, the immune system which has evolved over time is also complex and our understanding of it, despite miraculous advances over the past 200 years, remains incomplete.

The first immune cell, the phagocyte, was observed in 1882 by Elie Metchnikoff and subsequently many more have been found.[76] To date 13 distinct immune cells are known, summarized in Table (2.1), and identified by their unique lineages from pluripotent hematopoetic stem cells of the bone marrow.[75] Each cell type has its own distinct function but by act-

ing together they can encompass all responses necessary to combat invasive pathogens that are encountered throughout a human lifetime.

2.1.2 Adaptive and Innate Immunity

Cells within the immune system were initially found to be part of two distinct groups, firstly those that were 'innately' responsive and could enact their immune function immediately in response to a pathogen (or foreign antigen) and secondly 'adaptive' immune cells which required prior sensitization and a period of adaptation. This distinction ultimately meant that these groups became widely and simply referred to as innate or adaptive respectively.[75]

T cells and B cells and their antibodies make up the adaptive immune system and while requiring adaptation are, as a result, able to provide 'memory' as well as extreme specificity to pathogens. Specificity occurring through a complex multistep process of selective priming by foreign antigen, leading to both expansion of sensitized cells adapted to that antigen only, and prolonged survival of 'memory' cells. Despite these features the mechanisms which prime the adaptive immune system also take several days to be achieved.[75, 77, 78]

The innate immune system therefore provides the function of moderating the early stages of disease, particularly while the aforementioned adaptation occurs. The innate immune system fundamentally differs from the adaptive as it instead relies on germline encoded Pattern Recognition Receptors (PRRs) presented by the cells. These receptors recognise so called Pathogen-Associated Molecular Patterns (PAMPs) which are generic and conserved among a number of different pathogens and therefore require no further priming, facilitating a swift response.[75, 77]

The differences between innate and adaptive immunity are generally under-

Table 2.1: A list of the major cell types found within the mammalian vertebrate immune system.

Cell type	Functions	Adaptive or Innate
B cell	Antibody secretion; memory	Adaptive
T cell	Cytotoxicity; regulatory; memory	Adaptive
NK cell	Cytotoxicity; regulatory	Innate
ILC	Regulatory	Innate
Dendritic cell	Antigen processing and presentation	Innate
Neutrophil	Phagocytosis; antimicrobial; extra cellular traps (NETs)	Innate
Eosinophil	Protein/enzyme degranulation (against multicellular parasites), ROS production; regulatory	Innate
Basophil	Inflammation; allergy; regulatory	Innate
Mast cell	Degranulation of mediators for inflammation; allergy; wound healing	Innate
Macrophage	Phagocytosis; regulatory	Innate

stood to be the result of their separate evolutionary development. While this explanation still holds true in general, there are now well known areas of overlap between the two, for instance, some innate cells showing adaptive characteristics.[77]

2.1.3 Natural Killer Cells

The Natural Killer (NK) cell is a large granular lymphocyte first observed in 1970s. They were discovered indirectly through their non-sensitized killing of transplanted mouse bone marrow cells that were unmatched by their histocompatibility alloantigens[79], killing "naturally" and without sensitization hence defininining their name. Further observations of 'natural killer' cells with the ability to lyse grafted cell and tumor cell lines continued throughout the 70s and 80s. The observation of NK cell killing of grafted bone marrow cells in mice also lead to the proposed hypothesis that NK cells killed cells lacking self-Major Histocompatibility Complex (MHC). This "Missing Self" hypothesis as it became known remains central to understanding of NK cell function.[80]

Definition by function alone however continued to lead to difficulties understanding whether the NK cell was a distinct lineage.[81, 82] By 1986 Lanier et al defined the NK cell as a cell type rather than a cell function[83]. Distinguishing the NK cell absolutely from the certain T cell subsets with very similar characteristics and surface receptors, remained problematic.[84, 85] Nonetheless the current human NK cell is phenotyped as $CD3^-$, $CD56^+$ and $NKp46^+$.[84] Within the NK-like innate lymphoid cell lineage there are a number of subsets and conceivably more will be discovered in the future.[86, 87, 27]

Current understanding of NK cell functions are two fold. Primarily they exhibit innate cytotoxicity to virally infected and neoplastic cells and secondly they are immunoregulatory through the secretion of the cytokines for

instance IFN-γ and TNF-α and the chemokines of the CC, CCX families.[88, 89] NK cells provide their cytotoxicity through the directed secretion of a combination of perforin, granulysin and various granzymes.[90, 91]

A clear indicator of the NK cells' essential function in host immunity can be seen in the morbidity and early mortality of those with complete NK cell deficiencies.[92, 93, 94, 95, 96, 97, 98, 99, 100, 101, 102, 103, 104]

Receptor Function and Signaling

In the initial stages of understanding NK cells' innate function the "Missing Self" hypothesis was proposed to explain their functional killing.[80] The "Missing Self" hypothesized that one method NK cells used to distinguish foreign, from host cells was through recognition of the downregulation or absence of 'self' MHC class I on a target cell. It remained unknown however whether MHC class I acted to inhibit the activation of NK cells through binding an unknown inhibitory receptor or instead limit their activation by blocking another 'triggering' receptor.[105] In 1992 this question was answered with the discovery of an inhibitory MHC class I receptor in mice (Ly49) and soon after in humans (p58, now CD158a or KIR2DL1).[106, 107]

Of the receptors currently known and found on NK cells 5 main groupings can be made: activatory, inhibitory, cytokine, chemotactic and adhesion.[108] Activatory receptors are the most diverse repertoire of receptors found on NK cells[109, 108] and provide sensitivity to a number of PAMPs which are conserved across different pathogens and Damage Associated Molecular Patterns (DAMPs). Some of the most well studied of these are NKG2D, NKp46, KIR2DS1 and CD16[110]. This receptor diversity differs from the activatory receptors of the adaptive immune system, which instead undergo genetic rearrangement to provide diversity in receptor repertoire. For instance in the T cell receptor (TCR) of the T cell.[75, 111]

Both the cytotoxic and immunoregulatory functionality of NK cells are largely driven by signaling initiated by ligation of activatory receptors which lead to an activated phenotype[112, 113, 114, 115, 116, 117]. Of equal importance however are inhibitory receptors[118, 107, 119, 120] and their ligands which work in conjunction with an innate activatory threshold balance the response of the NK cell,[121, 122, 123, 124] and prevent autoimmunity from occurring.[110] A summary of both can be found in Figure 2.1. The combination of both activatory and inhibitory receptors provide the innate means for NK cells to distinguish healthy from morbid cells and are essential to controlling an NK cell's function.[121]

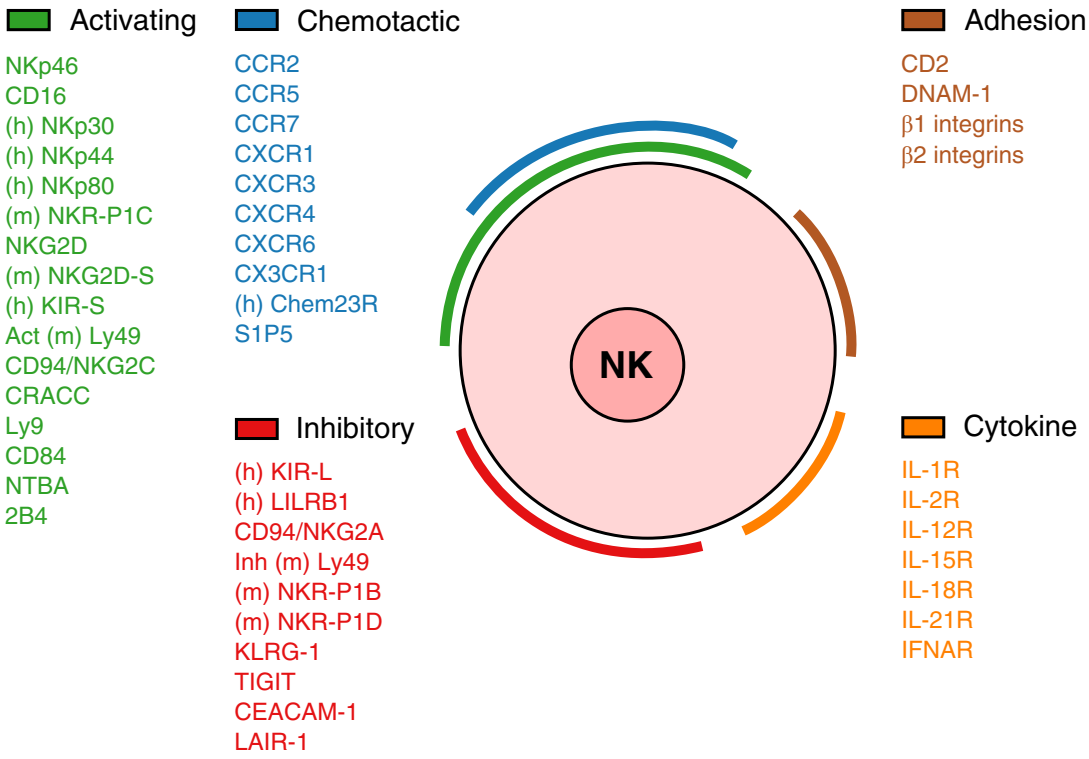

Figure 2.1: The receptor repertoire of NK cells. Where receptors are not equivalent across species human (h) and mouse (m) are noted. Reproduced from Vivier et al.[108]

Given the mixture of activatory and inhibitory receptors which can theo-

retically be ligated simultaneously the exact outcome of a random selection would still to date be difficult to know. In reality this problem is simplified as many disease states show a predominant ligand repertoire that interact with only a small combination of activatory or inhibitory receptors.[125, 126, 127] Still because of this complexity a large amount of work has gone into understanding which receptors when ligated together provide synergy or anergy.[122, 128] An example is NKG2D which showed synergy with 2B4 to secrete cytolytic granules, which by the ligation of each alone did not occur[122].

While receptor-ligand dynamics are essential to a NK cell's functionality, the physical interaction between the NK and target cell also determines the outcome of effector functions. The interaction between an NK cell and target cell occur in a number of steps; recognition, effector and termination, which are heavily summarized in Table (2.2) below.

CD16 & Antibody Dependant Cell Cytotoxicity

NK cells despite their established role in the innate immune system can contribute to a hosts adaptive immunity. CD16, a low-affinity receptor for Fc of IgG is expressed by almost all $CD56^{dim}$ NK cells and make up approximately 90% of circulating NK cells.[129, 130] Antibodies secreted by B cells of the adaptive immune system once bound to their target act as a ligand for NK cells through the Fc fragment and activate NK cells to lyse the opsonized cell. As this is a somewhat independent mechanism of cytotoxicity, due to its requirement of IgG, it is referred to separately as Antibody Dependent Cellular Cytotoxicity (ADCC).

ADCC has been shown to be an important mechanism for the elimination of neoplastic cells as well as in the clearance of certain viral infections.[131, 132, 133, 134, 135, 136, 137, 138] One well established treatment which utilizes ADCC is Rituximab/Rituxan, a chimeric antibody for CD20 which is

Table 2.2: A brief description of the stages of NK cell cytotoxic functionality.

Stage	Numerical designation	Brief description
Recognition	1	Adhesion
	2	Activatory and inhibitory receptor ligation and signaling
	3	Immune synapse formation
	3a	**IF** inhibitory signaling dominates, cell detachment
	3b	**IF** activatory signaling dominates, activatory synapse formation
Effector	4.1	MTOC polarization and anchoring
	4.2	Actin rearrangment and lytic granule docking
	5	Lytic granule secretion
Termination	6.1	Granule biogenesis
	6.2	Detachment

(MTOC – microtubule-organising centre.)

used to treat B cell lymphoproliferative malignancies.[139, 57] NK cells have been shown to contribute to increased B cell killing through ADCC after the opsonization of B cells by the Rituximab antibody.[140, 141, 58, 59]

Unlike the many other receptors NK cells express which require costimulation to trigger full effector functions including degranulation of cytotoxic granules and in some cases IFN-γ and TNF-α secretion, CD16 ligation has been shown to result in both in the absence of other stimuli.[122, 142] Using insect cell lines transfected with varying combination of NK receptor ligands Bryceson et al. showed that 20% NK cells upregulated CD107a (a marker of degranulation) in response to stimulation through CD16 by IgG, compared to $\sim$ 2% of cells stimulated through ULBP1, the ligand to NKG2D. Further stimulation of cells was still shown to be possible by a combination of stimulation through CD16 and NKG2D stimulation as $\sim$ 50% of cells were then found to upregulate CD107a.[122]

Surface Receptor Organization

The most prominent model for the cell membrane and proteins contained within it has been the 'Fluid Mosaic' model laid out in 1972 by Singer and Nicolson.[143, 144] It described:

> The model is consistent with the restrictions imposed by thermodynamics. In this model, the proteins that are integral to the membrane are a heterogeneous set of globular molecules, each arranged in an amphipathic structure, that is, with the ionic and highly polar groups protruding from the membrane into the aqueous phase, and the nonpolar groups largely buried in the hydrophobic interior of the membrane. These globular molecules are partially embedded in a matrix of phospholipid. The bulk of the phospholipid is organized as a discontinuous, fluid bilayer,

> although a small fraction of the lipid may interact specifically with the membrane proteins.[143]

Over the last 40 years this model has been improved upon to account for the segregation of proteins within the membrane[12] and explanations for these observations have been found, including lipid rafts and protein/glycoprotein complexes as well as membrane-associated cytoskeletal fences and extracellular matrix structures. All of which can limit the movement of membrane components.[144] Early observations of T cell and the TCR noted that the distribution of TCR, itself a membrane protein, are similarly segregated within the membrane.[145] This work using fluorescent microscopy showed that distinct areas of protein segregation occurred at the activatory synapse of a target cell. Later microclusters of TCR were observed[146, 147] and then at the nanoscale, protein islands of between $\sim$ 30–300 nm were discovered and found to be closely linked to the actin cytoskeleton at the membrane of T cells through the use of transmission electron microscopy.[15]

Similar immune synapse segregation, receptor microclusters and protein island or nanoclusters have now been observed in B cells[148, 16, 17] and NK cells[149, 150, 151, 18, 19]. As NK cells have a diverse range of receptors their organization at the cell surface is particularly relevant and interesting.

The discovery of segregation has with each advance in imaging technology been improved upon initially visualizing clusters of tens of micrometers and now nano scale clusters. To date, and with regards to NK cells alone, Pageon et al. have shown that the inhibitory receptor KIR2DL1 organized in nanoclusters of $\sim$ 110 nm which dynamically rearranged in response to NKG2D ligation.[18] Oszmiana et al. showed that both KIR2DL1 and KIR2DS1 organized as nanoclusters with the inhibitory KIR2DL1 ($\leq$ 80 nm) forming into clusters with a smaller average size than KIR2DS1 ($\geq$ 138 nm). Additionally they showed that the phosphorylation of ZAP-70 and SHP-1

are favored in larger nanoclusters.[19] See Figure 2.2.

It is now established that the type of receptor ligated, the presence or absence of co-receptor ligation and the phenotypic state of the NK cell, (whether through cytokine stimulation or prior activation) all influence the functional response of the cell. The question of whether the properties of nanoscale structures also contribute, particularly in the cytotoxic or immunomodulatory roles of a NK cell, are therefore seemingly important and yet have to date not been proven.

2.2 Graphene and Graphene Oxide

2.2.1 Overview of Bio/Nanomaterials

Artificial materials that enhance or repair the body without detriment have been used since early civilization. Evidence has for instance been found for sutures used by the early Egyptians[152, 153], dental implants using gold wire from the Etruscans (768–264 BCE, 600 BCE)[154, 155] and later nacre teeth fashioned from sea shells by the Mayans (600 CE).[156]

The scientific field founded on these early examples of materials is now referred to as Biomaterials and it has continued to develop steadily due to both its seeming requirement and potential. Between the biomaterials of early civilization and the present there have been a number of discoveries and applications which have contributed significantly to the field, some of the most important are biocompatibility which was a subject area was first examined in 1829;[157] the synthesis of plastics leading to improved contact lenses between 1939 and 1981 and high molecular weight poly-ethylene used in hip implants made them viable around 1961 with the Charnley hip;[158] osteointegration was documented in 1964[159] and accompanied by the controlled release of proteins using polymers in 1976;[160] soon after stents were produced to treat occluded arteries from 1978–85.[161, 162, 163]

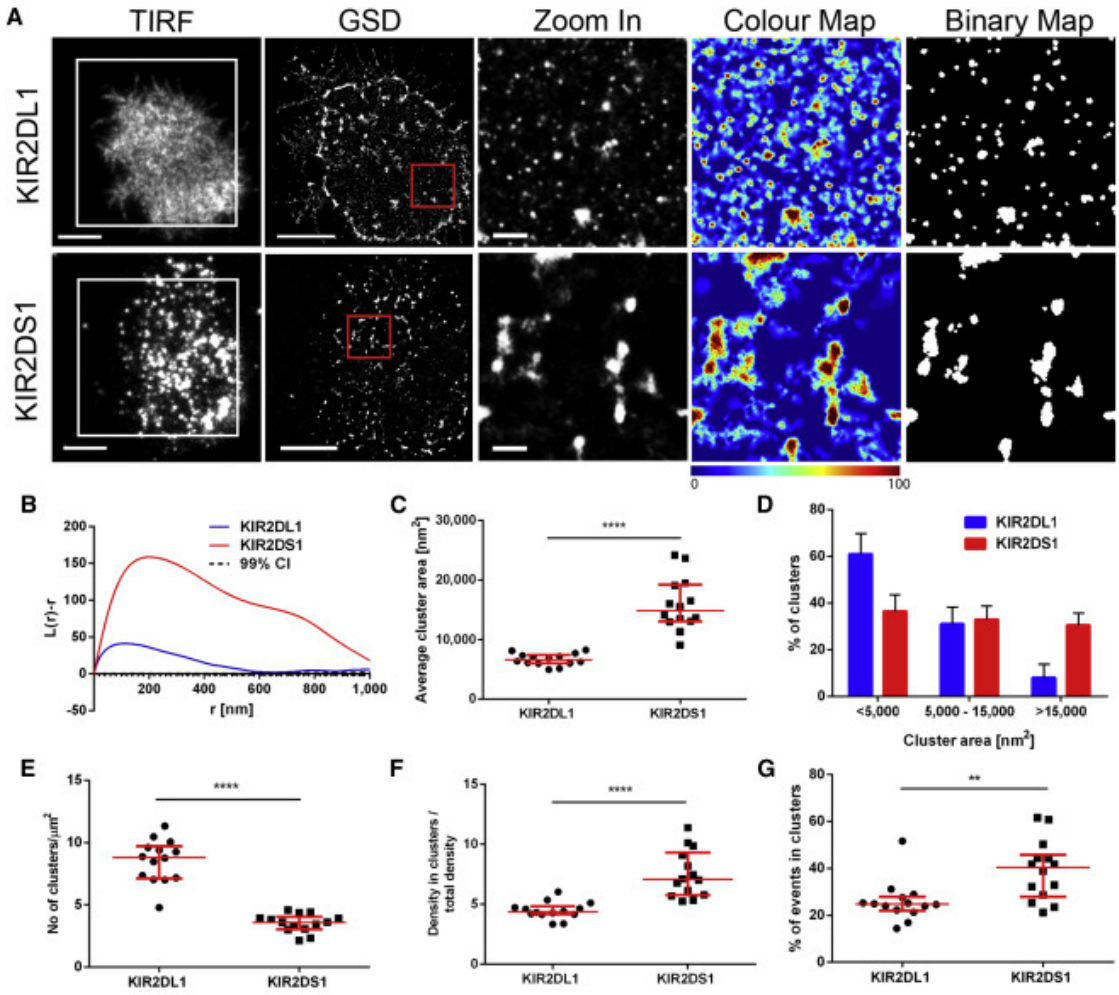

Figure 2.2: (A.) KIR2DL1 and KIR2DS1 are arranged in different sized nanoclusters on the surface of pNK cell clones. (B-G.) Comparisons between the KIR2DL/S1 nanoclusters properties. Reprinted with edits from Oszmiana et al.[19]

Biomaterials as a field, due to its cross disciplinary nature, has generally developed in response to advancements in a number of other fields. The most prominent of which are arguably Cell Biology (particularly Immunology) and Nanomaterial engineering, both of which grew rapidly in the mid to late 20th century.

The potential of nanotechnology was theoretically laid out by Richard Feyn-

man with his talk 'There's Plenty of Room at the Bottom' in 1959. It was only later however that such ideas could be practically implemented and in fact it would not be until 1974 that the term nano-technology was first used by Norio Taniguchi,[164] who was working to produce the first techniques required to process materials on the nanoscale such as ion-beam lithography. In 1981 K. Eric Drexler published 'Molecular engineering: An approach to the development of general capabilities for molecular manipulation'[165] and subsequently 'Engines of Creation: The Coming Era of Nanotechnology' in 1986 which added notoriety and interest to the area of nanomaterials.[166, 164, 167]

2.2.2 Overview

Graphene is a 2D crystal of carbon atoms exhibiting sp^2 bonding with a hexagonal 'honeycomb' lattice structure. Graphene Oxide (GO) is a similar 2D material with additional oxygen species such as hydroxyl, epoxide and carbonyl groups. GO is formed by the oxidation of graphene or graphite. Graphene being 2D, is part of a family of carbon structure which include quasi-0D Buckminster fullerenes, quasi-1D carbon nanotubes and 3D diamond or graphite.[168] The special properties of 2D graphene include its high electron mobility,[169] Young's modulus and strength,[170] thermal conductivity[171], optical properties in the Infrared (IR) region[172] as well as its unique geometry.[172, 173]

Although graphene can be readily functionalized using a number of approaches[39] the superior solubility of graphene oxide make it an obvious choice for biological applications.

The history of graphene and graphene oxide are interrelated as a result of their similar structure and origin. Especially since the mid 2000s 2D materials such as graphene and graphene oxide have become increasingly popular materials to study. Before this graphene as well as graphene oxide

have a history of study which dates back to 1948 (and vastly before if you include bulk graphite and couple layer graphite) when the first imaging of graphene oxide sheets by transmission electron microscopy were made.[174] Later studies were also made in 1966 providing images of single layers of graphene oxide and its chemical properties were studied by Boehm et al[175] which continued into the late 1960s and throughout the 1970s when epitaxal growth of graphene was carried out successfully and films were then studied extensively. The electronic properties were nonetheless inconsistent with true single layer graphene due to the interactions between the substrates it was grown on and the graphene itself.[176, 177]

It is for this reason that the seminal paper published in 2004 by Novoselov et al.[178] which separated graphene by mechanical exfoliation followed by deposition onto SiO_2 and uniquely allowed for the first experimental measurement of graphene's electronic properties to be made and confirmed. The advancement in the field of graphene research enabled by this was enough to lead to the award of the 2010 Nobel Prize in Physics and the number of publications have grown exponentially since 2005.

2.2.3 Synthesis of GO

Graphite oxide has historically been produced by the chemical oxidation of flake graphite. The first published example of this was by B. C. Brodie in 1859.[179] Brodie's method involved mixing flake graphite with fuming nitric acid HNO_3 and adding potassium chlorate $KClO_3$ yielding an oxygen containing graphite like material that after repeated oxidations further increased its oxygen content. L. Staudenmaier made small changes to this procedure through the addition of multiple aliquots of $KClO_3$ and H_2SO_4 throughout the reaction with the effect of producing a highly oxidized end product in a one pot reaction. A disadvantages was nonetheless the experimental risk involved in this procedure due to evolved chlorine dioxide.[180]

In 1937 the Hofmann method was produced using concentrated HNO_3, H_2SO_4 and $KClO_3$ from the beginning of the reaction. In contrast to the previous century of HNO_3, $KClO_3$ focused methods Hummer *and* Offeman in 1958 produced graphite oxide by reaction of graphite powder with concentrated H_2SO_4, sodium nitrate $NaNO_3$ and potassium permanganate $KMnO_4$ in a ratio of 1:0.5:3. This method has proved very popular and is the current standard with only small modification occurring since, for example an 'improved' variant (substituting $NaNO_3$ for phosphoric acid H_3PO_4 in a 6:9:1 ratio)[181] and 'modified' variant (generally increasing the $KMnO_4$ concentration giving a 1:0.5:6 ratio) though also used to describe a number of other modified methods.[182, 183]

To afford graphene oxide from this graphite oxide simple exfoliation by extended sonication, thermal exfoliation or stirring in polar solvents. Depending on the solvent chosen the stability of individual sheets can vary greatly. Good stability is, however, shown in water, DMF, THF and poor stability found in acetone, ethanol, DMSO.[184] Due to differences in the starting material (number of defects, surface area, purity) choice of oxidation method and subsequent purification steps the chemical structure of the produced graphite oxide can vary considerably a fact which is then transfered to the single layer GO. The lateral sheet sizes can similarly vary greatly from < 10 nm to many microns and various thicknesses. Exfoliation by sonication for instance greatly reduces lateral sheet size compared to stirring[185]

2.2.4 Physical & Chemical Structure

GO unlike graphene has both sp^2 and sp^3 carbon, as well as hydrogen and oxygen in a variety of functional groups including hydroxyl ($-OH$), epoxide ($-O-$) and carbonyl ($-C=O(OH)$). The exact structure of GO has been disputed for a long time and many models have been proposed. In chronological order these models (as designated by the surname of the proponent)

are the Hofman, Ruess, Scholz-Boehm, Nakajima-Matsuo, Lerf-Klinowski and Dékány. The most widely accepted is that shown in Figure 2.3 known as the Lerf-Klinowski model which was reported in 1998 by Lerf et al.[186]

The variation in structure which have been presented over the past 50 years is the result of a combination of factors encompassing both chemical and experimental origins. Chemically due to the fact that sample variability occurs and arises from different preparations resulting in a lack of definitive stoichiometry and amorphous nature. Experimentally this is compounded by the difficulty in characterizing an amorphous and complex material using techniques only capable of quasi-structural determination, which leads to ambiguity.

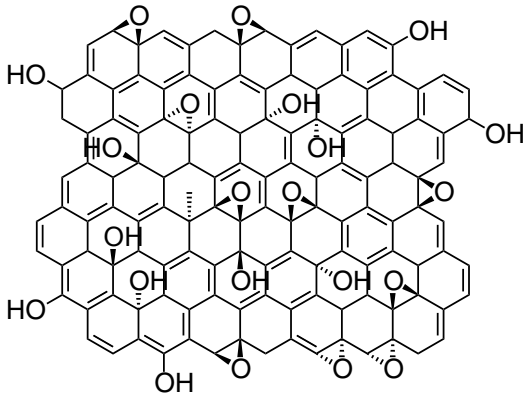

Figure 2.3: Proposed structure for GO based on the Lerf-Klinowski model. Reproduced from Perrozzi et al.[187]

The generally accepted Lerf-Klinowski structure of GO proposes a multi-region structure, one containing aromatic sp^2 carbon and aliphatic six membered rings of sp^3 carbon with the ratio of the two varying based on the oxidation. Relating first to the basal plane of GO, by nuclear magnetic resonance (NMR) they confirmed the presence of hydroxyl groups as well as epoxides—which they note are likely to be of the 1,2 variety in preference to 1,3 due to the complex and unlikely reaction mechanism required for

their formation. The sheet edges on the other hand, in variation to the basal plane, contain carboxylic acids in combination with hydroxyls which fit with Fourier Transform Infrared (FTIR) spectroscopic measurements. They also propose that isolated alkenes are likely to be present in minimal quantities due to their ease of oxidation.[186, 188, 189] Other techniques which have been used in conjunction with those described above to confirm the general GO structure include: UV-vis, Raman spectroscopy, X-ray Photoelectron Spectroscopy (XPS), High Resolution Transmission Electron Microscopy (HRTEM)[190], Transmission Electron Microscopy (TEM), Scanning Electron Microscopy (SEM), X-ray Absorption Near Edge Structure (XANES) and chemical reactivity.[191]

The generalized structure discussed above is still under dispute, a number of variations have been suggested which take into account a number of different readings and propose variations some of which are significant, for instance, Oxidative Debris (OD)[192, 193, 194] and dynamic models[195, 196] while others are less so[197]. Taking into account these variations, it currently seems most likely that in fact a combination of each may be correct. The model proposed by Nekahi et al., which is an extension to the Lerf-Klinowski model, taking into account the presence of phenols, lactones, ketones, the clustering of oxygen containing functional groups and trapped water molecules is certainly the most encompassing.[198, 197, 199]

2.2.5 Reduced GO

Understanding the reactivity of GO is important for its functionalization. One of the most studied reactions relating to GO is its reduction to produce reduced GO (rGO). One reason for this focus is due to it being hoped that rGO will be an easily scalable and cost efficient method to produce single layer graphene. The oxidation of GO necessarily disrupts the delocalized electron network by forming sp^3 carbon and therefore also disrupts the

sought after electronic properties which have potential for biological applications. Through reduction, to some degree at least, the electronic properties of graphene can be recovered and utilized.

There are three major methods for the reduction of GO; chemical, thermal and electrochemical. Chemical reduction can be achieved through hydrazine and hydrazine monohydrate which can be carried out in water.[200, 201] Results from this form of reduction do not return the properties of GO to that of graphene as shown by the Brunauer-Emmett-Teller (BET) surface area of 466 $m^2\ g^{-1}$ compared to the theoretical value of 2620 $m^2\ g^{-1}$ for pure graphene, in addition to the residual presence of oxygen in the rGO. A second method of reduction using sodium borohydride $NaBH_4$ produces better, though still suboptimal results, with reduced oxygen content compared to the hydrazine method.[202] Far less harsh reduction by alcohols has also been shown as plausible.[203]

Thermal reduction of GO by heating to 1050 °C have shown to both exfoliate and reduce graphite oxide in a single step to produce rGO. The CO_2 produced in combination with gaseous impermeability of GO causes exfoliation by presure induced mechanical cleavage. Using this method BETs of 600–900 $m^2\ g^{-1}$ have been acvhieved which represent a 2-fold improvement on hydrazine based reduction. A disadvantage of this method is the damage to the basal plane which is reported to occur.[204]

A two step process advantageously at much lower temperatures has also shown good results[205] and electrochemical reduction is theoretically possible with good small scale results already shown producing oxygen contents and conductivities surpassing all methods previously noted.[206]

2.2.6 Functionalization

Noncovalent

Certain functionalization strategies depend on the planar aromatic basal plane for functionalization and are therefore preferentially suited to rGO. The recovered delocalized electron structure of rGO can be beneficial for imaging in the NIR and loading of hydrophobic drugs, making it an interesting reagent for biomaterial applications.[207]

The physisorption of hydrophobic small molecules, polymers and proteins to rGO have all been demonstrated. Hydrophobic drugs that otherwise would be poorly suited to intravenous or oral delivery can be combined with rGO, the rGO acting as a carrier to transport these molecules into the cell for improved efficacy. The variation in chemical environment, for example the increased acidity of endosomes/lysosomes being a mechanism for the small molecule desorption.[208]

Advantages of non-covalent methods such as these are foremost the simplicity of the functionalization. Physisorption occurs primarily through $\pi - \pi$ stacking and van der Waals forces which are ideally formed on the basal plane. With some exceptions the mere combination and mixing of the two components is enough to result in attachment through this mechanism.

Example molecules for which this has been applied include 7,7,8,8-Tetracyanoquinodimethane (TCNQ) which was first dissolved in DMSO, combined with expanded graphite and after transfer to a basic solution stably bound to the exfoliated graphene.[209] Pyrenebutyrate was conjugate in a 'one-pot' reaction which combined both the reduction of GO using hydrazine monohydrate and loading of pyrenebutyrate together.[210] Many other polymers including Poly(sodium 4-styrenesulfonate) (PSS), Sulfonated Polyaniline (SPANI) and pluronic copolymers have been loaded using a similar 'one-pot' method, each with the primary goal of stabilizing the resultant

rGO in the aqueous solvents.[211, 212, 213] Molecules with greater biological relevance include DNA[214] and Doxorubicin (DXR). In the case of DXR it was shown that it could be loaded at up to five times the initial solution concentration thanks to the strong $\pi - \pi$ stacking and later released by varying the pH at either extreme.[215]

Covalent

Covalent functionalisation of graphene is another possible route to functional group addition. The formation of C−C bonds has been achieved by azo addition using 2,2′-Azobisisobutyronitrile (AIBN),[216] the reaction occurring through free radical addition at the aromatic carbon double bonds.[217] Addition at the C=C is equally applicable to rGO and GO however as it is dependent on the availability of sp^2 carbon the yields of AIBN addition is favorable with rGO.

The aqueous solubility (usually 2–4 mg mL^{-1}) and reactivity afforded by the presence of oxygen-containing functional groups arguably make GO superior to graphene and rGO for use in biological applications. As a result GO has been widely tested in applications relating to this area of interest.[218]

Functionalization by covalent bonding to the functional groups found on GO has been achieved through a number of different strategies and reagents. The most commonly targeted functional groups for functionalization are the the carboxylic acids, hydroxyls and epoxides. Given the ongoing debate regarding GO's structure many reaction rationales have unconsciously been proposed using mechanisms implied the Lerf-Klinowski model of the GO. This includes the dichotomy of epoxides and hydroxyls, generally in the basal plane, from carboxylic acid at the sheet edges. Given the success of the reactions presented to date, these results add some strength to the argument that the groups predicted in the Lerf-Klinowski model are indeed abundant.

Carboxylic acids have good reactivity towards a number of reagents but due to their likely presence on the sheet edges are found in lower numbers than both epoxides and hydroxl groups combined. Thionyl chloride $SOCl_2$ has been used in combination with non-nucleophilic solvents such as THF to chlorinate the carboxylic acid to form an acyl chloride which is reactive to nucleophiles such as amines ($-NH_2$) and hydroxyls leading to the formation of amides and esters with good stability in a aqueous solvents.[219, 220, 221]

A second common strategy for functionalization at the carboxyl involves carbodiimide coupling using dicyclohexyl carbodiimide (DCC) or 1-Ethyl- 3-(3-dimethylaminopropyl)carbodiimide (EDC) or 2-(7-aza-1*H* -benzotriazole-1-yl)-1,1,3,3-tetramethyluronium hexafluorophosphate (HATU).[222] In each case first the carboxylic acid is activated by N,N-Dimethylaminopyridine (DMAP) or N-hydroxysuccinimide (NHS) followed by both the carbodiimide coupling reagent and nucleophile containing molecule or protein (of choice) in a large excess forming a stable amide bond and isourea byproduct. This form of coupling can be carried out in polar solvents such as Dimethylformamide (DMF), water and N-Methyl-2-pyrrolidone (NMP) and is therefore more suited to functionalization of biological molecules which are stabilized and therefore retain their activity in these solvents. In both cases the excess reagents are usually removed by solvent exchange using desalting columns, centrifugal filtration or direct centrifugation and resuspension.[223, 224, 52, 225]

Hydroxyl groups together with epoxides being one of the most established functional groups on GO, are a second clear target for reactivity. In a reversal of the carbodiimide chemistry used for carboxylic acids the hydroxyl groups of the GO can be utilized as the nucleophile to attack carboxylic acid containing molecules of interest. Examples of this include conjugation of *S*-1-Dodecyl-*S'*-(*α*,*α'*-dimethyl-*α''*-acetic acid) trithiocarbonate (DDAT).[226] Other reagents reactive to hydrocyl groups are trialkoxysilanes

and alkyltrichlorosilanes whose linking is generally carried out in ethanol and other alcoholic solvents.[227, 228] A final example of a unique functionalization has been carried out using N,N-Dimethylacetamide dimethyl acetal (DMDA) which via Eschenmoser–Claisen ([3,3] sigmatropic) rearrangement forms a C−C bond which has greater stability than either of the more common ester and amide bonds.[229]

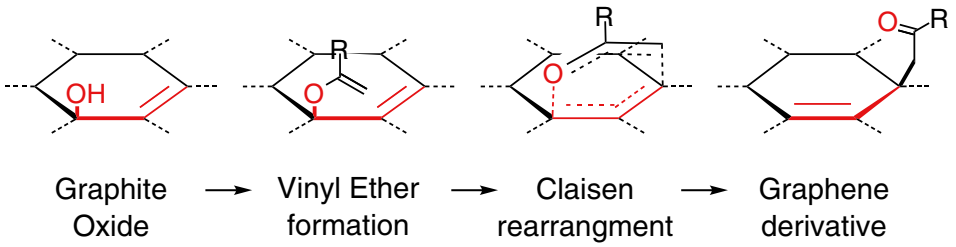

Figure 2.4: Oxygen to carbon bond transposition on GO by Claisen rearrangement to form a C−C bond. R = $N(CH_3)_2$ for Eschenmoser-Claisen rearrangement. Reproduced from Collins et al.[229]

Epoxides are a key route to functionalization thanks to the possibility of one step reactivity by ring-opening with nucleophiles. The ring-opening of epoxides by a nucleophile can be carried out in aqueous solvents and most likely occurs through Sn^2 mechanism which is typical for epoxides in neutral or basic conditions.[230] Examples of nucleophilic attack include using octadecylamine which improved stability in organic solvents and 1-(3-aminopropyl)-3-methylimidazolium bromide which did the same for polar solvents.[231, 232] 3-amino-propyltriethoxysilane (APTES), a common silanization reagent due to its amine groups, enable GO to be anchored to glass and Si substrates.[230] Other more unusual nucleophiles such as malononitrile salt has been used which forms C−C bonds which could be useful for very stable bond formation.[233]

In some instances achieving the final GO functionalization may require the selective combination of methods described above carried out in succession.

This has been demonstrated at least with the covalent functionalization of sterically stabilizing 6-arm Poly(ethyleneglycol) (PEG) polymer in combination with non covalent hydrophobic drug loading of the Camptothecin (CPT) analogue, SN38[54]. It is also possible to imagine the selective functionalization of basal epoxides and edge carboxylic acids to obtain a material with distinct properties which could potentially vary depending on its orientation or enable controlled assembly.[234] Other complex syntheses will require multiple additive reactions to produce a reagent with the desired functionality.[199]

2.2.7 Toxicity

Perhaps the most important step towards the use of graphene based materials in biology is to understand their toxicity. Given the amorphous chemical and physical nature of these materials the process is challenging. It is already well known for instance that the human body can break down and excrete molecules based on their size and shape as well as chemical structure.[235, 236, 237, 238] In cases where the material is unable to be excreted its accumulation often leads to destructive effects for including production of reactive oxygen species (ROS)[239, 240, 241] and stimulating other aberrant immune responses.[242] A good review of general nanoparticle toxicology has been made by Sharifi et al.[243]

Starting with the discovery and widespread interest in Carbon Nanotubes (CNTs) (beginning in the early 1990s), the toxicity and biocompatibility of these carbon based nanomaterials was established prior to any 2D carbon materials.[244] Carbon nanotubes were found to have toxicity analogous to other nanomaterials, depending both on the shape and size of the CNTs. Other important factors in the toxicity of CNTs later unearthed included contamination introduced in the synthesis and purification steps which drastically affected their biocompatibility.[245] The main findings for this class

of carbon based materials were that long CNT generally had greater toxicity than short, and particularly those of micrometer lengths compared to nanometer lengths.[246] Surface charge incidentally being found to have a minimal impact on the toxicity in in-vitro cell studies.[247]

Beginning with pristine graphene most studies have, to date, focused on the culture of cells atop graphene coated substrates. In various neuron cell types graphene has had little to no detrimental effect, causing at most small changes in gene expression and in enhanced cell growth when compared to polystyrene (a common cell culture plastic).[248, 249]

GO on the other hand of $\sim$ 100 nm in-vitro studies of toxicity showed almost no difference in ROS generation and cell apoptosis after 48 hours exposure.[250] Acting as a substrate for the growth of human Mesenchymal Stem Cells (hMSC), GO and rGO demonstrated biocompatibility with GO enhancing myogenic differentiation.[251] Lim et al. showed that aerated matrixes of GO nanosheets were biocompatible to MG63 cell line and allowed cell proliferation to occur ,however, with variation in the overall proliferation occurring over a 7 day period.[252] Similarly a comparison of pristine graphene to GO in-vitro with Vero cells noted accumulation of pristine graphene at the cell membrane leading to oxidative stress and cell death which did not occur in the presence of GO.[253]

In-vivo assessment of GO in mice have shown similar results amongst the multiple studies present with only small variations. At low doses of 25 mg kg^{-1} no toxicity was observed by Wange et al. although granulomas and cell death occurred at 40 mg kg^{-1}, each administered by intravenous injection.[254] The GO sheet sizes used appeared to be on the micron scale, although, they did not explicitly state characteristic sheets dimensions.

A study prepared by Zhange et al. carried out a more detailed study which assessed the biodistribution of GO after administration. For GO sheets of

10–800 nm, circulation times of $\sim$ 5 hours were normal. The GO was tolerated well at doses of 1 mg kg^{-1} while doses at 10 mg kg^{-1}, over 14 days, led to pulmonary edema and granuloma formation. The biodistribution was heavily biased towards the lungs and showed retention there at high concentration after two days. The second highest accumulation occurring in the liver and then the spleen. This biodistribution is similar to the pattern observed from other carbon based nanomaterials.[255] A similar study again corroborated the biodistribution in mice with the advantage of directly compariing the effect of sheet size. It found that GO with larger sheet size (1–5 μm) preferentially accumulated in the lung while small sheet size GO (100–500 nm) were found in highest concentrations in the liver. Concentrations used were 1–10 mg kg^{-1} b.w.[256] Intraperitoneal administration of 0.5 mL 100 μg mL^{-1} (mice weights not provided) showed similar biodistributions to those mentioned above and little to no significant granuloma formation or inflammation.[257]

One interesting study has noted that the method of GO synthesis seemingly had a dramatic affect on the toxicity. In this work Chng et al. compared Staudenmier, Hofmann, Hummers and Tour methods of synthesis, finding that toxicity correlated inversly with oxygen content of the GO, therefore making the Staudenmier synthesised GO (1.17 % C/O ratio) the most toxic. Sheet sizes were consistent at approximately 20 nm and viability was measured after 24 hrs incubation with human lung carcinoma epithelial cells at as low as 2 μg mL^{-1}.[258] These results also agreed with Singh et al. who showed that the thrombogenic nature of platelets varied between GO and rGO, the most likely cause was the higher charge distribution emanating from oxygen containing functional groups on the surface of GO.[259]

While toxicity may not be a direct consequence of GO's interaction with cells, a recent publication has shown unusual ruffling of the cell membrane and receptor shedding responses. It therefore seems likely that although GO

based materials can be non-toxic other relevant effects may be present that could be important in the decision of whether GO is a good candidate for therapeutic uses.[260, 261]

Although functionalized GO has a number of potential uses, it seems more likely that heavily functionalized GO will be the focus of biomaterial studies. In this regard GO sheets of 10–30 nm functionalized by 6-arm PEG have been studied for their toxicity in mice over extended periods at 20 mg kg^{-1} b.w. In contrast to previous studies the biodistribution appeared to favor the spleen and liver, and toxicity was found to be minimal. Importantly it was also corroborated that clearance was possible through both renal and fecal routes.[262]

These studies represent the first stages in understanding GO toxicity, focusing on the biodistribution and fundamental properties which define the materials toxicity. In the future research into specific interactions with cell types that uptake GO, cellular mechanisms of clearance in organs of importance, as well as individual toxicity of functionalized GO species will be important for clinically relevant applications. Examples of these types of studies are uncommon and will no doubt be the focus when clinical candidates emerge amongst the expanse of exploratory graphene and GO research.[263, 264]

2.2.8 Biological Applications

Stability

The drug delivery and therapeutic uses of (chemically modified graphene) CMG are another example of the wide ranging uses of these materials. One of the first challenges to be overcome for use in biological systems is the instability of CMG in solutions similar to bodily fluid. Within the field of biological research these conditions are replicated through the use of phosphate buffered saline (PBS), cell culture medium and serum solutions, all of

which are used extensively.

GO forms stable solutions in aqueous solvents best described as colloidal due to their observed Tyndall effect, a results of the dispersed nanometer GO sheet sizes. The stability of GO colloids in aqueous solutions occurs through the electrostatic repulsion from negatively charged functional groups (oxygen based in the case of GO) found across the basal plane, preventing sheet stacking.[265] This behavior is well described by Derjaguin–Landau–Verwey–Overbeek (DLVO) theory.[266] The mechanism of instability is therefore also well predicted. In solutions of high salt concentration salts contribute positive ions, neutralizing the surface charge, reducing electrostatic repulsion, and permitting sheet stacking which results in flocculation and sedimentation. In a similar but larger scale setting the adsorption of proteins onto the surface of GO by a combination of electrostatic, hydrophobic and van der Waals attraction again reduce intersheet electrostatic repulsion and stability.

One potential method to improve the colloidal stability of GO when electrostatic stability is diminished is through the addition of steric stabilization. This is achieved by the attachment of groups with large, lengthy chains, for instance polymers, particularly multi-arm star or dendrimers varieties, which provide appreciable steric hindrance and prevent sheets from flocculating.[267, 268] Examples of the conjugation of these polymers have been provided by Li et al. using 6-arm PEG star[265], Kim et al. using Poly(ethylene imine) (PEI)[269], Monica Veca et al. with Poly(vinyl alcohol) (PVA)[270] and lastly Yin et al. by hyaluronic acid.[271] The addition of hydrophilic groups to the surface of GO has also been suggested as a route to achieve better stability, for example using sulfonic acid.[272, 273]

Biosensing

Biosensing as a field has the goal of providing technologies that enable the detection of biological molecules. The standards by which biosensors are judged are their mode of detection, sensitivity of detection and reusability (commonly coupled with ease and cost of manufacture).

GO's theoretical advantages over some classes of biosensors are threefold. Firstly the distinct 2D structure provides a large surface area for adsorption of biological molecules or biosensitive modalities, secondly the production of uniformly coated surfaces on the macroscale is simple due to the aqueous solubility and thirdly the inherent electronic and fluorescent properties of GO and rGO enable detection by electrochemical or Forster Resonance Energy Transfer (FRET) methods. Specifically in the case of electrochemical sensing there is no requirement for the use of additional probes, in combination with or by attachment to the analytes, which improves both the preparation time and decreases complexity and cost. Together these properties have been shown to enhance sensitivity compared to devices with functionally added sensitivity.

The characteristic fluorescence and related potential for FRET as a sensing mode is slightly more rudimentary than probe free techniques but remains promising. This in part due to some analytes exhibit inherent fluorescence, in which case no additional overhead compared to probe free detection is involved. The flexibility of both is in itself a huge advantage where multi analyte sensors are required.

An initial example of intrinsic GO biosensing has been illustrated by Liu et al. for the detection of glucose. In their approach GO was simply deposited on a platinum electrode and functionalized with the enzyme Glucose Oxidase (GOx) using EDC, NHS linking previously discussed. Using this Pt/GO-GOx electrode in an electrochemical cell measurement of the

current for solutions of 0–30 mM glucose was made and showed a distinct linearity up to 28 mM mm^{-2} (sensitivity 8 mA cm^{-2} M^{-1}).[274] These results were less favorable than previously established glassy carbon electrode (GCE), GCE/rGO(chitosan) GOx which achieved sensitivity of 0.03793 μA cm^{-2} M^{-1} and linearity between 0.08–12 mM.[275] For reference diabetic glucose levels are normally above 7.0 mM.[276] In this case the chitosan used to stabilize rGO in solution and the increased sensitivity was most likely a result of the improved electron transfer between the enzyme and rGO. The most significant difference between these two approaches was the use of noncovalent adsorption of GOx by Kange et al. compared to covalent attachment used by Liu et al.

Using impedimetric detection thermally rGO has also been shown as a viable biosensor for Immunoglobulin G (IgG) by noncovalent deposition of anti-IgG onto a CMG electrode.[277] In comparisons with graphite oxide, electrochemically reduced GO and GO were also made, however, the best sensitivity was achieved by thermally reduced rGO. The sensitivity of this device for IgG was measured at 0.3–7 μg mL^{-1}. Overall this is lower than other graphene based electrochemical sensors (0.2–320 ng mL^{-1}) although in those cases labels were required to provide sensing unlike the label free approach used here.[278]

In a slightly more unusual system GO has been used as a nanocarrier to concentrate the detection probe of a sandwhich based assay for p53. In this capacity the large surface area to volume (and mass ratio) enabled the clustering of anti-p53 in combination with Horse Radish Peroxidase (HRP) to multiply the number of HRP bound per p53 antigen bound in the sandwhich assay. The increase in HPR amplifying the detection of even low levels of phospho-p53 and enabled detection of between 0.02–2 nM with a detection limit of 0.01 nM. This is a 10-fold improvement on conventional sandwhich assays.[279]

The sensing of numerous biological molecules has been achieved using graphene based materials including small molecule drugs,[280] chemicals,[281] heavy metals,[282] fungicides and pesticides,[283] proteins and enzymes, including DNA and nucelotides.[214] An extensive lists of GO based biosensors can be found in Chen,[284] Bitounis[285] and Geogakilas et al.[286]

Tissue Engineering

Tissue engineering is a subfield of Biomaterials that specifically deals with the production of tissues such that they can be used to replace, support or enhance damaged or destroyed tissue. For this reason engineered tissues should have functionality at least matching the original, if not improving upon it.[287] Given our complex knowledge of the cell types, tissues and organs producing biologically similar tissues remains a complex and arduous task particularly for regenerative medicine.

Many of the hurdles of tissue engineering revolve around the controlled development of tissues from individual cellular precursors. Over time this process has gradually become intrinsically linked with the environment in which the cells are found and develop.[288] In the body all tissues develop in the surrounding of stimuli provided by a number of chemical and mechanical factors related to the extracellular matrix and the cells within it. These factors include the presentation of ligands, the stiffness and the geometry provided by the ECM. It is therefore the goal of tissue engineering to produce materials which either through emulation of these factors or otherwise, can produce tissues and organs in settings which are amenable to there production i.e. ex-vivo and yet are viable for later transplantation.[289] Given GOs broad range of mechanical properties, reasonable record of biocompatibility, functionalizability and even electronic conductivity, it has naturally been investigated.

ECMs in recent years they have proven to be an indispensable component of tissue formation and are therefore a key area for biomaterial and GO substitution.[290, 291, 292] Some candidates for ECMs have focused on hydrogels included those made from Poly(ethylene glycol) (PEG),[293] gelatinouse protein mixtures such Matrigel[294] and peptide amphiphiles.[295] GO scaffolds have been formed in perhaps the most simple manner by self assembly using a hydrothermal one step process whereby an aqueous solution of GO was heated for 1–12 hours at 180 °C leading to a ECM like structure.[296] Seeding of MG63 cells onto these simple graphene hydrogels (post hydration) showed biocompatibility and adhesion but suboptimal proliferation.[252]

In a more advanced scaffold of GO-chitosan which with advantageous porous 3D network structures, water retention, stability, enzymatic degradation and negative charge led to more positive results. Osteoblasts seeded onto these structures showed good biocompatibility and formation of cell-cell interactions within.[297]

Foam like graphene aerogels have also been produced by various methods.[298] Unfunctionalized structures such as these have been seeded with Neural Stem Cells (NSC) successfully which showed differentiation towards astrocytes and neurons. Particularly exciting among these 3D structures is their electrical conductance, and using monophasic cathodic pulses of 20–30 μA the opening of calcium channels of graphene attached NSCs by fluorescence microscopy has been observed.[299] These results agree well with 2D planar growth and electrical stimulation driven neural differentiation of PC-12 cells.[300]

For application in bone regeneration the mechanical properties of materials such as Hydroxy Apetite (HA) have been a limiting factor in the production of successful biomaterials. Combining HA with GO in a nanocomposite

has been shown to increase the fracture toughness by 203%[301] Nanocomposites such as these have previously been demonstrated to exhibit no cytotoxicity[302] and specific material dependent morphologies.[303] The addition of polymers to GO-HA structures, such as Poly(lactic acid) (PLA), also enhanced the workability and allowed for them to be electrospun.[304]

Much of the work concerning graphene and GO based materials for tissue engineering properties are still rudimentary and the continuing developments will require research focused on adding biological motifs for controlled differentiation and proliferation, as well as studies into the biodegradation.[305]

Therapeutic Drug Delivery & Gene Transfection

Provided stability can be achieved the functionality which has been applied to GO is various. It encompasses drug delivery, targeting, imaging and phototherapy as well as combinations of each. Some of the most simple therapeutic strategies of these has been the loading of cytotoxic drugs onto the basal plane of GO by utilizing $\pi - \pi$ stacking. This method has been shown successful by Liu et al. who loaded SN38 (a DNA intercolator which has good anti-cancer activity) onto PEG stabilized GO (GO-PEG) which they tested on human colon cancer cell line (HCT-116). They reported cytotoxicity comparable to free SN38 with the advantage of good stability of the SN38 in both PBS and serum through the carrier ability of GO-PEG.[54] Extensions to this work, for instance by the combination of multiple anti-cancer drugs onto GO has also been attempted, although the increase in cytotoxicity was not drastically changed in the case of doxorubicin, camptothecin with human breast cancer cells (MCF-7).[272] One further extension shown by this work was the targeting of the MCF-7 cell line through the covalent addition of folic acid (FA), however, this time with variable success due to results only appearing significant at high GO concentrations of 20 μg mL^{-1}.

Other similar examples exist.[306, 307]

The combination of delivery and targeting in a single treatment has the theoretical potential for improved efficacy over application alone. Sun et al. for example demonstrated the loading of DOX in combination with the covalent attachment of anti-CD20 all in a single, nanometre GO (nGO) material. The combination had a approximately 3 fold higher cytotoxicity to Raji cells compared to non-targeted nGO.[46] They were also able to employ Near Infrared (NIR) imaging (1100–2200 nm) to image the attachment of nGO to target cells and showed some of the first potential of imaging of the intrinsic NIR fluorescence of GO.

Having shown efficient drug loading, GO has been used to deliver other bioactive proteins and molecules for instance plasmid DNA (pDNA) and short interfering RNA (siRNA). In the case of pDNA loading a noncovalent methodology was used, first the electrostatic attachment of cationic PEI to GO. This was then mixed with pDNA which bound by electrostatic attraction to the PEI. The combination was then used to deliver EGFP to the human cervical cancer cell line (HeLa) cells with results that showed the transfection efficiency of GO-PEI(1.2kDa) and GO-PEI(10kDa) was significantly greater than the unsupported PEI(1.2kDa) and PEI(10kDa). GO-PEI(10kDa) exhibited the best efficiency overall with the the unexpected advantage of decreased toxicity compared to the equivalent 10 μg mL^{-1} of unbound PEI which showed significant toxicity.[51]

Photodynamics

Graphene oxide sheets, especially those of nanometer size, absorb electromagnetic radiation in the Near-Infrared (NIR) region $\sim$700–1100 nm region of the spectrum. These wavelengths are particularly interesting as they penetrating tissue well due to their relatively uninterrupted passage though water and haem related proteins in tissue. As a result of the NIR absorbance

nano Graphene Oxide (NGO) sheets can therefore be used to target and destroy cells using photodynamic mechanisms, a method which is particularly suited to treating solid tumors. There are two mechanisms by which radiated energy from photodynamic therapy lead to cell death: photodynamic production of Reactive Oxygen Species (ROS) and photothermal heating.

The mechanism of photothermal heating occurs in a multistage process, after absorbing radiation[308, 309] GO relaxes back to a ground state and releases energy as a phonon which heats the surroundings and leads to cell death by disruption of the membrane.[310] Cell death through this pathway can result in both necrotic cell death or activation of the intrinsic mitochondrial pathway[311] and apoptosis.

Photodynamic therapy which uses a photosensitiser (light sensitive molecule), can be used to transfers the energy to oxygen species in the immediate surroundings. In turn ROS such as singlet oxygen and free radicals that are produced trigger cell death by apoptosis.[312, 313]

GO and rGO have both been demonstrated as excellent photosensitizers. Robinson et al. used rGO ($\sim$ 20 nm) to enact photothermal killing of brain tumor cells (glioblastoma, U87MG) using non-covalently functionalized rGO stabilized with amphiphilic PEGylated polymer chains and a RGD targeting motif. The rGO heated cells in-vitro to temperatures above 51 °C within 1.5 minutes of irradiation at 808 nm (15.3 W cm^{-3}), which was enough to lead to cell death despite having minimal toxicity without the RGD targeting.[207] An in-vivo photothermal treatment of skin melanoma (B16F1) in a SKH-1 mouse model has also shown to be very effective. Here the application of NGO functionalized with Hyaluronic Acid (HA) was carried out by administration of NGO-HA onto the skin (topically) which was effectively taken up by the cancerous cells due to the damaged skin barrier and leaky vasculature. Application of a single 10 mins of irradiation following 30 mins of

administration showed complete tumor death two days after treatment.[314] Further similar examples may also be found.[315]

The photodynamic therapy of GO with the addition of a second photosensitizer, Chlorin e6 (Ce6) was demonstrated by Tian et al. Ce6 loaded onto GO improved its uptake by cells, especially through photothermal excitation of GO at 808 nm and when combined with excitation at 660 nm lead to strong cell death thanks to the Ce6 photoinduced ROS generation.[52] A multimodal combination of GO gene delivery has also been carried out using GO's photothermal properties to improve cell membrane permeability by increased local temperature.[224]

Theranostics

Given the examples of multifunctionality which can be applied to CMG as well as its intrinsic NIR absorbance, fluorescence and photothermal properties, the potential for theranostic treatments are great. One demonstration of this potential was carried out by the successful covalent attachment of the tumor targeting antibody CD105 as well as loading with ^{64}Cu-NOTA for Positron Emission Tomography (PET) imaging. Despite the prospect of demonstrating targeting, imaging and photothermal therapy together in the study by Hong et al., only targeting and imaging were shown.[49] A second example of the theranostic potential of GO was achieved by Magnetic Resonance Imaging (MRI), magnetic tumor targeting, DOX loading for tumor cytotoxicity and photothermal therapy all in a single therapeutic. The addition of magnetic properties was achieved in this case through the functionalization using magnetic Iron Oxide Nanoparticles (IONP).[316] General results and structure are highlighted in Figure 2.5.

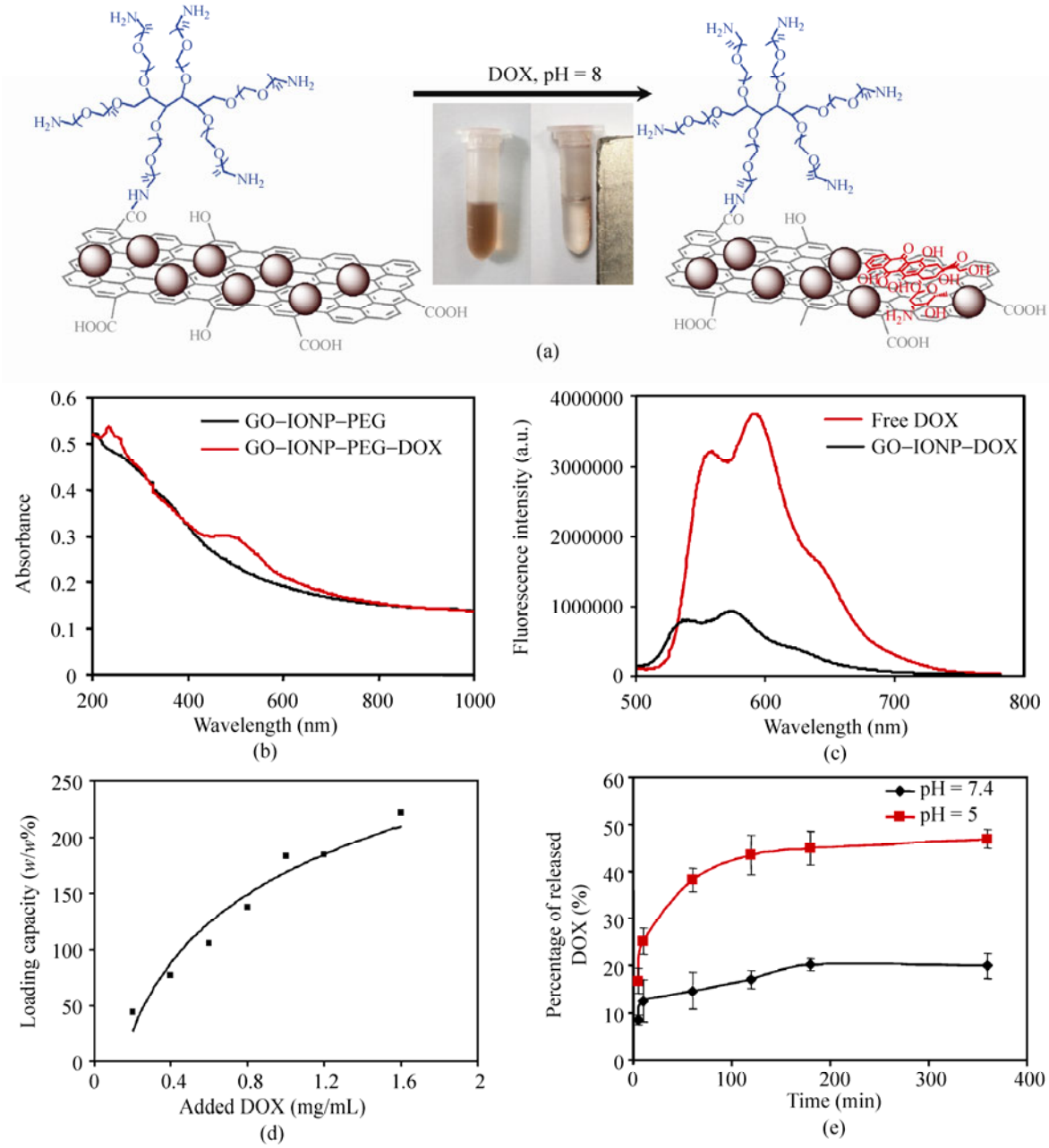

Figure 2.5: (A.) Schematic of GO-IONP-PEG (iron oxide nanoparticle) and GO-IONP-PEG-DOX (DOX – Doxorubicin). Image of GO-IONP-PEG-DOX without (left) and with a magnet in close proximity (right). Characterization of DOX loading and release from GO-IONP-PEG-DOX. Reprinted from Ma et al.[316]

Cell Biology

Some materials, due to their unique properties can be used to test and understand the mechanisms which underly the function of cells. Graphene and GO have been less widely used to produce these class of materials, although the field itself is generally smaller, giving an explanation for the reduced number of examples.

A few examples nonetheless exist for instance Li et al. who produced graphene barriers to constrain lipid bilayers. These surfaces contained lipid bilayer reservoirs between 5 and 10 μm connected by channels (with widths as little as 114 nm) to similarly sized reservoirs, allowing for diffusion of the lipid bilayers to be studied. The advantage of using GO in this case was the minimal edge effects thanks to the 1 atom thick 'wall' height which prevented vertical variation in roughness and achieved minimal interaction between the lipid bilayers and the graphene. The final results obtained using this system matched well with the theoretical predictions produced using computational modeling.[317]

Applications such as the one presented here allow for more accurate study of the lipid bilayer structure and function which is particularly important in receptor dynamics, an area already established in Section 2.1.3 as important.

2.3 Nanopatterning

2.3.1 Nanolithography

Since the 1960s a number of techniques have developed to produce materials and especially surfaces with precisely controlled nanoscale features.[318, 319, 320] Such micro and nanoscale features have perhaps found their most established use in the production of transistors an essential component of modern day computation. Two categories of lithographic techniques have

emerged over this time: conventional and unconventional. Conventional lithographic techniques include: photo and scanning beam lithography, and unconventional: scanning probe, imprint, edge and self assembly lithography. A summary of each can be found in Table 2.3.

Photolithography

The fabrication of nanoscale materials for biological purposes has generally been achieved by the adaptation and optimization of techniques produced and used first in other areas such as semiconductor fabrication[321] and nanoscale imaging.[322, 323] Photolithography is one of the main techniques still used for the production of microelectronics, it is achieved in a multistage process which despite step number can be completed quickly and over areas of several centimeters. In turn this produces rapid patterning and rates of over 10^{10} $\mu m^2 h^{-1}$ can be achieved.[324]

The process for photolithography can be summarized in 5 steps:

1. Coat a chosen substrate with a masking film.
2. Coat substrate and masking film with a photoresist.
3. Apply a mask (with given pattern) and exposure to UV light.
4. Bake and develop substrate to selectively remove photoresist.
5. Etch the masking film selectively to leave resultant nanopattern.

In the first step a masking film is applied atop a chosen inert substrate, for instance silicon. The masking film provides the material, which by its removal later produces the nanoscale features. A photoresist whose solubility will vary after exposure to UV light is then coated on top of the masking film by spin coating to produce an even coating.

Next a mask which is opaque to UV light (usually Chromium) is then applied above the photoresist and exposed to UV light. The mask is subse-

Table 2.3: A summary of lithographic techniques for nanopatterning. Reproduced with modification from Gates and Garcia et al.[325, 324]

Lithography	Minimum feature (nm)	Resolution (nm)	Throughput ($\mu m^2/h$)	Pattern
Photo	37	90	10^{12}	parallel generation, arbitrary patterns
Scanning beam	5	20	10^2–10^6 / 10^8–10^{12}	serial writing, arbitrary patterns
Scanning probe	<1	1	10^{-5} / 10^1–10^5	serial positioning of atoms, arbitrary patterns
Imprint	~ 5	30	10^{10}–10^{12}	parallel formation, arbitrary patterns
Edge	8	16	–	parallel, non crossing
Self-assembly	>1	>1	–	parallel formation, regular, repeating structures

quently removed and the substrate which is then submitted to a process of exposure, and development to remove the intended region of the photoresist based on whether its solubility increased or decreased.

In the final step the etching of the masking film is carried out, in doing so selectively removing the region left exposed by the photoresist. Etching can take many forms for instance anisotropic, which is typical of wet, chemical etching or isotropic for example Reactive Ion Etching (RIE) a form of plasma etching. To produce the completed patterning the photoresist is removed by a process known as 'stripping' which leaves the etched masking film atop the substrate.[326]

The most important factor determining the resolution of photolithography is the wavelength of UV light used to expose the photoresist. From the mid 1980s until mid 1990s UV wavelengths of 365 nm were used as the standard for photolithography. Since then UV wavelengths today are 193 nm which can produce feature sizes of 50 nm and lower with optical enhancements. To produce features of less than 10 nm Extreme Ultraviolet (EUV) wavelengths of 13.5 nm will be needed with the drawback of far larger power consumptions.[327]

Scanning Beam Lithography

The second conventional lithographic technique is Scanning Beam Lithography (SBL) which in general refers to both Electron Beam Lithography (EBL) or Focused Ion Beam (FIB) lithography. In the case of EBL an electron beam produced in the same manner to electron microscopy (a source of electrons is focused using successive electromagnetic lenses to produce a focused beam < 5 nm in diameter) is used to selectively alter the solubility of a electron sensitive resist material such as Poly(methylmethacrylate) (PMMA) or Poly(dimethylsiloxane) (PDMS). After exposure to the beam the resist can then be removed and developed ready for etching in a manner

synonymous with photolithography described above. The clear difference with EBL compared to photolithography is that a mask is not required and therefore direct writing and unique patterning are possible with each use. In some cases the use of the patterned photoresist in itself may be sufficient for further use in which case the subsequent development, etching and stripping which would otherwise be carried out is not required.

Focused ion beam (FIB) lithography was developed in the 1980s[328, 329, 330] and utilizes an accelerated beam of ions which directly pattern a substrate by sputtering. The most common ions used are H^+, Be^{2+} and Ga^+. At lower energies FIB can also deposit ions onto the surface of a substrate as a second mode of lithography. In comparison to both photolithography and EBL, FIB is clearly simpler thanks to its direct patterning of a substrate.[331]

Scanning Probe Lithography

Scanning Probe Lithography (SPL) are a group of techniques which rely on a probe, either the tip of a Scanning Tunneling Microscope (STM) or Atomic Force Microscope (AFM) cantilever, to pattern a substrate by removal of material through scraping, positioning of material or the transfer and deposition of new material onto a substrate.

STM has a resolution of 0.005 nm vertically and 0.02 nm horizontally[332] and is therefore extremely sensitive and in fact capable of imaging single atoms. This resolution also enables STM to pattern on the similar orders of magnitude and examples of Fe atoms which were displaced and rearranged on top of a Cu substrate are documented.[333, 334] Given the sensitivity, SPL and STM have a low throughput on the order of 10^{-5} μm^2 h^{-1} which in comparison to 10^{10} obtained by NIL illustrates that the sensitivity is balanced by its lack of speed.[324] In most biological contexts there is a reduced requirement for nanopatterning methods which do not pattern large areas however STM has found uses for high resolution biological imaging.[335]

Utilizing AFM tips to nanopattern by 'writing' onto a substrate is another area of SPL which is known as Dip Pen Lithography (DPL).[336] Here the cantilever tip is coated with a experimentally relevant substance, such as an alkanethiol or biological molecule and the tip traced over the surface in a given pattern.[337, 338, 339] The line resolution of DPL using a cantilever is as low as 40 nm although the patterning area is again small, not generally greater than 100×100 μm for a single region with multiple regions adding to the patterning time significantly.[61] While the name dip pen lithography suggests the need to insert the cantilever tip into a solution (initially a limitation of the technique) it is now common that a modified feed system with reservoir can be used to allow for continuous patterning over an area without dipping steps.[325]

The removal of a pre-coated material from the surface of a substrate is also possible with SPL. In this mode the tip is placed in contact with a coated layer which is subsequently scraped from the surface with the movement of the tip.[340] This technique has been used for instance to remove a self assembled monolayer of thiolated molecules from a gold surface.[341]

A final possibility for SPL techniques is the application of a voltage between a conductive cantilever and the substrate creating a current. The current then enables electrochemical deposition as well as chemical oxidation of surface coated layers.[342, 343, 344, 345, 346]

Imprint Lithography (Molding and Embossing)

Imprint lithography concerns itself with the molding and embossing of a soft substrate with a harder 'master' pattern. There are many forms of imprint lithography coming under two umbrella terms of hard and soft molding. Within hard molding a hard master is used to shape a soft or liquid substrate which is further hardened while in contact transferring the master pattern. An example of this is Step-and-Flash Imprint Lithography (SFIL)

where a master is used to mold a UV hardening liquid polymer, which after irradiation, can be separated causing the pattern to be transferred. A version of this technique (Nanoscale orthogonal biofunctionalization imprint lithography (NOBIL)) is presented in Figure 2.6.

A variation of this is found with Nanoimprint Lithography (NIL) which instead involves heating a polymer above its glass transition temperature (T_g), making it moldable for embossing with a master. The polymer is then cooled to below the T_g allowing the master to be removed and the patterning preserved in the polymer.

Soft molding works in contrast to hard by applying a 'soft' liquid polymer over a hard master. In replica molding (a soft molding technique) a liquid polymer is poured on top of a master and allowed to harden producing an intermediate mold. The hardened mold is then used to reproduce a 'replica' of the master by casting a second polymer against the intermediate mold.

Self Assembly Lithography

Self assembly is a method by which one or more components aggregate, organizing themselves reproducibly into a larger repeating structure without any further requirements. Self assembly occurs thermodynamically to reduce the free energy of the system which occur as a result of the forces acting on the individual components. The most common components which are known to self assemble include block copolymers, nanoparticles and proteins. The forces that drive self assembly are varied and are generally non-covalent, for instance magnetic properties or intermolecular forces such as hydrogen bonding.[347] Examples of self assembled structure are the formation of Self Assembled Monolayers (SAMs) of alkanethiols on gold substrates[348] and chains of magnetic Janus nanoparticles.[349]

There are many advantages of non-directed self assembly, it has a low cost,

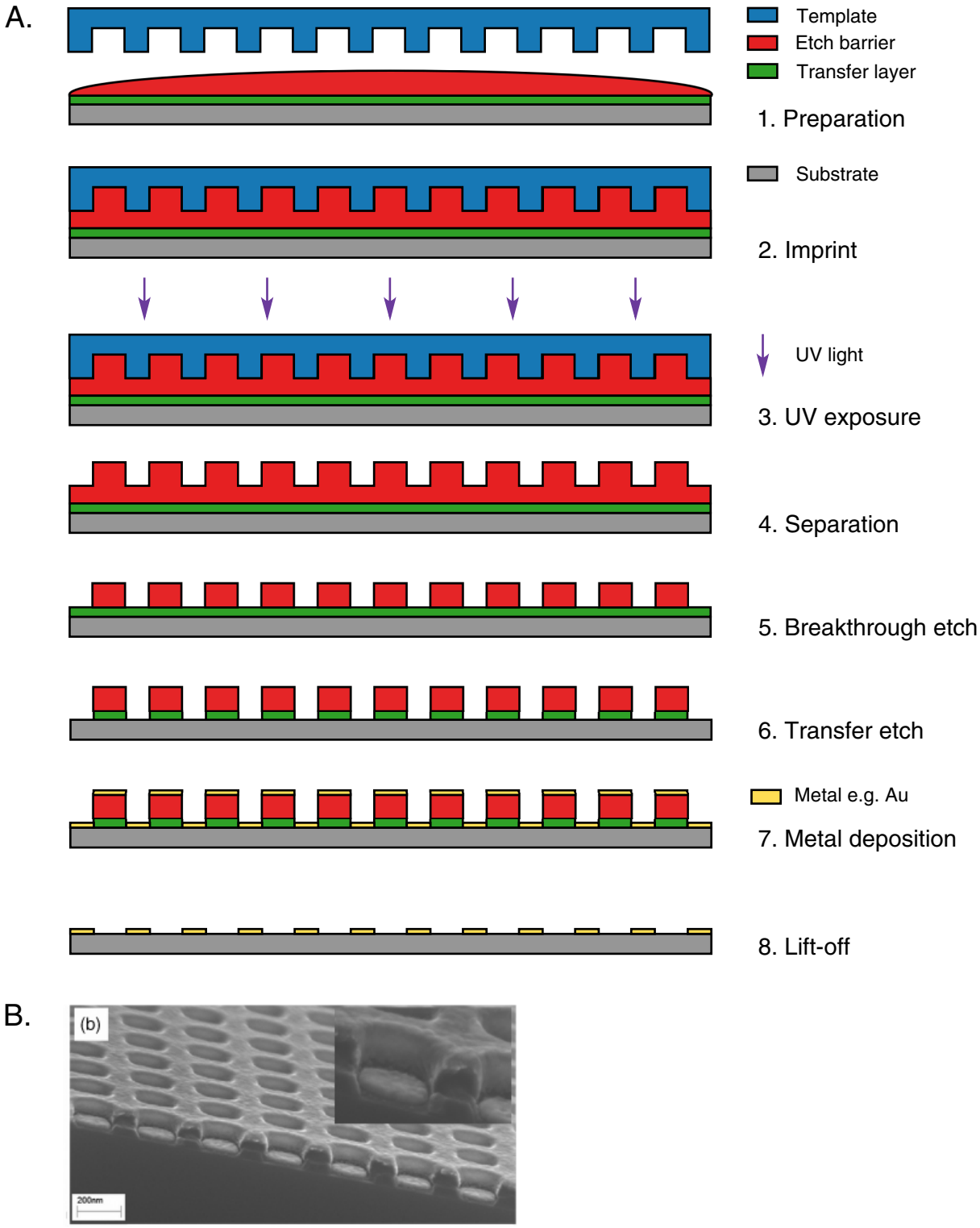

Figure 2.6: (A.) Schematic of Nanoscale Orthogonal Biofunctionalization Imprint Lithography (NOBIL) (B.) SEM image of a nanopatterned sample at the metal evaporation step (before lift-off). Reproduced and reprinted from Gaubert et al.[350]

high throughput and simple fabrication. These properties are balanced by the limited control of patterning which is largely determined by the chemical properties of the components as opposed to willful design. The second commonly encountered issue is defects. These are prone to occur in self assembled nanopatterns due to nanoscale substrate imperfections and configurations which remain trapped in a non ground state energy configuration.

Although self assembly occurs spontaneously it can also be directed or templated to provide patterning which is configurable and preferred. In this case techniques such as photolithography may be combined with self assembly to produce self assembly with fewer defects and enhanced dimensionality.[351]

Block Copolymer Lithography

One of the most common components for self assembly are Block Copolymers (BCP).[352] Block copolymers can come in a number of forms, the simplest and most common being di-block copolymers, though tri-block, alternating and tapered are available. Copolymer of these types will produce varying assemblies or morphologies based on the properties of the system in which they are found i.e. as a bulk[353, 354] or in solution.[355, 356] For block copolymers in solution the morphologies which can be produced include spheres, rods, bicontinuous rods, lamellar vesicles, 'onions', 'hamburgers' and more, in total numbering over 20. Solvent formation of morphologies is complex and dependent on a number of parameters in addition to the polymer itself, these encompass the solvent, polymer concentration, presence of additives, pH and temperature.[357, 358] Configurations can further be tailored by the polymer lengths to feature nanoscale dimensions which may later be transferred to substrates by dip coating, spin coating and roll casting.[359, 360, 361, 362] To apply the pattern to a substrate conventional etching techniques such as RIE may be used to remove the polymer

and etch the pattern.

Di-block copolymers as the simplest self assembling polymer have been studied extensively, generally in aqueous solutions. Some example copolymers which have been widely used and studied include PS-*b*-PAA, PS-*b*-PEO, PS-*b*-PVP[363] and PB-*b*-PEO,[364] PLA-*b*-PEO,[365] PBO-*b*-PEO.[366, 357]

Biological Applications

Lithography on the nanoscale has been adapted for biological use in areas of biosensing, bioengineering, bioimaging and bioassaying.[367] Regarding the conventional techniques, photolithography has yet to be used to produce patterning of biologically relevant proteins and molecules on the nanoscale, though microscale patterning has been shown.[368, 369, 370] From these microscale examples the majority focus on biosensing, creating surfaces that were chemically uniform and patterned through photodeprotection of selective regions that were subsequently functionalized to produce an bioactive surface.[369, 371]

Scanning beam lithography due to its ease at producing features at high resolution has been used to produce nanoscale pillars which in turn can increase the sensing capabilities of Fourier Transform Visible and IR spectrometry (FT-VIS-IR) by increasing the surface area for the attachment of biological species and enhancing photonic effects.[372, 373] SAMs have also been patterned by electron beam lithography to ablate regions which were then backfilled with species amenable to biological functionalization, for instance cysteamine, however, the patterning for this was microscale rather than nanoscale.[374, 375] Hong et al. have produced nanoscale arrays of as little as 50 nm feature size over 5 μm through electron beam etching of hydrogels which were later successfully functionalized with fluorescent markers.[376] Similar techniques and results (with some variation) have also been shown by others.[377, 378, 379]

FIB while having many of the same properties as EBL has been specifically utilized due to its precise milling capabilities which are relevant to cross section biological samples for further imaging by TEM.[380, 381]

SPL in the form of DPL has been used widely to produce biologically relevant patterned surfaces which are reviewed here.[61] Some interesting examples of which include the use of DPL to produce 400×50 nm^2 (lxw) rectangles with 16-thiohexadecanoic acid (MHA) metal ion coupling that were used to enable individual viruses to be patterned for biorecognition and infectivity studies.[382] Lee et al. have produced 6 μm arrays with < 100 nm circles 'painted' by DPL of MHA on gold which they could functionalize and use for biosensing of HIV-1 in in human blood samples.[382] Considering the conventional small areas which are usually produced by DPL, serial writing using cantilever arrays have also been used for biological purposes and have made it possible to pattern areas over 1 cm in tens of seconds and with resolutions of approximately 1 μm.[383, 384]

Imprint lithography thanks to its combination of potential high resolution and quick patterning rate (high throughput) has been used to fabricate protein arrays usable for bioligical experiments with < 100 nm features.[62] Similar results have been achieved with two biochemical functionalities and proof of concept 60 nm arrays of fibronectin were successfully seeded with human umbilical vein endothelial cells (HUVEC).[350] Although multicomponent patterning with NIL is difficult due to alignment, interesting results have been obtained by patterning with two separate, non conflicting stamps on the microscale and alternatively cross hatched patterns which conveniently overlap have been produced.[385, 386, 387, 388]

2.3.2 Nanoparticle Arrays

Fabrication

Spherical micelles formed from di-block copolymers are particularly interesting due to their ability to pattern large areas quickly and have been widely used to produce nanoparticle arrays. In this application micelles of given sizes are deposited onto substrates such as Si, glass or plastic and naturally pack into hexagonal lattices (arrays) due to the hexagonal packing providing a minimum energy configuration. The micelle diameter can be used to control the micelle density per unit area as well as the inter-micelle distance to $\sim$ 10 nm, while still patterning areas of multiple centimeters to produce large nanopatterned surfaces.

Despite their use in patterning large areas quickly and cheaply, BCL is not indefinitely robust and the unstable nature of polymer micelles over time in ambient conditions is a problem. To utilize the nanoscale patterning and enhance the stability spherical micelles can be used as a template, with an internal cargo acting as the stable patterning component.

An example of this technique is the loading of micelles with metal ions that are then dip coated into hexagonal arrays. The polymer shell is subsequently removed to leave the nanoparticle in a hexagonal pattern. Methods to selectively remove the polymer micelle shell while and reduce the metal ions to metallic nanoparticle have been optimized using plasma etching making the whole procedure relatively simple.

The production of stable metallic hexagonal nanoarrays in this way has the advantages of both nanometer resolution and feature size, large patterning areas and rapid production particularly if carried out in bulk. The main downside is, however, the lack of absolute pattern control. Overall these characteristics have made nanopatterning by BCP lithography best suited to applications which necessitate large patterning areas while tolerating a

small proportion of defects, for example biomaterial applications.

Metallic Arrays

Nanoscale arrays of metal nanoparticles formed from BCP lithography were initially produced in 1992.[64, 65, 66] Due to the nature of BCP lithography these arrays can be produced with uniform particle sizes of $\sim$ 10–100 nm, and interparticle spacing between 20 and 100 nm based on the properties of the BCP chosen.[63] Nanoparticle arrays of gold enabled relatively facile bio-functionalization through gold-thiol binding which has near covalent bond strength.[67] In comparison to other lithographic techniques BCP lithography has been used successfully for a number of biological studies and through patterning glass substrates has made it especially amenable to microscopic studies. The ability to pattern large areas has also been favorable when trying to obtain bulk characteristics of a cell population as only large areas can accommodate the many hundreds to thousands of cells which are needed for each experiment.[389]

Biological Applications

Arrays of nanoparticles are particularly controllable in terms of their interparticle spacing and biological studies have therefore focused on using this specific characteristic. Spatz et al. have functionalized hexagonal nanoarrays with a multitude of ligands and through variation of the nanoparticle spacing investigated the effect on cell behavior. Nanopatterned surfaces functionalized with integrin ligands spaced at 58 nm had over three times the number of adhered cells compared to similarly prepared 110 nm spaced surfaces.[69]

Other examples include single RGDfK peptides (a peptide responsible for cell recognition and adhesion) linked to gold nanoparticle arrays formed on a hydrogel substrate which caused selective cell adhesion of fibroblasts com-

pared to areas which did not contain the RGDfK peptide as shown in Figure 2.7.[70] To establish the effectiveness of BCP produced gold nanoparticle arrays the direct attachment of cells to functionalized nanoparticles has also been directly observed, confirming the effectiveness of this form of lithography for biological study.[67]

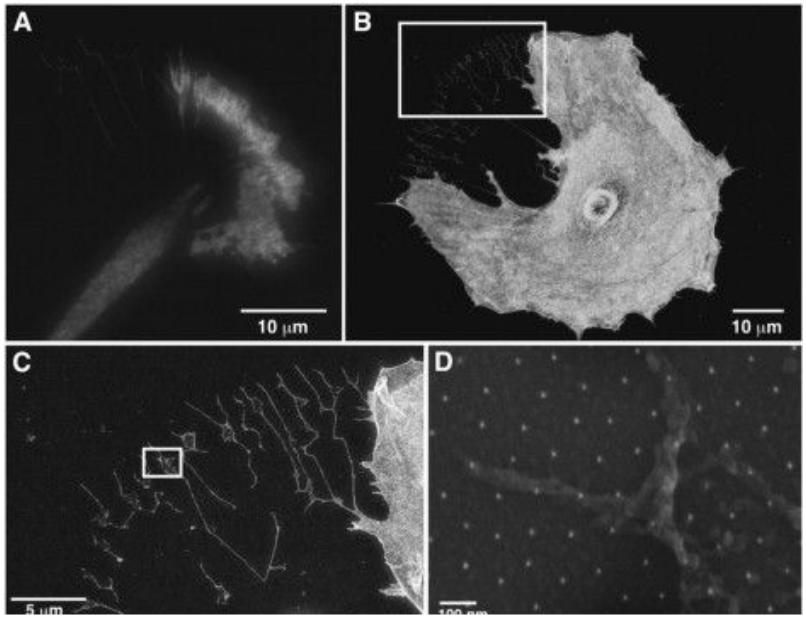

Figure 2.7: (A.) TIRF image of Rat Embryonic Fibroblasts (REF) cells expressing GFP-integrin β3 (B–D.) SEM images of REF in contact with 108 nm RGD nanopatterns. Reprinted from Cavalcanti-Adam et al.[70]

With the success of adhesion based nanoparticle array studies other ligands have been successfully conjugated and comparisons made between nanoarrays of various spacings. Tumor Necrosis Factor (TNF) which stimulates controlled cell apoptosis was presented as a ligand on a spatially organized gold nanoparticle surface. In a TNF receptor positive cell line, ligands spaced between 58 nm and 200 nm were capable of causing apoptosis whereas if the TNF spacing was greater than 200 nm almost no apoptosis was observed. In the case of these findings it was proposed that TNF receptors may be found in small domains of approximately 200 nm[60].

More recently, using hexagonal gold nanoparticle arrays with spacings between $\sim$ 20 and 100 nm have been employed to study immune cells. These arrays have then been used to assay T cell activation through the TCR using the same ligand at different spacings yielding results that suggesting T cells are only activated if the ligand spacing is less than 70 nm.[68, 37]

More advanced substrates combining BCP nanolithography and hydrogels,[390] binary patterning of different nanoparticles[391] and micropatterning combined with nanopatterning[392] have each been achieved giving greater flexibility for biological applications.

It can therefore be argued that biological studies utilizing BCP lithography and nanoparticle arrays are powerful techniques for advancing our understanding of cell biology. The current uses of nanoparticle arrays has for instance contributed to the specific hypothesis that the nanoscale spacing and or density of ligands is broadly relevant and important to cellular signaling and hence function.

2.4 Superresolution Microscopy

2.4.1 Overview

Optical light microscopes using compound lenses have been used since the 17th century to observe the details of biological specimens that were otherwise indiscernible by the human eye. With subsequent developments in optics that provided higher Numerical Apertures (NA), magnifications and improved engineering, microscopes continued to provide greater resolution. Using the highest magnification lenses and largest NA, sample features which are $<$ 250 nm in air and $<$ 200 nm with oil objectives (thanks to the smaller difference in refractive index between the oil and the lens) nonetheless remained unobservable.

The upper limit of conventional light microscopy is defined by the diffraction of the light used to illuminate and observe the sample, a result of the lights wavelength, which leads to optical micrscoscopes being known as diffraction limited. The effect of diffraction limited microscopy is the blurring of features, which at spacings of $\sim$ 250 nm hinder the resolution of any two objects separated by less than this distance. This inherent limit is defined by the Abbe resolution shown in Equation 2.1 and relates the wavelength of light, the NA with the resolution, and was understood as far back as 1873.[393, 394]

$$d = \frac{\lambda}{2NA} \tag{2.1}$$

Where d is the resolvable feature size, λ the wavelength of light and NA the numerical aperture of the length. For optical microscopes $\lambda \sim 550$ nm and the maximum NA possible with oil objectives is ~ 1.5, giving the equivalent resolution of $\sim$ 200 nm.

This level of resolving power is sufficient to observe cells, their nuclei and some structures such as filopodia but was not great enough to image subcellular structures less than 200 nm in size. Despite the inherent resolution limit, another restriction was the primary cause of subcellular structures from being determined by optical microscopy—the lack of visible contrast between structures and the background. To enhance contrast dyes which provided selective subcellular staining were used, the first of which being carmine in 1858.[395] Other dyes with various staining preferences continued to be discovered, important examples are: haematoxylin and eosin in 1896 which stains the nucleus purple and cytosol pink,[396] eosin in combination with methylene blue and Azure B (Giemsa stain) in 1904 which stained parasites such as malaria, and provided enough contrast for histopathological diagnosis.[397] and the Feulgin stain in 1924

which stains chromosomal material red.[398] Later other microscopic developments which enhanced contrast such as phase contrast (1935) and polarization microscopy (1939) would also be developed to great success within the field of Cell Biology.[399, 400]

Rather than discerning objects by the scattered, reflected and absorbed light from illuminated objects the next great development in microscopy—fluorescence microscopy—offered the potential for even greater contrast between objects within the cell. Fluorescent dyes had been known since 1871 with fluoresceine, and theoretically could provide contrast between a huge number of components by their individual excitation.[401] In 1911 the first fluorescence microscope was used by Heimstädt, however, it was made difficult by the major challenge of collecting only emitted fluorescent light[402] It was not until 1929 with Ellinger and Hirt's development of epifluorescent microscopy which filtered the excitation light (to select for the optimal excitation wavelength) and gave contrast by blocking subsequent excitation light using a filter just before the ocular, that fluorescence microscopy became useful.[403]

In 1941 Coons et al. demonstrated the first effective use of fluorescence microscopy in a biological context using anthracene isothiocyanate, with the caveat that autofluorescence of tissues at similar wavelengths led again to poor contrast.[404] In 1942 then fluorescein-iso-cyanate was used as a fluorochrome for labeled antibodies to selectively stain *Pneumococcus* strain 3, this time with excellent results.[405] The staining of structures with labeled antibodies is now referred to as immunostaining and has become an indispensable technique in cell biology especially as antigens related to cell structures and specific proteins have been targeted with relative ease. Combined with dichroic mirrors (taking place in the year 1967) which reflect narrow wavelength bands while transmitting all other, immunostaining fluorescence microscopy was greatly enhanced by allowing the emission of fluorescent

light to be split, so that detection of multiple fluorochromes (and therefore cell structures/proteins) could be imaged together.[406] The combination of fluorescent microscopy—to enable contrast, and immunostaining—to label almost any structure within the cell, were arguably two of the most important developments for microscopic study of cellular biology.

Following the body of work which was achieved as a result of these advancements the focus again returned to improving the resolution of immunostained structures within the cell. Laser Scanning Confocal Microscopy (LSCM) in 1961/87 improved greatly the Z-axial resolution by eliminating out of focus light using a pinhole between the objective and the detector.[407, 408, 409] Fluorescence imaging of even thick samples which would otherwise be be flooded with light from the bulk sample was thanks to this development made possible. Total Internal Reflection Fluorescence (TIRF) in 1981 would improve the Z-axial resolution further still to 100 nm, with the caveat of only imaging a cell's structure within the same 100 nm of the glass coverslip they were required to be in contact with.[410] The invention of TIRF would later also be a crucial stage in enabling the XY-axial resolution to be pushed beyond the diffraction limit.[411]

2.4.2 Superresolution Techniques

It was only after the long list of developments described above that the first superresolution (resolutions beyond the diffraction limit of light) microscopy techniques would be achieved. To date, there are a multitude of methods used to 'break' this diffraction limit, each using a different fundamental principle to obtain resolutions below $\sim$ 200 nm. The techniques proven by time and commercial success are Stimulated Emission Depletion (STED),[412] structured illumination (SIM),[413] and single molecule localization methods, which include Photoactivated Localisation Microscopy (PALM)[32] and Stochastic Optical Reconstruction Microscopy (STORM).[414] An overview

Table 2.4: A list of the superresolution microscopic technologies, their resolutions, benefits and drawbacks.

Technique	X,Y-resolution (nm)	Z-resolution (nm)	Benefits	Drawbacks
STED	35	550	multifluorochrome (3), no post-processing, tissue and in-vivo	high axial resolution, photo-bleaching
SIM	100 (SSIM $\sim$ 50)	300	multifluorochrome (4), large field of view	post-processing, artefacts
PALM	2–25	50	multifluorochrome (3–6), single molecule counting	dim, post-processing
STORM	20	50	multifluorochrome (3–6), bright	post-processing

(All values are approximate and depend on a combination of factors.[73])

of each technique is shown in Table 2.4.

Stimulated Emission Depletion Microscopy

Current confocal fluorescent microscopes excite only a small region of the sample using a focused laser which scans laterally across the sample to produce a 2D image. The excitation beam, as before, is diffraction limited and can represented by a point spread function which describes the shape and intensity of the beam in both lateral and axial directions. In diffraction limited systems the PSF has the form of a disc (Airy disc[393]) with a width equal to the resolution limit i.e. $\sim$ 200 nm. Given that the excitation beam is diffraction limited, the fluorochrome fluorescence emission is similarly restricted.

Stimulated Emission Depletion Microscopy (STED) as a superresolution technique works by decreasing the size of the point spread function (PSF) produced by a conventional laser scanning confocal microscopes (LSCM). To achieve this result a second 'STED' beam, shaped to resemble a ring is aligned around the excitation beam, overlapping with it and leaving only a $\sim$ 35 nm hole in the center which is illuminated by the excitation beam. STED beams are chosen with the correct wavelength to cause stimulated emission from the fluorochromes which were otherwise excited by the excitation beam, preventing their relaxation by fluorescent emission. Instead in the process of stimulated emission the excited state emits a photon at the same wavelength as the STED wavelength, which can be separated from fluorescent emission.[415]

Through this mechanism fluorochromes stimulated by the excitation beam and STED beam will not fluoresce while the central region of the excitation beam with no STED overlap still result in fluorochrome fluorescent emission. The best possible resolution of STED is currently $\sim$ 35 nm and images obtained require no post-processing. Difficulties that arise using STED often

include the accurately alignment of the STED and excitation beams, as well as the high power required to achieve effective stimulated emission which rapidly and permanently bleach most fluorochromes.[415]

Structured Illumination Microscopy

Structured Illumination Microscopy (SIM) uses a drastically different method to bypass the diffraction limit; a sample is first illuminated by a grid like pattern rather than a single beam (as is common for LSCM) and the image captured by a sensor. The grid like illumination is then rotated about a central point, and subsequent diffraction limited images are captured sequentially, in the first published use for example 12. The collection of images when overlaid form a moiré effect due to the overlapping grid illumination and at the fringes of this moiré effect information about the structure can be computationally restored giving a final apparent resolution 2-fold greater than the original i.e. a final resolution of 100 nm. SIM to its advantage requires no additional lasers or complex fluorochrome choice, it can also be used with wide field microscopes producing high resolution images of large areas. Drawbacks include the need for post-processing which must be applied to obtain the superresolved image. Errors in image acquisition or sample preparation can also be problematic and lead to artifacts in the final image.[416]

Single Molecule Localization

PALM and STORM microscopy are Single Molecule Localization Microscopy (SMLM) techniques which share the same underlying principle to localize fluorochromes (and therefore generate an image) but differ in the experimental procedures used to produce fluorescent signal. SML microscopies excite fluorochromes similar to other fluorescence microscopies and detect their fluorescence in a diffraction limited image. As long as the diffrac-

tion limited PSF ($\sim$ 250 nm) of a single fluorochrome has no overlap with another fluorochrome its position can be accurately determined by computational fitting the PSF to determine the highest intensity region where the fluorochrome is located. The result of this procedure is a reduction in the apparent resolution from 250 nm to $\sim$ 20 nm, as shown in Figure 2.8 (A.).

The experimental challenge of SMLM is in exciting only a small proportion of fluorochrome at any one time so that their fluorescence emission does not overlap which would otherwise prevent a single PSF from being localized accurately. To prevent fluorochrome overlap conditions which promote stochastic fluorescence emission are chosen, where fluorochromes cycle between 'bright' and 'dark' states making them appear to blink (Figure 2.8 (B.)). Assuming a small proportion of the total fluorochromes are 'bright' at any one time and the fluorescence, when it does occur, is stochastic, there is a comparatively low likelihood of two fluorochromes next to each other fluorescing at the same time. Of course to produce an image from individual localized points a huge collection of images must be obtained over a given time period, subsequently localized by post-processing, and then later combined.[417] An example of this process is shown in Figure 2.8.

2.4.3 PALM and STORM

The methods used to cause stochastic fluorochrome emission vary between SMLM techniques and define their naming. PALM uses endogenously expressed fluorescent proteins such as Photoactivatable Green Fluorescent Protein (PA-GFP), Eos Fluorescent Protein (EosFP) and Kaede, Kikume Green-Red (KikGR) which have the properties that they photoswitch intrinsically by a number of mechanisms (photoactivated from a nonfluorescent state, photoswitched from one spectral state to another and reversible photoswitching between dark and bright states or between two bright states) giving stochastic emission. For PALM each endogenous fluorescent protein has

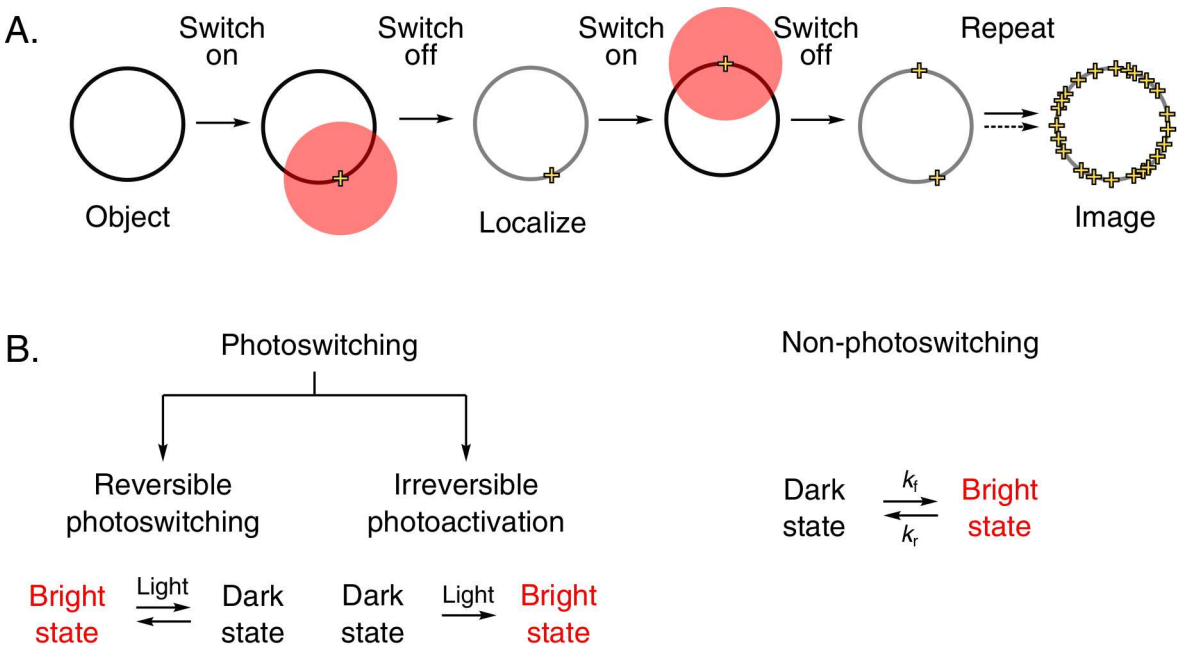

Figure 2.8: (A.) Principle of point spread function localization and image reconstruction from combined frames. (B.) Mechanisms of stochastic transition from bright to darks states by photoswitching and non-photoswitching. Reproduced from Dempsey et al.[418]

differing properties, requiring optimized excitation wavelengths and beam power to achieve blinking. The nature of stochastic blinking of fluorescent proteins varies little and for many proteins only a single or few cycles occur before bleaching.[419]

The other popular SML technique, STORM instead uses immunostaining with conventional small molecule fluorochromes attached and combined with conventional immunostaining to label structures. Stochastic blinking is induced by a number of methods depending on the fluorochrome. In the simplest instance continuous excitation at a given wavelength alone can result in stochastic photoswitching, for instance with Alexa Fluor 647. In other instances fluorochromes may transition from bright to dark states due to the influence of the chemical solvent in which they are found. This effect can be caused by primary thiols and hence β-Mercaptoethanol (βME) and

2-Mercaptoethylamine (2-MEA) are often used in superresolution imaging buffers. Dempsey et al. have evaluated a number of fluorochromes for their stochastic properties.[418]

Limitations

In general, for both PALM and STORM, a clear limitations is that acquisition times needed to collect the huge number frames (thousands–millions) so that each fluorochrome can be individually localized and later combined to reconstruct the superresolved image, this makes these methods difficult for anything but fixed samples. Up until very recently to obtain accurate PSFs with minimal overlap and low bulk/background excitation TIRF was the only imaging method available, bringing with it its inherent limitation of imaging at the cell-glass interface. Light sheet excitation (a thin beam of light shone laterally through a sample) is currently under development as a method to excite fluorochromes in a thin slice (thin axial region) selectively. This would eliminate the need for TIRF, allowing SMLM to image deep within the cell and also be used for 3D imaging.

The collection of large numbers of images requires some computationally demanding analysis to localize each point and given the variation in algorithms used to carry out the localization process, superresolved images produced from identical data can differ with different algorithms. This is a particularly important consideration if quantitative data is required from a SMLM, for instance fluorochrome counting.

Due to the single photoswitching cycles of some fluorescent proteins before bleaching, PALM can theoretically be used to carry out single molecule counting. As a result of the single transition the number of localizations is, however, low and images can contain less detail especially if the protein expression is not extremely high which at times can be difficult to achieve. STORM on the other hand, due to the greater switching cycles, which are

commonly at least 1 order of magnitude greater than fluorescent proteins therefore produce far more localizations in a given acquisition time. Localizations can also be enhanced by increasing the fluorochrome labeling of an antibody. Examples of all superresolution imaging modalities can be seen in Figure 2.9.

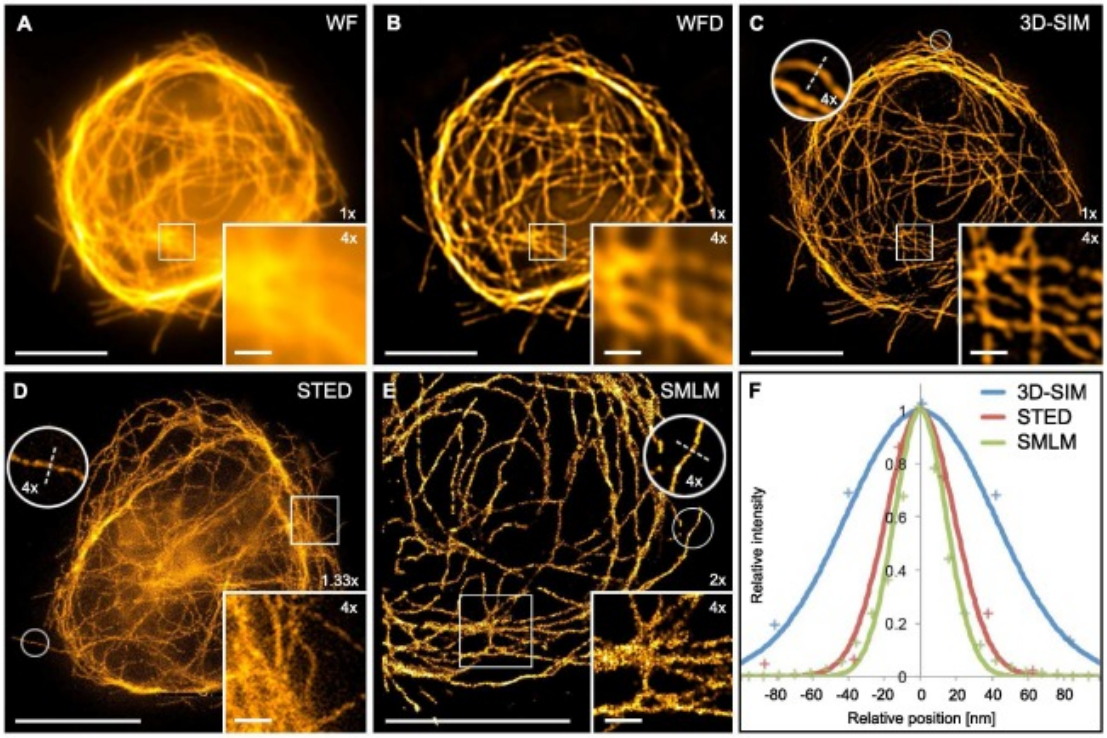

Figure 2.9: (A–E.) Comparison images of superresolution techniques using immunofluorescence labeled microtubules in Drosophila macrophages. WF – Widefield, WFD – Widefield and Deconvolution, 3D-SIM – 3D Structured Illumination Microscopy, STED – Stimulated Emission Depletion Microscopy and SMLM – Single Molecule Localization Microscopy, here using Stochastic Optical Reconstruction Microscopy (STORM). (F.) The relative resolutions of each technique has been measured by comparison of the line scans from single microtubules. Reprinted from Demmerle et al.[420]

Biological Applications

Superresolution microscopic techniques were produced with the hope of uncovering the nanoscale workings of the cell by observing them directly. To date they have been used to produce insights into a number of biological structures and processes for instance Betzig and Schroff et al. utilized two color PALM to show that adhesion complexes formed from pairs of proteins are a part of a more complex interlocking protein nano-aggregate. This observation was impossible to make by confocal microscopy.[421] STORM has been applied to image the synapses between neurons and their target cells in the brain, showing that there is a large degree of variation in neurotransmitter receptor composition and distribution between synapses. It has also revealed the highly orientated organization of presynaptic scaffolding proteins.[422] Using live cell STORM, hippocampal neuron were imaged showing dynamics of the membrane, mitochondria and endoplasmic reticulum (ER).[423] Together these applications make up only a small collection of the total biological investigations carried out using superresolution techniques.[424]

Material Characterization

Superresolutions techniques have generally been applied to biological systems, however, they are applicable to a number of imaging applications which would benefit from the extremely high resolution. Ullal et al. in 2009 used STED to image the morphology of poly(styrene-block-2-vinylpyridine) block copolymers which self assembled into numerous structures including mesoporous, lamellar and helicoidal screw dislocations.[425] Similarly phase separation in a poly(styrene-block-ethylene oxide) diblock copolymer thin film has been imaged using PALM.[426] Gustafsson in his exemplary publication of SIM in fact images 50 nm polystyrene beads which although not the focus of the paper give another example of superresolution micro-

scopies potential in non-biological applications.[413]

In the realm of nanoparticle nanoarrays Lohumeller et al.[427] briefly used PALM to image ephrin-mEos-His10 attached to the gold nanoparticles. They demonstrated the ephrin-mEos-His10 localizations were spaced similarly to the nanoparticle arrays interparticle spacing by calculating the radial distribution function.

Chapter 3

Synthesis of Graphene Oxide Antibody Nanoclusters

3.1 Scope

In this chapter Nanoscale Graphene Oxide (NGO) sheets have been used as a framework for the tethering, and hence clustering, of Monoclonal Antibodies (mAbs), which are used as ligands to form supramolecular species (NGO-mAb). NGO sheet sizes of between $\sim$ 50–300 nm have been created forming clusters of comparable size to the the receptor nanoclusters found on primary (human) NK (pNK) cells.[18, 19]

A bottom up approach for the synthesis has been used, beginning with covalent conjugation of 8-arm Poly(ethylene glycol)-amine (PEG(8)) to provide NGO sheet stability in physiologically relevant salt solutions. The addition of PEG also adds functional groups for the attachment of the mAbs, which were conjugated using a biotin-streptavidin linking methodology.[428] Anti-human CD16 (α-hCD16) and an isotype control antibody—anti-mouse IgG1 (α-mIgG1), were seperately conjugated to NGO forming two supramolecular species—NGO-α-hCD16 and NGO-α-mIgG1. A schematic of the contrived structure for these is illustrated in Figure 3.1.

The measurement of both the NGO-mAb conjugation efficiency in combina-

tion with the NGO sheet size distribution was used to calculate the ratio of antibodies to NGO sheets (NGO:mAbs) in each NGO-mAb species. The results of this showed that between 70–200 mAbs were covalently tethered to NGO sheets of between 70 and 170 nm in diameter creating ligand densities mimetic to receptor nanoclusters.

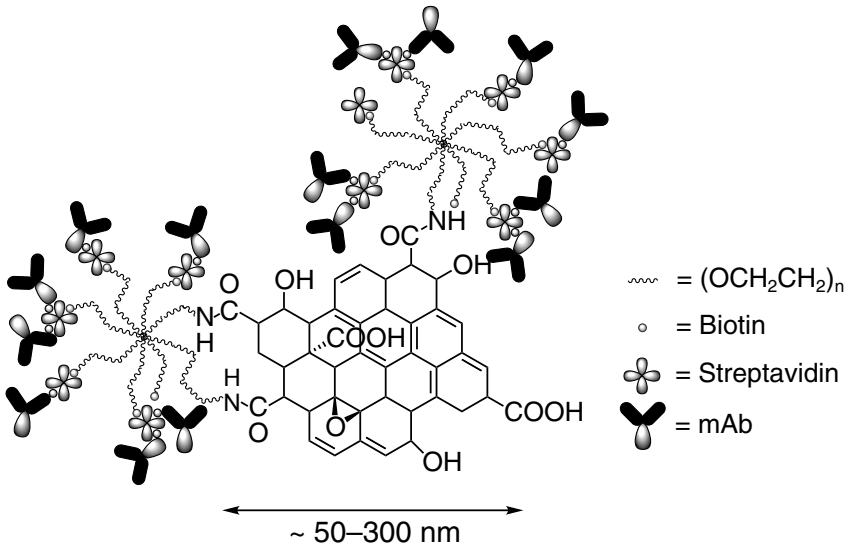

Figure 3.1: Schematic illustration of NGO-mAb nanoclusters showing key features of the structure including: NGO sheet framework, 8-arm star PEG for steric stability, biotin-streptavidin conjugation and conjugated mAbs. Not to scale.

3.2 Methods

3.2.1 NGO Stabilization with Poly(ethylene glycol)

7.5 mL graphene oxide (GO) aqueous suspension (2-DTech) was diluted with 7.5 mL ultrapure water (Milli-Q, 18.2 MΩ cm) to give a final concentration of $\sim$ 1 mg/mL. The solution was then bath ultrasonicated for 1 hr. 1.80 g NaOH and 1.50 g chloroacetic acid were added to the GO suspension and bath sonicated for a further 4 hrs. The resulting nano GO-COOH (NGO-COOH) solution was purified by repeated rinsing with

ultrapure water and centrifugal filtrations using a 100 kDa MWCO filter (Amicon Ultra, Millipore). A final pH $\sim$ 7 was achieved using 1M HCl or H_2SO_4. 0.30 g (20 mg/mL) 8-arm poly(ethylene glycol)-amine (8-arm PEG-amine 40,000 MW, Creative PEGWorks) was added to the NGO-COOH suspension and the mixture sonicated for 5 min after which 0.0225 g (8 mmol/L) N-(3-Dimethylaminopropyl-N'-ethylcarbodiimide) hydrochloride (EDC, Sigma-Aldrich) was added in two parts, and the mixture left to react overnight with constant agitation. 30 μL (40 mmol/L) 2-mercaptoethanol (Invitrogen) was then used to quench any unreacted EDC giving unpurified nano GO-PEG (NGO-PEG). Unreacted EDC and 8-arm PEG-amine were removed by repeated rinsing and centrifugal filtrations as above. Solvent exchange from water to Dulbecco's Phosphate Buffered Saline with $MgCl_2$ and $CaCl_2$ (PBS, pH 6.9–7.1, Sigma-Aldrich) was then carried out by repeated rinsing with PBS with $MgCl_2$ and $CaCl_2$ and centrifugal filtration. Large unstable aggregates were removed by centrifugation 10,000 g, 30 mins, discarding the pellet to yield NGO-PEG(8). NGO-PEG(4) was produced in the same manner except using 4-arm poly(ethylene glycol)-amine (4-arm PEG-amine 20,000 Mn, Sigma-Aldrich).

Batch 2 of NGO-PEG was produced using the same method as above except for an additional, final centrifugation at 16,000 g for 4 hrs, discarding the pellet to yield the final stable NGO-PEG.

3.2.2 Labeling and Biotinylation of Antibodies

Anti-human CD16 (clone 3G8 Ultra-LEAF, Biolegend or BD Biosciences) and mouse IgG1 κ-isotype (clone MOPC-21 Ultra-LEAF, Biolegend BD Biosciences) were concentrated to 5 mg/mL by centrifugal concentration using a 10 kDa MWCO filter (Amicon Ultra, Millipore). 100 μL, 5 mg/mL anti-human CD16 or anti-mouse IgG1 was reacted with 1.5 μL, 10 mg/mL Alexa Fluor 546 NHS ester (final concentration 0.148 mg/mL, Thermo Fisher

Scientific) for 1.5 hrs at RTP. Unreacted Alexa Fluor 546 NHS ester was removed by repeated rinsing and centrifugal filtration at 8000 g using a 10 kDa MWCO filter yielding anti-human CD16-AF546 and anti-mouse IgG1-AF546.

80 μL, 4 mg/mL anti-human CD16-AF546 or anti-mouse IgG1-AF546 were reacted with 2.1 μL, 20 mmol/L NHS-PEG_4-biotin (final concentration 0.512 mmol/L, EZ-Link^{TM} NHS-PEG_4-Biotin, No-Weigh^{TM}, Thermo Fisher Scientific) dissolved in PBS with $MgCl_2$ and $CaCl_2$ and left for 30 mins at RTP. Unreacted NHS-PEG_4-biotin was removed by repeated rinsing and centrifugal filtration at 8000 g using a 10 kDa MWCO filter giving anti-human CD16(biotin)AF546 (α-hCD16-(biotin)AF546) and anti-mouse IgG1(biotin)AF546 (α-mIgG1-(biotin)AF546).

3.2.3 NGO-Streptavidin Synthesis

100 μL, $\sim$ 0.7 mg/mL NGO-PEG(8) was reacted with 9 μL, 20 mmol/L NHS-PEG_4-biotin (EZ-Link^{TM} NHS-PEG_4-Biotin, No-Weigh^{TM}, Thermo Fisher Scientific) dissolved in PBS with $MgCl_2$ and $CaCl_2$ and allowed to react for 1 hr at RTP. Excess NHS-PEG_4-biotin was removed by repeated rinsing and centrifugal filtration at 8000 g using a 10 kDa MWCO filter (Amicon Ultra, Millipore) yielding NGO-biotin.

200 μL, 0.6 mg/mL ($A_{700} = 0.2$) NGO-biotin in PBS with $MgCl_2$ and $CaCl_2$ was then mixed with 144 μL, 5 mg/mL streptavidin with thorough mixing. Excess streptavidin was removed by repeated rinses and centrifugal filtration 6000 g, 100 kDa MWCO (Amicon Ultra, Millipore) yielding NGO-streptavidin.

Batch 2 was produced using the same principle except for 4 mL, 0.006 mg/mL NGO-biotin in PBS with $MgCl_2$ and $CaCl_2$ was added dropwise to 8 mL, 1 mg/mL streptavidin (Thermo Fisher Scientific) with constant stir-

ring and left to react for 2 hrs at RTP. Excess streptavidin was removed by repeated rinses and centrifugal filtration 6000 g, 100 kDa MWCO yielding NGO-streptavidin.

3.2.4 Antibody Conjugation to NGO-Streptavidin

17 μL, 1.5 mg/mL anti-CD16-AF546-biotin or anti-mouse IgG1-AF546-biotin κ-isotype (final concentration = 0.418 mg/mL) was added to 44 μL, (A_{700} = 0.128) 0.4 mg/mL GO-streptavidin and allowed to react overnight at 4 °C. The final product NGO-α-hCD16 and NGO-α-mIgG1 were then separated into fractions by successive centrifugation at 10000 g for 5 mins. The supernatants were removed and then re-spun with the pellet resuspended in 10 μL PBS with $MgCl_2$ and $CaCl_2$. This was repeated a further 2 times yielding NGO-mAb samples labeled NGO-mAb fraction 1-4 (fraction 4 in this case was the final stable NGO-mAb supernatant).

In Batch 2, 450 μL, 0.008 mg/mL NGO-streptavidin in PBS with $MgCl_2$ and $CaCl_2$ was added dropwise to 50 μL, 4 mg/mL anti-CD16-AF546-biotin or anti-mouse IgG1-AF546-biotin (final concentration = 0.4 mg/mL) with constant stirring and then allowed to react overnight at 4 °C.

3.2.5 Infrared & Ultraviolet-Visible Spectroscopy

Absorbance IR spectra of freeze dried NGO-PEG were obtained on a PerkinElmer Spectrum 100 Series FT-IR after background subtraction with a 10 scans average. Absorbance measurements of the UV-vis spectra were carried out using a Nanodrop 2000 UV/Vis Spectrophotometer. NGO, NGO-PEG and protein/antibody solutions were measured using a 1 mm pathlength with automatic background subtraction using the appropriate solvent.

3.2.6 Stability of NGO-PEG in Salt Solutions

1 M NaCl was produced by dissolving 1.461 g NaCl in 25 mL ultrapure water (Milli-Q, 18.2 MΩ cm). Serial dilution with ultrapure water of the stock 1 mol/L solution was carried out to produce solutions of concentration 1, 0.5, 0.3, 0.15, 0.1 and 0.05 mol/L. 450 μL of each NaCl solution was then taken and 50 μL of either GO, NGO-PEG (4-arm) or NGO-PEG (8-arm) (NGO-PEG(4) and NGO-PEG(8)) were added and mixed thoroughly. Images were taken immediately after mixing and 48 hrs later for comparison.

3.2.7 Atomic Force Microscopy

Atomic Force Microscopy (AFM) measurements were made on a Bruker Innova microscope in tapping mode using aluminium-coated silicon probes tips (NCHV-A, Bruker Nano). Samples were prepared by depositing a droplet onto a silicon wafer substrate followed by drying in air.

3.2.8 Thermal Gravimetric Analysis

Thermal gravimetric analysis (TGA) was carried out on a Mettler Toledo TGA-DSC1 using sample masses of $\sim$ 1 mg. Experiments were carried out in an N_2 atmosphere introduced at 50 mL/min using a temperature range of 100–800 °C and using a heating rate of 10 °C/min. The percentage of PEG(8) grafted to NGO-COOH was calculated by accounting for complete decomposition of PEG(8) on NGO-PEG between 300 and 440 °C.

3.2.9 NGO-mAb Conjugation Confirmation

For Batch 1, 8 μL NGO-α-mIgG1 and NGO-α-hCD16 were centrifuged at 16,500 g for 5 hrs to fully pellet the NGO-mAb. The resultant supernatant was carefully removed and measured by UV-vis spectroscopy to check for

absorbance at 556 nm related to unbound anti-human CD16-AF546-biotin and anti-mouse IgG1-AF546-biotin.

For Batch 2, the resultant NGO-α-hCD16 and NGO-α-mIgG1 were purified by repeated centrifugation 16,000 g, 6 hrs and washes with 200 μL PBS with $MgCl_2$ and $CaCl_2$ with a final resuspension in 5 μL PBS with $MgCl_2$ and $CaCl_2$. The supernatant from the final wash step was measured by UV-vis spectroscopy to check for absorbance at 556 nm related to unbound anti-human CD16-AF546-biotin and anti-mouse IgG1-AF546-biotin.

3.2.10 Biotinylation Quantification

Biotinylation levels of antibodies were measured using the Pierce^{TM} Biotin Quantification Kit using the provided instructions. HABA-avidin premix was dissolved in 100 μL ultrapure water (Milli-Q, 18.2 MΩ cm). 160 μL PBS was added to each well of a 96 well plate (Corning). 20 μL of the HABA-avidin solution was added to each well and thoroughly mixed. The absorbance at 470 nm was then measured. 470 nm was chosen in preference to the recommended 500 nm to minimize the absorbance associated with the Alexa Fluor 546 labeled antibodies. 20 μL of sample or positive control (HRP) was then added to the HABA-avidin solution, mixed thoroughly and allowed to equilibrate for 5 minutes. The absorbance was then remeasured at 470 nm. Each absorbance measurement was read using a VersaMax^{TM} ELISA microplate reader and repeated three times with an average taken.

The equation used to calculate the biotin:mAb ratio here shown in Equation 3.1.

$$\text{biotin:mAb} = \frac{(\Delta A_{470}/(\varepsilon_{470} \times \text{path length})) \times \text{mAb dilution}}{\text{mAb conc (mol/L)}} \tag{3.1}$$

Where, HABA/avidin ε_{470} (M^{-1} cm^{-1}) $\approx$ 20500, the path length (cm) $= 0.5$ and the protein dilution $= 200/20 = 10$.

To determine the biotinylation of NGO-biotin and account for the absorbance of graphene at 500 nm a control absorbance measurement of NGO-PEG at equal concentration (as measured by their absorbance at 700 nm using Uv-vis) was taken and subtracted from the absorbance of the NGO-biotin.

3.3 Results and Discussion

3.3.1 Stabilization

3.3.2 PEGylation

Unfunctionalized NGO is unstable in solutions with salt concentrations relevant to biological study as illustrated in Figure 3.3. The stability of NGO is, however, well established in water with low salt concentrations due to the electrostatic repulsion of negatively charged functional groups, including epoxides, hydroxyl and carbonyls, which prevent flocculation. In solutions of high salt concentration, charge shielding occurs, reducing the repulsive forces and resulting in sheet stacking parallel to the basal plane. Such stacking over time results in the colloidal instability which reduces the potential uses of unfunctionalized NGO.

The addition therefore, of sterically hindering groups on the basal plane of NGO sheets is a common method to prevent instability even at high salt concentration. Steric hindrance was applied here by the covalent conjugation of an 8-arm poly(ethylene glycol)-amine star (40 kDa) polymer using a previously established method with modifications[46]. The first step in this synthesis was the conversion of hydroxyl groups to carbonyl groups in a Williamson ether synthesis by the reaction with chloroacetic acid under basic conditions. The carbonyl groups in this case were used as linking points for the attachment of the amine terminated PEG chains by EDC coupled

amide formation.

The initial conversion of hydroxyl groups of NGO to carbonyl groups and the intermediate product, termed NGO-COOH, was confirmed by FTIR spectroscopy, shown in Figure 3.4. Freeze dried samples of the initial NGO starting material showing weak C=O absorption at 1725 cm^{-1} which shifted to a relatively strong absorption at 1591 cm^{-1} most likely low as it was the salt, in addition to a marked decrease in the C−O stretch intensity at 1063 cm^{-1} indicating a decrease in alcohol functional groups. After EDC coupling of the PEG the FTIR showed the emergence of a C=O stretch at 1638 cm^{-1} expected of amide bond formation, C−H stetch at 2870 cm^{-1} due to the ethylene backbone and finally the reappearance of a strong C−O at 1090 cm^{-1} due to the ether groups present in PEG.

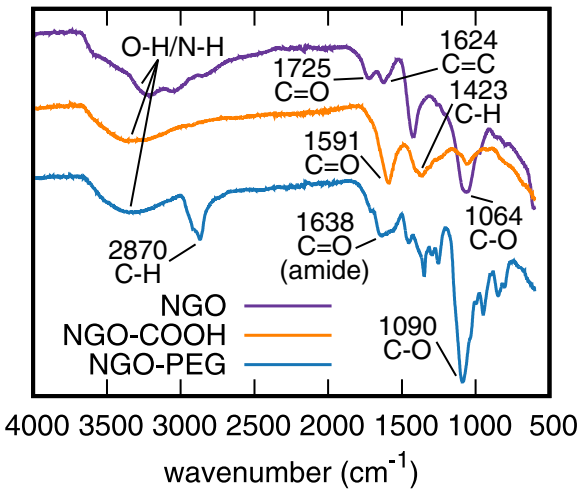

Figure 3.2: Confirmation and characterization of the PEGylation of NGO. FTIR spectra of NGO, NGO-COOH intermediate and NGO-PEG. Characteristic absorptions associated with C=O (amide), C−H (alkane) and C−O ether appearing between NGO and NGO-PEG.

3.3.3 Salt Stability Testing

The simple conjugation of any PEG chain does not singly afford steric stability. A number of different PEG polymers were therefore conjugated and the stability of each assessed. This included linear PEG amine chains (MW = 2000 Da), 4-arm (Mn = 10,000 Da, PEG(4)) and 8-arm (MW = 40,000 Da, PEG(8)) PEG-amine star polymers respectively, and their stability tested by addition to solutions of varying NaCl concentrations from 0.1-1 M, and a separate PBS condition due to its pervasive use in the field of cell biology. The salt concentration of medical saline is $\sim$ 0.15 M and total salt concentration of PBS is similar.

Initially the NGO was added to each salt solution and thoroughly mixed to ensure dispersion. After 48 hours the stability was compared by visual inspection with the results shown in Figure 3.3. UnPEGylated NGO shows no stability in all solutions after 48 hrs as shown by the flocculation of the NGO in the images compared to the well dispersed solution at time 0. NGO-PEG(4) on the other hand was stable between 0.5 and 1 M and PEG(8) showing stability at all concentrations.

While stability in salt solutions above 0.15 M was sufficient for biological use, later functionalization steps used in the formation of NGO-mAb, including the addition of hydrophobic biotin and fluorochromes further negatively impacted the stability of the NGO-mAb species. It was therefore beneficial to continue functionalization using only the most stable NGO-PEG(8) species, with the additional benefit of the larger number of functional groups due to the 8 amine terminated arms.

3.3.4 PEG Grafting Quantification

The exact mass percentage grafting of PEG(8) was obtained by Thermo Gravimetric Analysis (TGA) from two batches of NGO-PEG(8), to accurately

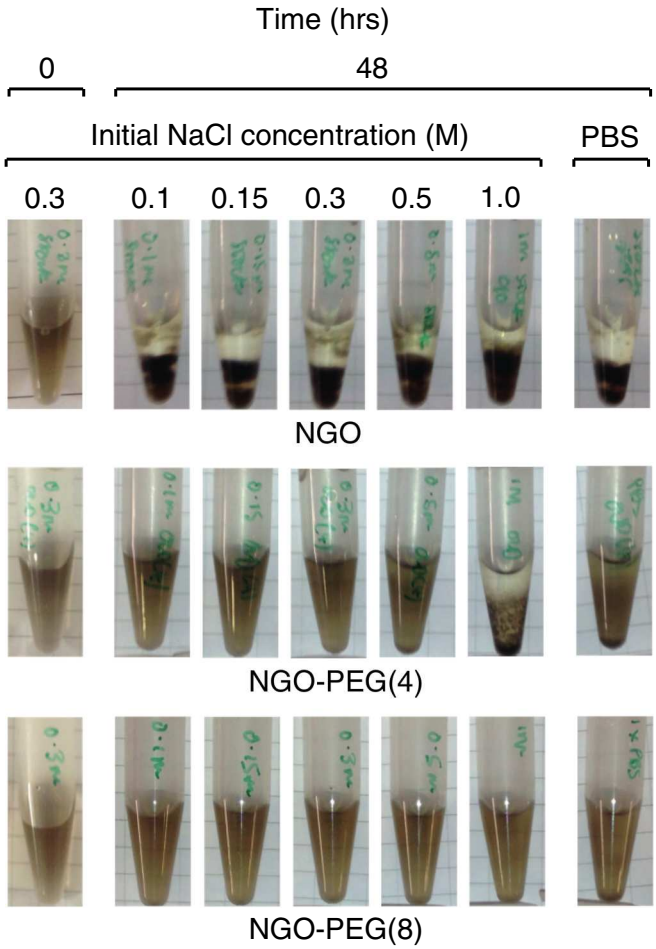

Figure 3.3: Comparative stability of NGO and NGO-PEG at increasing salt concentrations and using different PEG polymers for stability. The NGO-PEG(4) used to indicate a 4-arm PEG star polymer and PEG(8) the 8-arm PEG star polymer. Time 0 indicates immediately after mixing, hence good homogeneity of all NGO solutions. Only one salt concentration shown for this timepoint as all others are similar. PBS contains a total salt concentration similar to 0.15 M.

quantify its contribution to the total mass of NGO-PEG. TGA plots can be seen in Figure 3.4 (B, C.) with the results summarized in Table 3.1. PEG(8) decomposed completely between 300 and 440 °C and therefore its mass contribution could be accurately determined by comparison with the TGA plot of NGO and NGO-PEG. Across the two batches the average PEG mass percentage was 69.7 $\pm$ 5.4% indicating that a significant mass proportion had

been grafted to the NGO with reasonable reproducibility as shown by the less than 10% differences between repeats.

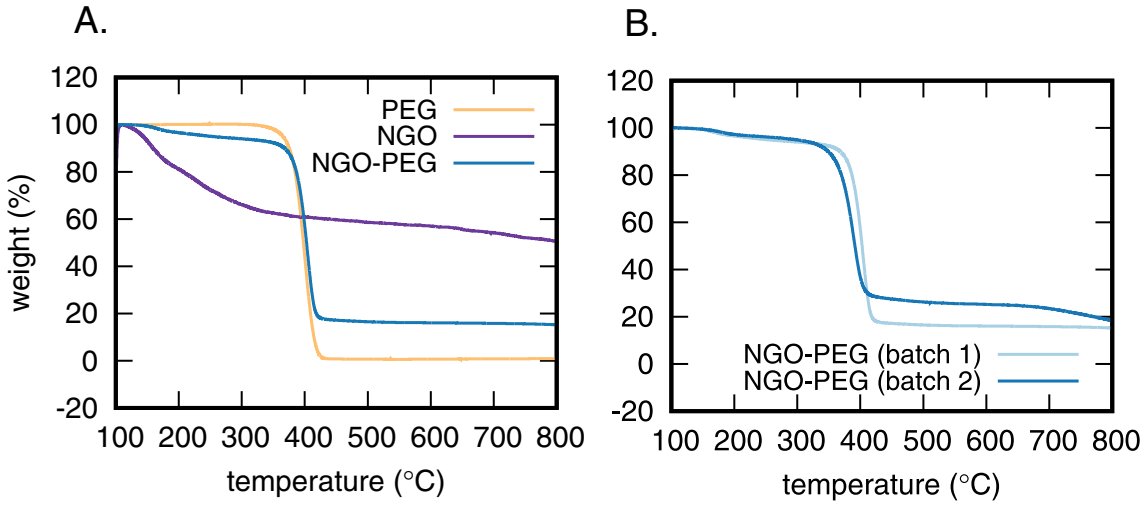

Figure 3.4: Quantification of the PEGylation of NGO. (A.) TGA curves of PEG, NGO and NGO-PEG(8). (B.) TGA curves for two distinct batches of NGO-PEG(8).

Table 3.1: The grafted % mass of PEG onto NGO from two destinct NGO-PEG(8) synthesis batches.

Batch	Sample	PEG mass grafting percentage (%)
1	NGO-PEG(8)	75.1
2	NGO-PEG(8)	64.3

3.3.5 Optical Properties

Extinction Coefficients

The extinction coefficient of both NGO and NGO-PEG(8) were next established in both deionized water (NGO and NGO-PEG(8)) and PBS (NGO-PEG(8)) as an important stage of characterization required for future work. NGO displays a distinctive UV-vis profile with λ_{max} at 230 nm, and decaying absorbance from 230–800 nm, remaining nonzero across the entirety of this

region of the spectra as shown in Figure 3.5 (A.). The extinction coefficients were measured by determining the absorbance at a number of dilutions between 0.01–2 g/L from a stock solution of each NGO species. The mass of NGO or NGO-PEG in each stock was obtained by weighing the freeze dried solid. In the case of NGO-PEG(8) in PBS a salt exchange was required before freeze drying and weighing.

From this data the extinction coefficient was calculated at a number of absorbances although unlike more common determination at the λ_{max} of 230 nm it was calculated at 700 nm as subsequent conjugation of streptavidin and mAb, as well as the fluorochrome AF546, would otherwise supply overlapping absorbances from 200–320 nm (streptavidin and mAbs) and 460–620 nm (AF546). The fit of the extinction coefficients is shown in Figure 3.5 (B–D.) and the values with standard errors tabulated in Table 3.2.

In addition to these extinction coefficients and as a result of the accurate mass percentage of PEG(8) obtained from TGA measurements a value for the 'TGA corrected' extinction coefficient was also calculated. In the TGA corrected value, instead of the total measured mass of NGO-PEG(8), only the mass associated with the NGO was taken into account. This is not without justification as PEG exhibits no absorbance in the 200–800 nm region of the spectrum and therefore has no contribution to the extinction coefficient at 700 nm. Accurately obtaining the mass associated solely with the NGO was again important to calculate NGO concentrations for future conjugation steps.

3.3.6 Biotin-Streptavidin Conjugation

The next stage in the process of preparing the NGO framework for the conjugation of mAbs was the attachment of biotin-streptavidin moieties. The huge benefit and reason for this strategy of functionalization is the extremely high biotin-streptavidin affinity and stability. In the use case of high value

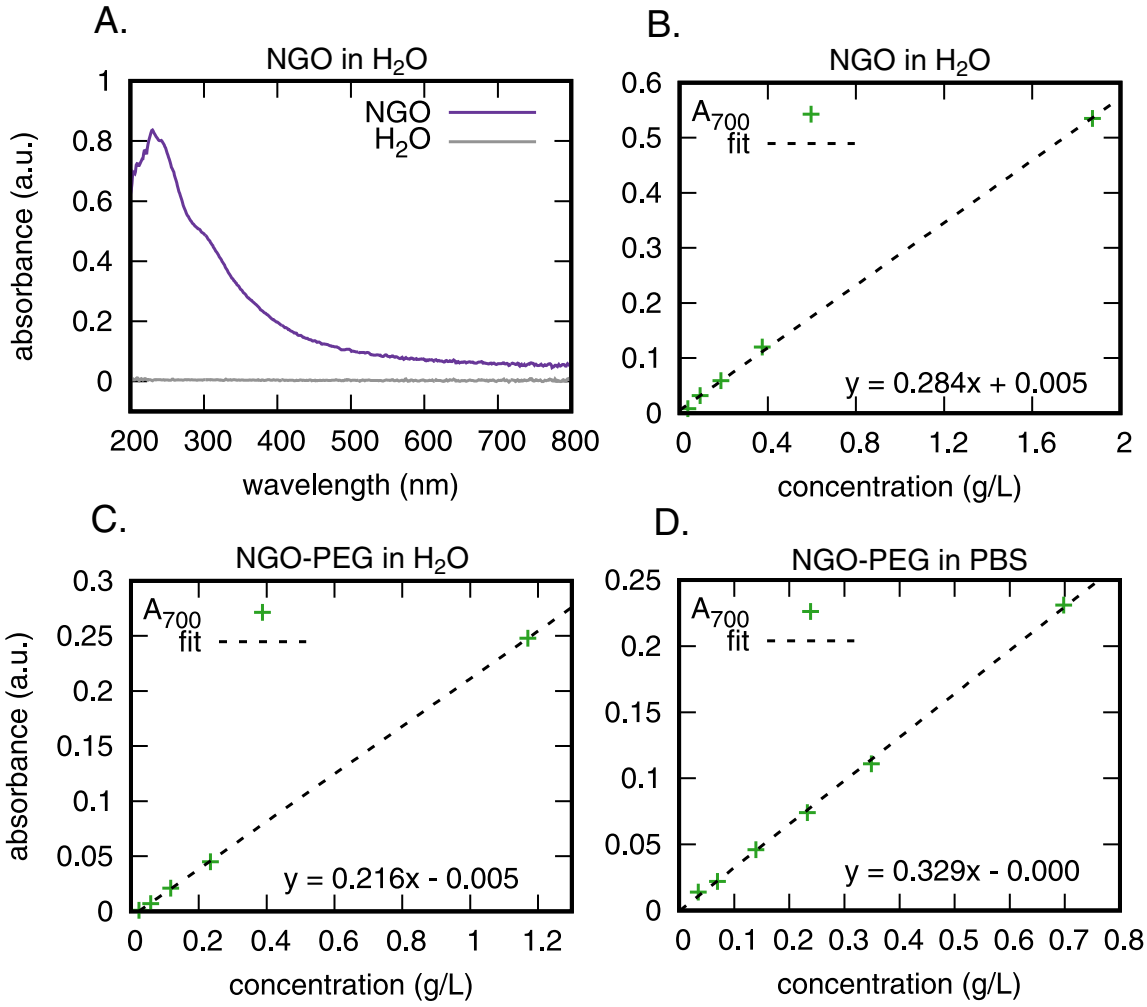

Figure 3.5: Extinction coefficients (ε_{700}) of NGO and NGO-PEG in H_2O and PBS. (A.) Characteristic UV-vis absorbance spectra for NGO with peak at 230 nm. H_2O baseline also shown. (B–D.) Extinction coefficients ε_{700} calculated for NGO and NGO-PEG in H_2O and PBS solvents by measurement of the absorption at 700 nm across a number of NGO/NGO-PEG concentrations and fitting the data using linear regression.

mAb biologics, using carbodiimide (i.e. EDC)/amine, maleimide/thiol (i.e. Trauts reagent) or similar crosslinkers, a high conjugate excesses is required to provide large conjugation numbers. In the case of mAbs it is simply not financially feasible given the efficiency. In the case of streptavidin-biotin the burden of using excess reagents to achieve high conjugation number falls

instead on the biotin and streptavidin steps which are considerably cheaper. The final expensive combination of NGO-streptavidin with a biotinylated mAb on the other hand has excellent theoretical conjugation efficiency and therefore benefit in terms of cost.

Biotinylation

Biotin groups were added to the NGO through the linking of commercially available sulfo-NHS-PEG-biotin with the primary amines found on the covalently bound 8-arm PEG-amine. This step was carried out with a large excess of biotin, approximately 1:1 by mass ratio, (the MW of biotinylation reagent was 443.43 g/mol compared to approximately 2×10^6 g/mol for 70×70 nm NGO sheet) to biotinylate a large number of the amine groups for later conjugation with streptavidin. The product of this conjugation was labeled NGO-biotin.

An approximation of the number of biotins attached to NGO in this step was made using a commercially available HABA/avidin assay. The HABA/avidin assay is a colorimetric method to determine the molar concentration of biotin in a solution by the change in absorbance at 500 nm of the HABA/avidin complex which occurs as a result of the HABA displacement by biotin.

To ensure accurate determination of the biotin levels of NGO-biotin the absorbance of NGO at 500 nm, which would otherwise contribute to the

Table 3.2: Summary of the extinction coefficients of NGO and NGO-PEG at 700 nm. Both uncorrected and corrected values for the mass associated with grafted PEG are included.

Sample	Solvent	ε_{700} (L g^{-1} mm^{-1})	Standard error
NGO	H_2O	0.284	0.004
NGO-PEG	H_2O	0.216	0.001
NGO-PEG	PBS	0.329	0.005
NGO-PEG (TGA corrected)	PBS	1.085	0.016

observed absorbance of HABA/avidin, and artificially decrease the perceived quantity of biotin was accounted for. To establish the contributed absorbance of NGO, a solution of NGO-PEG(8) at equivalent concentration (determined by matching absorbance at 700 nm using UV-vis spectroscopy) was measured under the same conditions and then the absorbance subtracted from the NGO-biotin reading.

By combining the measured extinction coefficient with the mass per unit area of NGO ($\sim$ 1726 m^2 g^{-1}) from the literature[41] and the obtained molar concentration of biotin the average number of biotins per unit area of NGO was calculated and found to be approximately 1 every 10.5 nm^2.

Streptavidin Conjugation

NGO-biotin was then further functionalized by the addition of streptavidin to form NGO-streptavidin. This step was carried out with a large excess of streptavidin to reduce the potential for crosslinking, a consequence of the multivalent (four binding sites) streptavidin tetramer and a problem that has been previously noted in the literature.[428] In the first batch (Batch 1) production streptavidin was added in a mass ratio excess of 6:1 (6 mg streptavidin for 1 mg NGO) with the resulting product showing suitable stability. A later second batch (Batch 2) was produced with a greater excess of 1000:1, more in keeping with Liu et al. 200:1[428] to further minimize any crosslinking and further improve the NGO-streptavidin product.

After filtration using 100 kDa Molecular Weight Cut-Off (MWCO) filters, monitoring the filtrate for streptavidin, the conjugation of streptavidin was confirmed by UV-vis spectroscopy. In comparison to the NGO and NGO-PEG(8) spectra, NGO-streptavidin showed a strong absorbance at 280 nm in keeping with streptavidin and proteins in general due to tyrosine and tryptophan amino acids.[429] Figure 3.6 (A.) shows the spectra for streptavidin and Figure 3.6 (B.) an example spectra of NGO-PEG(8) and NGO-streptavidin at

almost equivalent NGO concentrations, clearly exhibiting an additional peak at 280 nm as a result of the streptavidin.

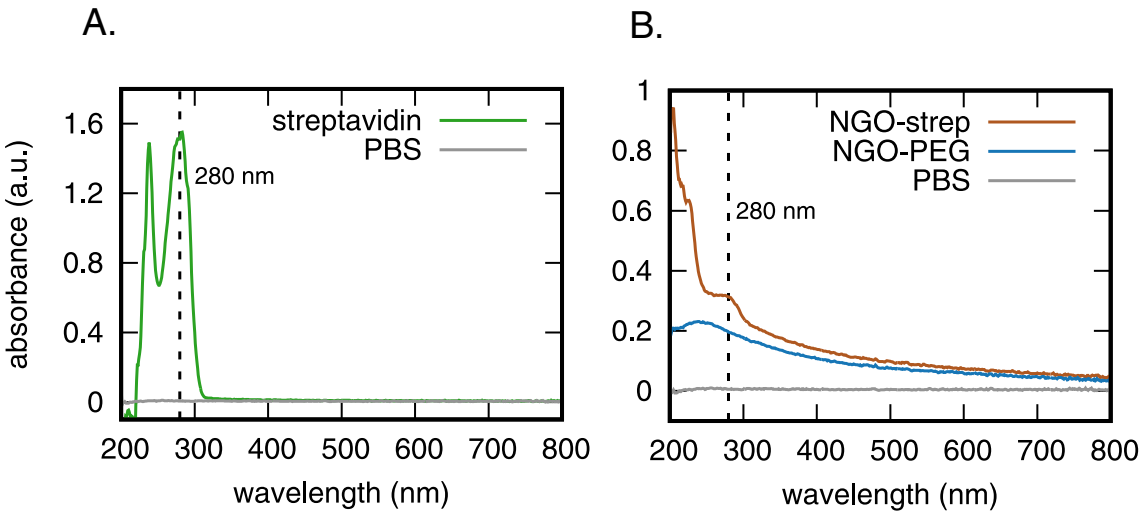

Figure 3.6: Confirmation of the conjugation of streptavidin to biotinylated NGO-PEG(8). (A.) UV-vis spectra of streptavidin with characteristic protein peak absorbance at 280 nm. (B.) UV-vis spectra of NGO-strep after purification showing peak at 280 nm and NGO-PEG at similar concentration with no peak.

3.3.7 Monoclonal Antibody Preparation

Fluorochrome Labeling

Having produced NGO-streptavidin the procedures necessary to conjugate the mAbs of choice were considered next. Given the receptor chosen to be targeted was CD16, anti-human CD16 (α-hCD16) was selected and simultaneously anti-mouse IgG1 κ-isotype control (α-mIgG1) was also used for conjugation seperately, as a negative control, producing two NGO-mAb species for later experiments (NGO-α-hCD16 and NGO-α-mIgG1). For effective conjugation biotinylation of the mAb is the only essential step required for binding to NGO-streptavidin, however, alone there would be no method able to determine if conjugation was successful nor if any unbound conju-

gate mAb remained after purification.

To overcome this both α-hCD16 and α-mIgG1 mAbs were prepared for conjugation by first labeling with Alexa Fluor 546 (AF546) to form α-hCD16-AF546 and α-mIgG1-AF546. AF546 was chosen as its UV-Vis absorbance was in a region of the spectra apart from the λ_{max} of NGO and streptavidin.

Labeling with AF546 was carried out using Alexa Fluor 546 NHS ester in a simple 1-step coupling with the primary amines mAb possess due to lysine residues and N-terminus amino acids. Despite the multitude of lysine residues (approximately 80 for IgG[430]) labeling with AF546 was optimized by control of the AF546:mAb stoichiometry to produce a Degree of Labeling (DOL) of approximately 1. Higher DOL would be especially beneficial for antibody quantification however increasing fluorochrome conjugation past 7 affects the stability of the mAb in aqueous solution, as well as antigen binding specificity. In addition to this there remained the biotinylation step which also utilized primary amines for its attachment. The DOL was determined here using UV-vis spectroscopy by comparing the ratio of absorbance at 556 nm (A_{556}) to 280 nm (A_{280}) as shown in Figure 3.7, each fluorochrome having established extinction coefficients in the literature to determine the molar concentration of each species.

Biotinylation

The biotinylation utilized the same kit previously used for the attachment of biotin to NGO and the conjugation was similarly controlled thanks to the potential for both the mAb antigen binding to be diminished, as well as the serious likelyhood of crosslinking of the NGO-mAb species at high biotin:mAb labeling ratios.

An intitial comparison of high ($>$ 7 biotins per mAb) to low ($<$ 7) biotinylation was investigated to see the affect it had on the presentation of the mAb.

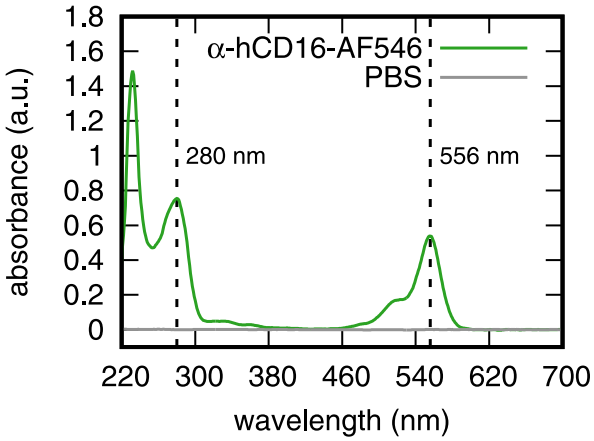

Figure 3.7: AF546 fluorochrome labeling of α-hCD16. UV-Vis spectra showing the absorbance peaks associated with the mAb (280 nm) and AF546, (556 nm) after purification. Using these peak absorbances in combination with the literature extinction coefficients for both mAbs and AF546 the degree of labeling (DOL) was calculated, and in this case found to be 1.4:1, AF546:α-hCD16.

The result of this showed the benefit of low biotinylation. The first NGO batch was, however, produced on the principle of complete 100% mAb conjugation to the NGO-streptavidin and hence sufficient biotin was required to reduce the possibility of unbiotinylated mAb which would be unable to conjugate to the NGO. An average of 6 biotins per mAb, which was finally used, gives an average of only 2% mAbs with 0 biotins if a a Poisson distribution is assumed for the labeling. 6 biotins is therefore a reasonable compromise between ensuring minimal unbound mAb and non-excessive biotinylation.

The biotinylation of mAbs was therefore optimized to have $\sim$ 6 biotins per mAb with both the α-hCD16-(biotin)AF546 and α-mIgG1-(biotin)AF546 labeled mAbs. After each biotin conjugation the biotinylation was measured by the HABA/avidin assay. The exact results of which are shown in Table 3.3.

Table 3.3: Summary of the quantified number of biotins per mAb. Assayed values measured using a HABA/Avidin assay.

Batch	Component	Quantity of biotin per mAb or NGO-PEG
1	α-mIgG1	4.2
1	α-hCD16	6.1
2	α-mIgG1	6.2
2	α-hCD16	6.0

3.3.8 NGO Antibody Conjugation

Since the the required components had been produced, the final conjugation of mAbs was then carried out through the addition of each α-hCD16-(biotin)AF546 and α-mIgG1-(biotin)AF546 mAb to a solution of NGO-streptavidin with rapid mixing. Following incubation overnight at 4 °C, the bulk products of NGO-α-hCD16 (bulk) and NGO-α-mIgG1 (bulk) [fluorochrome and biotin not written for brevity] were produced. Any unstable, sedimented NGO-mAb was removed after overnight incubation by transfer of the supernatant to a fresh Eppendorf.

Batch 2 of NGO-mAb used a greater excess of mAb, with a mass ratio of $\sim$ 60:1 mAb:NGO, compared to the previous $\sim$ 4:1. Given the higher mAb:ratio complete conjugation of mAb to NGO-streptavidin was not expected, and to remove the excess unbound mAb the NGO-mAb product was repeatedly purified. This was completed by pelleting the NGO-mAB using centrifugation, followed by separation of the supernatant and resuspension in PBS. The process repeated until the final supernatant showed no unbound mAb by UV-vis measurement at 556 nm. The procedure for the confirmation of conjugation after this was identical to that described hereafter.

Conjugation Confirmation

Antibody conjugation was confirmed in a two step process, first measuring the fluorochrome absorbance at 556 nm of the NGO-mAb (bulk) using UV-vis spectroscopy Figure 3.8 (A.) followed by pelleting the NGO-mAb by centrifugation and re-measurement of the supernatant (again at 556 nm) Figure 3.8 (C.). Thereby showing that all fluorochrome derived signal was associated with the NGO-mAb species.

The complete spectra of NGO-α-hCD16 (bulk) exhibits the expected peaks at 556 nm (inset showing zoom of 500–600 nm region) as well as peak at 280 nm and characteristic NGO absorbance previously discussed. Due, however, to the absorbance of NGO across the 200–800 nm region of the UV-vis spectra the peak at 556 nm is superimposed with the NGO absorbance. To decouple the two contributions and accurately quantify the antibody background levels a fit of the spectra (black dashed line) was made between 350 and 700 nm (not including the 500–600 nm region) so that a numerical solution could be found and the contribution of NGO subtracted.

The fit-subtracted spectrum shown in Figure 3.8 (B, D.) illustrates the decoupled signal associated solely with the α-hCD16-AF546. Figure 3.8 (D.) showing the decoupled absorbance from 400–700 nm of the NGO-α-hCD16 supernatant, measured after the removal of the pellet. The decoupled, or subtracted spectra, displays no clear peak associated with the AF546 and therefore indicates the successful conjugation of α-hCD16 as minimal unbound mAb is present in the final NGO-α-hCD16 (bulk) product.

As a confirmation of the numerical fitting procedure and subtraction, the same methodology was applied to NGO-streptavidin. As NGO-streptavidin possesses no AF546 labelled species, a signal at 556 nm would not be expected, which is what is observed. Figure 3.8 (E, F.) show both the spectra, fit and resulting subtracted data with no signal at 556 nm confirming that

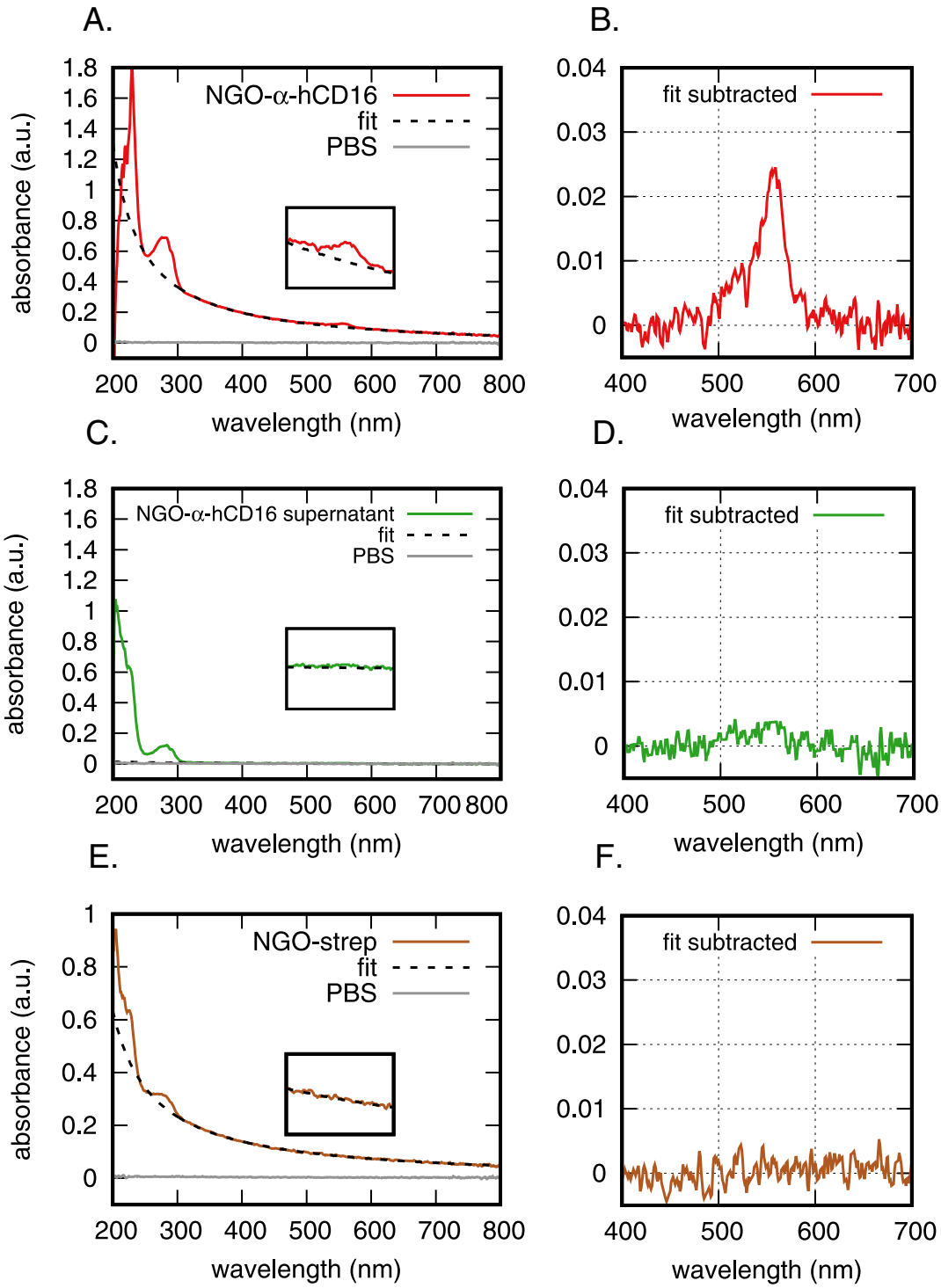

Figure 3.8: Successful conjugation of α-hCD16-(biotin)AF546 to NGO-streptavidin. (A.) UV-vis spectra of the NGO-α-hCD16 (bulk) product showing absorbances at 230 nm, 280 nm and 556 nm. Inset zoomed 500–600 nm region. Fit of the NGO absorbance in the 400–700 nm region (B.) Absorbance of NGO-α-hCD16 after subtraction of the numerical fit of NGO absorbance showing clearly the absorbance associated with the AF546 conjugated α-hCD16 (C.) Similar UV-vis spectra for supernatant after pelleting all NGO-α-hCD16 using centrifugation (D.) Fit-subtracted 400–700 nm region showing negligable absorbance and hence lack of unbound α-hCD16. (E, F.) Fitting applied to NGO-streptavidin also showing no absorbance at 556 nm as expected due to the absence of a species labeled with AF546.

the fitting procedure works as expected.

3.3.9 Sheet Separation by Size

The next challenge in the production of NGO-mAb with mimetic properties was ensuring the general sheet diameters was between 50 and 200 nm, in keeping with receptor nanoclusters of NK cells (as measured by superresolution microscopy[18, 19, 16, 17, 14]). From the bulk solution of NGO-mAb separation of fractions with narrow size distributions was carried out by successive centrifugation, pelleting a fraction of the NGO-mAb followed by separation of the supernatant and resuspension.

In total four fractions were produced by three sequential centrifugations steps. Fractions 1–3 were removed after resuspension of the first three pellets and fraction 4 was the remaining supernatant. The first fraction, and hence largest NGO-mAb sheets, are henceforth referred to as NGO-mAb and the final 4th fraction, NGO-mAb (small sheets), where mAb is as before either α-hCD16 or α-mIgG1. Fractions 2 and 3, being unneccesary, were discarded.

Physical Properties

Atomic force microscopy (AFM) was carried out to obtain the sheet height and width distributions of both NGO-mAb and NGO-mAb (small sheets) produced by fractionation. The physical properties of the NGO starting material and intermediary NGO-PEG(8) were also imaged acting as points of comparison. Figure 3.9 (A, C, E, G.) shows example images from all NGO species with (B, D, F, H.) showing the profiles associated with an object selected in the neighbouring images (green line).

Starting with the NGO image, large flat sheets between 200 and 1000 nm with characteristic sheet height of $\sim$ 1 nm. NGO-PEG, as a result of the extended 4 hour sonication step used in the conjugation of PEG has smaller

sheet sizes and a seemingly and homogeneous distribution. The sheet height, however, demonstrating very little change as a result of the unhydrated PEG adding little to the thickness.

In comparison NGO-α-hCD16 is generally characterized by larger sheets (as a result of the centrifugal separation), an increased sheet height, and large distribution of object widths. NGO-α-hCD16 (small sheets) on the other hand appear smaller in size, despite having similarly greater sheet heights than NGO-α-hCD16 and when compared to NGO-PEG(8).

Size Distributions

The distribution of sheet widths and height for each species, after measurement of between 80 and 110 sheets from multiple images has been plotted in Figure 3.10 and tabulated in Table 3.4.

For the initial purchased NGO the median sheet width was measured to be 347 $\pm$ 96 nm (half Interquartile Range (IQR)). The NGO-PEG(8) median sheet width decreasing to only 76 $\pm$ 21 nm as a result of ultrasonication. After the multiple steps to produce NGO-α-hCD16 this width had increased to 151 $\pm$ 30 nm while the small sheets of NGO-α-hCD16 were 72 $\pm$ 15 nm, similar to the NGO-PEG(8) species.

The increase in median sheet width of NGO-α-hCD16 from 76 to 151 nm was consistent with the addition of the biotin-linkers (with a length of 2.9 nm), streptavidin $\sim$ 11 nm and IgG1 antibodies $\sim$ 20 nm (diameters as measured by AFM[431, 432, 430]).

The median sheet height of both large and small NGO-mAb sheets also increased in a similar manner from the median value of 1.3 $\pm$ 0.25 nm for NGO-PEG(8) to 4.0 $\pm$ 1.5 for NGO-α-hCD16 and 3.5 $\pm$ 0.8 nm for NGO-α-hCD16 (small sheets). This height increased again within reasonable and expected limits for the conjugation of streptavidin-biotin and mAbs. Other

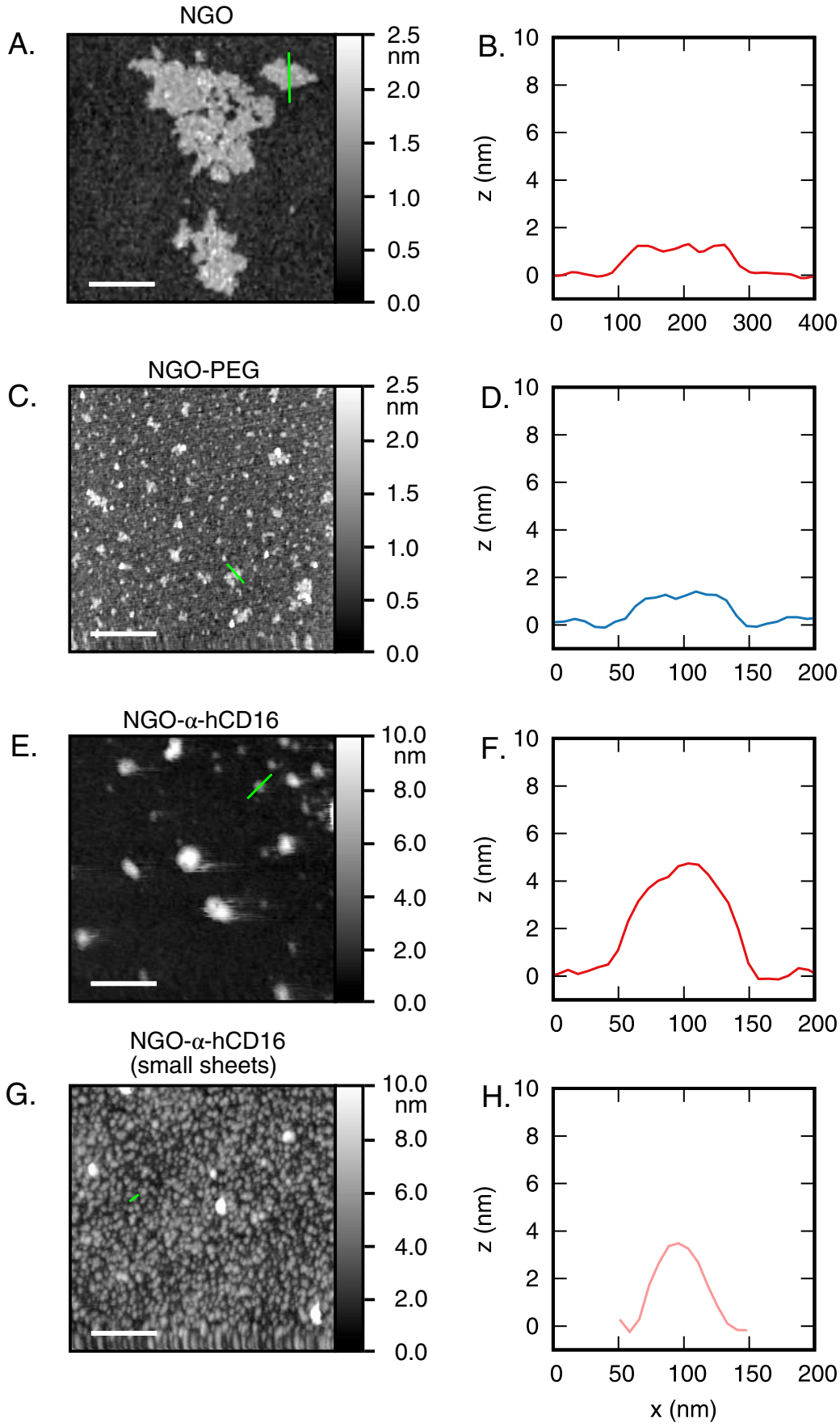

Figure 3.9: Functionalization of NGO leads to changes in the physical dimensions of the NGO species. (A, C, E, G.) AFM images of labeled NGO species at labeled stages of their functionalization, including NGO, NGO-PEG(8), NGO-α-hCD16 and NGO-α-hCD16 (small sheets). Scale bars = 500 nm (B, D, F, H.) Height profiles associated with the indicated (green line) for each neighboring AFM image.

work for instance reporting streptavidin to have a measured height of 2 nm[431] and mAbs (IgG1) also $\sim$ 2 nm[432].

In addition, the NGO-mAb heights also agree well with the measurements of Hong et al. for NGO-mAb species, $\sim$ 4–7 nm,[49] however, Liu et al. measure heights for NGO-streptavidin closer to $\sim$ 13 nm,[428] perhaps indicating differences in crosslinking, oxidation of NGO starting material or synthesis procedure.

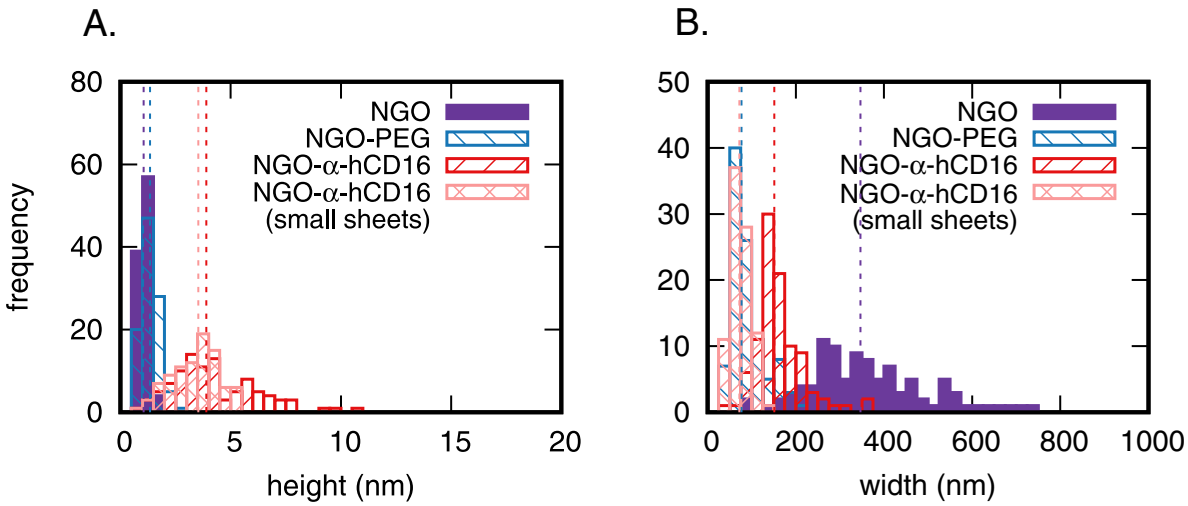

Figure 3.10: NGO-mAb sheets have heights representative of mAb functionalization and median widths corresponding with the known dimensions of receptor nanoclusters. (A.) Height distributions of various NGO species. With successive functionalization steps the median height increases. The median species height of both NGO-α-hCD16 and NGO-α-hCD16 (small sheets) were also similar. Bin width = 0.5 nm (B.) Width distributions of NGO species showing the decrease in width after formation of NGO-PEG(8), due to ultrasonication and separation of NGO-α-hCD16 (bulk) in to larger and smaller fractions (NGO-α-hCD16 and NGO-α-hCD16 (small sheets)). Bin width = 25 nm. Dashed lines representing median values for each species (matched by color) for each dimension. Each histogram produced using measurements of between 89 and 110 individual sheets.

The final NGO-mAb species synthesized and separated using the centrifugal procedure at 70–170 nm fit within the desired 50–200 nm size range required to match the receptor nanoclusters they were created to simulate.

The approximately two fold difference between NGO-mAb and NGO-mAb (small sheet), was also an excellent biologically relevant point of comparison for later cell experiments.

Hong et al. have also made a direct comparison between NGO-mAb species measured by AFM (in air) and dynamic light scattering (DLS) (in solution). The two measurement showed AFM widths of 10–50 nm while by DLS, 27.0 $\pm$ 0.9 nm.[49] Aside from the clear difference in the error of the DLS reading compared to the range measured by AFM, the mean values appear in good agreement and suggest there is not a significant difference between the measurements.

3.3.10 Approximation of NGO:mAb Ratio

Calculation Overview

After producing a well characterized NGO-mAb product, further effort was made to calculate the average number of antibodies attached to each NGO-mAb species. For the application of NGO-mAb as mimetic nanoclusters, the number of antibodies per sheet made up another important and defining characteristic.

To calculate the number of antibodies per NGO-PEG sheet both the molar concentration of NGO, and mAbs, in a given NGO-mAb solution was needed. The ratio of moles of mAb to moles of NGO was used to provide the average number of mAb per NGO sheet.

To simplify the steps used to obtain the mAb:NGO ratio the methodology is broken down into three main steps. 1. Obtaining the approximate molecular weight (MW) of NGO in a given NGO-mAb species. 2. Obtaining the mass concentration of NGO in a NGO-mAb solution. 3. Obtaining the molar concentration of mAb in a NGO-mAb solution. Combining 1. and 2. to obtain the molar concentration of NGO.

Table 3.4: Complete summary of the AFM measured dimensions of NGO species at various stages of functionalization. Interquartile range (IQR).

Batch	Sample	Median sheet height (nm)	Upper quartile (nm)	Lower quartile (nm)	IQR (nm)	Mean sheet height (nm)	Stdev (nm)	Median sheet width (nm)	Upper quartile (nm)	Lower quartile (nm)	IQR (nm)	Mean sheet width (nm)	Stdev (nm)
1	NGO-α-mIgG1	5.777	7.609	2.426	5.183	6.293	5.362	163	199	146	53	179	48
	NGO-α-hCD16	3.896	5.611	2.921	2.690	4.284	1.958	151	186	127	59	160	54
	NGO-α-hCD16 (small sheets)	3.532	4.211	2.601	1.61	3.368	1.059	72	91	61	30	75	21
2	NGO	1.052	1.174	0.917	0.257	1.051	0.228	347	457.3	266	191.3	392	217
	NGO-PEG	1.348	1.600	1.067	0.533	1.372	0.380	76	104	62.9	41	89	38

1. To convert from the mass concentration which was available from the already obtained extinction coefficient (see Section 3.3.5), the approximate MW was needed to convert the mass concentration to a molar concentration. To approximate the MW, first the median sheet size of NGO in a given NGO-mAb species was obtained from the AFM measurement. This value was then combined with the mass per unit area of NGO from the literature ($\sim$ 1726 m^2 g^{-1}[41]) as well as Avogadro's number (N_A) resulting in the molecular weight (MW) in g/mol for the given NGO in an NGO-mAb species.

2. To measure the mass concentration for a solution the previously calculated extinction coefficient for NGO-PEG corrected for the mass of PEG (as previously described in Section 3.2.8) in PBS at 700 nm (ε_{700}) was used in conjunction with the Beer-Lambert law. By UV-vis measurement of the absorption at 700 nm (A_{700}) from a NGO-mAb solution the mass concentration of NGO was obtained.

3. The molar concentration of the mAb was obtained similarly to 2., by the measurement of the absorbance at 556 nm (λ_{max} for AF546) by UV-vis. Again to obtain the absorption solely from the fluorochrome (removing the contribution of NGO) the fitting and subtraction procedure previously described in Section 3.2.9 and shown in Figure 3.8 were used. The fit-subtracted absorbance of the AF546 in combination with the literature extinction coefficient (11200 M^{-1} mm^{-1}) (again using the Beer-Lambert law) provided the molar concentration of AF546 from which the mAb molar concentration can simply be obtained from the AF546:mAb DOL.

Converting the measured mass concentration provided in 2. using the MW calculated in 1. the molar concentration of NGO is obtained. A final division of this value by 3., the mAb molar concentration, resulting in the calculated average ratio of mAb to NGO (mAb:NGO) and hence the mean number of mAbs attached to the NGO.

NGO:mAb Ratios

The results of these calculation for each NGO-mAb species are shown in Figure 3.11 and the the important individual measurements for each solution i.e. median sheet size, A_{700} and subtracted A_{556} are summarized in Table 3.5.

NGO-mAbs nanoclusters synthesized here had mAb:NGO ratios of $\sim$ 70–170:1. The larger sheets of NGO-α-hCD16 and NGO-α-mIgG1 for instance possessed 134 $\pm$ 40 mAb per sheet and 168 $\pm$ 33 mAb respectively. The NGO-α-hCD16 and NGO-α-mIgG1 (small sheets) calculated to have 112 $\pm$ 25 and 79 $\pm$ 17 mAbs per sheet respectively. It can be expected that the functionalization of NGO sheets occurs equally on both sides, hence the number of mAbs actually presented to a cell can therefore be halved. As such the NGO-mAb cluster size will realistically be $\sim$ 70 for the normal NGO-α-hCD16 species and $\sim$ 55 for the NGO-α-hCD16 (small sheets).

Studies measuring the number of receptors per nanocluster in NK and T cells approximate the number to be 20–25[13, 18] which in the case of KIR2DL1 further increased after their ligation. The nanoclusters produced here therefore contain a 2–3 fold excess of ligand which is still, arguably, within a realistic range. An excess is very likely preferable for a complex synthetic species given the multiple functionalization steps which increase the possibility for reduced antigen binding.

3.4 Conclusions

3.4.1 Summary of Findings

The goal set out in this chapter was to synthesize a supramolecular species with clustered ligands using an NGO framework. The structure was conceived in mimicry of the receptors nanoclusters observed on immune cells

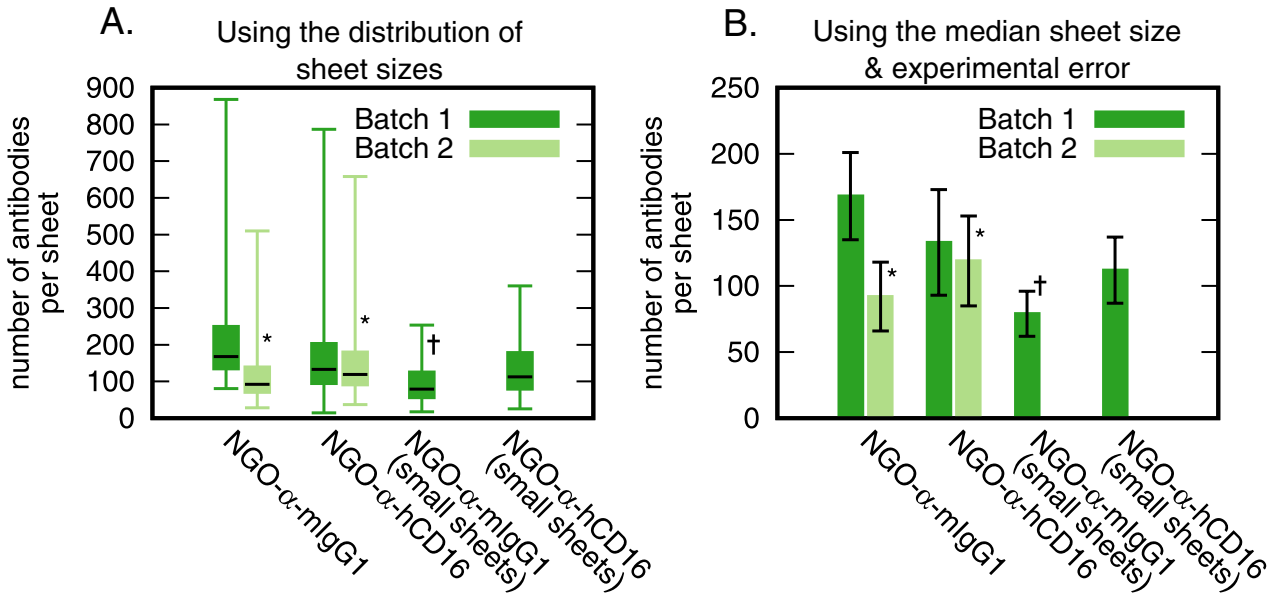

Figure 3.11: The number of antibodies calculated per NGO-mAb species. (A.) Distribution of the number of antibodies per NGO-mAb species based on the distribution of NGO-mAb sheet sizes. Whiskers represent the min and max values, top and bottom of box, the 3rd and 1st quartiles, and black line, the median calculated value. (B.) Error associated with the experimental measurements used to caculate each NGO-mAb species (median sheet size) number of mAbs. Error bars represent the combined error of the experimental methods. ⋆ Sheet dimensions taken from the average of Batch 1 measurements. † Sheet dimensions used from NGO-α-hCD16 (small sheets).

and therefore should have properties of nanocluster size and ligand density similar to those naturally observed. In relation to those goals experimental evidence has been provided showing:

1. NGO can be stabilized in solution containing high salt concentration using 8-arm PEG star polymers.

2. Conjugation of any desired mAbs can be achieved via a bottom-up approach with streptavidin-biotin linking strategies.

3. Subsequent NGO-mAb species can be separated to give species with varied physical dimensions matching receptor nanoclusters.

4. The bulk mAb:NGO ratio of a NGO-mAb species can be approximated

Table 3.5: Number of antibodies per GO sheet

Batch	Sample	Median sheet width (nm)	IQR (nm)	A_{700}	A_{556}	Calculated number of antibodies
1	NGO-α-mIgG1	163	53	0.113	0.028	168 ± 33
	NGO-α-hCD16	151	59	0.086	0.009	133 ± 40
	NGO-α-mIgG1(small sheets)	72†	30	0.038	0.023	79 ± 17
	NGO-α-hCD16(small sheets)	72	30	0.046	0.017	112 ± 25
2	NGO-α-mIgG1	157*	56	0.101	0.009	93 ± 26
	NGO-α-hCD16	157*	56	0.080	0.009	119 ± 34

* Assumed for calculations based on the mean of NGO-α-mIgG1 and NGO-α-hCD16 Batch 1 measurements. † Based on measurement of NGO-α-hCD16 (small sheets).

as a result of the synthesis strategy and characterization described.

3.4.2 Concluding Remarks

Supramolecular mAb constructs utilizing NGO as a framework are relatively rare in the literature and present a novel use of NGO as a biomaterial. The rationale put forward here for NGOs use focuses on its unique 2D planar structure which provides a mimetic structure with the dimensions, geometry and ease of functionality required to create supramolecular nanoclusters. Judged on these properties NGO is superior to all other currently available biomaterials to mimic nanoclusters, and the use of NGO as a mimetic biological species is in itself without precedent.

In this chapter there has been a focus to extending the characterization applied to the functionalization procedure, making significant improvements over the previously reported literature. Earlier synthetic methodologies for instance have not demonstrated the specific conjugation of mAb to NGO, or the absence of unbound mAb leading to difficulty stating the mAb:NGO

conjugation ratio, which we demonstrate a method for here.[279, 49, 46]

In some cases the level of characterization was not the primary goal of the work and therefore deemed in excess of necessity. Given however how the variety of diverse physical[256] and chemical[258] properties of NGO alone, which have been shown to affect toxicity and cellular response there are now strong arguments that robust characterization should be an essential component of future work. A primary example of this sensitivity was the novel cell membrane ruffling response to NGO, which was recently presented. A later re-examination, however, demonstrated the observed ruffling was critically dependent on the buffer in which the cells were incubated, and the variation in response was presumed to be linked to the different salt concentrations and NGO aggregation levels.[260, 261]

Using TGA to quantify the PEGylation could, for example, later be found to be essential, as the presence or absence of PEG alone has only very recently been shown to affect biological outcomes in immune cells.[433] A strong effort towards the robust characterization of this class of biomaterial at every stage of their synthesis will need to be made going forward to ensure their future in biological applications and particularly as therapeutic reagents.

Chapter 4

NGO-α-hCD16 Functionality and Natural Killer Cell Response

4.1 Scope

In this chapter the clustered NGO-α-hCD16, whose synthesis is outlined in the previous chapter was first assessed for its ability to present functional mAbs. The ability of the NGO-α-hCD16 to specifically bind primary (human) NK (pNK) cells was then made, including a brief inquiry into the binding kinetics.

The ability of clustered NGO-α-hCD16 to stimulate pNK cells through the activatory CD16 receptor was assayed and compared to unconjugated, and hence unclustered α-hCD16. An isotype control NGO-α-mIgG1 was used throughout as a negative control to distinguish the effect of the clustering from the other differences found in the NGO-mAb species (for instance presence of PEG, streptavidin-biotin linkers and NGO framework).

pNK cells sourced from healthy human donors were selected for this work as the best ex-vivo model for natural human NK cell behavior. This choice was further supported by the lack of human NK cell lines which stably expressing the CD16 receptor.

The stimulation of pNK cells was measured by functional responses including the upregulation of Lysosomal Associated Membrane Protein 1 (LAMP1, alternatively known by CD107a), a marker identifying NK cell degranulation[434] and secondly Interferon-γ (IFN-γ) secretion, a cytokine of the interferon group able to stimulate many cell types within the immune system[435, 436, 437, 438]. These two markers give an indication of both the cytotoxic and immunomodulatory function of pNK cells in response to NGO-α-hCD16.

4.2 Methods

4.2.1 Presentation of Monoclonal Antibodies

200 μL poly(styrene) beads (3–3.4 μm, BD Biosciences) were mixed in equal parts with Dulbecco's Phosphate Buffered Saline (PBS) with $MgCl_2$ and $CaCl_2$ (Sigma-Aldrich). An equivalent of 1 μL, 2 μg/mL anti-human CD16-AF546, anti-mouse IgG1-AF546, goat anti-mouse IgG2b-AF546 (γ2b, Invitrogen) NGO-α-mIgG1 or NGO-α-hCD16 (3.9 μg/mL final concentration) were then added to 50 μL diluted beads and incubated for 20 mins at 4 °C. They were then washed using PBS with $MgCl_2$ and $CaCl_2$, and analysed by flow cytometry.

4.2.2 Primary (Human) Natural Killer Cells

Primary (human) NK (pNK) cells were isolated from healthy donor peripheral blood under negative magnetic selection (NK cell isolation kit, Miltenyi Biotec) and were cultured in RPMI-1640 supplemented with 10% human serum, 1 mM L-glutamine, 1 mM sodium pyruvate, 1 mM penicillin-streptomycin, 1 mM MEM nonessential amino acids and 20 μM 2-mercaptoethanol (clone media, all Invitrogen). Freshly isolated pNK cells were stimulated with 150 U/mL human recombinant IL-2 (Roche) and cul-

tured for 6 days prior to use unless otherwise stated.

4.2.3 Binding of NGO-α-hCD16 to pNK Cells

pNK cells were resuspended in 100 μL flow buffer (2% FCS in PBS) at 1×10^6 cells/mL and stained with either 1μL, 2 μg/mL anti-human CD16-AF546, anti-mouse IgG1-AF546, NGO-α-hCD16 or NGO-α-mIgG1 in addition to Zombie NIR^{TM} and anti-human CD56-BV421 (clone HCD56, Biolegend) for 20 mins at 4 °C. For FMO conditions all stains except anti-human CD16-AF546 were added (for instance only Zombie NIR^{TM} and anti-human CD56-BV421). Cells were then washed with flow buffer and fixed with PFA in PBS at final concentration of 2% PFA. Cells were measured using a BD LSRFortessa^{TM} and analyzed using FlowJo^{TM} version 10.

4.2.4 Stimulation of pNK Cells with NGO-α-hCD16

A 96 well plate (Nunc Maxisorp) was coated with either 50 μL, 1 μg/mL anti-human CD16 (clone 3G8, BD Biosciences) or anti-mouse IgG1 κ-isotype (clone MOPC-21, BD Biosciences) diluted in carbonate bicarbonate buffer (binding buffer, Sigma-Aldrich) and left overnight at 4 °C. The plate was washed with 0.05% Tween-20 in PBS (washing buffer) prior to the plating of cells.

pNK cells were resuspended in clone media with 150 U/mL human recombinant IL-2 at days 7 and 9 prior to use. At day 10 pNK cells were resuspended in R10 at 1×10^6 cells/mL, 100 μL per condition, supplemented with 1 in 1000 dilution of both Golgi Plug (BD Biosciences) and Monensin (eBiosciences) as well as 15 μg/mL anti-LAMP1 Alexa Fluor 647 (clone H4A3, Santa Cruz Biotechnology) or 15 μg/mL mouse IgG1 κ-isotype Alexa Fluor 647 (BD Biosciences), again per condition. For fluorescence minus one (FMO) conditions either anti-LAMP1 Alexa Fluor 647 or IgG1 κ-isotype Alexa Fluor 647 were omitted. For stimulation conditions either 2

μg/mL soluble anti-human CD16-AF546, anti-IgG1-AF546, fabricated NGO-α-hCD16 or NGO-α-mIgG1 was also added. pNK cells were then plated onto the prepared 96 well plate, centrifuged for 10 seconds at 300 g after 30 mins and incubated at 37 °C for 6 hrs.

4.2.5 CD107a Degranulation Assay

After incubation for 6 hrs cells were removed by repeated pipetting, washed and resuspended in flow buffer (2% FCS in PBS) with human serum added to block. After 20 mins in flow buffer with human serum they were then stained with Zombie Aqua^{TM}, anti-human CD56-BV421 (clone HCD56, Biolegend), 7 μg/mL anti-LAMP1-AF647 for 20 mins at 4 °C, washed and fixed.

4.2.6 IFN-γ Secretion ELISAs

For conjugate enzyme-linked immunosorbent assays (ELISAs) a 96 well plate (stimulation plate, Nunc Maxisorp) was coated with either 50 μL, 1 μg/mL anti-human CD16 (clone 3G8, BD Biosciences) or anti-mouse IgG1 κ-isotype (clone MOPC-21, BD Biosciences) made in carbonate bicarbonate buffer (binding buffer) (Sigma-Aldrich) and left overnight at 4 °C. The plate was washed with 0.05% Tween-20 in PBS (washing buffer) prior to the plating of cells. pNK cells (1×10^6/mL, 100 μL) were plated. After 6 hrs stimulation, cells were removed by repeated pipetting, spun down in a v-bottom plate, the culture supernatant collected and stored at -20 °C.

ELISA plates (Nunc Maxisorp) were coated with 1 μg/mL anti-human IFN-γ (clone NIB42, BD Biosciences) in binding buffer (carbonate bicarbonate, Sigma-Aldrich), blocked with 1% bovine serum albumin (BSA)/0.05% Tween-20 in PBS (blocking buffer). 80 μL of the supernatants were mixed with 80 μL 2% BSA in 2$\times$ PBS, added in triplicate (50 μL per condition) for 1 hour as well as a standard curve 0–500 pg/mL in duplicate of hu-

man IFN-γ (BD Biosciences) diluted in 50 μL blocking buffer. Plates were incubated with 50 μL per condition, 1 μg/mL biotinylated anti-human IFN-γ (clone 4S.B3, BD Biosciences) then 50 μL per condition streptavidin horseradish peroxidase (strep-HRP, BD Biosciences) followed by 50 μL 3,3',5,5'-Tetramethylbenzidine (TMB) ELISA substrate (Sigma-Aldrich) and the reaction was halted with 100 μL 1 N H_2SO_4. Washing of the plate with washing buffer was carried out between each incubation step up until the addition of TMB. Absorbance was measured at 450 nm with a correction at 570 nm using a Tecan Infinite 200 PRO microplate readers.

4.2.7 IFN-γ Intracellular Staining

For intracellular stains, cells stimulated as described in Method 4.2.4 were washed twice with Perm/Wash^{TM} and then blocked with human serum. Cells were stained with anti-human IFN-γ-AF488 (clone B27, BD Biosciences) at 1/5 the manufacturers recommended dilution, for 30 mins at 4 °C, washed a further two times and fixed again.

4.2.8 Statistical Significance

Statistical significance was determined using Prism 7 software (Graphpad) by performing two-tailed, paired, parametric, t tests. In statistical analysis, unless expressly stated otherwise, $p \geq 0.05$ is indicated as not significant (ns) and statistically significant p values are indicated by asterisks as follows * $0.01 \leq p < 0.05$, ** $0.001 \leq p < 0.01$, *** $0.0001 \leq p < 0.001$

4.3 Results and Discussion

NOTE: *Throughout this chapter both α-mIgG1 and α-hCD16 are always labeled with AF546 and come from the same batch as the equivalent NGO-mAb.*

4.3.1 Functionality

Presentation of Antibodies

Given the multi-step process and potential for crosslinking in the production of both NGO-α-mIgG1 and NGO-α-hCD16 (and their small sheet equivalents) a functional assessment of the mAbs availability for binding was made. To carry out this assessment another species, polystyrene beads coated with anti-mouse Ig (α-mIg) were used. The α-mIg beads bind the antigen binding site of mAbs raised in mouse (as the conjugated α-mIgG1 and α-hCD16 mAbs were) and would therefore show if the NGO-mAb sheets presented the conjugated mAbs.

To measure the individual binding of NGO-mAb species to a α-mIg beads flow cytometry was used. Flow cytometry is a common technique used to determine the differences in characteristic properties of a mixture of particles (or cells), including qualitative particle sizes, shape and presence of fluorescence. The technique independently and successively measures a large number of the component particles to obtain statistically significant populations based on each characteristic. In this case for instance the non-fluorescent α-mIg beads would be detected by their size and shape and secondly as fluorescent only if they were able to bind the conjugated mAbs of the NGO-mAb species due to the associated AF546 fluorochrome. Combined particle properties can then plotted against each other and 'populations' with similar properties differentiated. 'Gates' as their name suggests are used as designated cut-off points, and are drawn around populations so that particles can be categorized as either within or outside a population.

The poly(styrene) α-mIg beads in addition to identical beads without mIg (uncoated beads) were mixed at a 1:1 ratio and hence a population of 50% fluorescence positive beads, as measured by flow cytometry, would be expected for complete binding of all α-mIg beads. Greater than 50% indicating

that nonspecific binding was occurring through attachment to the uncoated beads, and less than 50%, incomplete specific binding.

As a measure of the nonspecific binding of mAbs to the beads in general, goat anti-mouse IgG2b mAb was used. The goat anti-mouse isotype differs from antibodies raised in mouse and therefore could not be bound by the α-mIg beads. The goat anti-mouse IgG2b mAb resulted in a less than 1% positive beads and indicated that nonspecific binding of mAbs to the beads was low.

Both unconjugated α-mIgG1 and α-hCD16 showed almost equivalent binding of α-mIgG1 beads with 48–51% positive counts as would be expected for complete binding of the α-mIg beads. The α-mIgG1 mAb, later used as a negative control, also has strong binding to the beads as it too has the same isotype as the α-hCD16 and can therefore be bound by the α-mIg beads giving a positive staining response.

In comparison, the NGO-α-mIgG1 showed slightly lower average binding at 37%, though still high, while NGO-α-hCD16 exhibited almost complete binding at 48% showing that the conjugated mAb are in general presented (not obstructed) and available to be bound. The small sheets on the other hand both exhibited $\sim$ 58% binding indicating that they exhibited a small degree of nonspecific binding.

Specific Binding of CD16

After showing that the mAb conjugated to the NGO were not obstructed and able to be bound by another material, the specific binding of the NGO-α-hCD16 to primary human NK (pNK) cell was next examined. In this case comparisons to both the isotype control NGO-α-mIgG1 and equivalent unconjugated mAbs (for each NGO-mAb species) were used to further characterize the NGO-mAb clusters in regards to their specific binding abilities.

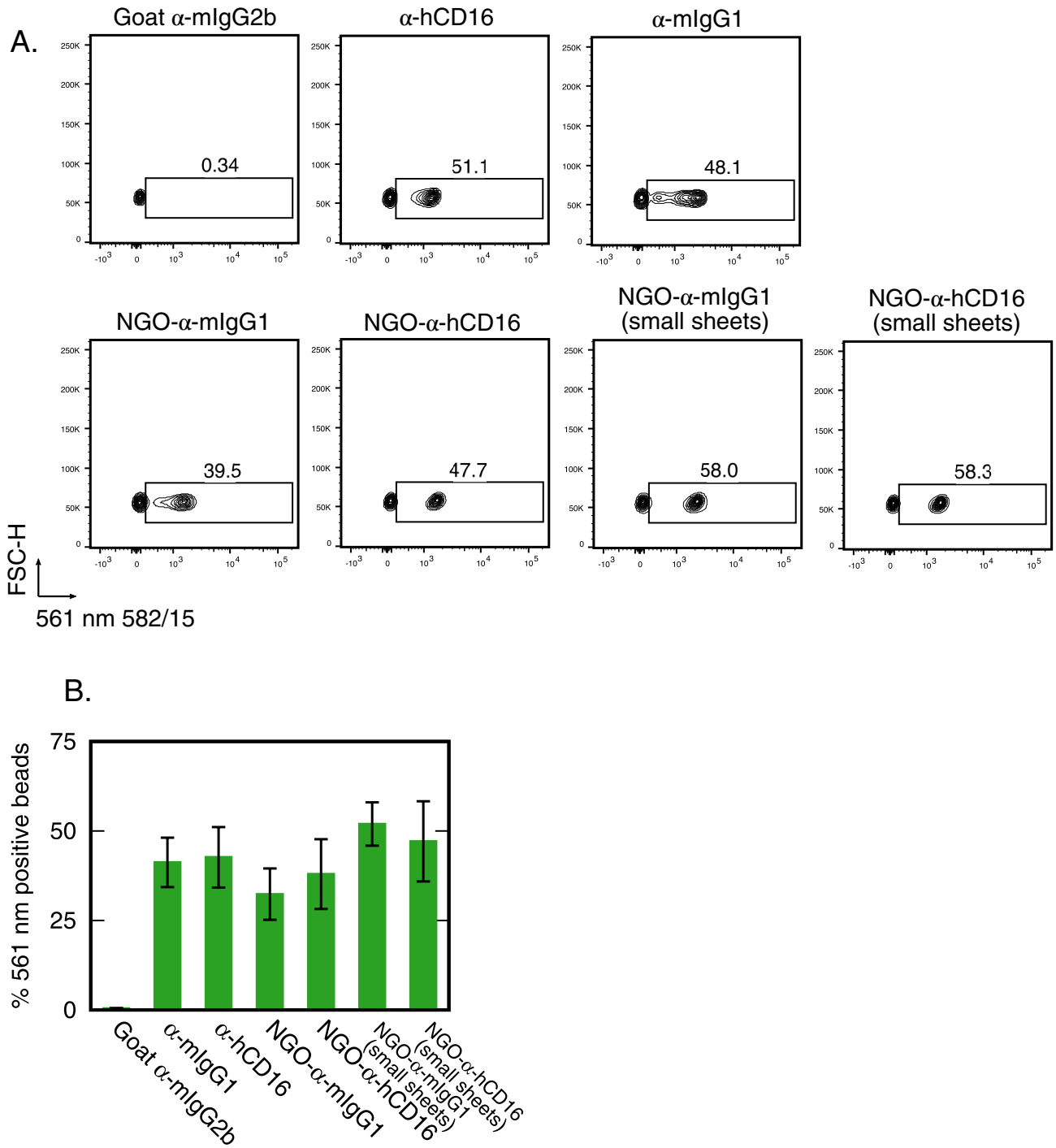

Figure 4.1: The mAbs conjugated to NGO are able to be bound by α-mIg beads showing that they are not obstructed in the NGO-mAb synthesis (A.) Flow cytometry plots of the forward scatter (y axis) and 582 $\pm$ 15 nm (x axis) detectors. The gate and percentage of beads within stated above. (B.) Quantification of the percentage of 582 fluorescence positive beads. As a 1:1 ratio of α-mIg beads and uncoated beads were used 50% is equivalent to the complete binding of α-mIg beads. Results are the mean and standard deviation of 2 independent measurements.

First to ensure the correct mAb concentration was used to saturate all receptors on the pNK cells, a titration of the unconjugated α-hCD16 was made using 0.6, 2.0 and 4.0 μg/mL (final mAb concentration) and compared to the equivalent concentrations of the isotype control α-mIgG1 mAb. For each condition 100 μL of pNK were used at a concentration of 1×10^6 pNK cells/mL which would be maintained throughout binding and stimulation experiments.

Figure 4.2 (A.) shows the overlaid histograms of the fluorescence intensity measured in the 582 nm detector (for which the α-hCD16 is detected) at the increasing concentrations of α-hCD16 and α-mIgG isotype control. At each concentration a clear CD16 positive population is shown, however, this population is better separated between 0.6 and 2.0 μg/mL. There was no further shift between 2.0 and 4.0 μg/mL. In each case the negative isotype controls showed little variation and only a small broadening at a concentration of 4.0 μg/mL.

The quantified results shown in Figure 4.2 (B.) show the minor differences between concentrations, however, the combined small increase in % CD16 positive cells between 0.6 and 2.0 μg/mL in combination with the increased nonspecific binding of the isotype control at 4.0 μg/mL (1–2% nonspecific binding) indicates that 2.0 μg/mL is an ideal concentration for α-hCD16 to be used at to maximize specific and minimize nonspecific binding of the mAb.

Provided with the 2.0 μg/mL optimal concentration of α-hCD16 antibody, the binding of each of the NGO-mAb species was determined in comparison to the unconjugated equivalents. To fairly compare between the conjugated antibody and unconjugated, an equivalent final concentration of mAb was used explicitly including the NGO-mAb solutions. The mAb concentration of these were calculated from the absorbance at 556 nm and the previously

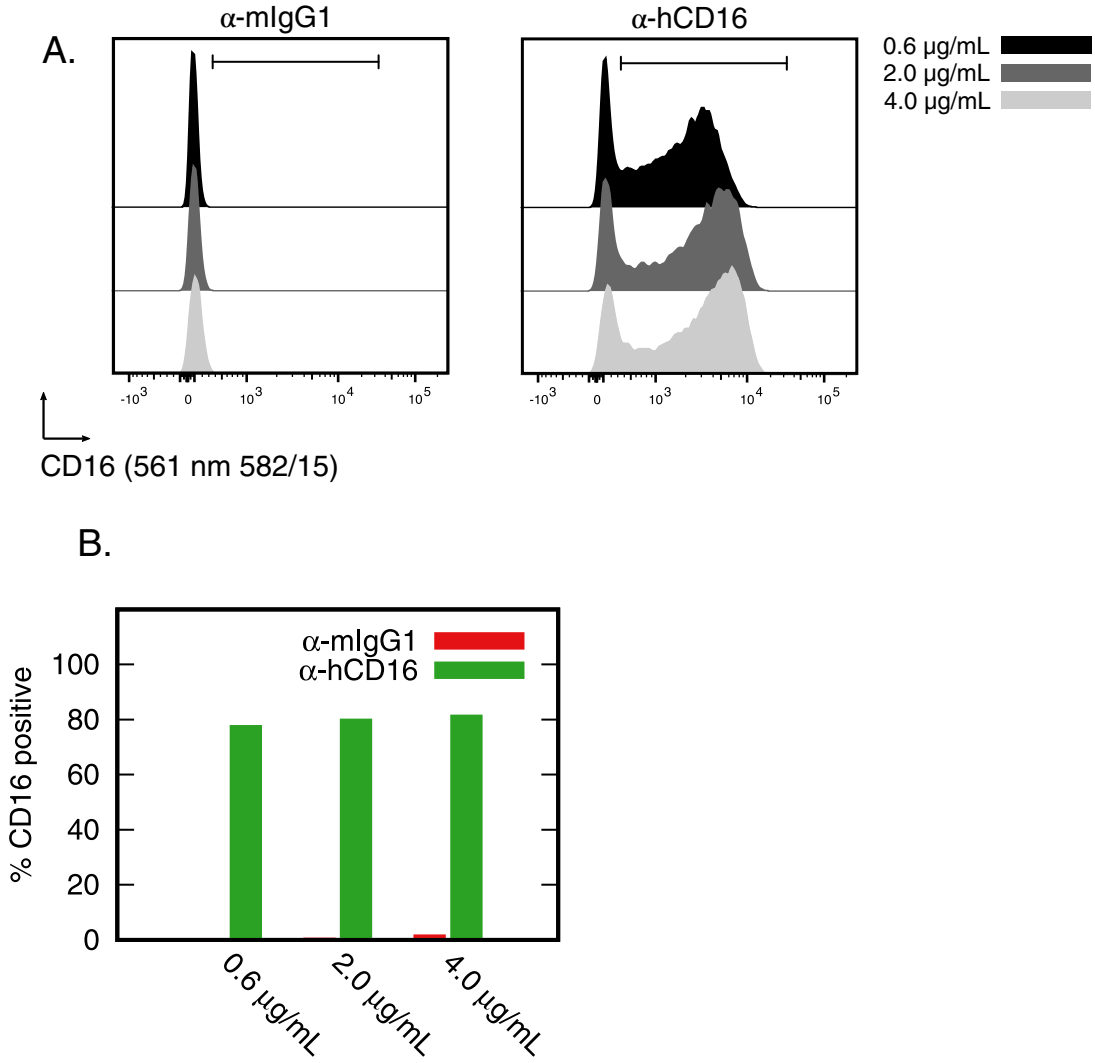

Figure 4.2: A final α-hCD16 mAb concentration of 2.0 μg/mL is optimal for the staining of the CD16 receptor on human pNK cells. (A.) Overlayed histograms of the fluorescence intensity measured in the 582 $\pm$ 15 nm detector associated with using either an α-mIgG1 isotype control or α-hCD16 mAb at 0.6, 2.0 and 4.0 μg/mL used to bind the human CD16 receptor. CD16 positive gate shown by the black bar. (B.) Quantification of the binding associated with α-mIgG1 or α-hCD16.

measured DOL. Binding of mAb for staining purposes is commonly carried out using incubation times of 20 minutes for the mAb and cells. Wishing to test the NGO-α-hCD16 against these standard conditions an incubation time of 20 minutes was also used.

In the binding assays (Figure 4.3 (A, B.)) NGO-α-hCD16 showed an average decrease in binding to pNK (53% positive) compared to unconjugated α-hCD16 (85% positive) across the three donors, this was a 0.6-fold decrease. The nonspecific binding of NGO-α-mIgG1 was found to be low, averaging 6% pNK cells bound and the small sheets exhibited very little nonspecific binding at only 2%, with an average of 71% positive pNK cells bound by the NGO-α-hCD16 (small sheets).

These results indicate the small reduction in binding of NGO-α-hCD16 compared to unconjugated α-hCD16 which was interesting, and could be explained by a number of factors. An initial consideration for the observed variation was the binding kinetics of NGO-α-hCD16. The binding kinetics may reasonably be expected to differ for a large supramolecular structure such as the NGO-mAb in comparison to unconjugated small molecules and proteins. In studies of other multicomponent systems, including ligands to the FK506 binding protein conjugated to dextranated magnetic nanoparticles, it has been shown that binding kinetics can vary considerably compared to the unconjugated ligand alone as a single component. Many different ligand variations within this system have shown slower Association Constants (k_a) for conjugated multi-ligand species than the 'free' unconjugated ligand alone.[439] Given the relatively short 20 minute binding time at 4 °C temperature (used to reduce nonspecific binding) it was therefore possible that binding saturation of the CD16 receptors would take longer for the NGO-α-hCD16. This explanation was further supported by NGO-α-hCD16 (small sheets) showing still reduced but improved binding at the same time point, averaging 72% rather than 53%.

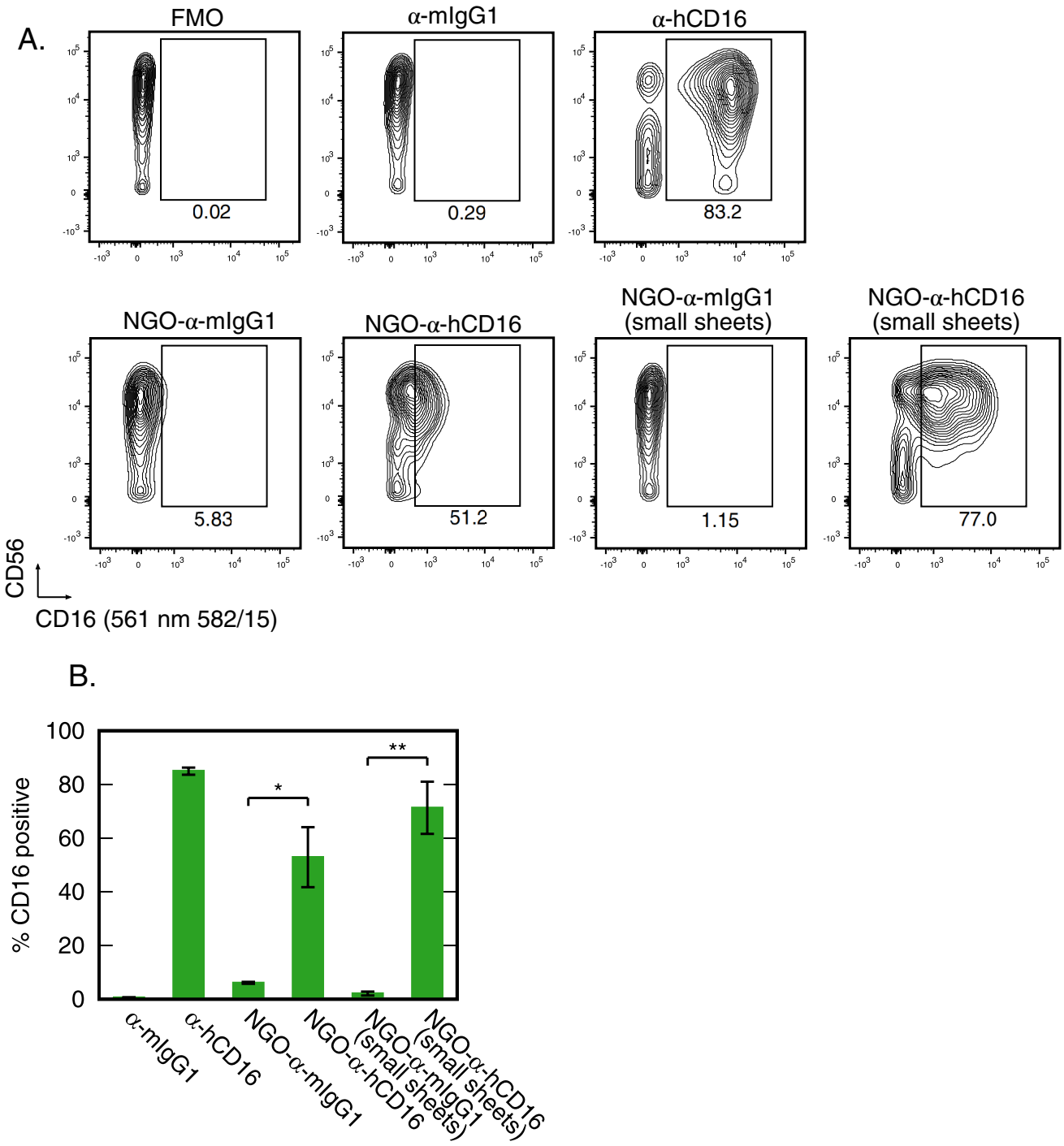

Figure 4.3: NGO-α-hCD16 can bind pNK in a specific manner (A.) Representative flow cytometry plots of NGO-α-hCD16 and its controls. CD16 binding measured by excitation of the AF546 fluorochrome using the 561 nm laser and detection at 582 ± 15 nm. Gates show the CD16 positive threshold and percentage of cells within a gate given below. (B.) Quantification of the binding of the different NGO-mAb species in comparison to the unconjugated mAbs. Results show the mean and standard deviation of three independent experiments with three human donors. Statistical significance is assigned as follows, * $0.01 \leq p < 0.05$, ** $0.001 \leq p < 0.01$

Binding Kinetics

To test the binding kinetics of each species the binding was measured using two incubations time points for the mixture of cells and NGO-mAb, one at 20 mins, and a later one after 60 mins, all other conditions remaining equivalent. In these experiments the binding of NGO-α-hCD16 exhibited increased from 59% to 69% across two measurements between the 20 to 60 minute time points. The NGO-α-hCD16 (small sheets) on the other hand only increased from 78% to 80% and unconjugated α-hCD16 showed no change, averaging 85% for both. The 10% change in binding measured for NGO-α-hCD16 compared to 0% for α-hCD16 is visible in Figure 4.4 (A.), particularly as the NGO-α-hCD16 positive population shifts noticeably to the right (within the positive gate) between 20 and 60 mins while all other conditions do not.

The difference in binding at two time points supports the argument that the reduced binding observed at 20 mins is, in part, due to the slower binding kinetics of the large supramolecular structure. It does not, however, fully account for the reduced binding as the expected binding of 85% is not observed even after incubation times of 60 minutes (69%). Two possibilities would account for the observed behavior. Firstly insufficient AF546 labeling of the α-hCD16 antibody. This argument is nonetheless made mute by the equivalent fluorescence intensity of the populations in the bead binding experiment. A second explanation of the observed results is that an overall smaller number of the α-hCD16 attached to NGO-α-hCD16 bind the cell. This could be a result of reduced binding affinity of the CD16 mAb. Assuming this was the case, each cell would have a lower overall density of mAb and therefore a lower average fluorescence intensity that would be observed as a reduced separation of the CD16 positive population and in turn lower binding percentages.

Explanations for the reduced α-hCD16 affinity include the additional biotinylation step necessary to conjugate the mAbs to the NGO-streptavidin which can restrict antigen binding as shown by Acchione et al.[440] The Dissociation Constant (k_D) increasing from 397 pM to 546 pM after the addition of 6.4 biotins and further to 825 pM after 14.2 biotins. In combination with the conjugation of biotin, the enhanced potential for the biotin-streptavidin binding to further restrict antigen binding could also contribute to the reduction in binding observed here. This seems a logical conclusion in spite of evidence directly supporting the hypothesis.

4.3.2 Natural Killer Cell Response

Assays of pNK Cell Activation

Considering the specific binding of NGO-α-hCD16 to the CD16 receptor on pNK cells previously documented, it was was next necessary to determine assays of activation that could be used to measure the affect NGO-α-hCD16 ligation has on the cell.

NK cells in line with their numerous functions can be activated by a range of stimuli, variation in ligands, ligand combinations (costimulation) and time point are all known to leading to differences in the type and magnitude of the cell's response. Assaying therefore for the relevant response at the optimal time point for the stimulation provided is a critical step in understanding the NK cells' response. Some general pNK responses which can be assayed include: direct measurement of target cell killing,[441] upregulation of surface marker proteins,[442, 434] secretion of cytokines and chemokines,[443] intracellular Ca^{+} flux[128] as well as imaging for phenotype changes such as formation of actin rings (a sign of an activatory synapse)[37] and polarization of the microtubule-organising centre (MTOC).[444]

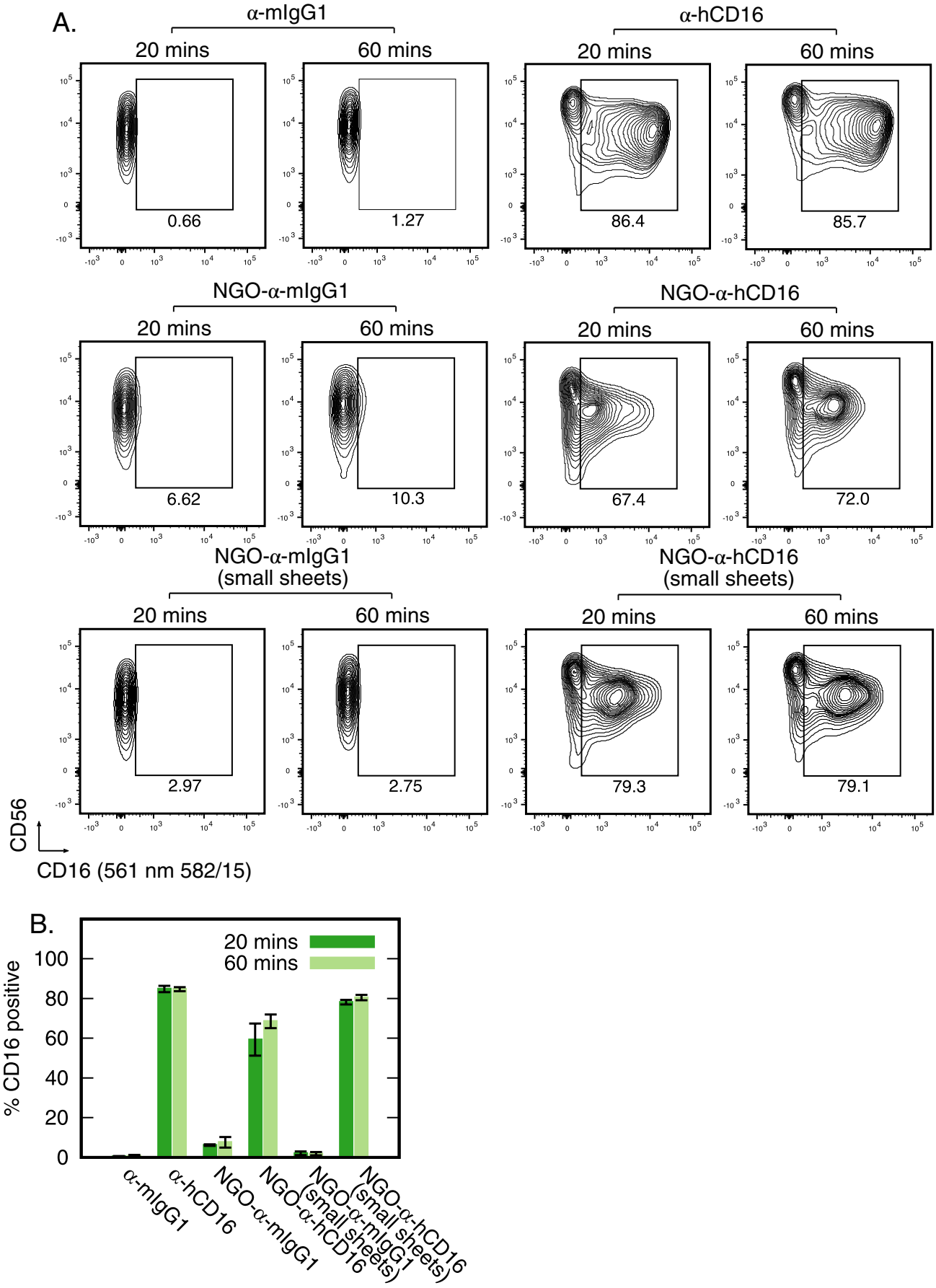

Figure 4.4: NGO-α-hCD16 has slower binding kinetics compared to unconjugated α-hCD16 and NGO-α-hCD16 (small sheets) (A.) Representative flow cytometry plots of NGO-mAbs and controls binding to pNK cells after incubation of 20 or 60 minutes. CD16 binding measured by excitation of the AF546 fluorochrome using the 561 nm laser and detection at 582 $\pm$ 15 nm. Gates show the CD16 positive threshold and percentage of cells within the gate are given below. (B.) Quantification of the binding kinetics. Results are the mean and standard deviation from two independent experiments using two human donors.

In the case of stimulation via the CD16 receptor a number of responses have previously been shown as markers of pNK activation. Upregulation of both CD69 and CD25 on the pNK cells' surface, secretion of interferon-γ and degranulation, which can directly be measured through the accumulation of the lysosome membrane protein CD107a (LAMP1), for example.[434]

CD69 is a homo-dimeric protein and receptor for currently unknown ligands (for T cells one established ligand was found to be galectin-1[445]) expressed on the surface of NK cells and other immune cells following activation.[446] CD69 expression has been shown to occur quickly following activation, within as little as 60 minutes, and is therefore a primary choice as an early stage assay to quickly determine if activation has been induced. CD69 upregulation is also known to be stimulated by rIL-2, as well as ligation of either the CD16 or IFN-γ receptors.[447, 448]

CD107a conversely is an intermediate to late stage marker for NK cell activation. Also known as the Lysosomal Associated Membrane Protein 1 (LAMP1) CD107a is a marker of degranulation due to it being present within the lipid membrane of lysosomes[449, 450] which transport the cyctotoxic granules delivered by NK in the process of their cytotoxic effector functionality.[434, 122] After fusion of the lysosome membrane with the cell membrane, CD107a is subsequently deposited on the cell surface where it can be stained for and detected using flow cytometry. The addition of monensin and brefeldin-A, both small molecules, are used to enhance CD107a detection by preventing it from later being re-internalized, leading to its accumulation and hence improving the detected signal to noise ratio. Unlike upregulation of CD69, CD107a accumulation is a direct observation of a known and integral effector function (cytotoxicity via degranulation), making it a commonly utilized assay.

The final marker of activation looked at here was Interferon-γ (IFN-γ). IFN-

γ is a cytokine with wide ranging affects on a number of cell types, it is, in general, required for immunity against viruses, intracellular bacteria and tumorogenesis. One example of its function in the immune system is the stimulation of dendritic cells to produce Interleukin 12 (IL-12).[436] The detection of IFN-γ secreted by NK cells is therefore a key indicator of the cell's activation through its immunomodulatory functionality.[435, 451, 437, 438]

Initially each assay was tested for its compatibility with the particular requirements needed for this work. One of these was the need for an unambiguous response, here defined as a large separation between the signal resulting from the positive and negative controls. In each case the chosen assay was tested using the immobilized α-hCD16 acting as the positive control and an equivalent immobilized isotype control, the negative. Soluble α-CD16 was also tested in each case to gauge the response induced by ligation of CD16 using soluble uncrosslinked α-hCD16. The gating strategy used to separate individual, viable, pNK cells is shown in Figure 4.5 (A–D.).

The response of pNK cells to each assay was tested at time points generally regarded as optimal. Of the three perspective assay only CD69 was found to be incompatible with future work, as shown in Figure 4.5 (E.). The expression of CD69 is clearly high ($> 80\%$) on all cells irrespective of stimulation, for instance on the α-mIgG1 control surface, and equally with unbound, unconjugated α-mIgG1. These results were virtually unchanged when measured at either 60 or 120 mins. There was also no significant increase shown in response to surface bound α-hCD16, here used as a positive control and potent inducer of NK stimulation, likely indicating that the expression of CD69 was already maximal. These results are perhaps best explained by studies which have shown CD69 upregulation occurs in response to IL-2 alone, which, the pNK cells used here were cultured in, necessarily, to promote their proliferation. The clear result is that pNK cells cultured in these conditions are incompatible with an assay of CD69 upregulation.

Results for CD107a upregulation, IFN-γ secretion by ELISA and intracellular staining were each successful having expected response to positive controls and baseline responses to negative controls. Despite the otherwise predictable responses, unexpectedly 5–25% pNK cells showed strong CD107a upregulation after culture for 7 days. The assay was therefore re-tested after 10 days of cell culture resulting in only 2–4% cells showing the same upregulation. This change in response as a function of the culture time could be the result of a change in pNK cell phenotype, for example changes in the expression of CD16.[452, 453, 454]

In combination the successful distinguishing of positive and negative controls shown by the assays for both the CD107a upregulation, as measured by flow cytometry and IFN-γ secretion by ELISA, made them ideal for use with the NGO-α-hCD16 species. Together they also encompassed both major effector functions of the cell—cytotoxicity and immunomodulation—providing a wide scope from which any affect resulting from NGO-α-hCD16 binding could be seen.

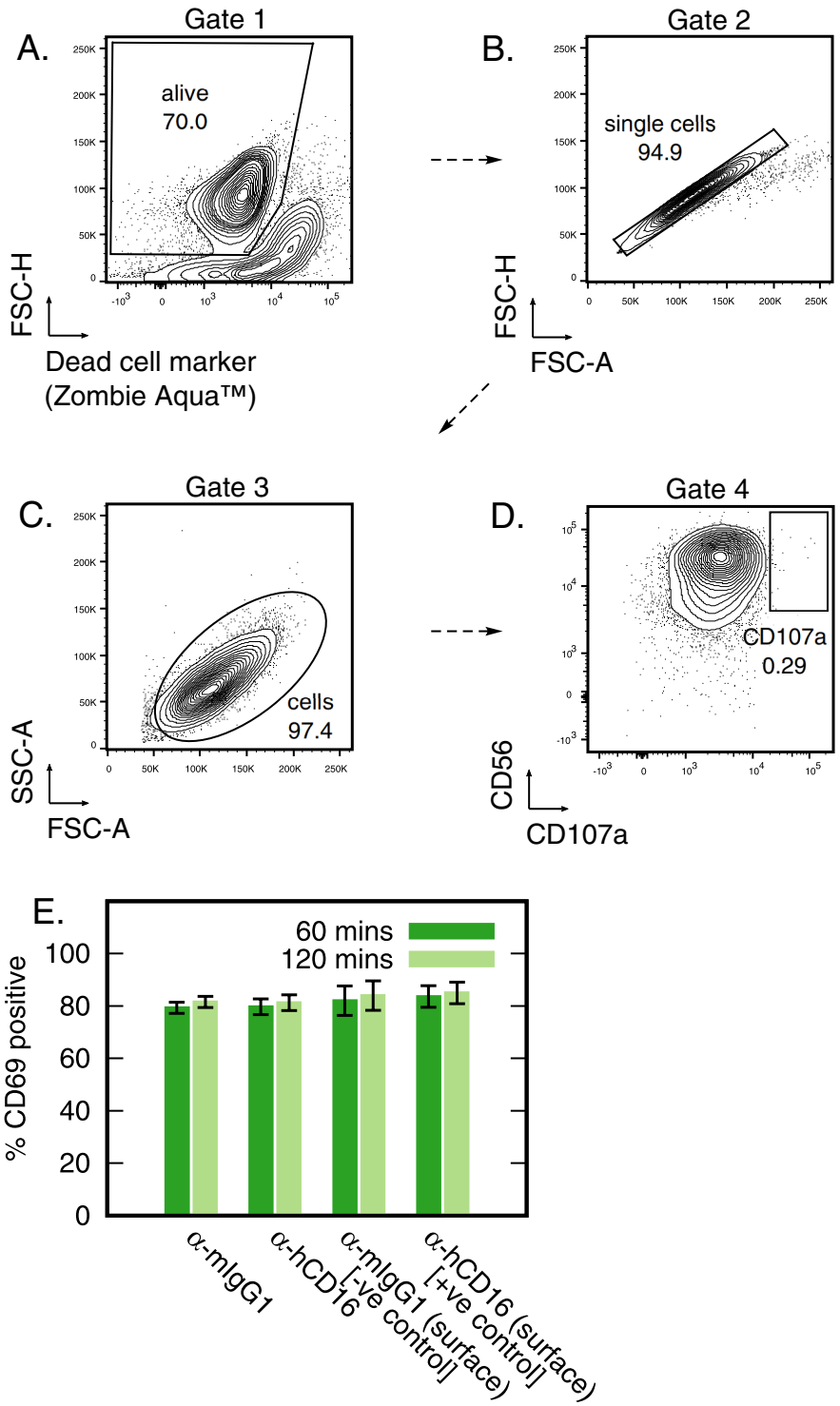

Figure 4.5: The expression of pNK cell surface receptors/proteins can be measured by gating stained cells after measurement by flow cytometry. (A–D.) Representative example of flow cytometry gating strategy used to separate alive, single, pNK cells. (A.) Live-Dead stain using dead cell marker Zombie Aqua™. (B.) Separation of single cells from doublets and triplets by comparison of forward scatter area and height. (C.) Selection of the general lymphocyte population by forward scatter side scatter comparison. (D.) An example of a final surface marker gate for the upregulation of CD107a. Gate drawn based on an FMO control. (E.) Quantitative results of the assay for CD69 after incubation with labeled controls for either 60 or 120 minutes.

Cytotoxic (Degranulation) Response

After establishing assays able to determine the markers of pNK stimulation in response to activation by ligation of the CD16 receptor, the response to clustered ligand was next tested using NGO-α-hCD16. In these experiments a specific comparison to the response provided by unconjugated α-hCD16 was made, to compare this accurately the concentration of mAb in solution for both α-hCD16 and NGO-α-hCD16 conditions was again matched at 2 μg/mL (consistent with the binding experiments). This equivalence was chosen so as to enable conclusions to be drawn from the different configurations of the same antibody, especially the differences that resulted from the clustering of the mAb in NGO-α-hCD16.

To begin, the CD107a upregulation was tested and representative plots with quantified results from 6 independent donors are shown in Figure 4.6 (A, B.). The first notable observation from these experiments was the difference in activation between the unconjugated α-hCD16 and clustered NGO-α-hCD16 (with median sheet size of 151 $\pm$ 59 nm and 134 $\pm$ 84 mAbs per sheet). On average across the two donors and two batches of NGO tested, 10.3% of pNK upregulated CD107a, $\sim$ 2-fold more than the 5.7% of unconjugated α-hCD16.

The augmented activation of degranulation was also witnessed in the NGO-α-hCD16 (small sheets) [median sheet widths of 72 $\pm$ 30 nm and 112 $\pm$ 71 mAbs per sheet], however to a lesser extent (average of 9% vs 10.3%). In each case the isotype control species NGO-α-mIgG1, including small sheets, showed no observable CD107a upregulation, thus making it clear that the effect was not the result of a nonspecific activation caused by other factors such as the NGO, streptavidin or biotin linker.

The donor–donor information for this data is plotted in Figure 4.7 (A, B.). Of the 6 donors tested 5 showed an increased response to the clustered ligands

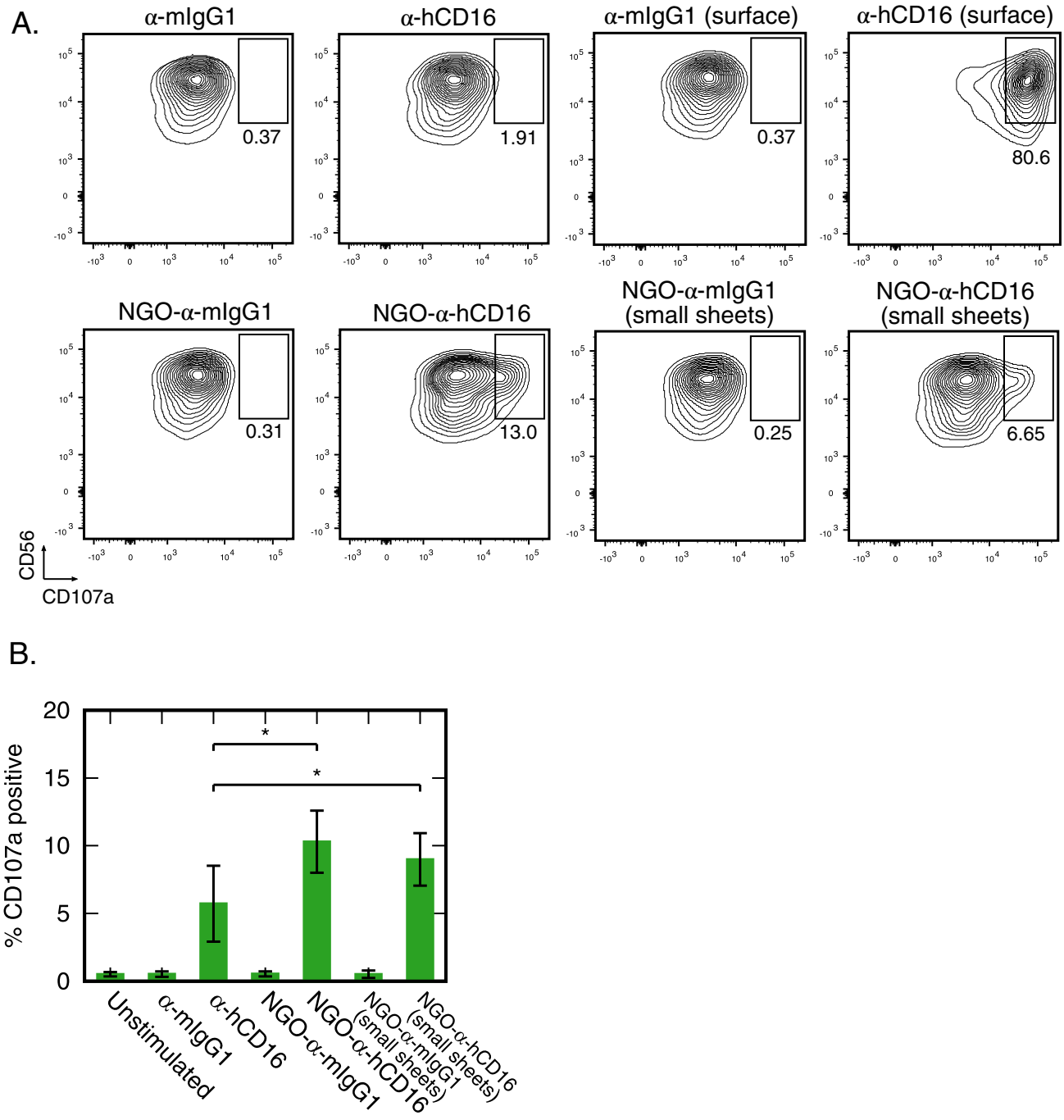

Figure 4.6: NGO-α-hCD16 augments the upregulation of CD107a on pNK cells. (A.) Representative flow cytometry plots from a single human donor showing the expression of CD107a in response to 6 hours incubation with the indicated conditions. Gate shows the location of the CD107a upregulated population and numbers are percentages of cells within the gate. Contours are 5% i.e 20 lines. (B.) Quantified % CD107a upregulation response of pNK to NGO-α-hCD16 and stated controls. Results are the mean and standard deviation from 6 human donors (3 for small sheets). Results combined from two similar NGO-mAb batches. Statistical significance is assigned as follows, $^{*}p < 0.05$

presented by NGO-α-hCD16 and of the 3 donors tested using the small sheet, all showed an augmented response.

The consistent donor–donor increases strengthen the confidence that the observed enhanced activation is the result of the clustered antibodies supplied using the NGO-α-hCD16. Donor variability as a result of using primary human cells is generally expected, however, the consistency of the principle donor–donor augmentation strengthens the general observation of NGO-α-hCD16 augments degranulation in pNK cells.

Another potentially interesting observation from these results is the percentage of the pNK cell population which respond to NGO-α-hCD16. Across all responses a 5–20% subset of pNK cells appear to upregulate CD107a in response to stimulation by NGO-α-hCD16 representing a small subset of the NK population. Work on determining the contribution of individual NK cells to the bulk cytotoxicity has shown that only a small proportion of the total population are responsible for the majority of the toxicity. For instance Vanherberghen et al. noted that it was a small 10–20% subset of the total pNK cells which were responsible for the majority of cytotoxicity towards 293T target cells.[455] The exact characteristics of these pNK cells he was, however, unable to define. Results such as this nonetheless show the variability of the pNK cell population, an affect which could be contribute to the observed results presented above. Excitingly it also highlights that small increases in the stimulation, as demonstrated here using NGO-α-hCD16, may be physiologically significant.

Biocompatibility

The toxicology of graphene based materials has been mentioned previously due to its importance in determining if the material is viable in a biological context. Being a relatively new biomaterial, NGO and NGO-PEG's toxicity is still to be comprehensively determined. GO alone has been shown

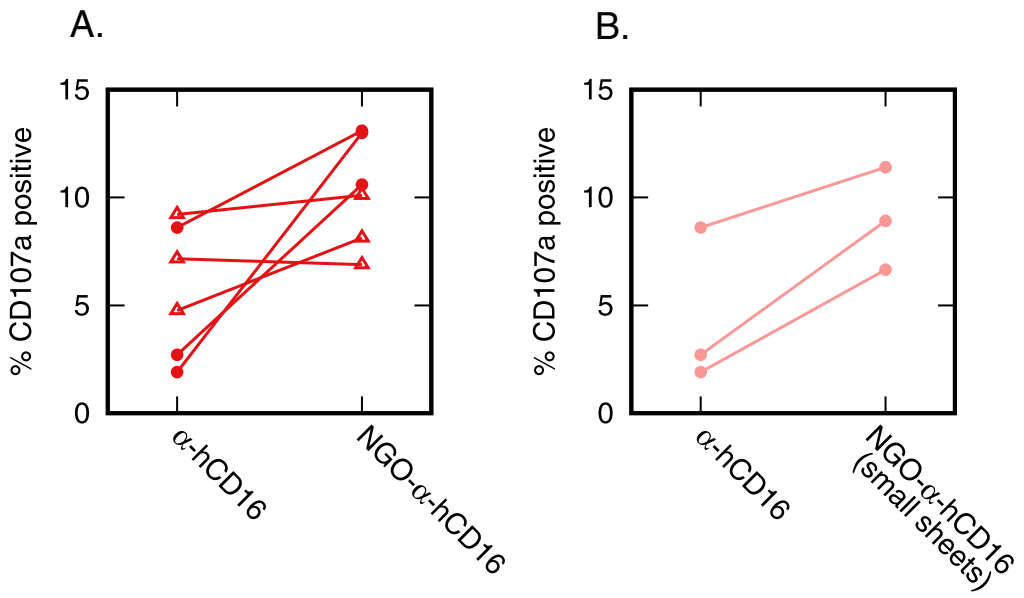

Figure 4.7: Compared by donor, NGO-α-hCD16 augments CD107a upregulation in 5 of 6 tests. (A.) Results for NGO-α-hCD16 and α-hCD16. (B.) Results for NGO-α-hCD16 (small sheets). In all conditions are linked by donor using solid red lines. Results combined from two similar NGO-mAb batches, Batch 1 (filled circles), Batch 2 (unfilled triangles).

to induce membrane ruffling and shedding[260] while NGO-PEG on the other hand has exhibited good compatibility with Raji cells,[456] and Mesenchymal Stem Cells (MSC),[457] though it was noted to induce enhanced secretion of TNF-α, IL-6 and MCP-1 in macrophages.[433]

The work presented here, focusing on the response to a protein conjugated NGO species, has little to no toxicological precedent in the literature. The absence of observed nonspecific degranulation presented in the previous section, particularly in response to the isotype variant of NGO-α-mIgG1, is a positive first indication of the compatibility of NGO-mAb materials.

Having demonstrated the potential of clustered α-hCD16 it was important to measure the viability of the pNK cells after prolonged interaction with the NGO-α-hCD16 supramolecular species. This acted as one measure of the toxicity of the NGO-mAb species. To assess the biocompatibility a dead

cell marker (Zombie Aqua^{TM}) stain, permeable to cells with disrupted membranes only, was added in combination with the NGO-mAb and controls. After 6 hours of incubation with each species, flow cytometry was used to assess the differences in viability. The results of which can be seen in Figure 4.8.

pNK cells were separated first by gates based on their size and shape, followed by their viability (Figure 4.8 (A.)). The quantified results of this data (Figure 4.8 (B.)) showed no appreciable difference between any NGO-mAb species and the unstimulated control. In all cases the percentage of alive cells assessed in this way exceeding 80% after 6 hours. As a primary indicator of the NGO-mAb toxicity these results are particularly pleasing, although it is clear that significant further experimentation at multiple time points and concentrations would be required to be confident in the overall biocompatibility.

Immunomodulatory (Cytokine) Response

The secretion of IFN-γ, an immunomodulatory response predominantly attributed to pNK was next investigated.[458] CD16 ligation is known to stimulate IFN-γ secretion when plate bound, though ligation with unbound α-hCD16 mAb, has to our knowledge not been published. The unconjugated α-hCD16 mAb here again was again used as a control to assess the response elicited by NGO-α-hCD16, and hence clustered CD16.

After separately mixing unconjugated α-hCD16 and NGO-α-hCD16 with pNK cells for 6 hours in the presence of monensin and brefeldin-A inhibitors, the supernatant was collected and using an ELISA the secretion of human IFN-γ was measured. For stimulation by unconjugated soluble α-hCD16 no enhanced secretion of IFN-γ was observed when compared to unstimulated and isotype controls conditions (averaging 40 pg/mL, see Figure 4.9 (A.)). The NGO-α-hCD16 condition on the other hand, lead to an average across

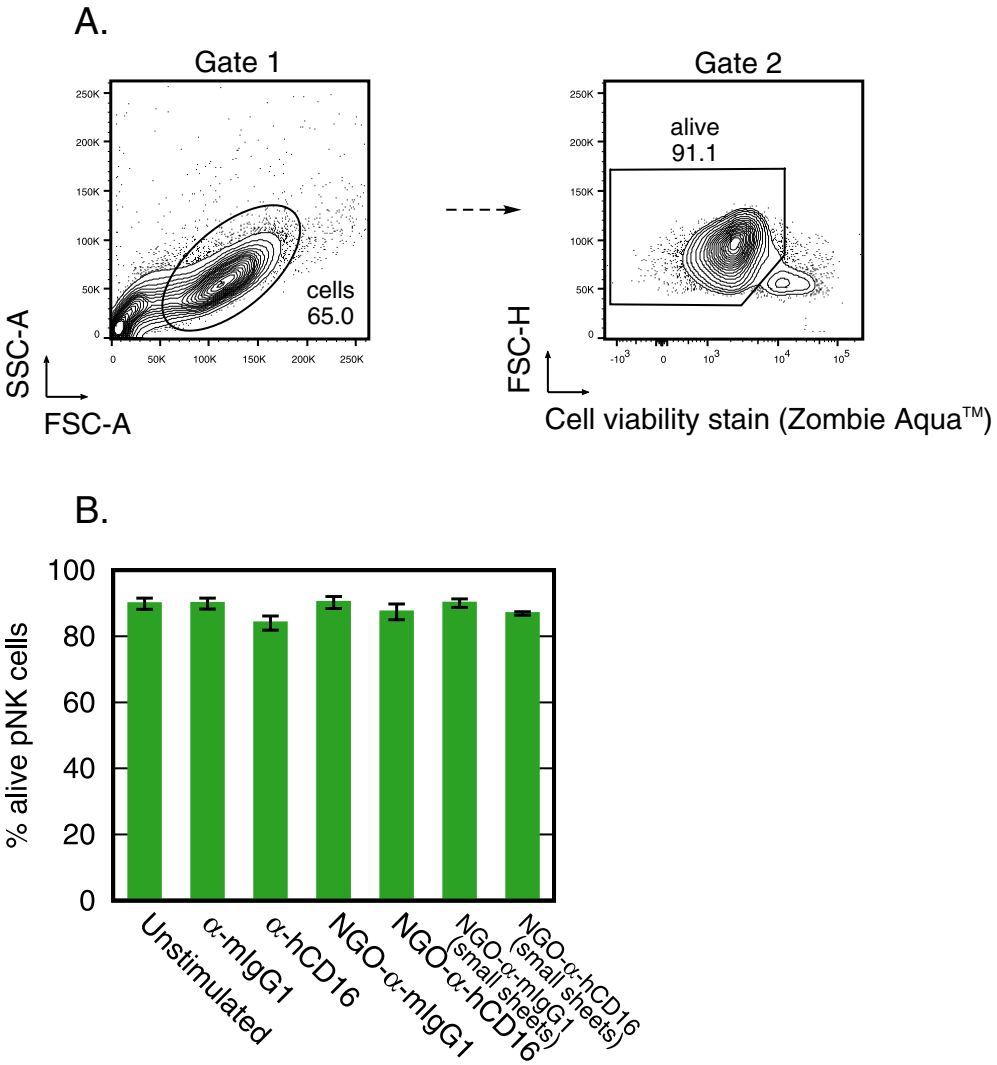

Figure 4.8: NGO-mAb has no adverse affect on the viability of pNK after incubation together for 6 hours. (A.) Gating used to distinguish first pNK cells from detected debris and secondly the cells viability, achieved using the Zombie Aqua^{TM} stain. Cell viability before experiment was measured at $>$ 85% by hemocytometer and the measured proportion of debris between conditions are equivalent. (B.) Quantified percentages of alive pNK after 6 hour incubation with each condition. Alive cell determined by their inability to be stained by the cell viability dye. Results are the mean and standard deviation from 6 human donors (3 for NGO-α-hCD16 (small sheets)).

three donors of 81 pg/mL IFN-γ secreted, a 2-fold average increase compared to the unconjugated α-hCD16. The overall concentrations of secreted IFN-γ were for comparison similar to those previously reported for pNK stimulation by insect target cells at 6 hours[142].

Across the three donors tested all showed a similar increase in the secretion of IFN-γ as shown by the donor-donor comparison in Figure 4.9 (B.), the fold increase between donors for the clustered vs unclustered α-hCD16 was 2.7-fold. Interestingly however secretion from surface bound α-hCD16 was not noted to be significantly greater than the unstimulated controls despite the enhanced secretion measured for NGO-α-hCD16. Other studies have shown that IFN-γ secretion measured after 6 hours are sufficient to enable its detection and one kinetic study has indicated the maximum secretion occurs after 6 hours incubation with K562 target cell.[142].

In previous assessments of IFN-γ secretion by ELISA at 16 hours, there was clear secretion of the cytokine above background levels, making the response at 6 hours unexpected. One potentially important difference was the presence of monensin and brefeldin-A present in these experiments. Both of these small molecules are generally accepted to interfere with the secretion of newly synthesized cytokines,[459, 460] making them commonly used to enhance the brightness when staining for cytokines intracellularly.[461].

O'Neil-Anderson et al. have demonstrated in T cells that monensin has little affect on the secretion of IFN-γ, resulting in 90% of the secretion without its addition. Brefeldin-A on the other hand affects IFN-γ secretion considerably at 2–4 hour time points where it prevented any secretion, a difference they attribute to the glycosylation of IFN-γ which brefeldin-A effects significantly. In the same study after 18 hours secretion was nonetheless observed, indicating that brefeldin-A slows but does not prevent secretion (there work using a 10-fold higher concentration of brefeldin-A than used here).[462] To there-

fore understand if despite the lack of observed secretion, there had been internal IFN-γ produced by the cells, intracellular staining for its presence was carried out.

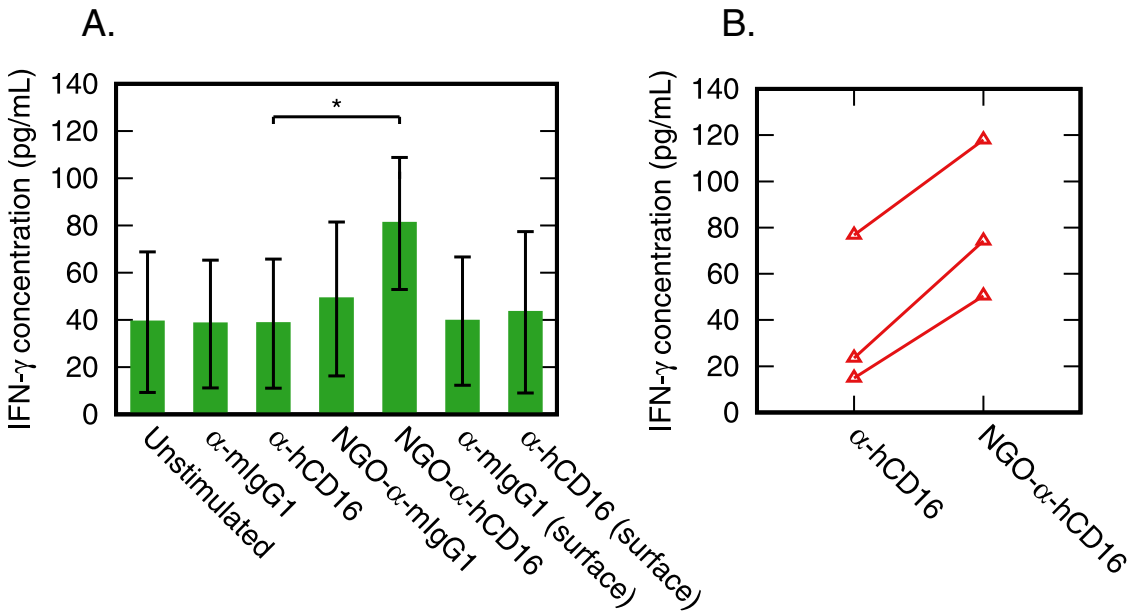

Figure 4.9: NGO-α-hCD16 stimulates secretion of IFN-γ. (A.) Concentration of IFN-γ secreted as measured by ELISA. Results are the mean and standard deviation from three human donors. Statistical significance is assigned as follows, $^{*}p < 0.05$ (B.) Donor–donor comparison of the secretion from unconjugated α-hCD16 and clustered α-hCD16 in NGO-α-hCD16. Conditions linked by donor using solid red lines.

The intracellular results are shown in Figure 4.10 (A, B.), and indicate that the surface bound α-hCD16 resulted in intracellular production of IFN-γ, with 5% pNK cells positive for its intracellular staining. Conversely there was no detected intracellular production caused by NGO-α-hCD16 which were less than 1%.

In combination these results are suggestive of kinetic differences in the cytokine secretion induced by NGO-α-hCD16 compared to surface bound α-hCD16. One hypothesis which would explain these observations is that NGO-α-hCD16 causes relatively rapid secretion, perhaps by a 'readily re-

leasable pool' (RRP) of vesicles containing IFN-γ[463, 27] or another mechanism such as the mobilization of retained nuclear IFN-γ mRNA[464]. Evidence supporting this hypothesis includes the kinetic differences in IFN-γ secretion observed between $CD56^{bright}$ and $CD56^{dim}$ pNK cell subsets.[27] NGO-α-hCD16 would, given this explanation cause preferably excitation of the rapid secretors i.e. the $CD56^{dim}$ subsets shown by De Maria et al.

On the other hand the results could be due to the dominant cytotoxic activation of pNK cells by the α-hCD16 surface stimulation. The separation of cytotoxicity and immunomodulation have, for example, been shown to be mutually exclusive in a number of studies.[465, 466, 467] This hypothesis would propose that the the α-hCD16 surface stimulation, as a result of the dominant cytotoxic response, would lead to a delayed immunomodulatory activation and intracellular synthesis of IFN-γ in preference to secretion. The CD107a data in the previous section could be used to support this conclusion as the positive control condition produced a greater upregulation of CD107a compared to NGO-α-hCD16 (45–80%).

Both hypothesis discussed above remain very much speculative. The unusual difference in pNK response to NGO-α-hCD16, surface and soluble α-hCD16 stimulation nevertheless indicates that the use of the NGO-α-hCD16 nanoclustered material produces exclusive responses which are likely a result of its unique properties.

4.4 Conclusions

4.4.1 Summary of Findings

The goal of this chapter was to determine if the NGO-α-hCD16 species synthesized was functional as judged by its expected use, and secondly if it promoted a unique response in pNK cells. Evidence presented here shows:

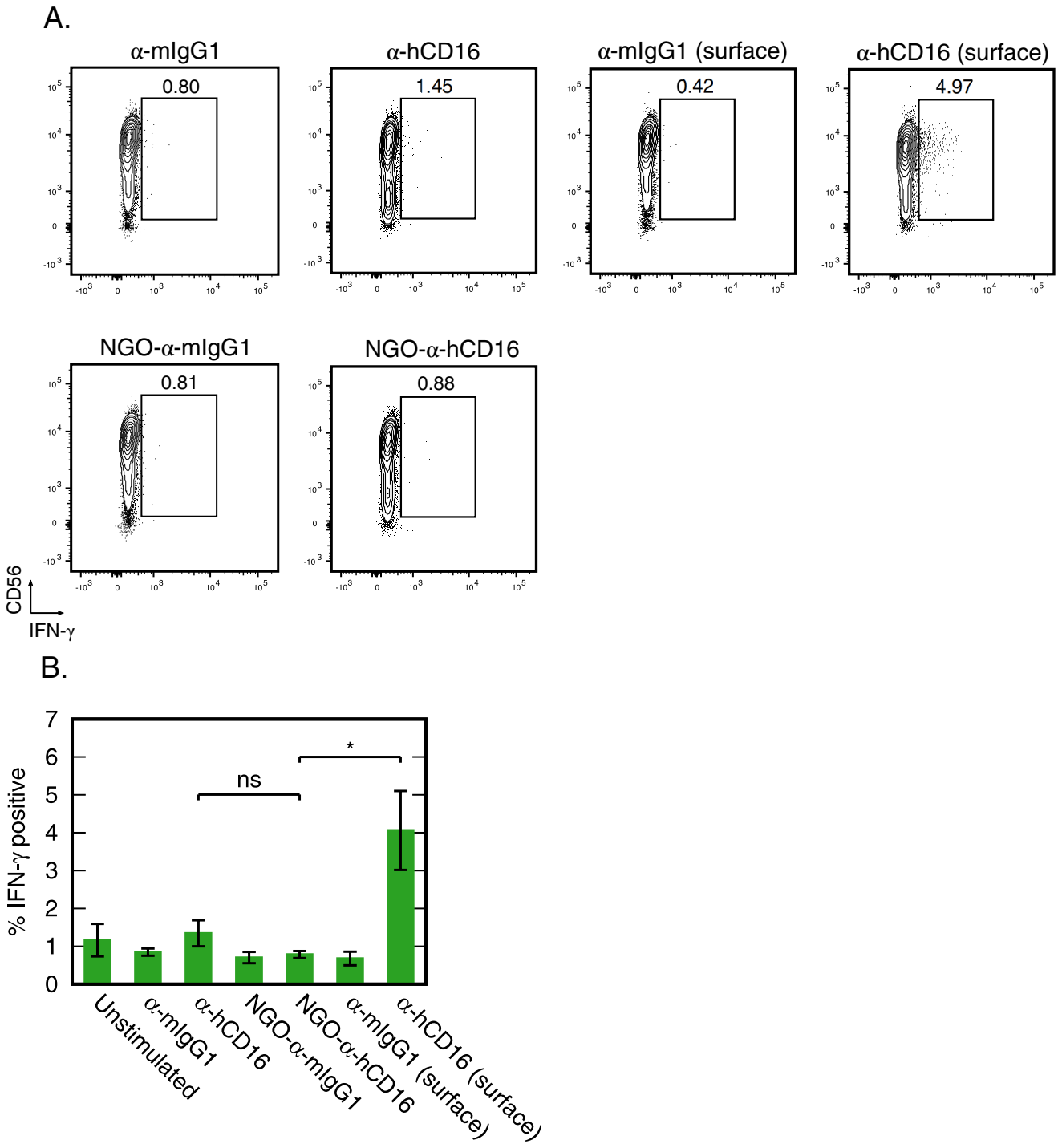

Figure 4.10: Surface bound α-hCD16 causes intracellular IFN-γ production while NGO-α-hCD16 does not. (A.) Representative flow cytometry plots of intracellular IFN-γ staining after 6 hrs incubation with each condition. IFN-γ positive gate and percentage of cells within shown. (B.) Quantified percentage IFN-γ positive pNK cells as measured by intracellular staining of IFN-γ. Results are the mean and standard deviation from three human donors. Statistical significance is assigned as follows, ns $p \geq 0.05$, $^{*}p < 0.05$

1. NGO-α-hCD16 shows the ability to specifically bind the CD16 receptor of pNK cells, exhibiting a small reduction in binding efficiency but little nonspecific binding.

2. NGO-α-hCD16, most likely a result of its supramolecular structure, has slower binding kinetics compared to unconjugated α-hCD16.

3. NGO-mAb species exhibit good biocompatibility with pNK cells after 6 hrs of interaction.

4. NGO-α-hCD16 stimulates an, on average, 2.7-fold enhancement in CD107a upregulation, between the same donors, when compared to the equivalent concentration of unconjugated α-hCD16.

5. NGO-α-hCD16 causes an, on average, 2.7-fold increase in the secretion of IFN-γ, when compared to unconjugated α-hCD16.

4.4.2 Concluding Remarks

The results obtained here using NGO-α-hCD16, present hybrid bio-nanomaterials as an emerging class of therapeutic reagents. Hybrid nanomaterials which use NGO for its distinctive properties have generally focused on improving diagnostic or therapeutic function.[49, 50, 52, 46, 53, 54] Here, however, a focus on the structural use of the NGO has been made, utilizing it as a framework to confine and cluster mAbs, which in turn, has enabled the mimicry of an otherwise complex structure—the receptor-ligand nanocluster. The receptor-ligand nanocluster itself being an interesting structure to target due to its suspected influence on immune cell function.

Evidence presented further support the hypothesis that the clustering of ligands influences the activation of pNK cells, at least in relation to the CD16 receptor. This is shown by both the augmented degranulation and cytokine secretion, compared to unclustered ligands. The magnitude of improvement

was on average 2–3-fold, while larger enhancements may still be possible considering the reduced overall binding NGO-α-hCD16 exhibited.

The mechanism behind the enhanced response to clustered ligands, to-date, remain unclear. Contributions from mechanotransduction that could be enhanced during the receptor-ligand interaction, a result of the inherently crosslinked mAbs of NGO-α-hCD16, may be crucial, or alternatively the affects of the spatial dependence of receptor ligation, that in turn leads to enhanced signaling due to proximity.[37, 19, 68, 31] Both remain leading theories and the potential for each to contribute to the observed effects, as well as other explanations, are possible.

To-date there are no examples of materials utilizing NGO as a scaffold for a NK cell ligand, nor any showing that such a species can activate a NK cell or any immune cells for that matter. The augmented activation of NK cells by this system is therefore a novel result. NGO has been applied to a number of established uses,[49, 50, 52, 46, 53, 54] again none, however, have used the material to create a system tailored to manipulate surface nanostructure and affect a cellular response. This concept alone has very little precedent, the only related finding being that receptor crosslinking is an important step to immune cell activation. This crosslinking concept has been demonstrated by secondary antibodies,[468, 128] cells,[128] microscale beads,[469] and streptavidin tetramers,[470] although none of these have the potential that NGO can offer to control crosslinking on the 50–250 nm scale that nanoclusters are observed to exist. This difference makes the work presented here important. The functionalization of colloidal NGO by biotin-streptavidin to form a stable reagent has been reported,[428] although this work is the first to apply this methodology to mAb conjugation, and the first example tested in a biological system with a successful outcome.

Therapeutically these results may also be significant. The ability to enhance

activation using equivalent concentrations of mAbs through their clustering is an exciting finding that could be influential. The development of a system which targets a sub-cellular structure i.e. receptor nanoclusters, to induce a response is a novel concept and this early demonstration of the principle is novel. Conceivable uses would focus on the treatment of diseases dependent on immune responses, for instance chemotherapeutics, autoimmune disorders, and chronic infections.

Another consequence of these findings is the confirmation that understanding nanoscale features of biological structures is crucially important to understanding their function—a perspective which is still gaining acceptance. Similar studies will, it is hoped, provoke ongoing interest in this area of cell biology and result in further improvements to therapeutic treatments.

Chapter 5

Superresolution Microscopy of Biofunctionalized Nanoparticle Arrays

5.1 Scope

In this chapter the production of Au nanoparticle arrays with reproducible properties, including nanoparticle size and interparticle spacing is shown. Relatively large ($\sim$ 100 nm inter-nanoparticle spacing) nanoparticle arrays were fabricated and then combined with a new, simple, nanoparticle functionalization strategy using Alexa Fluor 647 labeled, reduced IgG antibodies (rIgG), which bind the nanoparticles via thiol-gold bonding. Other control surfaces are also produced using glass without the addition of nanoparticles or by ommiting the passivation step which is used to prevent a passivation step used to prevent nonspecific binding.

Stochastic Optical Reconstruction Microscopy (STORM) is then used to image these functionalized arrays so that comparisons can be made between them. Later complimentary data analysis, including the Nearest Neighbor (NN) and Ripley's *K*-Function analysis is applied to the STORM dataset of a fully functionalized array, and simulated datasets, including; a random distribution of points, an ideal nanoparticle array both with points missing (to simulate underoccupancy) and added uncertainty in the nanoparticle po-

sition (to simulate errors in the rIgG localisation). Together this analysis was used to show if the data obtained from STORM imaging was representative of a functionalized array.

5.2 Methods

5.2.1 Nanoparticle Array Fabrication

Nanoparticle arrays were prepared by block copolymer micelle nanolithography using poly(styrene)-*b*-poly[2-vinyl pyridine] in xylene according to Spatz et al,[63] with modifications. 5 mg/mL micellar solutions were first prepared by dissolving 0.1 g poly(styrene)-*b*-poly[2-vinyl pyridine] (PS-*b*-P2VP) (Polymer Source) in 20 mL *p*-xylene with magnetic stirring overnight. Micellar solutions were prepared with PS-*b*-P2VP of various molecular weight (MW) including PS(110 kDa)-*b*-P2VP(52 kDa), PS(52 kDa)-*b*-P2VP(31 kDa), PS(34 kDa)-*b*-P2VP(18 kDa) and PS(16 kDa)-*b*-P2VP(3.5 kDa). To these gold (III) chloride trihydrate (Sigma-Aldrich) was added at Au:VP ratios of between 0.5 and 0.1. For example for 20 mL, 5 mg/mL PS(110 kDa)-*b*-P2VP(52 kDa) loaded at 0.1 Au:VP, 12.2 mg $HAuCl_4 \cdot 3\,H_2O$ was added. The solution was then covered to prevent photodegradation and stirred overnight or until no solid $HAuCl_4 \cdot 3\,H_2O$ remained. Rectangular glass coverslips (0.15 mm thickness, VWR) were first cleaned using a piranha solution 1:3 H_2O_2 to H_2SO_4 overnight followed by successive rinsing with ultrapure water (Milli-Q, 18.2 MΩ cm). Loaded micelles were transferred to glass coverslips by dip coating at a rate of approximately 0.4 mm/s. Removal of polymer coating and reduction of Au(III) salt was achieved by plasma etching using a 5% hydrogen plasma (25 sccm, 350 W, 0.4 mbar, 45 mins). Nanoparticle array interparticle distance and nanoparticle size were measured by Scanning Electron Microscopy (SEM) using multiple samples within fabrication batches. All chemicals were purchased from Sigma-Aldrich unless

explicitly stated otherwise.

5.2.2 Scanning Electron Microscopy

Scanning Electron Microscopy (SEM) was carried out using a Field Emission Scanning Electron Microscope (FEG-SEM) LEO Gemini 1525. Glass substrate samples were sputter-coated with either carbon or chromium to prevent surface charging and improve image stability. Chromium coating was carried out with a sputtering current of 75 mA for 1 min giving an estimated 15 nm thick layer. SEM images were taken using an accelerating voltage of 5 keV. Analysis of nanoparticle size and interparticle spacing was achieved using FIJI software (ImageJ version 1.51n) and the analyze particles function[471, 472].

5.2.3 Antibody Reduction

Antibody reduction was carried out using 2-Mercaptoethylamine (2-MEA) in PBS. 10 mg 2-MEA (Sigma-Alrich) was dissolved in 70 μL PBS to give 881 mM stock solution. 0.4 μL, 500 mM EDTA, 10 μL, 2 mg/mL goat anti-mouse IgG-AF647 (Invitrogen) and 0.15 μL 2-MEA, final concentration $\sim$ 15 mM in PBS were mixed and allowed to react for 90 mins at 37 °C. Reduced antibody mixture was then purified by repeated rinsing with PBS containing 10 mM EDTA. For comparison of 2-MEA reducing concentrations 2 mg/mL goat anti-mouse IgG-AF647 was reacted with 2-MEA at final concentrations of 15, 50, 150 and 500 mM at 37 °C. After 90 and 120 mins samples of each condition were taken and the degree of antibody reduction resolved by SDS-PAGE. SDS-PAGE was carried out using Bolt 4–12% Bis Tris Plus Gels (Thermo Fisher Scientific) with a ColorPlus Prestained Protein Ladder, Broad Range (10–230 kDa) (New England BioLabs).

5.2.4 Nanoparticle Array Functionalization

Nanoparticle arrays were first exposed to UV light for 20 mins, after which 12-well silicone chambers (Ibidi) were then applied to the glass and pressed evenly to ensure good adherence. For nanoparticle array + PLL-g-PEG + rIgG, 100 μL, 1 mg/mL PLL(20 kDa)-g[3.5]-PEG(2 kDa) (SuSoS) in ultrapure water (Milli-Q, 18.2 MΩ cm) was added for 1 hr followed by removal and rinsing using 2 $\times$ 200 μL PBS, and 100 μL, 20 μg/mL reduced goat anti-mouse IgG-AF647 (rIgG) was then applied and incubated overnight. The rIgG was then removed and the surface washed with 3 $\times$ 200 μL PBS before imaging by STORM.

5.2.5 Coverslip Functionalization

Glass coverslips were cleaned by ultrasonication in 1M KOH for 5 mins followed by rinsing with with ultrapure water (Milli-Q, 18.2 MΩ cm) and drying under a N_2 stream. 12-well silicone chambers (Ibidi) were then applied to the glass and pressed evenly to ensure good adherence. For glass + rIgG condition, 100 μL, 20 μg/mL reduced goat anti-mouse IgG-AF647 was then applied and incubated overnight. For Glass + PLL-g-PEG + rIgG, 100 μL, 1 mg/mL PLL-g-PEG (SuSoS) in ultrapure water (Milli-Q, 18.2 MΩ cm) was added for 1 hr followed by removal and rinsing using 2 $\times$ 200 μL PBS, and 100 μL, 20 μg/mL reduced goat anti-mouse IgG-AF647 was then applied and incubated overnight.

5.2.6 STORM Imaging

STORM imaging was carried out on a N-STORM Nikon Ti microscope with a CFI SR Apochromat TIRF 100$\times$ 1.49 NA oil immersion objective. A Ti-NSFC N-STORM filter cube was used to separate excitation and emission fluorescence signals. Fluorescence signal was detected by an Andor IXON Ultra DU-897 X-9315 electron multiplying charge coupled device (EMCCD)

camera (Andor Technology) (105.2 nm pixel size, CCD sensitivity of 6.09 A/D count and 98.8 electron single pixel noise). Images were captured with a 256×256 pixel (mono 16 bit) region of interest (ROI) by using a 1.5× zoom, an electron multiplying (EM) gain of 200, and conversion gain of 3. Excitation was achieved by a 170 mW 647 nm (Agilent Ultra High Power Dual Output Laser) using an initial 30% pulse followed by image aquisition of 15000 frames. Initial TIRF imaging for region selection was achieved using 2% power. Imaging was carried out after addition of imaging buffer made of 50 mM Tris-HCl, 10 mM NaCl, 10% glucose, 1% v/v 2-mercaptoethanol and 1% v/v GLOX solution. GLOX solution was 14 mg glucose oxidase, 50 μL catalase (17 mg/mL) in 200 μL 10 mM Tris, 50 mM NaCl buffer (pH $\sim$ 8). All buffers filtered through 0.22 μm filter.

5.2.7 STORM Data Analysis

Peaks in raw single molecule image data were extracted using ThunderSTORM[473] with image filtering (B-spline, order 3, scale 2), local maximum approximation of molecule localization (2*std(wave.f1), 8 neighborhood connectivity) and sub-pixel localization using integrated Gaussian point spread function (PSF) (5 pixel fitting radius, maximum likelihood fitting method, 1.6 pixel initial sigma and multi-emitter fitting analysis disabled). From this initial dataset any drift was corrected using ThunderSTORM built in drift correction (cross correlation, 5 bins, 3× magnification), followed by filtering (uncertainty < 15). Three regions of 5×5 μm were selected for each 26.93×26.93 μm region size (256×256 pixel ROI) and visualized using average shifted histograms with 3 lateral shifts using 10× magnification. Maxima were selected using FIJI software (ImageJ version 1.51n), Process – Find Maxima (noise tolerance = 21) and exported as comma separated values by Analyze – Measure – Save As. Nearest neighbor (NN) analysis was carried out by importing X,Y data into MATLAB (R2017a)

and analysing with the nearest neighbor.m script written by Richard Brown (http://uk.mathworks.com/matlabcentral/fileexchange/12574-nearestneighbor-m) using a custom script written to loop over all points in dataset. Ripley's *K*-Function analysis was calculated using MATLAB (R2017a) and a script written by Carina Dunlop.

5.2.8 Simulated Datasets

Simulated nanoparticle data was created using the MATLAB, rand, uniformly distributed random number function. Simulated freedom of movement (FOM) was applied by selection of a random radius between 0 and 25 nm and a random angle between 0 and 360° from which to transform the point position. Removal of points from the extracted SEM dataset was carried out using the MATLAB uniformly distributed random number function to select points at random for removal.

5.3 Results and Discussion

5.3.1 Nanoparticle Array Fabrication

Production

The fabrication of nanoparticle arrays by block copolymer lithography has been generally discussed within Section 2.3.1 and Section 2.3.2. The specifics of the lithography used here, and its applications nonetheless require examination. Figure 5.1 (C.) illustrates the experimental methodology used to produce nanoparticle arrays with distinct and reproducible interparticle spacing and nanoparticle size. The choice of di-block copolymer and specifically the copolymer block lengths is particularly important for the control of interparticle spacing as illustrated in Figure 5.1 (A, B.) where the interparticle spacing varies from 130 nm for a PS(110 kDa)-*b*-P2VP(52 kDa) to 40 nm for PS(34 kDa)-*b*-P2VP(18 kDa) with minimal variation of the nanoparticle

size. Other factors which can be manipulated to affect the interparticle spacing include, the dip coating retraction speed, polymer concentration, solvent choice, use of thermal annealing and micelle loading.

For the purpose of carrying out STORM on nanoparticle arrays, arrays with larger interparticle spacings were favored to minimize the potential for problems associated with the resolution limit of the microscopy. The lateral resolution for STORM is approximately 20 nm laterally for all superresolution techniques, including STORM, under ideal conditions. Nonetheless large interparticle spacing were best produced with PS(110 kDa)-*b*-P2VP(52 kDa) which forms arrays with interparticle spacing of 95–130 nm given the stated conditions. Arrays used for imaging had mean interparticle spacings of 94.1 nm $\pm$ 17.3 nm (standard deviation).

Cai et al. have demonstrably shown that the occupancy (number of molecules per nanoparticle) of gold nanoparticles with biotin-alkylthiol linked streptavidin increases with nanoparticle diameter.[72] The occupancy of nanoparticles has a direct effect on the use of nanoparticle arrays to control receptor-ligand interactions as this directly affects the resultant spacing between ligated receptors. It has been shown by our own laboratory and others that the control of receptor spacing can effect immune cell signaling.[37, 68] Studies such as these assume the single occupancy of a nanoparticle to reliably understand the affect of the receptor spacing on cell activation.

Characterization

From the outset nanoparticle arrays which had equivalent nanoparticle diameters of less than 15 nm irrespective of interparticle spacing were therefore produced. Figure 5.2 (A.) shows the that the decreased loading of micelles with $HAuCl_4 \cdot 3\,H_2O$ salt produced with equivalent block copolymers, decreases the nanoparticle size from 17.9 $\pm$ 3.0 nm to 14.8 $\pm$ 2.7 nm. The

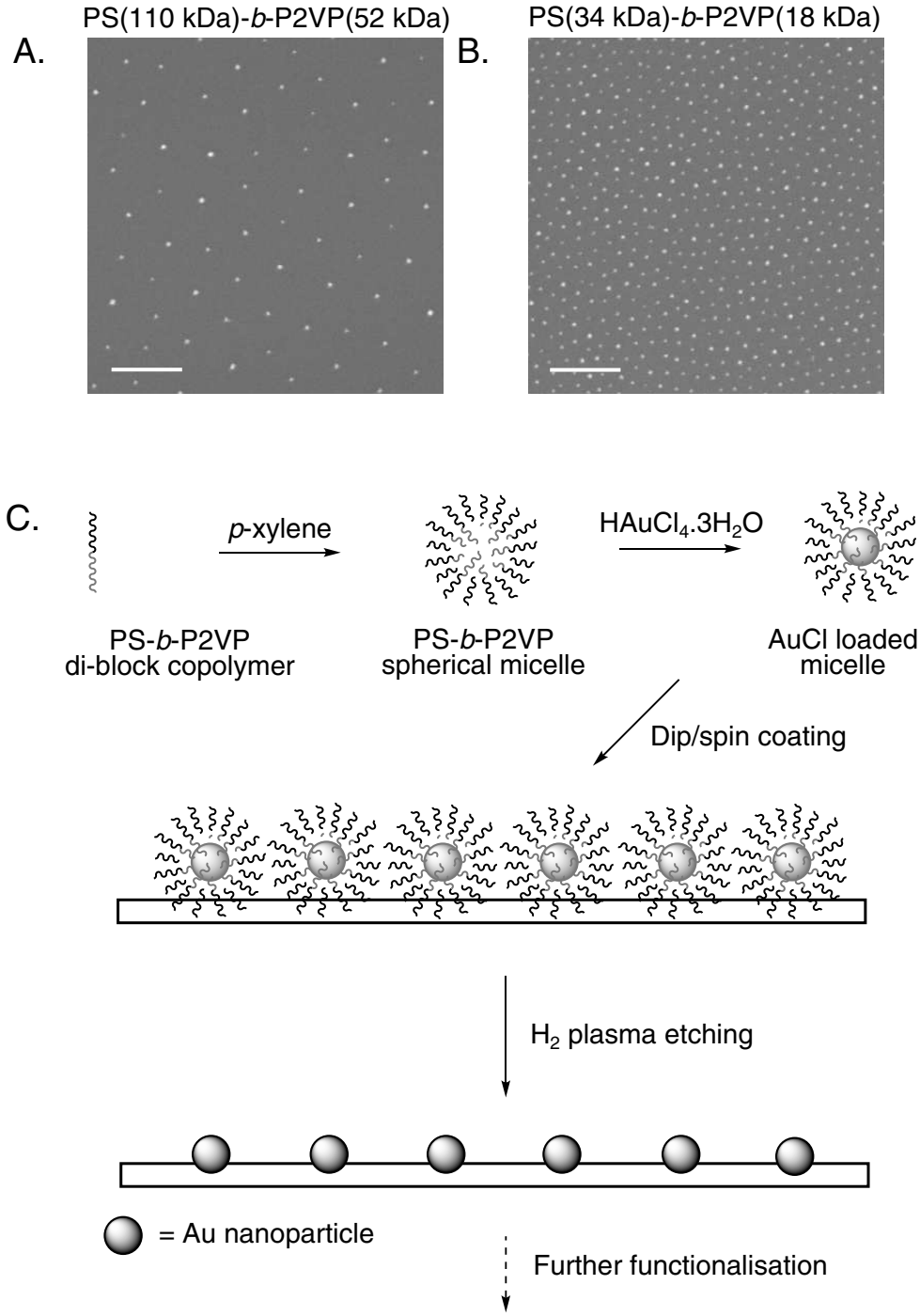

Figure 5.1: Hexagonal Au nanoparticle arrays can be produced with controlled interparticle spacing by using PS-*b*-P2VP block copolymer of varying MW. (A.) Nanoparticle array with interparticle spacing of $\sim$ 130 nm produced with PS-*b*-P2VP di-block copolymer with separate block MW of 110 kDa and 52 kDa respectively. Scale bar = 200 nm (B.) Nanoparticle array with interparticle spacing of $\sim$ 40 nm produced with PS-*b*-P2VP di-block copolymer with separate block MW of 34 kDa and 18 kDa respectively. Scale bar = 200 nm (C.) Schematic of nanoparticle array production using block copolymer micellar lithography.

general convention of describing the loading with respect to the molar ratio of the gold (Au) and Vinyl Pyridine (VP) has been used here. Variation of the Au:VP loading ratios for di-block copolymers that produce nanoparticle arrays with spacings between 20 and 130 nm was carried out and the results can be seen in Figure 5.2 (B.). Mean nanoparticle sizes that are consistently less than 15 nm irrespective of interparticle distance were achieved.

With control of nanoparticle size, arrays fabricated from each diblock copolymer system were selected to produce interparticle spacings with an even distribution on length scales which remain important for biological study. Figure 5.2 (C.) shows the conditions used to produce nanoparticle arrays of between 20 and 100 nm. This scale was consistent with the length scales that have shown significant for patterning of ligands and the activation of both T and NK cells.[37, 68]

Functionalization

Protein functionalization strategies for Au nanoparticle arrays have been widely researched.[427, 71, 37] The initial binding of the Au nanoparticle in each case utilizes the sulfur-gold bond, which despite being well established in the field of bioconjugation is not fully understood.[474, 475] From this sulfur-gold bond usually in the form of a thiolated linker, functional end groups permit the subsequent attachment of biologically relevant molecules in bottom up approaches. These include Ni(II)-coordinating NTA-thiol linkers which bind His tagged proteins (proteins with greater than six histidine amino acids at the N- or C- protein terminus). NHS-thiol linkers can be used by reacting the NHS group with a range of proteins using the catalyzed amide bond formation to primary amines found on almost all proteins. Complimentary single stranded DNA pairs have also been used, one thiolated and the second attached to a corresponding protein with the complimentary strand. Biotin-streptavidin conjugation has also been used due

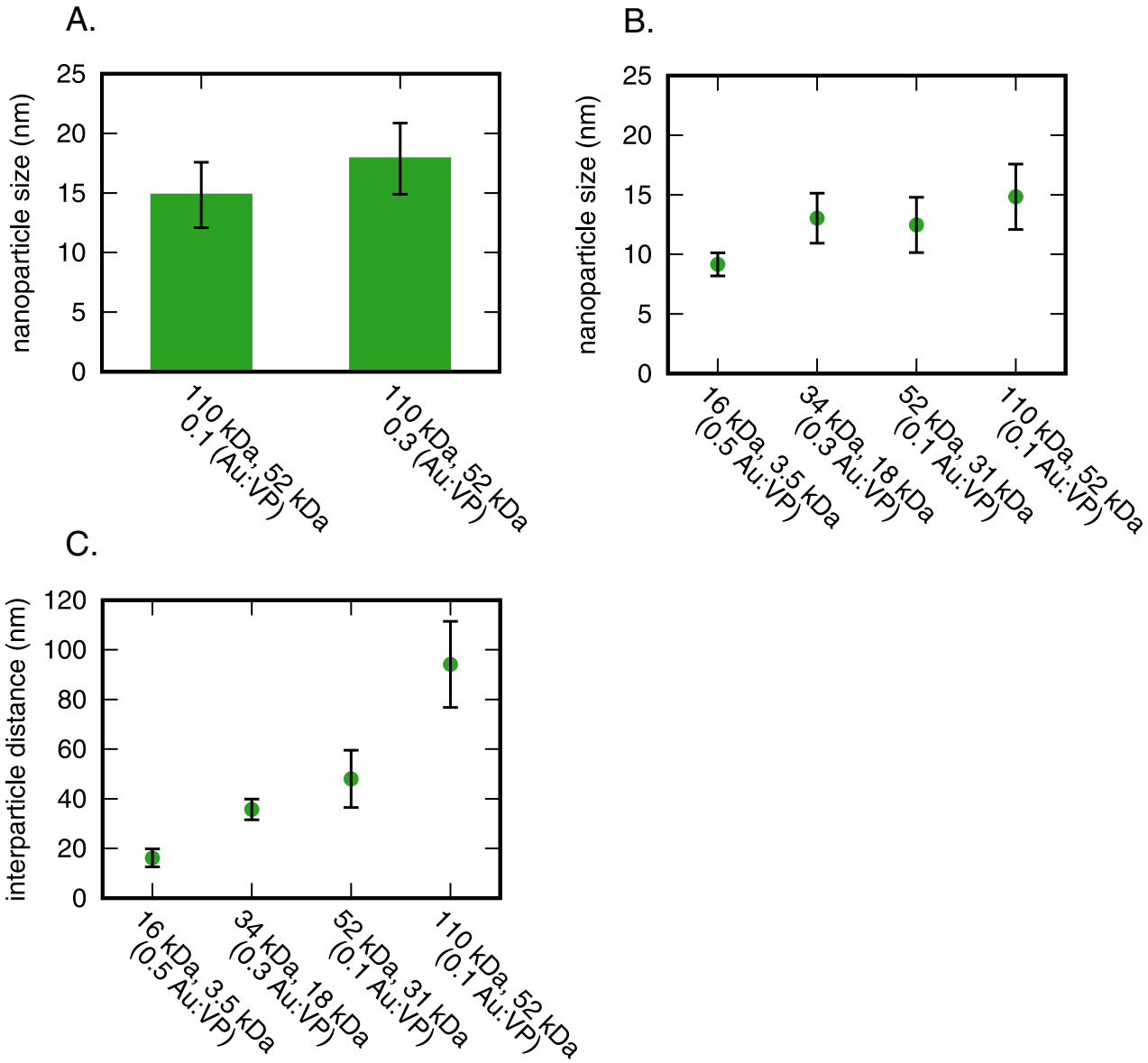

Figure 5.2: Nanoparticle array properties can be controlled by gold:Vinyl Pyridine (Au:VP) loading ratio and the Molecular Weight (MW) of di-block copolymer (A.) Variation of nanoparticle size produced by 0.3 and 0.1 Au:VP loading of PS(110 kDa)-*b*-P2VP(52 kDa). (B.) Nanoparticle sizes produced by controlling the Au:VP loading of arrays produced with different MW di-block copolymers. (C.) Measured interparticle spacings produced by di-block copolymers of varied MW and Au:VP loading ratio.

to the strong binding and ease of biotinylation.

While each has their advantages even simpler approached have been achieved, for instance using F(ab')$_2$ fragments with exposed disulfide bridges that enable direct conjugation with no linkers.[37] Given the extreme sensitivity required for any reproducibility and accuracy on the nanoscale, functionalization strategies with the fewest steps were sought.

Following the line of thought hoping to reduce experimental complexity, the reduction of antibodies at the hinge disulfide bridge using 2-Mercaptoethylamine (2-MEA) to produce reduced IgG fragments (rIgG) with unprotected thiol (sulfurhydryl) groups was carried out. Free thiols have been shown capable of specifically binding Au nanoparticles making them an ideal direct linkage.[476, 477] With this approach single rather than binary antigen binding per nanoparticle (assuming single occupancy) can also be achieved, a characteristic previously discussed as important for cell experiments. In addition the antigen binding ability, due to the rIgG orientation (a result of the thiol groups location) has also been shown to be improved compared to whole antibodies.[478]

The three commonly used chemicals to reduce IgG antibodies include 2-MEA, Dithiothreitol (DTT) or (Tris(2-carboxyethyl)phosphine) (TCEP). In this work 2-MEA was used thanks to its availability. Early experiments with supplied protocols (Pierce) indicated a 10 mg/mL concentration of IgG with a 50 mM 2-MEA final concentration incubated at 37 °C for 90 mins would be sufficient to selectively reduce the hinge disulfide. In testing, this protocol although successful at hinge cleavage, also showed significant reduction of heavy-light chain disulfides as shown by SDS-PAGE in Figure 5.3 (B.) Given the same 90 min 37 °C conditions, a range of 2-MEA concentrations were tested. 15 mM 2-MEA was selected as it resulted in sufficient rIgG production while producing far less heavy and light chain cleavage. Preventing

heavy–light chain cleavage was preferable as fully cleaved heavy and light chains, due to their own free thiols, would compete with the rIgG to occupy Au nanoparticles despite offering no antigen binding capabilities.

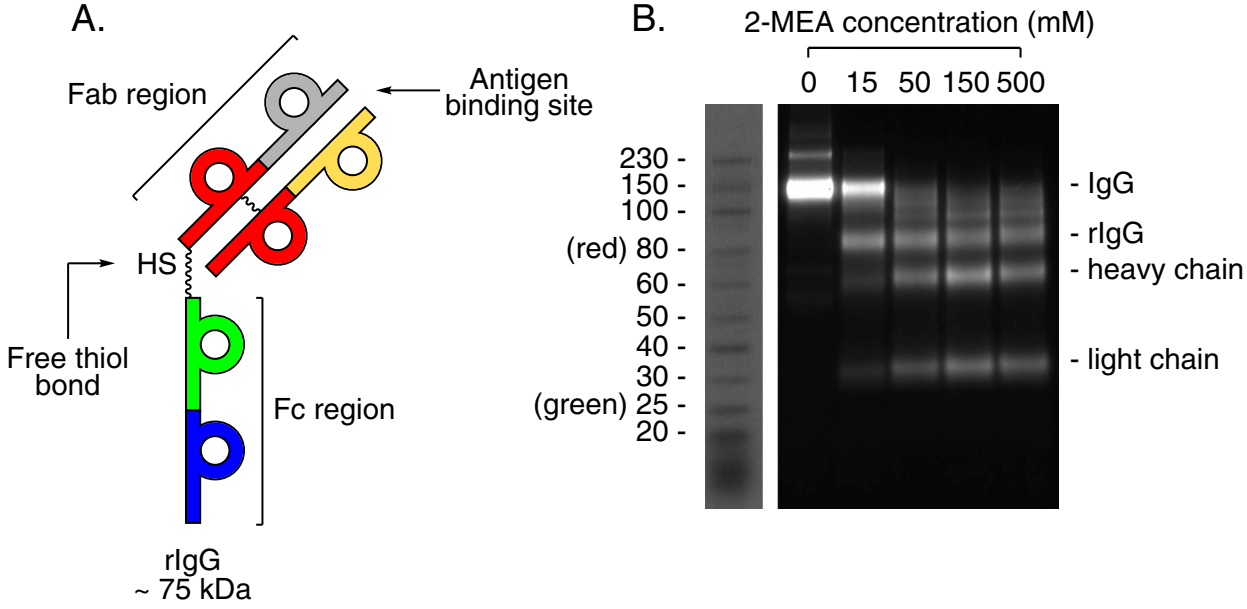

Figure 5.3: Selective reduction of IgG using 2-MEA produces reduced IgG (rIgG) exhibiting a thiol group at the hinge region and a preserved antigen binding site. (A.) Schematic of rIgG showing important structural features. (B.) SDS-PAGE of IgG reaction mixture after reduction by 2-MEA at various concentrations and labeled with the reduction products. Protein ladder and MWs given for reference.

The full functionalization strategy summarized in Figure 5.4 illustrates the 3-step functionalization procedure developed to functionalize Au nanoparticle arrays. In the first step, passivation of the surface against non-specific binding is carried out by the addition of PLL-g-PEG. PLL-g-PEG electrostatically binds to the glass substrates through the positively charged lyine groups, anchoring the well established antifouling reagent, poly(ethylene glycol) PEG.[479, 480, 481] Uncharged elemental Au nanoparticles are not coated by this treatment and are selectively available after removal by washing away excess PLL-g-PEG for functionalization by the thiol of rIgG. Dur-

ing the incubation of PLL-g-PEG with the nanoparticle array surface, conveniently the IgG antibody of choice is reduced (2.) resulting in rIgG. The third step is then the simple addition of rIgG immediately after its production to the passivated nanoparticle array surface, and following incubation, removal by washing.

5.3.2 STORM Imaging

Image Examples and Controls

STORM imaging of functionalized nanoarray surfaces was carried out in conjunction with a number of control surfaces created on both equivalent nanoarrays as well as glass slides with no nanoparticles. Figure 5.5 illustrates representative regions from each condition imaged. Each image shows individual points (red points) which are the result of the STORM localization of individual blinking events (fluorochrome fluorescence), herein these localizations are referred to solely as 'events'.

Figure 5.5 (A.) shown larger in Figure 5.6 (A.) shows events (individual red points) falling close together, forming circular clusters of high density with regions of few and no events in between. In some areas events can be seen forming clumps of various small sizes, although these are comparatively less common. The surface has a clear uniformity and there is homogeneity across the regions.

As a positive control surface the nanoparticle array was functionalized without the prior addition of PLL-g-PEG (B.). Without the passivation provided by PLL-g-PEG events can be seen homogeneously covering the regions with no clear structure visible. This observation fits well with the expected non-specific binding of rIgG to both glass and Au nanoparticle which would occur given no passivation.

A second positive control of glass slides with no Au nanoparticles was also

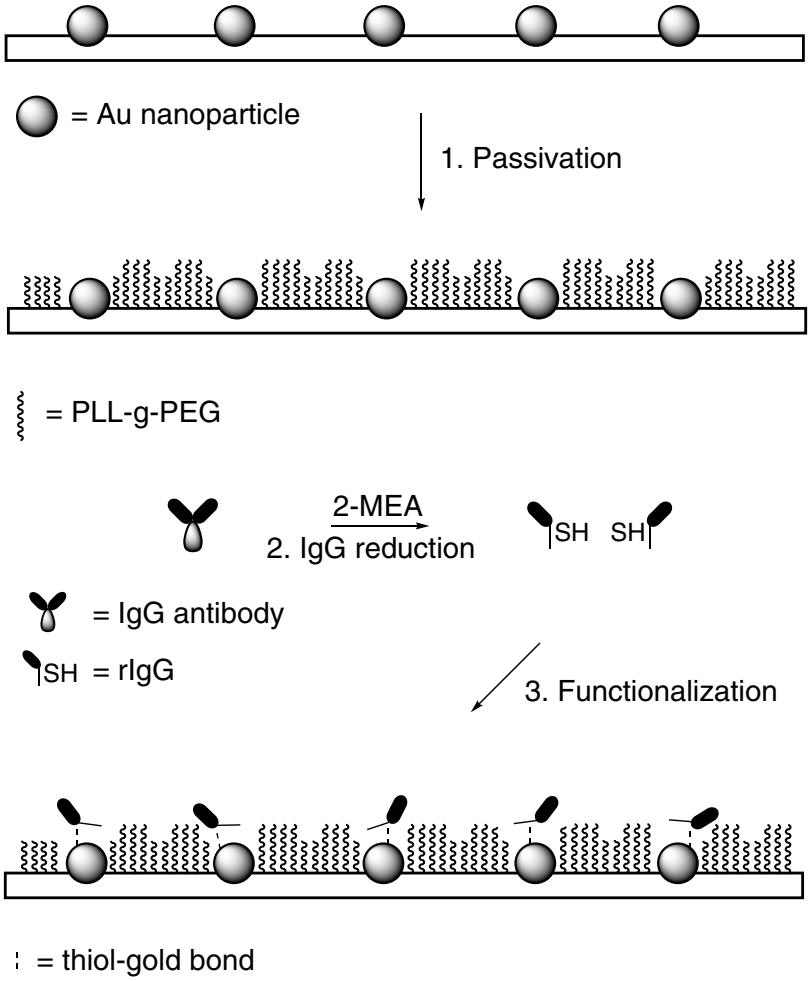

Figure 5.4: Schematic of the developed procedure used to successfully functionalize Au nanoparticle arrays using rIgG. (1.) Passivation of the nanoparticle array to prevent nonspecific protein adsorption using PLL-g-PEG (2.) Reduction of IgG using 2-MEA to produce rIgG with available thiol groups capable of binding Au nanoparticles (3.) Functionalization of Au nanoparticles by addition of rIgG in the presence of a passivated background to prevent nonspecific rIgG binding.

used and functionalized by addition of rIgG directly. These surfaces show extremely inhomogeneous coverage, both within given regions and between regions. Events form large clusters of varying shape and do not appear to exhibit any uniformity. The non-specific binding of rIgG expected fits well with these observed results.

The final negative control surface was that of glass pretreated with PLL-g-PEG and then rIgG added. In this case the effectiveness of PLL-g-PEG is demonstrated as most regions show no events, indicating a surface free of protein. Across the three only a single clear cluster of events (D. - region 2) can be seen showing that the events originating from background signal are minimal.

To observe the difference in fine structure obtained from STORM imaging of functionalized nanoarrays and control surfaces Figure 5.6 shows large 5x5 μm regions plotted side by side. The comparison between the two clearly illustrate the differences in the distribution of events between the surfaces as a result of the different distribution of fluorochromes on the surfaces.

STORM Image Considerations

To initially understand and analyze the images produced by STORM the properties of this imaging modality must be considered. These properties include the number of switching cycles, blinking properties, and survival fraction of the fluorochrome. Switching cycles are the repeated cycling between the fluorescent and dark states which in turn lead to the measurement of multiple events from a single molecule. It is this stochastic nature which gives STORM imaging its name. If a fluorochrome is static then clusters of events which are detected due to single fluorochrome exhibiting stochastic switching cycles in combination with the localization precision causing small localization variations. There are many factors which affect the number of switching cycles including the imaging buffer, fluo-

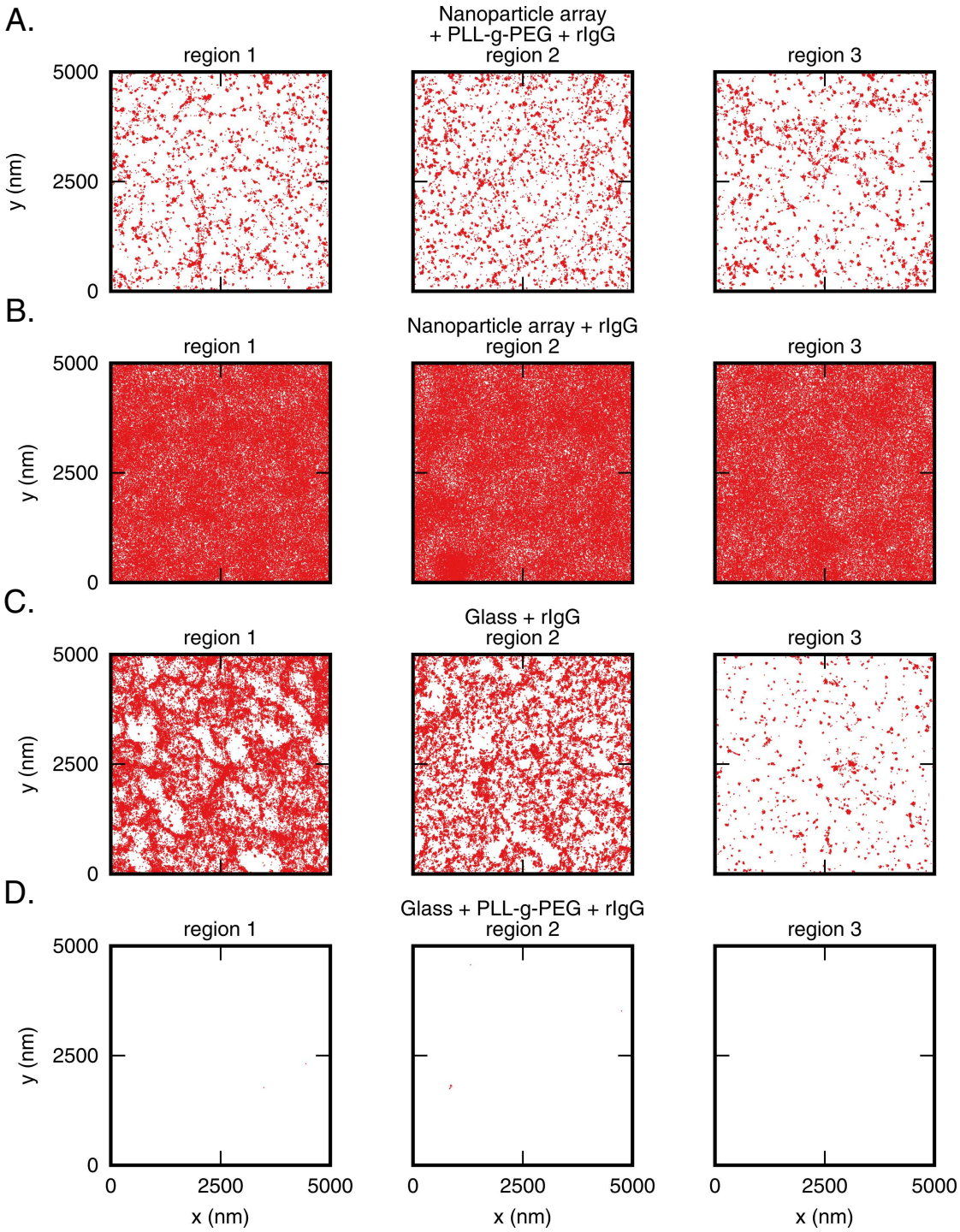

Figure 5.5: Example regions of functionalized nanoparticle arrays and control surfaces. (A.) Processed STORM images of three 5×5 μm regions of a nanoparticle array functionalized first with PLL-g-PEG followed by rIgG. (B.) Images of three 5×5 μm regions of a positive control surface functionalized using an identical nanoparticle array coated solely with rIgG. (C.) Images of three 5×5 μm regions of a positive control glass slide coated with rIgG. (D.) Images of three 5×5 μm regions of a negative control surface composed of a glass slide coated first with PLL-g-PEG followed by rIgG. Given the excellent passivation afforded by PLL-g-PEG almost no events are visible. All STORM processing was identical for each condition and region.

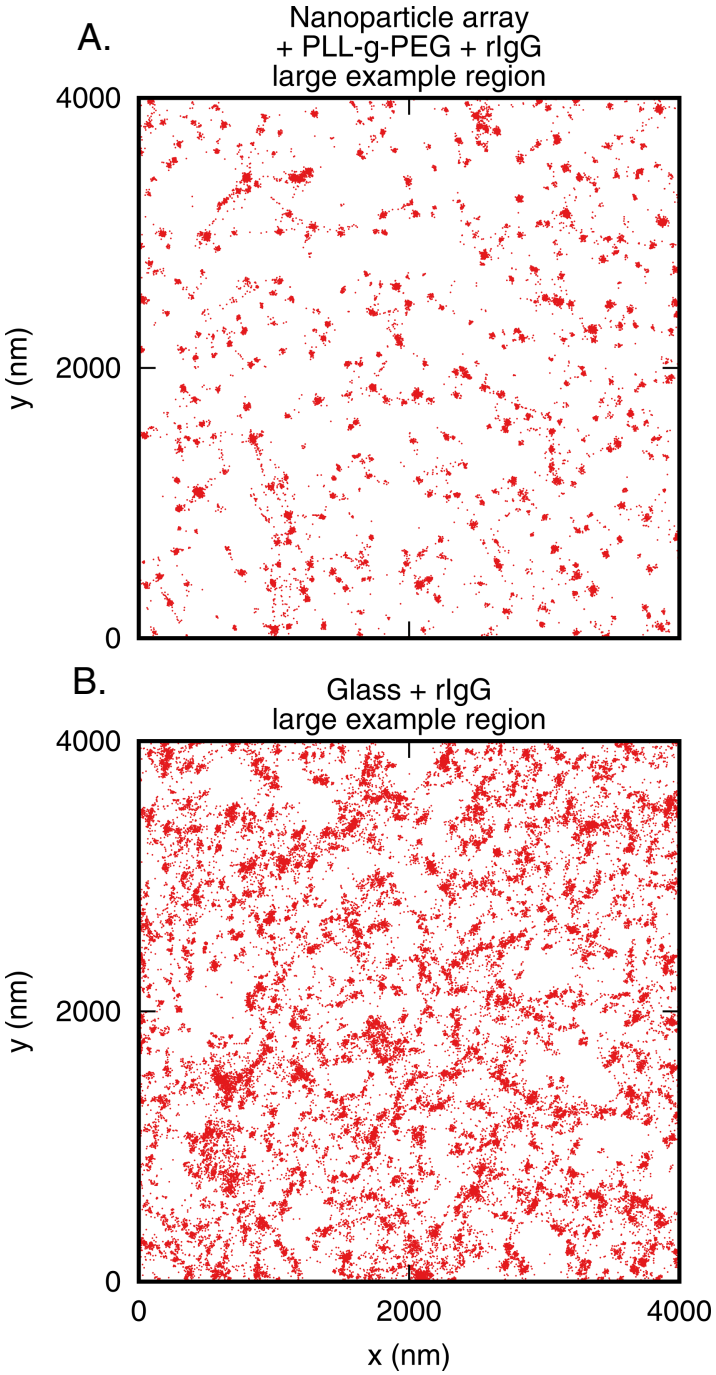

Figure 5.6: Characteristic features displayed by single molecule localization STORM images of a rIgG functionalized nanoparticle array and control glass slide coated with rIgG. (A.) Functionalized nanoparticle array (PLL-g-PEG + rIgG) show clusters of events (fluorochrome localization) interspersed with areas of no localizations (B.) rIgG coated glass coverslip control surface show a combination of large clumps of localizations, smaller clusters and areas of no localizations.

rochrome, laser power and application of 'back-pumping'. Given certain conditions, however, mean values have been measured for some commonly used fluorochromes.[418]

In addition to the switching cycles, the number of blinking events produced by a fluorochrome as it cycles between fluorescent and dark states is also stochastic in nature, and a second reason for the number of events within a cluster varying.

The final factor affecting the number of events observed is the survival fraction i.e. the number of switching cycles achieved before a fluorochrome remains permanently in the dark state. The permanence of the dark state is most commonly attributed to chemical or chemical or structural modification of the fluorochrome.[418]

Taking into account the nature of STORM images, in regards to nanoparticle arrays there are three characteristic features; 1. point like events 2. hexagonal structure and 3. constant interparticle distance, are expected to be observed. First the spherical-point like events from the underlying attachment of a fluorochrome to a nanoparticle and second the hexagonal packing with periodic interparticle distance. Beginning with the first characteristic, for labeled rIgG bound to a single nanoparticle with no diffusion events from the attached fluorochrome would be expected to appear as spherical point like clusters. It should be noted, however, that any non-mobile fluorochrome would produce a similar cluster of points. As such, it is then important that characteristics 2. and 3. are observed.

Figure 5.6 (A, B.) provides representative example images from large areas of both a functionalized nanoparticle array and a control rIgG coated glass coverslip. The example functionalized array demonstrates the expected clustering of events separated by areas of minimal events. In comparison the rIgG coated coverslip does not show these features and is instead character-

ized by the coalescence of event clusters into larger fibril shaped areas. In addition to this there is an increase in the number of events outside of local clusters. These are best ascribed to the diffusion of fluorochromes during imaging.

While features expected of a nanoparticle array are present in the functionalized nanoparticle array, as shown be the representative image in Figure 5.6 (A.), the distinct hexagonal periodic structure observed in SEM images of similar arrays are not. To some degree this is the result point like structures not possessing linked complex geometries which allow small deviations from perfection to lead to a rapid decrease in the perceived structure.[482, 483] A robust mathematical analysis of the data is therefore required, and here carried out, to determine if the STORM data collected is representative of a functionalized nanoparticle array.

Data Extraction

To analyze the STORM event dataset it was first supposed that small dense clusters of events were representative of well localized, stationary fluorochromes as argued above. This is based on the theoretical nature of fluorochromes and backed by superresolution data of dilute fluorochromes attached to substrates, which exhibit similar characteristic clusters of localization (events) when imaged by STORM.[19]

There is with little doubt a multititude of ways to define clusters and extract their coordinates. Figure 5.7 (A.) shows the process applied for this work. In the first step a density estimation was first applied using an average shifted histogram (ASH) algorithm. The ASH effectively used to change the 2 dimensional coordinate data into a 3-dimensional intensity profile of the surface. Small areas with a large number of events therefore produce a greater intensity than sparse areas with minimal events which allows for a threshold intensity (characteristic of a given fluorochrome) to be selected,

and from the position of maximal intensity, its position extracted.[484, 485] These steps are shown in Figure 5.7 (A.) 2., the selection of clusters of high intensity (using a maxima point selection algorithm with a supplied noise tolerance) and lastly the extraction of the coordinates at the point of highest intensity.

To accurately compare the features of the STORM dataset a nanoparticle array from the same production batch, and hence with similar interparticle spacing and nanoparticle size, was used a point of comparison. Data from this 'ideal' example of a nanoparticle array was extracted using a comparable method, i.e. Figure 5.7 (B.) step 3., where the maxima point selection and extraction is applied directly to a SEM image. An example of the result of this point extraction can be seen in Figure 5.7 (B.), where the extracted points have been replotted (blue points).

5.3.3 Data Analysis

Occupancy of Nanoparticle Arrays

The most simple analysis that can be made is a comparison of the density of points measured for the extracted STORM data and the 'ideal' SEM image. Assuming 100% functionalization and 100% detection of bound rIgG it would follow that both should have comparable densities. Figure 5.8 (A, B.). illustrates the number of points detected in two representative regions of—(A.) the points extracted from the ideal nanoparticle array and (B.) points extracted from a functionalized array imaged by STORM. Figure 5.8 (C.) quantifies the difference in the number of points over multiple (12 regions by STORM, 3 by SEM) 4×4 μm. Nanoparticle arrays produced using the PS(110 kDa)-*b*-P2VP(52 kDa) exhibited a mean density of 124.8 nanoparticles/μm^2 while the similarly functionalized, imaged and point extraction giving a mean density of only 42.3 nanoparticles/μm^2 for the STORM dataset. Over-

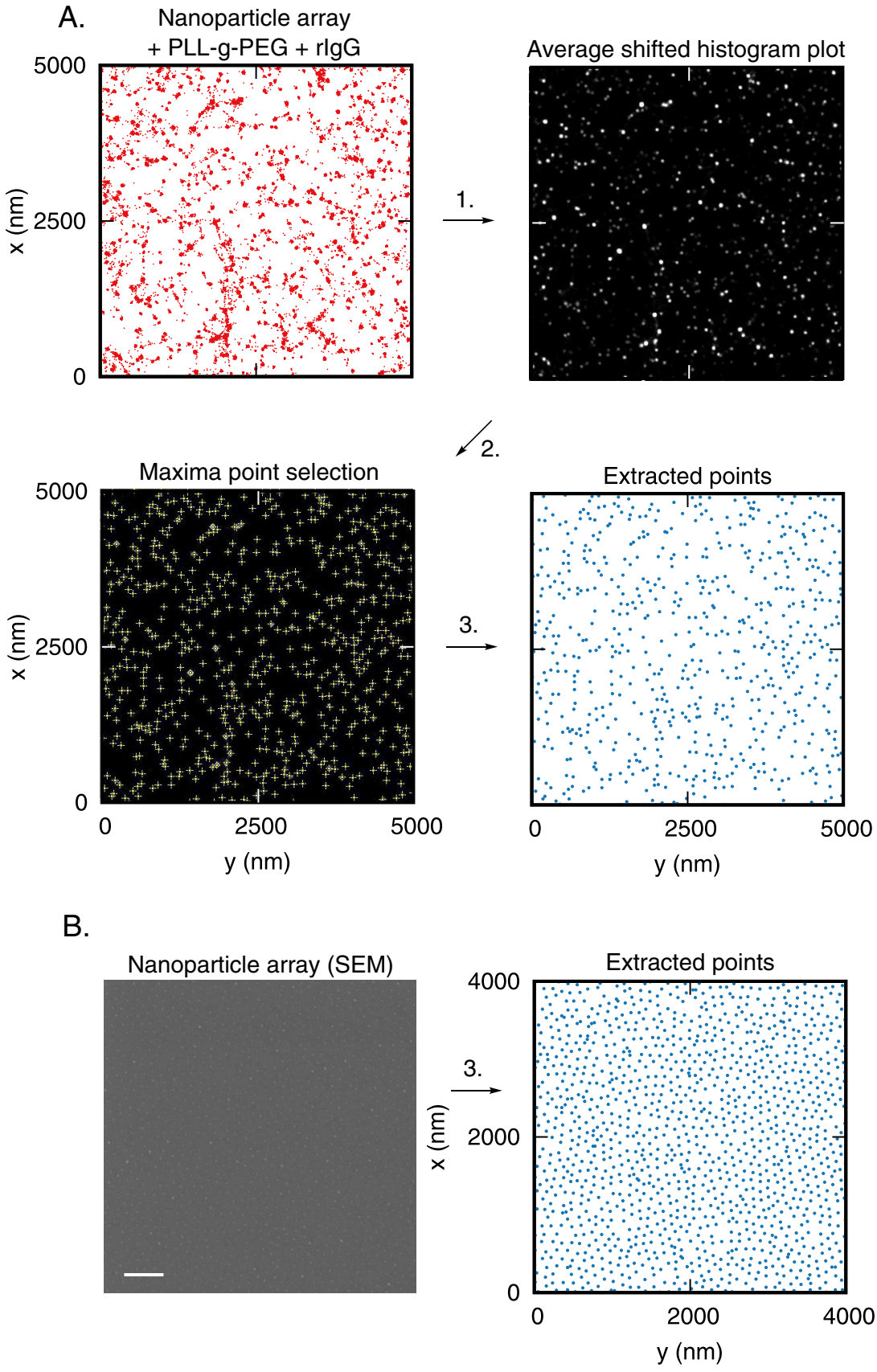

Figure 5.7: Extraction of nanoparticle coordinates from both raw event data, and an 'ideal' SEM image of a similar array (A.) Three step process starting with the raw STORM fluorochrome localizations (events) converted in 1. to and intensity profile using the Average Shifted Histogram (ASH) density estimation. 2. The selection of clusters with a minimum intensity and 3. The extraction of the selected cluster coordinates. (B.) The similar extraction of nanopartilce coordinates from an ideal SEM image of an array with properties matching the nanoparticle array functionalized and imaged by STORM. Blue points are the extracted coordinates replotted. Scale bar = 500 nm

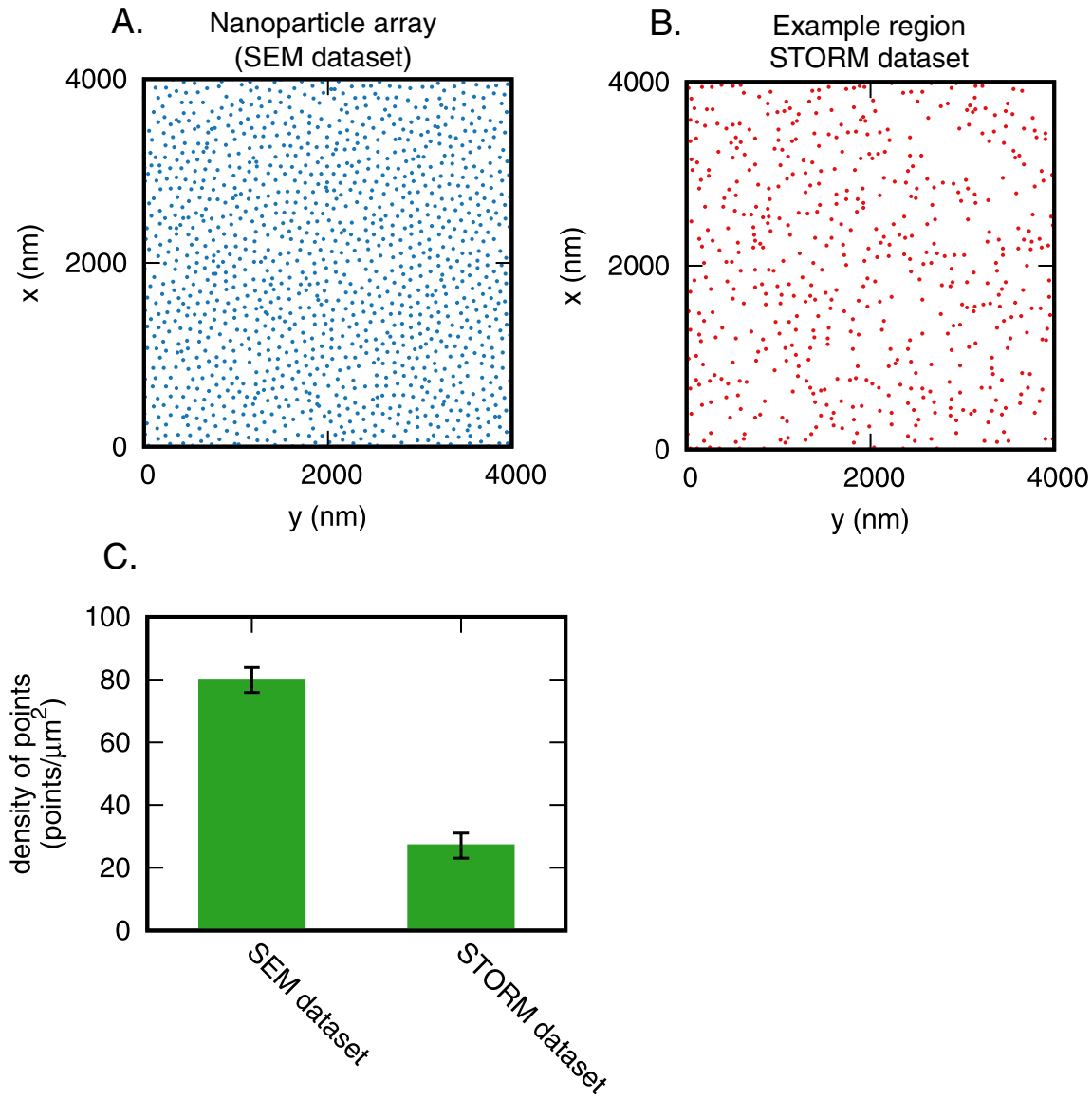

Figure 5.8: The mean detected number of points is approximately 33% the expected number of total nanoparticles i.e. 33% Au nanoparticle occupancy. (A.) Position of nanoparticles (blue dots) as detected in a 4×4 μm region of an PS(110 kDa)-*b*-P2VP(52 kDa) array imaged using SEM. (B.) Position of rIgG (red dots) as detected in a 4×4 μm region of a matching functionalized nanoparticle array imaged using STORM (C.) Quantification of the mean density of nanoparticles as measured from three matching nanoparticle arrays and 12 regions of STORM data analyzed as described in Figure 5.7 (A.).

all this gives an inferred 33% occupancy of the nanoparticle array.

There are three underlying possibilities which would lead to the observed low occupancy. These are, 1. a problem relating to the underlying nanoparticles, 2. the functionalization and 3. the detection.

Starting with the underlying nanoparticles, a potential cause of observed under occupancy would be missing nanoparticles or arrays with a lower density of nanoparticles than expected. To minimize any chance of this, characterization of individual batches by SEM was carried out on a subsection of the fabricated batch. This step, in addition to ensuring quality, also determines the properties of the batch and ensures the quality of the micellar lithography. As such it is unlikely that large regions of the hexagonal array would be found with voids that would lead to the observed occupancy. While this is true of the unfunctionalized array, there remains the possibility that the process of functionalization itself disrupts attachment of nanoparticle to the substrate. This outcome is thought to be unlikely given the stability of Au nanoparticle arrays observed by other studies using procedures with similar reagents.[72, 63, 427]

Considering next the functionalization procedure, the first explanation for observed under occupancy would be the result of incubation with a quantity of rIgG insufficient to saturate all nanoparticles. This hypothesis can quickly be refuted as the STORM images shown in Figure 5.5 (B.) of the positive nanoparticle array + rIgG control surface indicate complete coverage. A second potential hypothesis is that the passivation layer also prevents rIgG binding to the Au nanoparticles. Again this is unlikely given the radius of gyration of hydrated 2 kDa MW PEG (as used in the PLL-g-PEG) has been measured to be 1.36 nm.[486, 487, 488] Taking into account the well defined nanoparticle diameter of 15 nm, it is implausible that the PEG could extend beyond the nanoparticle and sterically block prevent binding. It is, however,

possible that impurities collected over time deposit onto the surface, preventing binding. This is difficult to quantify, and each nanoparticle surface was incubated under a UV light source for 30 minutes prior to functionalization so that produced ozone could remove organic deposits.

Regarding functionalization, binding of rIgG is only specific if an available thiol or disulfide bond is present and therefore processes which drastically reduce the thiol availability would result in under occupancy. The reduction of IgG is a reversible process and the oxidation of the hinge thiols, reforming the disulfide occurs spontaneously over a 20 hour period. To reduce the effects of the reformation of disulphides, functionalization was carried out immediately after reduction, and the reduction step in itself was confirmed as shown by Figure 5.2.3 (B.).

Detection of rIgG by STORM involves a number of factors which could contribute to the reduced occupancy observed. The first and most obvious of these is the labeling ratio of fluorochrome to rIgG, and its inherent underlabeling. The goat anti-mouse IgG-AF647 used here had a Degree of Labeling (DOL) (AF647:IgG) of 3 which is typical for commercial antibodies. After mAb reduction the value would naturally be reduced to 1.5 (assuming equal likelihood of fluorochrome labeling sites), which is reasonable given the equal distribution of light and heavy chains by rIgG formation. A DOL of 1.5 may be considered sufficient initially, however, given it is a mean value calculated based on bulk UV-vis measurements, the labeling of fluorochromes on the single molecule level will instead be a distribution. The large number of primary amines relative to the labeling ratio for NHS/EDC coupling has been shown to allow for the DOL to be reasonably modeled by a Poisson distribution. Applying this model the contribution of 0, 1, 2, 3, and so on DOL can be calculated as shown in Figure 5.9 (A.). When a mean DOL of 1.5 is measured this distributions shows that just over 22% of individual rIgG will have zero fluorochromes and 33% just a single one.[489, 490, 491]

The distribution of fluorochromes with zero fluorochromes would clearly be a contributing factor towards the 33% occupancy observed. To have less than a 5% contribution of rIgG without a fluorochrome a mean DOL of 5 would be necessary, again assuming a Poisson distribution. While a DOL of 5 and above would be possible for a characterization step (given the approximately 80 primary amines available for fluorochrome coupling) considerations realting to the antibody solubility and functionality may become essentail as these are crucial for later use in cell experiments.[430]

Given no other sources sufficiently account for the remaining underoccupancy the $\sim$ 50% is therefore hypothesized to be the result of Au nanoparticle quenching of the AF647 fluorochrome fluorescence.[492, 493] Recently the distance dependent quenching of Atto647N was demonstrated by 10 nm Au nanoparticles. At 10.4 nm from the Au nanoparticle surface the relative fluorescence intensity was measured to be 0.5, and by fitting it is expected to be 0.25 at around 7 nm.[494] The decreased fluorescence intensity will, it is reasonably speculated, affect the localization of single molecules by introducing greater uncertainty in fluorochrome localization as a result of a more diffuse PSF.

Superresolution image processing determines the localization based on a number of parameters, that if found to be below a threshold, lead to single molecules being discarded due to the localization unreliability.[495] In addition, the filtering choices common for single molecule localization, and used here to remove localizations with uncertainties greater than a threshold (15 nm), although necessary for precise analysis, will with all likelihood also remove data originating from fluorochromes of occupied nanoparticles.[496] While the exact affect of the fluorescence quenching of AF647 has not been shown by nanoparticles of 15 nm, the comparison here with ATTO647N is likely appropriate considering their near identical fluorescence absorbance and emission spectra. Figure 5.9 (B.) schematically indicates the described

quenching with, to relative scale, an Au nanoparticle ($r \sim 7.5$ nm) and mAb (length ~ 15 nm), at various distances from each other.

Finally, with respect to the extraction of fluorochromes coordinates from the STORM image data, the process outlined in Figure 5.7 (A.) was produced to select clustered features associated with detected fluorochromes and may also contribute to the underoccupancy by preventing false positive localizations.

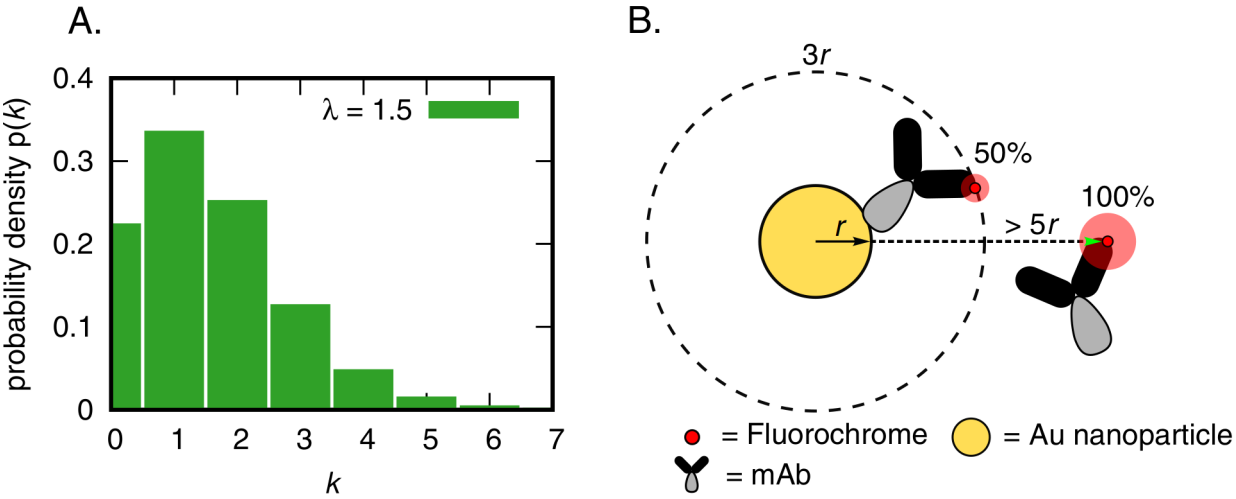

Figure 5.9: Factors likely to cause the observed 33% occupancy. (A.) The Poisson distribution for an average of 1.5 events per interval. This plot shows that a mean fluorochrome Degree of Labeling (DOL) = 1.5 has a 22% contribution of rIgG with 0 fluorochromes. (B.) Schematic indicating the fluorescence quenching of a fluorochrome (here attached to a mAb) in relation to the distance from the Au nanoparticle. For an Au nanoparticle of radius, r 5–7 nm, at 15–20 nm ($3r$) the relative fluorescence intensity is $\sim$ 50% its value at distances of greater than $5r$. The mAb dimensions are correct relative to an Au nanoparticle of diameter 15 nm.

Spatial Analysis Techniques

In spite of the reduced occupancy further analysis was carried out to determine if the rIgG positions were distributed such that the likelihood of attachment to the underlying array could be made. A comparison first of

the interparticle distances which are characteristic of the nanoparticle array was therefore made. A simple yet robust methods to determine the mean interparticle distances is through the Nearest Neighbor (NN) Analysis. In this analysis, for each point the nearest neighboring point is found and the distance between the two measured as illustrated in Figure 5.10 (A.). By iterating over every point in a given area or ROI, the mean nearest neighbor distance can be calculated to provide a good description of the spatial dispersion. A second method of analysis, the Ripley's *K*-Function was used to compare the spatial distribution of points in a dataset, and hence provides a description of the spatial homogeneity. Ripley's *K*-Function Analysis is commonly used to distinguish between clustered, random or uniform and dispersed distributions of points, therefore complimenting the mean NN analysis. The Ripley's K-Function is defined in Equation 5.1 below.

$$K(r) = \frac{A \sum_{i=1}^{n} \sum_{j=1, i \neq j}^{n} \delta_{ij}}{n(n-1)} \tag{5.1}$$

Where A is the total area, r the radius from a given point, n the total number of points and δ_{ij} the Euclidean distance between points i and j.

A common method to visualize the results of the Ripley's *K*-Function (*K(r)*) instead uses the *L*-Function (Equation 5.2) and specifically *L(r)-r* sometimes termed the *H*-Function. Plotting *L(r)-r* is favorable as *L(r)* for a Poisson distribution of points = r and hence *L(r)-r* $= 0$. The value of *L(r)-r* therefore becomes positive when data is clustered, and negative for dispersed distributions, see Figure 5.10 (C, D.) producing plots which are visually easy to comprehend and compare.[497, 498, 499, 500]

$$L(r) = \sqrt{\frac{K(r)}{\pi}} \tag{5.2}$$

Where r is the radius and *K(r)* the Ripley's *K*-Function.

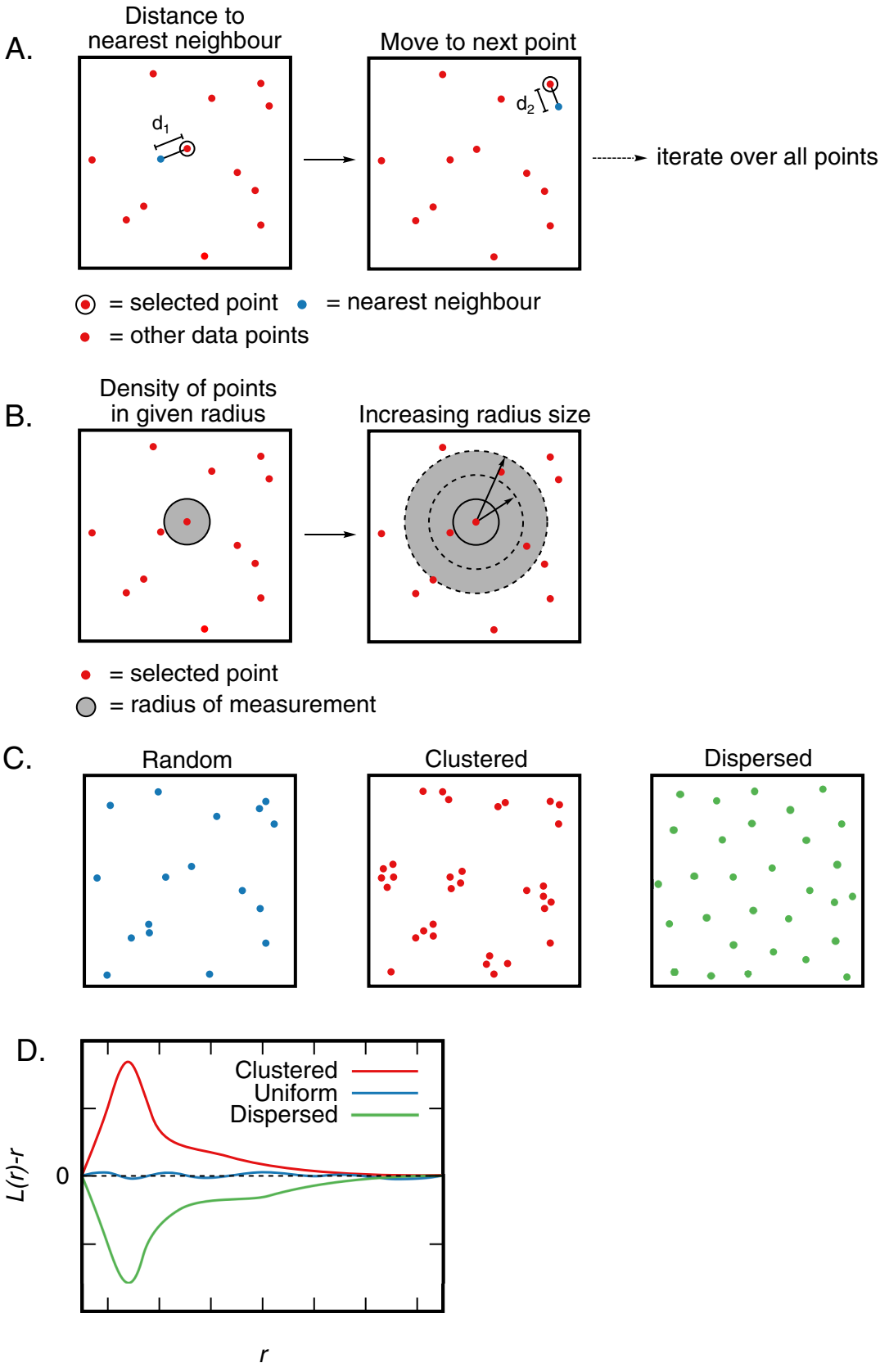

Figure 5.10: Schematic of the analysis techniques used on the measured STORM and simulated datasets. (A.) Nearest Neighbor (NN) analysis for n = 1 i.e. the first nearest neighboring point. First a point is selected, its nearest neighboring point is then determined and the distance between them measured. This process is repeated for all data points and the mean NN distance then computed for a given dataset. (B.) The Ripley's *K/L*-Functions calculates the number of points in a radius surrounding a data point. The radius increases by a predetermined distance and the density of points is compared for a given radius to the global density of points. (C.) Three example datasets with different spatial characteristics. (D.) Shows representative results of the Ripley's *K*-Function analysis on datasets with the spatial characteristics as indicated in (C.).

Simulated (Control) Datasets

For the initial analysis the most simple n = 1 NN was computed for each point in a 5×5 μm region extracted from STORM images of functionalized nanoparticle arrays. It was initially assumed that this value could be directly compared to the mean NN distance computed for the ideal nanoparticle array as imaged by SEM. As a fundamental limitation of the NN method it is not possible to use a single measurement as an accurate comparison of the mean NN distance given dissimilar point densities. The reduced occupancy measured and discussed earlier, for instance, would affect any calculation of the NN as the loss of neighboring points effectively increases the mean NN distance. A second issue also arises due to the variation in the occupancy across imaged regions (27–42%). A computed mean NN distances would, for instance, be different for one region at 27% occupancy compared to one at 42% irrespective if they were otherwise idetical. This is due to the mean NN varying non-linearly with respect to the number of particles measured. As a result it is implicit that a single measured comparison of mean NN distance of an ideal array is not suitable, to analyze the STORM dataset.

A solution to this problem was produced by comparison instead to the ideal nanoparticle array after artificially removing a percentage of the total number of points (points selected at random) to simulate the underoccupancy observed in the STORM dataset. The removal of points was applied at 12.5% (250) increments of the total number of points (2000 points) and the mean NN distance calculated for each underoccupied dataset. Example datasets labeled as 100% (no points removed), 75%, 50% and 25% are shown in Figure 5.11 (A.). Figure 5.11 (A.) also illustrates that while a complete nanoparticle array shows noticeable features originating from a hexagonal array, as points are removed the hexagonal regularity is quickly lost to the naked eye.

The results of the simulated underoccupancy followed by measurement of

the mean NN distance is plotted in Figure 5.11 (B.). A fit of the data has been applied such that readings between data points could also be inferred. In this case a reciprocal function with fitting parameters was chosen (see Equation 5.3).

$$f(x) = \frac{a}{x} + b \tag{5.3}$$

Where a and b are the fitting parameters.

The affect of underoccupancy on the calculated NN distance is shown in the ideal SEM dataset, where at 100% the mean NN distance was 94.1 $\pm$ 17.4 nm, which at 50% increases to 106.5 $\pm$ 25.0 nm, and at 25% is 134.2 $\pm$ 46.8 nm. The increase in the mean NN between 100% and 25% is substantial at 1.4–fold, and quantitatively illustrates the importance of comparing the calculated NN distance at different point densities.

While a mechanism to accurately account for the underoccupation has been applied to the NN analysis of the interparticle distance, other important controls and points of comparison were considered. STORM data inherently localizes the position of the fluorochrome, which in turn is used to infer the position of the rIgG and the nanoparticle. While still the best approach, possible error associated with each of these measurements together add an uncertainty to the final location which does not occur with direct measurement of the nanoparticles position by SEM as in the ideal dataset.

To account for this uncertainty a Freedom of Movement (FOM) was added in a third control dataset. Here the coordinates of every point of the ideal nanoparticle array was, at random, shifted within a 25 nm radius of their initial position. This SEM + FOM dataset was created as hypothetical 'best' model for the experimentally measured STORM dataset. The mean NN analysis, including the simulated reduction of occupancy, was again calculated for this dataset to produce similar plots accounting for the variation in mean

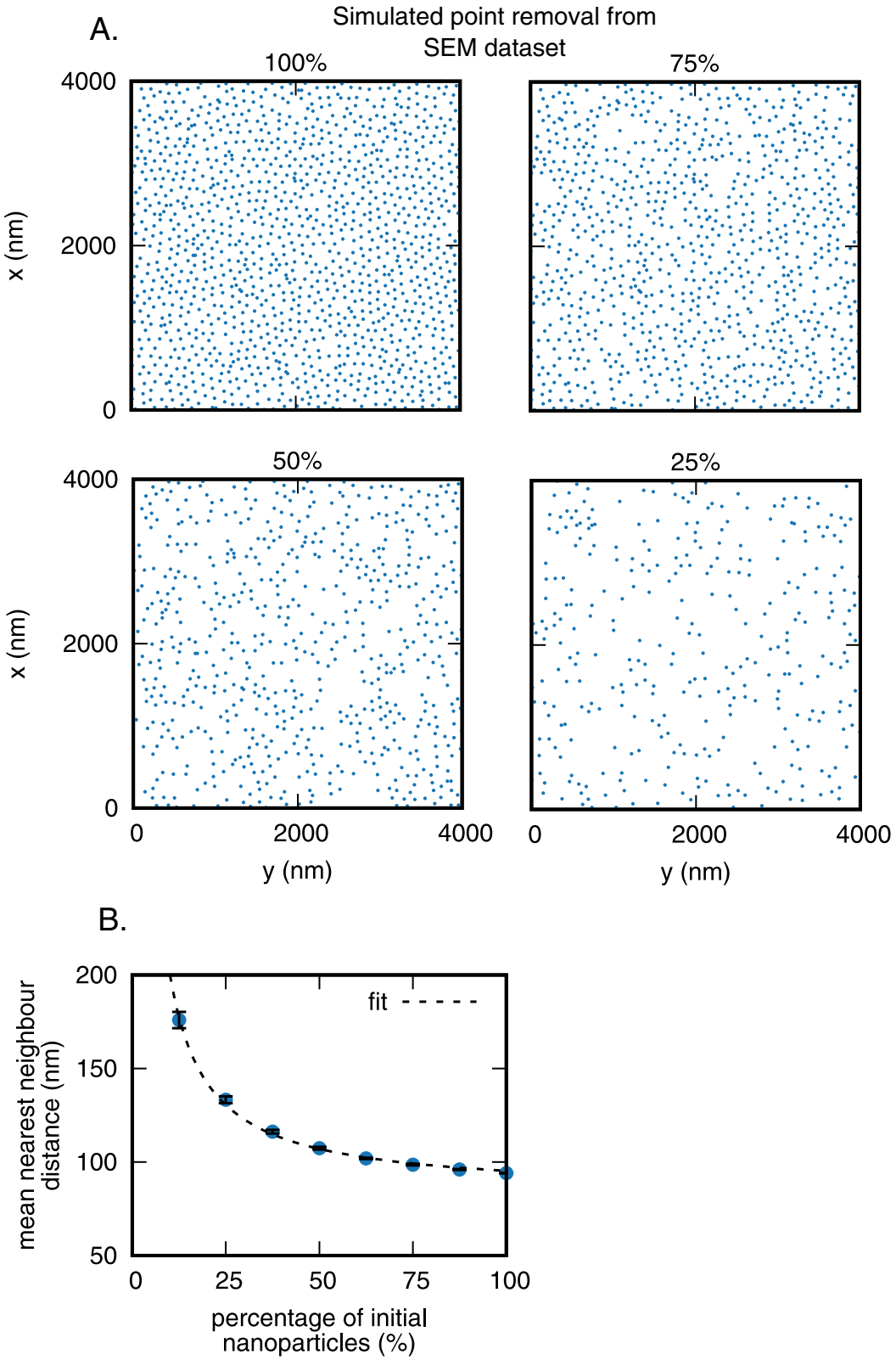

Figure 5.11: Mean first Nearest Neighbor (NN) distances as measured for a non functionalized hexagonal nanoparticle array vary in a reciprocal manner to the number of points in the array. (A.) Example images, first showing all points extracted from an ideal nanoparticle array (100%), and then with a given percentage removed by random selection, including 75%, 50% and 25% of the initial total. (B.) The mean NN distance computed for each simulated underoccupied dataset. Results are shown as the average of twenty measurements of the mean NN distance computed from twenty datasets, each produced by randomly removing the desired number of points to give the indicated percentage underoccupancies. Error bars represent the standard deviation of the twenty individually computed mean NN distances.

NN distance. An example of the SEM dataset with a density matched to a STORM region and a 25 nm FOM can be seen in Figure 5.13 (B.).

A final fourth control dataset was also used. This control was composed of a random distribution of points, and again the mean NN measurement made to account for point density. In spite of the low likelihood of the STORM data resulting from the measurement of a random distribution of rIgG across the nanoparticle array (as shown by images of the control surfaces), this dataset provides another good point of comparison. Again the mean NN distances of an equivalent density of randomly generated points was used and an example of this region can be seen in Figure 5.13 (C.).

Nearest Neighbor (NN) Analysis

The result of the mean NN analysis (mean NN distance plotted against the density of points in the dataset) with the combined controls mentioned above and all 12, 5×5 μm regions of STORM data can be seen in Figure 5.13 (D.).

Compared to the SEM array dataset, the addition of the 25 nm FOM affects the mean NN distance by consistently decreasing its value. In the case of 100% simulated occupancy (78.2 points/μm^2) the addition of the FOM alone decreases the mean NN distance from 94.1 $\pm$ 17.4 nm to 87.41 $\pm$ 19.27 nm. This difference, which results from the FOM ,is maintained as the number of nanoparticles decreases up until approximately half of the nanoparticles have been removed (39.1 points/μm^2) and further decreases in occupancy contribute minimally to the mean NN distance.

The randomized dataset shows a significantly lower mean NN distance (at higher densities) compared to both the SEM dataset and FOM dataset, as the points lack the regular interparticle distance produced by the BCP lithography. At high densities the difference in the SEM dataset compared to the

Random dataset was 94.1 $\pm$ 17.4 nm vs 56.8 $\pm$ 30.0 nm respectively.

Plotting each measured STORM dataset by the individual regions from which the NN analysis was applied (red crosses), they clearly fall consistently closest to the simulated nanoparticle array with 25 nm FOM. All regions had lower mean NN distances than the comparable 'ideal' array which was measured using SEM, as well as the SEM + FOM datasets. Of the 12 regions analyzed, 6 fall within the simulated envelope (max and min measurements from 19 independent simulations) for the SEM + FOM indicating they are not significantly different (p = 0.05) from this dataset. All data points on the other hand fall outside of the envelope for a random distribution showing that these regions are statistically unlikely to be the result of rIgG attached at random across the surface.

The deviation of some data points from the expected envelope for the exact array and FOM could be the result of a number of factors. Variation across the sample on the nanoscale can firstly be expected especially given the multistep nature of the functionalization. The inhomogeneity of the nanoparticle arrays, due to environmental variations such as evaporation of the solvent over the period of dipping, although minimized by batch characterization, may nonetheless lead to individual regions of disorder, and SEM alone is impractical to asses a full 4$\times$2.4 cm coverslip.

One hypothesis which for the deviation in the STORM dataset from the simulated dataset with FOM, without relying on inconsistencies in the array is that a larger FOM than predicted here better describes the exact nature of the mAb, nanoparticle and fluorochrome localization for the lower than expected mean NN distance. The value of 25 nm was used as the length of an IgG antibody is approximately 15 nm which in addition to the 15 nm particle diameter give a potential maximum variation in the potential position of the fluorochrome relative to the nanoparticle of 23 nm (15 +

$15/2 \sim 23$ nm). What remains unaccounted for, however, is the localization precision associated with the single molecule detection.

Another important factor is that while the mean NN distance provides a clear measurement for the comparison of the spatial dispersion of both datasets, it is possible that its value could be influenced by uneven distributions of points across the surface. In unusual cases the mean NN distance could, for instance, in absolute terms be similar despite a large spread in the actual distribution of measured NN distances. To combat this a comparison of the distribution of NN distance is another important consideration. The Coefficient of Variation (c_v) as defined in Equation 5.4, (briefly the standard deviation of the measured mean NN distance divided by the mean), has therefore also been plotted in Figure 5.12. Given the non periodic nature of the randomized dataset the calculated value of c_v is consistently greater than the SEM and SEM + FOM datasets, and also remains constant despite the changing density of points. The STORM dataset has a small spread in the measured c_v with values of ~ 0.4, and they are well outside the simulated min/max envelop of the Random dataset. The spread therefore of the NN distances is again best represented by the SEM + FOM dataset and 4 of the 12 regions measured fall within the computed envelope showing that they are not significantly different. The regions falling outside of the envelope have a statistically significant difference equal to $p = 0.05$, as a result of the envelope represents the minimum and maximum values calculated from 19 separate simulations.

$$c_v = \frac{\sigma}{\mu} \tag{5.4}$$

Where c_v is the coefficient of variation, σ the standard deviation and μ the mean.

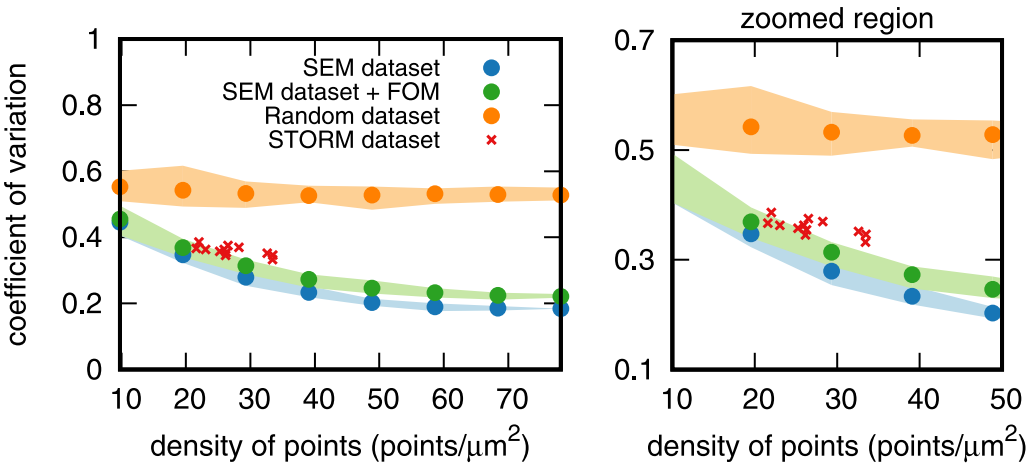

Figure 5.12: The spread in the nearest neighbor distances represented by the Coefficient of Variation (c_v) is statistically dissimilar to a random distribution of points and closely matches the spread of the SEM + FOM dataset. Zoomed region of the same plot more clearly indicates that 4 of the 12 measured regions fall within the simulated envelope composed of the min/max values calculated from 19 simulations.

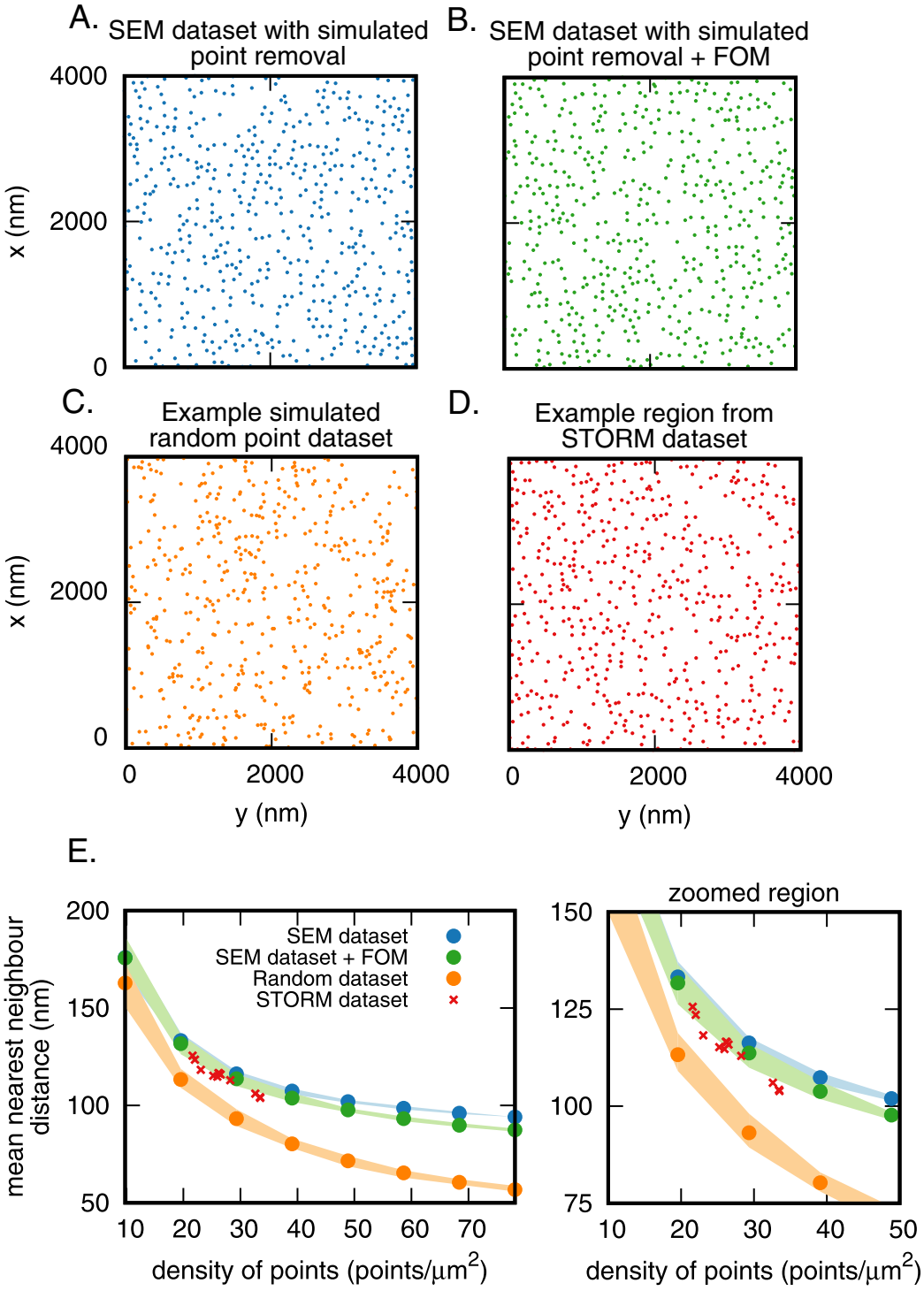

Figure 5.13: The mean Nearest Neighbor (NN) distance of the STORM dataset is most closely represented by the SEM dataset with a 25 nm Freedom of Movement (FOM). (A.) An example SEM dataset with occupancy mimicking the measured STORM datasets. (B.) An example SEM dataset with an additional 25 nm FOM applied to each point at random. (C.) Example of a random distribution of points with equivalent point density. (D.) A representative STORM dataset region. (E.) The variation in the mean NN distance for all datasets plotted against the density of points. Simulation envelopes showing the max and min values from 19 simulations of each dataset and density of points.

Ripley's K-Function Analysis

By comparison of the NN distance and coefficient of variation, the bulk spatial dispersion of the STORM datasets has been compared to the results expected of a random distribution of points and an ideal nanoparticle array (both with and without a FOM) at various occupancies. To compare the spatial distribution of points within the dataset the Ripley's *K*-Function has been used, a visual summary of which can be found in Figure 5.10 (B, C.).

Nanoparticle arrays created by BCP micellar lithography by their nature show strong spatial dispersion. This is a result of the initial hexagonal packing of micelles, caused by the steric repulsion of BCP in opposing micelles. As a result the calculated *L(r)-r* quickly becomes negative as the distance *r* from the nanoparticle increases. At the mean interparticle spacing, *L(r)-r* begins to increase, periodically decreasing and increasing with *r* due to the periodic array structure.

In a perfect hexagonal array the magnitude of *L(r)-r* at the interparticle distance would remain the same as the distance *r* increases due to the perfect periodicity of the array. In practice micellar arrays created by BCP lithography show decreasing order at larger distances and hence the periodic change in *L(r)-r* decays. Figure 5.14 (A.) illustrates this decay. It is particularly clear from $r \sim 350$ nm, where *L(r)-r* ~ 5, and does not vary greatly thereafter.

Plots of the calculated *L(r)-r* for the random, SEM dataset with 25% occupancy (below the average 33% of all 12 STORM regions), SEM + FOM with 25% occupancy and the STORM dataset can be seen in Figure 5.14 (B–E.) Both the SEM and SEM + FOM datasets show the expected periodic *L(r)-r* with the minimum at the interparticle (r_I) distance and local minima at $2\times r_I$ and $3\times r_I$. In both cases the decreased density of points (25% occupancy) increases the noise in the plot. In the case of the SEM + FOM the FOM has also contributed to the noise, and in some cases has caused the position

of the minimum to shift, while also resulting in a more rapid decay of the periodicity compared to the 'ideal' nanoparticle array.

In the case of the STORM dataset the most apparent feature is the clear negative value of *L(r)-r* which occurs from 0–100 nm. This demonstrates that there is a dispersion of points (within this range of *r*) with this dataset. Such an effect is observed across all regions shown, and all regions measured. The maximum of *L(r)-r* varies between regions and is found at lower *r* ($\sim$ 50 nm) than would be otherwise expected for an ideal nanoparticle array ($\sim$ 90 nm) and even compared to the mean the SEM + FOM dataset ($\sim$ 85 nm).

The second major feature which would be expected is the periodic variation of *L(r)-r*. With regards to this point, almost no periodicity is observed and only a non-periodic decay is present. Two regions exhibit small but noticeable increases in *L(r)-r* at $\sim$ 180 nm that are characteristic of the nanoparticle array, but these are only a small proportion of the 12 measured. The regions exhibiting this increase are, it should be noted, also members of the group which fall within the envelope for the SEM + FOM mean NN calculation and are therefore more likely to represent data expected of a specifically functionalized and imaged nanoparticle array. The calculation of *L(r)-r* strongly demonstrates the dispersed nature of the STORM datasets, and is in itself a representative feature of specific nanoparticle array functionalization.

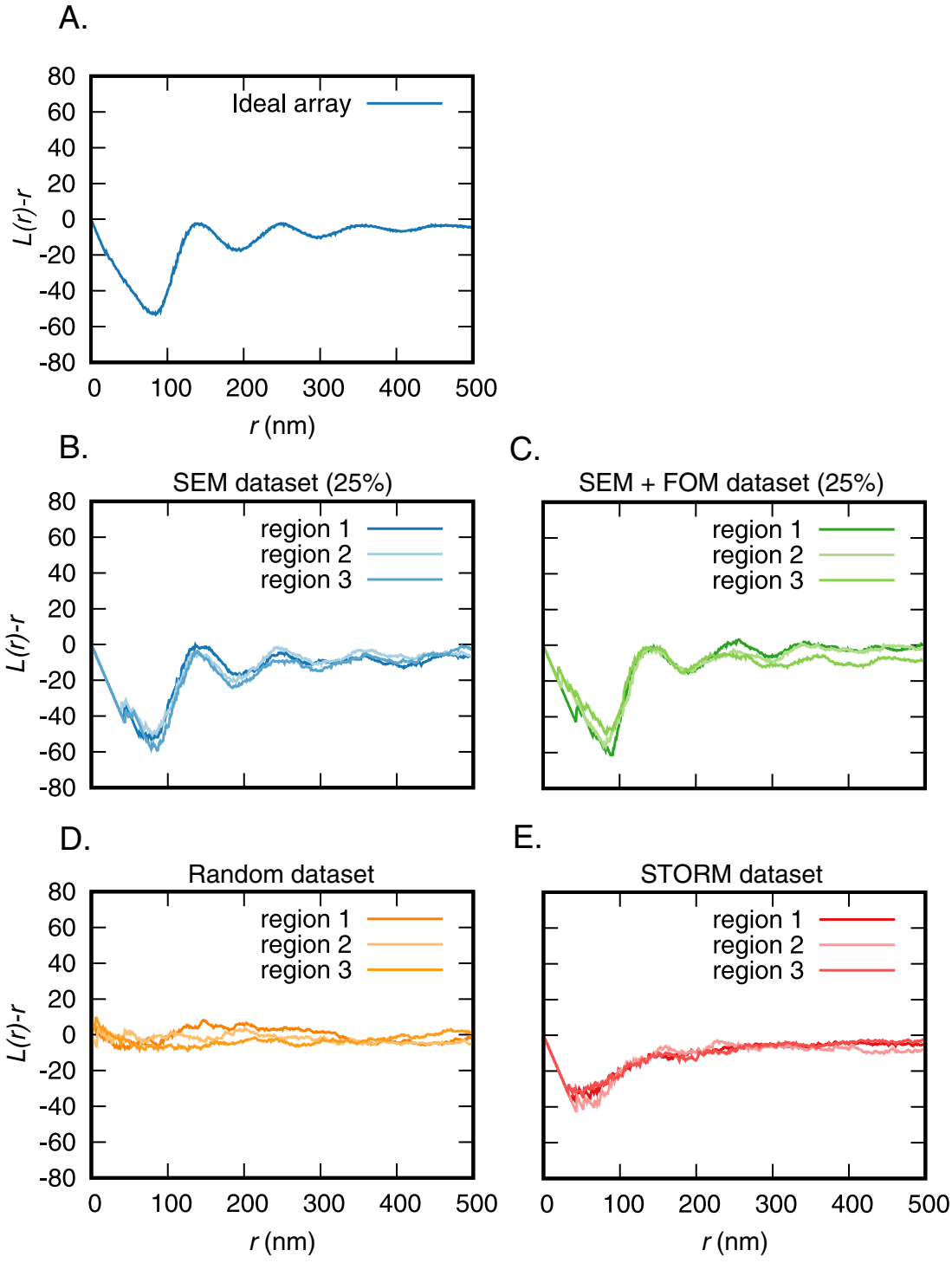

Figure 5.14: Ripley's *K*-Function analysis replotted as *L(r)-r* and calculated over 500 nm from each data point. *L(r)-r* of 3 regions from each dataset including the ideal nanoparticle array to illustrate the expected features. (A.) *L(r)-r* plotted for the ideal array consisting of 2000 data points (78.2 points/μm^2). (B.) The SEM dataset, (C.) SEM + FOM dataset, (D.) random dataset and (E.) the STORM dataset.

5.4 Conclusions

5.4.1 Summary of Findings

The goal of this chapter was to produce Au nanoparticle arrays, biologically functionalize them, and determine whether STORM superresolution microscopy could be used as a method to characterize the biofunctionalization of the arrays. The experimental evidence shows that:

1. Nanoparticle arrays produced by BCP micellar lithography have controllable, regular, well defined spatial properties, including interparticle spacing and nanoparticle size.
2. Antibodies can be reduced to produce antibody fragments with free thiols that are ideal for simple and direct array functionalization.
3. STORM images of functionalized array surfaces are distinctly different from control surfaces i.e. nanoparticle arrays functionalized without passivation, glass functionalized without passivation and glass functionalized after passivation.
4. Through combination of the Nearest Neighbor (NN) and Ripley's *K*-Function Analyses, a STORM dataset can be analyzed to determine whether it is representative of a specifically functionalized array.
5. Of the datasets measured here by NN and Ripley's *K*-Function Analysis, between a third and a half are best represented by a functionalized array with a 25 nm FOM in the localization of the bound antibody.

5.4.2 Concluding Remarks

To date there has been very little progress in characterizing the functionalization of nanoparticle arrays. This work represents the second attempt to do so using superresolution microscopy, however, in this example using a different SMLM technique—STORM. STORM has some advantages for this ap-

plication including signal:noise ratio, experimental design and ease of setup, making it, for some use-cases, the preferred superresolution technique.

In this chapter it has been shown that using a simple and direct functionalization method, Au nanoparticle arrays nonetheless appear underoccupied (the apparent lack of some nanoparticles having an attached antibody) through comparison of the density of nanoparticles expected and the density of points measured using STORM. Underoccupancy was similarly mentioned by Lohmüller et al. despite differing functionalization approaches.[427] Lohmüller et al. reported only 25% occupancy was while in this work 33% was measured. Potential explanations provided, include the relatively low degree of fluorochrome labeling of the antibody, followed by fluorescence quenching caused by the Au nanoparticles.

Taking into account the reduced molecular occupancy of the nanoparticles, two spatial analysis methods were utilized to characterize the localization data. The Nearest Neighbor (NN) Analysis to determine the average interparticle distance and the Ripley's *K*-Function Analysis to determine the spatial distribution of points. By comparing the obtained data with simulated datasets produced from either randomly distributed points with a similar density, an ideal nanoparticle array or an ideal array with points removed at random to simulate underoccupancy, it was possible to show the STORM dataset was more representative of the ideal array with underoccupancy. By adding a Freedom of Movement (FOM) to the ideal array dataset (to simulate the expected inaccuracy brought about by the random binding position of the protein relative to the nanoparticle, as well as the random location of the fluorochrome on the protein), the FOM dataset was shown to be a better model for the measured and analyzed STORM data. Half of the time (6 of 12) for example, the STORM dataset was found to be not significantly different in terms of the NN distance. The coefficient of variation also sharing more similarities between the FOM and the STORM dataset, as 4 of 12

regions measured were not statistically dissimilar. Both results indicated the similarities between the simulated and observed datasets.

Similarly, by comparison of the Ripley's *K*-Function, it was found that the STORM dataset was dispersed in a manner similar to what could be expected of a functionalized nanoparticle array, however, with far less periodicity than would be expected. This caveat was best explained by the occurrence of nonspecific antibody binding or irregularities in the array.

By both comparison to controls, and spatial analysis, it is likely the underlying nanoparticle is, in regions, specifically functionalized. The combined spatial analysis was also robust as it relied on two distinct techniques that maintained this conclusion. Together, this work is therefore, to our knowledge, the most rigorous analysis of functionalized nanoparticle arrays by superresolution imaging.

Chapter 6

Final Remarks

This thesis has developed two technologies from the fields of Nanomaterials and Biomaterials for use in immunology, and cell biology more generally. In the case of the synthesis of a NGO supramolecular species (NGO-α-hCD16), methods to conjugate mAbs have been implemented and tested in biological systems for the first time, demonstrating its applicability. Exciting findings have been made concerning NGO's potential to cluster antibodies and through this, augment NK cell activation relative to unclustered, unconjugated antibody. The data presented also indicate that the effect is most likely a result of the nanoscale size and mAb clustering. This is the first observation of NK cells stimulation by nanoscale (50–200 nm) clusters of ligand, and the first example of activation of any immune cell using an NGO based material.

These initial results have been demonstrated in NK cells where the importance of the cells' surface receptor organization is beginning to be linked to function, and is increasingly, because of this important development, a point of focus. At the same time, the observation that an augmented response in comparison to equivalent concentration of unconjugated antibody makes these finding exciting for therapeutic applications. The concept of using a nanomaterial to manipulate the surface nanostructure as a means

to affect cellular outcome is novel in comparison to traditional targeting or drug delivery, and this early example which has demonstrating an effect in both the degranulation of NK cells and IFN-γ secretion is notable. It can be seen as a first step in determining the full potential of the technology and the novel mechanism.

Other results obtained here, which combine the increasingly used SMLM methods with nanoparticle arrays to understand the functionalization of nanoparticle arrays, and provide a system for two color imaging is the second documented attempt and the only using STORM, making it unique. It is also the most robust analysis available as it uses four independent measures for comparison to control surfaces. This will be useful to the field of Nanomaterials for those wishing to utilize both technologies concurrently in the future. The results have differentiated regions likely to be well functionalized from those not exhibiting the expected properties. The work presented here has also outlined some good practices with regards to analysis, and highlighted points regarding nanoparticle occupation for future consideration.

Together these results contribute to both the fields of Nanomaterials and Immunology, while also providing significant new avenues of potential interest for future exploration.

Bibliography

[1] P Cuatrecasas. Membrane receptors. *Annual Review of Biochemistry*, 43(1):169–214, 2016/12/11 1974.

[2] Peter W. Zandstra, Douglas A. Lauffenburger, and Connie J. Eaves. A ligand-receptor signaling threshold model of stem cell differentiation control: a biologically conserved mechanism applicable to hematopoiesis. *Blood*, 96(4):1215–1222, 2000.

[3] Barrett J. Rollins. Chemokines. *Blood*, 90(3):909–928, 1997.

[4] Paul Waring and Arno Mullbacher. Cell death induced by the fas/fas ligand pathway and its role in pathology. *Immunol Cell Biol*, 77(4):312–317, 08 1999.

[5] Jordan A. Krall, Elsa M. Beyer, and Gavin MacBeath. High- and low-affinity epidermal growth factor receptor-ligand interactions activate distinct signaling pathways. *PLOS ONE*, 6(1):e15945–, 01 2011.

[6] Wanli Liu and Zhengpeng Wan. Single molecular force sensitivity and threshold for the activation of b cell receptors. *The Journal of Immunology*, 196(1 Supplement):198.9, 2016.

[7] Lieping Chen and Dallas B. Flies. Molecular mechanisms of t cell co-stimulation and co-inhibition. *Nat Rev Immunol*, 13(4):227–242, 04 2013.

[8] Yenan T. Bryceson, Michael E. March, Hans-Gustaf Ljunggren, and Eric O. Long. Activation, coactivation, and costimulation of resting human natural killer cells. *Immunological Reviews*, 214(1):73–91, 2006.

[9] Kai Simons and Elina Ikonen. Functional rafts in cell membranes. *Nature*, 387(6633):569–572, 06 1997.

[10] Rajat Varma and Satyajit Mayor. Gpi-anchored proteins are organized in submicron domains at the cell surface. *Nature*, 394(6695):798–801, 08 1998.

[11] Tim Friedrichson and Teymuras V. Kurzchalia. Microdomains of gpi-anchored proteins in living cells revealed by crosslinking. *Nature*, 394(6695):802–805, 08 1998.

[12] Maria F. Garcia-Parajo, Alessandra Cambi, Juan A. Torreno-Pina, Nancy Thompson, and Ken Jacobson. Nanoclustering as a dominant feature of plasma membrane organization. *Journal of Cell Science*, 127(23):4995–5005, 2014.

[13] Bjorn F Lillemeier, Manuel A Mortelmaier, Martin B Forstner, Johannes B Huppa, Jay T Groves, and Mark M Davis. Tcr and lat are expressed on separate protein islands on t cell membranes and concatenate during activation. *Nat Immunol*, 11(1):90–96, 01 2010.

[14] Sophie V. Pageon, Thibault Tabarin, Yui Yamamoto, Yuanqing Ma, Philip R. Nicovich, John S. Bridgeman, André Cohnen, Carola Benzing, Yijun Gao, Michael D. Crowther, Katie Tungatt, Garry Dolton, Andrew K. Sewell, David A. Price, Oreste Acuto, Robert G. Parton,

J. Justin Gooding, Jérémie Rossy, Jamie Rossjohn, and Katharina Gaus. Functional role of t-cell receptor nanoclusters in signal initiation and antigen discrimination. *Proceedings of the National Academy of Sciences*, 113(37):E5454–E5463, 2016.

[15] Björn F. Lillemeier, Janet R. Pfeiffer, Zurab Surviladze, Bridget S. Wilson, and Mark M. Davis. Plasma membrane-associated proteins are clustered into islands attached to the cytoskeleton. *Proceedings of the National Academy of Sciences*, 103(50):18992–18997, 2006.

[16] Pieta K. Matilla, Christoph Feest, David Depoil, Bebhinn Treanor, Beatriz Montaner, Kevin L. Otipody, Robert Carter, Louis B. Justement, Andreas Bruckbauer, and Facundo D. Batista. The actin and tetraspanin networks organize receptor nanoclusters to regulate b cell receptor-mediated signaling. *Immunity*, 38(3):461–474, 2013.

[17] Kathrin Kläsener, Palash C Maity, Elias Hobeika, Jianying Yang, and Michael Reth. B cell activation involves nanoscale receptor reorganizations and inside-out signaling by syk. *eLife*, 3:e02069, jun 2014.

[18] Sophie V. Pageon, Shaun-Paul Cordoba, Dylan M. Owen, Stephen M. Rothery, Anna Oszmiana, and Daniel M. Davis. Superresolution microscopy reveals nanometer-scale reorganization of inhibitory natural killer cell receptors upon activation of nkg2d. *Science Signaling*, 6(285):ra62–ra62, 2013.

[19] Anna Oszmiana, David J. Williamson, Shaun-Paul. Cordoba, David J. Morgan, Phillipa R. Kennedy, Kevin Stacey, and Daniel. M. Davis. The size of activating and inhibitory killer ig-like receptor nanoclusters is controlled by the transmembrane sequence and affects signaling. *Cell Reports*, 15(9):1957–1972, 2016.

[20] Mariella Della Chiesa, Emanuela Marcenaro, Simona Sivori, Simona Carlomagno, Silvia Pesce, and Alessandro Moretta. Human {NK} cell response to pathogens. *Seminars in Immunology*, 26(2):152 – 160, 2014.

[21] Timothy O'Sullivan, Robert Saddawi-Konefka, William Vermi, Catherine M. Koebel, Cora Arthur, J. Michael White, Ravi Uppaluri, Daniel M. Andrews, Shin Foong Ngiow, Michele W. L. Teng, Mark J. Smyth, Robert D. Schreiber, and Jack D. Bui. Cancer immunoediting by the innate immune system in the absence of adaptive immunity. *The Journal of Experimental Medicine*, 209(10):1869, 09 2012.

[22] G Feuer, S A Stewart, S M Baird, F Lee, R Feuer, and I S Chen. Potential role of natural killer cells in controlling tumorigenesis by human t-cell leukemia viruses. *Journal of Virology*, 69(2):1328–33, 1995.

[23] Mark J. Smyth, Nadine Y. Crowe, and Dale I. Godfrey. Nk cells and nkt cells collaborate in host protection from methylcholanthrene-induced fibrosarcoma. *International Immunology*, 13(4):459–463, 2001.

[24] Klas Karre, Hans Gustaf Ljunggren, Gerald Piontek, and Rolf Kiessling. Selective rejection of h-2-deficient lymphoma variants suggests alternative immune defence strategy. *Nature*, 319(6055):675–678, 02 1986.

[25] William E. Carson, Todd A. Fehniger, and Michael A. Caligiuri. Cd56bright natural killer cell subsets: Characterization of distinct functional responses to interleukin-2 and the c-kit ligand. *European Journal of Immunology*, 27(2):354–360, 1997.

[26] Yenan T. Bryceson, Cyril Fauriat, João M. Nunes, Stephanie M. Wood, Niklas K. Björkström, Eric O. Long, and Hans-Gustaf Ljunggren. *Functional Analysis of Human NK Cells by Flow Cytometry*, pages 335–352. Humana Press, Totowa, NJ, 2010.

[27] Andrea De Maria, Federica Bozzano, Claudia Cantoni, and Lorenzo Moretta. Revisiting human natural killer cell subset function revealed cytolytic cd56dimcd16+ nk cells as rapid producers of abundant ifn-γ on activation. *Proceedings of the National Academy of Sciences*, 108(2):728–732, Jan 2011.

[28] Gina Fiala, Daniel Kaschek, Britta Blumenthal, Michael Reth, Jens Timmer, and Wolfgang Schamel. Pre-clustering of the b cell antigen receptor demonstrated by mathematically extended electron microscopy. *Frontiers in Immunology*, 4:427, 2013.

[29] Mario Castro, Hisse M. van Santen, María Férez, Balbino Alarcón, Grant Lythe, and Carmen Molina-París. Receptor pre-clustering and t cell responses: Insights into molecular mechanisms. *Frontiers in Immunology*, 5:132, 2014.

[30] Pieta K. Mattila, Facundo D. Batista, and Bebhinn Treanor. Dynamics of the actin cytoskeleton mediates receptor cross talk: An emerging concept in tuning receptor signaling. *The Journal of Cell Biology*, 212(3):267–280, 2016.

[31] Sun Taek Kim, Koh Takeuchi, Zhen-Yu J. Sun, Maki Touma, Carlos E. Castro, Amr Fahmy, Matthew J. Lang, Gerhard Wagner, and Ellis L. Reinherz. The $\alpha\beta$t cell receptor is an anisotropic mechanosensor. *Journal of Biological Chemistry*, 284(45):31028–31037, 11 2009.

[32] Eric Betzig, George H. Patterson, Rachid Sougrat, O. Wolf Lindwasser, Scott Olenych, Juan S. Bonifacino, Michael W. Davidson, Jennifer Lippincott-Schwartz, and Harald F. Hess. Imaging Intracellular Fluorescent Proteins at Nanometer Resolution. *Science*, 313(5793):1642–1645, September 2006.

[33] Michael J Rust, Mark Bates, and Xiaowei Zhuang. Sub-diffraction-limit imaging by stochastic optical reconstruction microscopy (storm). *Nat Meth*, 3(10):793–796, 10 2006.

[34] Andrew M. Sydor, Kirk J. Czymmek, Elias M. Puchner, and Vito Mennella. Super-resolution microscopy: From single molecules to supramolecular assemblies. *Trends in Cell Biology*, 25(12):730–748, 2016/12/07 2015.

[35] Marta Fernandez-Suarez and Alice Y. Ting. Fluorescent probes for super-resolution imaging in living cells. *Nat Rev Mol Cell Biol*, 9(12):929–943, 12 2008.

[36] Jovana Matic, Janosch Deeg, Alexander Scheffold, Itamar Goldstein, and Joachim P. Spatz. Fine tuning and efficient t cell activation with stimulatory acd3 nanoarrays. *Nano Letters*, 13(11):5090–5097, 11 2013.

[37] Derfogail Delcassian, David Depoil, Dominika Rudnicka, Mengling Liu, Daniel M. Davis, Michael L. Dustin, and Iain E. Dunlop. Nanoscale ligand spacing influences receptor triggering in t cells and nk cells. *Nano Letters*, 13(11):5608–5614, 2013. PMID: 24125583.

[38] Karlo Perica, Ang Tu, Anne Richter, Joan Glick Bieler, Michael Edidin, and Jonathan P. Schneck. Magnetic field-induced t cell receptor clustering by nanoparticles enhances t cell activation and stimulates antitumor activity. *ACS Nano*, 8(3):2252–2260, 03 2014.

[39] Vasilios Georgakilas, Michal Otyepka, Athanasios B. Bourlinos, Vimlesh Chandra, Namdong Kim, K. Christian Kemp, Pavel Hobza, Radek Zboril, and Kwang S. Kim. Functionalization of Graphene: Covalent and Non-Covalent Approaches, Derivatives and Applications. *Chemical Reviews*, 112(11):6156–6214, November 2012.

[40] Xiao Huang, Xiaoying Qi, Freddy Boey, and Hua Zhang. Graphene-based composites. *Chem. Soc. Rev.*, 41:666–686, 2012.

[41] Tamás Szabó, Etelka Tombácz, Erzsébet Illés, and Imre Dékány. Enhanced acidity and ph-dependent surface charge characterization of successively oxidized graphite oxides. *Carbon*, 44(3):537–545, 3 2006.

[42] Hongji Jiang. Chemical preparation of graphene-based nanomaterials and their applications in chemical and biological sensors. *Small*, 7(17):2413–2427, 2011.

[43] Yanwu Zhu, Shanthi Murali, Weiwei Cai, Xuesong Li, Ji Won Suk, Jeffrey R. Potts, and Rodney S. Ruoff. Graphene and graphene oxide: Synthesis, properties, and applications. *Advanced Materials*, 22(35):3906–3924, 2010.

[44] Dimitrios Konios, Minas M. Stylianakis, Emmanuel Stratakis, and Emmanuel Kymakis. Dispersion behaviour of graphene oxide and reduced graphene oxide. *Journal of Colloid and Interface Science*, 430:108–112, 9 2014.

[45] J. I. Paredes, S. Villar-Rodil, A. Martínez-Alonso, and J. M. D. Tascón. Graphene oxide dispersions in organic solvents. *Langmuir*, 24(19):10560–10564, 10 2008.

[46] Xiaoming Sun, Zhuang Liu, Kevin Welsher, Joshua Tucker Robinson, Andrew Goodwin, Sasa Zaric, and Hongjie Dai. Nano-graphene oxide for cellular imaging and drug delivery. *Nano Research*, 1(3):203–212, September 2008.

[47] Yong Liu, Dong Zhang, Shiwu Pang, Yanyun Liu, and Yu Shang. Size separation of graphene oxide using preparative free-flow electrophoresis. *Journal of Separation Science*, 38(1):157–163, 2015.

[48] Sami Makharza, Giuseppe Cirillo, Alicja Bachmatiuk, Orazio Vittorio, Rafael Gregorio Mendes, Steffen Oswald, Silke Hampel, and Mark H. Rummeli. Size-dependent nanographene oxide as a platform for efficient carboplatin release. *J. Mater. Chem. B*, 1:6107–6114, 2013.

[49] Hao Hong, Kai Yang, Yin Zhang, Jonathan W. Engle, Liangzhu Feng, Yunan Yang, Tapas R. Nayak, Shreya Goel, Jero Bean, Charles P. Theuer, Todd E. Barnhart, Zhuang Liu, and Weibo Cai. In Vivo Targeting and Imaging of Tumor Vasculature with Radiolabeled, Antibody-Conjugated Nanographene. *ACS Nano*, 6(3):2361–2370, March 2012.

[50] Liming Zhang, Zhuoxuan Lu, Qinghuan Zhao, Jie Huang, He Shen, and Zhijun Zhang. Enhanced chemotherapy efficacy by sequential delivery of sirna and anticancer drugs using pei-grafted graphene oxide. *Small*, 7(4):460–464, 2011.

[51] Liangzhu Feng, Shuai Zhang, and Zhuang Liu. Graphene based gene transfection. *Nanoscale*, 3(3):1252–1257, 2011.

[52] Bo Tian, Chao Wang, Shuai Zhang, Liangzhu Feng, and Zhuang Liu. Photothermally Enhanced Photodynamic Therapy Delivered by Nano-Graphene Oxide. *ACS Nano*, 5(9):7000–7009, September 2011.

[53] Hongqian Bao, Yongzheng Pan, Yuan Ping, Nanda Gopal Sahoo, Tongfei Wu, Lin Li, Jun Li, and Leong Huat Gan. Chitosan-functionalized graphene oxide as a nanocarrier for drug and gene delivery. *Small*, 7(11):1569–1578, 2011.

[54] Zhuang Liu, Joshua T. Robinson, Xiaoming Sun, and Hongjie Dai. PEGylated Nanographene Oxide for Delivery of Water-Insoluble Cancer Drugs. *Journal of the American Chemical Society*, 130(33):10876–10877, August 2008.

[55] Michael E. Weinblatt, Edward C. Keystone, Daniel E. Furst, Larry W. Moreland, Michael H. Weisman, Charles A. Birbara, Leah A. Teoh, Steven A. Fischkoff, and Elliot K. Chartash. Adalimumab, a fully human anti–tumor necrosis factor monoclonal antibody, for the treatment of rheumatoid arthritis in patients taking concomitant methotrexate: The armada trial. *Arthritis & Rheumatism*, 48(1):35–45, 2003.

[56] Edward H. Romond, Edith A. Perez, John Bryant, Vera J. Suman, Charles E. Jr. Geyer, Nancy E. Davidson, Elizabeth Tan-Chiu, Silvana Martino, Soonmyung Paik, Peter A. Kaufman, Sandra M. Swain, Thomas M. Pisansky, Louis Fehrenbacher, Leila A. Kutteh, Victor G. Vogel, Daniel W. Visscher, Greg Yothers, Robert B. Jenkins, Ann M. Brown, Shaker R. Dakhil, Eleftherios P. Mamounas, Wilma L. Lingle, Pamela M. Klein, James N. Ingle, and Norman Wolmark. Trastuzumab plus adjuvant chemotherapy for operable her2-positive breast cancer. *New England Journal of Medicine*, 353(16):1673–1684, 2005. PMID: 16236738.

[57] D. R. Anderson, A. Grillo-López, C. Varns, K. S. Chambers, and N. Hanna. Targeted anti-cancer therapy using rituximab, a chimaeric anti-cd20 antibody (idec-c2b8) in the treatment of non-hodgkin's b-cell lymphoma. *Biochemical Society Transactions*, 25(2):705–708, 1997.

[58] Sébastien Dall'Ozzo, Sophie Tartas, Gilles Paintaud, Guillaume Cartron, Philippe Colombat, Pierre Bardos, Hervé Watier, and Gilles Thibault. Rituximab-dependent cytotoxicity by natural killer cells. *Cancer Res*, 64(13):4664–4669, July 2004.

[59] Dominika Rudnicka, Anna Oszmiana, Donna K. Finch, Ian Strickland, Darren J. Schofield, David C. Lowe, Matthew A. Sleeman, and Daniel M. Davis. Rituximab causes a polarization of b cells

that augments its therapeutic function in nk-cell–mediated antibody-dependent cellular cytotoxicity. *Blood*, 121(23):4694–4702, 2013.

[60] Julia Ranzinger, Anja Krippner-Heidenreich, Tamas Haraszti, Eva Bock, Jessica Tepperink, Joachim P. Spatz, and Peter Scheurich. Nanoscale arrangement of apoptotic ligands reveals a demand for a minimal lateral distance for efficient death receptor activation. *Nano Letters*, 9(12):4240–4245, 2009.

[61] Khalid Salaita, Yuhuang Wang, and Chad A. Mirkin. Applications of dip-pen nanolithography. *Nat Nano*, 2(3):145–155, March 2007.

[62] J. Damon Hoff, Li-Jing Cheng, Edgar Meyhöfer, L. Jay Guo, and Alan J. Hunt. Nanoscale protein patterning by imprint lithography. *Nano Letters*, 4(5):853–857, 2004.

[63] Roman Glass, Martin Müller, and Joachim P Spatz. Block copolymer micelle nanolithography. *Nanotechnology*, 14(10):1153, 2003.

[64] Y. Ng Cheong Chan, R. R. Schrock, and R. E. Cohen. Synthesis of single silver nanoclusters within spherical microdomains in block copolymer films. *Journal of the American Chemical Society*, 114(18):7295–7296, 1992.

[65] Y. Ng Cheong Chan, G. S. W. Craig, R. R. Schrock, and R. E. Cohen. Synthesis of palladium and platinum nanoclusters within microphase-separated diblock copolymers. *Chemistry of Materials*, 4(4):885–894, 1992.

[66] Y. Ng Cheong Chan, R. R. Schrock, and R. E. Cohen. Synthesis of silver and gold nanoclusters within microphase-separated diblock copolymers. *Chemistry of Materials*, 4(1):24–27, 1992.

[67] Stefan V. Graeter, Jinghuan Huang, Nadine Perschmann, Mónica López-García, Horst Kessler, Jiandong Ding, and Joachim P. Spatz. Mimicking cellular environments by nanostructured soft interfaces. *Nano Letters*, 7(5):1413–1418, 2007.

[68] Janosch Deeg, Markus Axmann, Jovana Matic, Anastasia Liapis, David Depoil, Jehan Afrose, Silvia Curado, Michael L. Dustin, and Joachim P. Spatz. T cell activation is determined by the number of presented antigens. *Nano Letters*, 13(11):5619–5626, 2013. PMID: 24117051.

[69] Elisabetta A. Cavalcanti-Adam, Alexandre Micoulet, Jacques Blümmel, Jörg Auernheimer, Horst Kessler, and Joachim P. Spatz. Lateral spacing of integrin ligands influences cell spreading and focal adhesion assembly. *European Journal of Cell Biology*, 85(3–4):219 – 224, 2006.

[70] Elisabetta Ada Cavalcanti-Adam, Tova Volberg, Alexandre Micoulet, Horst Kessler, Benjamin Geiger, and Joachim Pius Spatz. Cell spreading and focal adhesion dynamics are regulated by spacing of integrin ligands. *Biophysical Journal*, 92(8):2964 – 2974, 2007.

[71] Tobias Wolfram, Ferdinand Belz, Tobias Schoen, and Joachim P. Spatz. Site-specific presentation of single recombinant proteins in defined nanoarrays. *Biointerphases*, 2(1):44–48, 2007.

[72] Haogang Cai, Haguy Wolfenson, David Depoil, Michael L. Dustin, Michael P. Sheetz, and Shalom J. Wind. Molecular Occupancy of Nanodot Arrays. *ACS Nano*, 10(4):4173–4183, April 2016.

[73] Marta Maglione and Stephan J. Sigrist. Seeing the forest tree by tree: super-resolution light microscopy meets the neurosciences. *Nature Neuroscience*, 16(7):790–797, July 2013.

[74] Kristine N. Brazin, Robert J. Mallis, Dibyendu Kumar Das, Yinnian Feng, Wonmuk Hwang, Jia-huai Wang, Gerhard Wagner, Matthew J. Lang, and Ellis L. Reinherz. Structural features of the $\alpha\beta$tcr mechanotransduction apparatus that promote pmhc discrimination. *Frontiers in Immunology*, 6:441, 2015.

[75] Kenneth Murphy and Casey Weaver. *Janeway's Immunobiology*. Garland Science, 9th edition, March 2016.

[76] L. Vikhanski. *Immunity: How Elie Metchnikoff Changed the Course of Modern Medicine*. Chicago Review Press, 2016.

[77] Martin F. Flajnik and Masanori Kasahara. Origin and evolution of the adaptive immune system: genetic events and selective pressures. *Nat Rev Genet*, 11(1):47–59, January 2010.

[78] Max D. Cooper and Matthew N. Alder. The evolution of adaptive immune systems. *Cell*, 124(4):815 – 822, 2006.

[79] Gustavo Cudkowicz and Michael Bennett. Peculiar immunobiology of bone marrow allografts. *Journal of Experimental Medicine*, 134(6):1513–1528, 1971.

[80] Hans-Gustaf Ljunggren and Klas Kärre. In search of the 'missing self': Mhc molecules and nk cell recognition. *Immunology Today*, 11:237 – 244, 1990.

[81] R. Kiessling, Eva Klein, H. Pross, and H. Wigzell. "natural" killer cells in the mouse. ii. cytotoxic cells with specificity for mouse moloney leukemia cells. characteristics of the killer cell. *European Journal of Immunology*, 5(2):117–121, 1975.

[82] Ronald B. Herberman, Myrthel E. Nunn, Howard T. Holden, and David H. Lavrin. Natural cytotoxic reactivity of mouse lymphoid cells

against syngeneic and allogeneic tumors. ii. characterization of effector cells. *International Journal of Cancer*, 16(2):230–239, 8 1975.

[83] L L Lanier, J H Phillips, J Hackett, M Tutt, and V Kumar. Natural killer cells: definition of a cell type rather than a function. *The Journal of Immunology*, 137(9):2735–2739, 1986.

[84] Michael A. Caligiuri. Human natural killer cells. *Blood*, 112(3):461–469, 2008.

[85] Lewis. L. Lanier. Back to the future –defining nk cells and t cells. *European Journal of Immunology*, 37(6):1424–1426, 2007.

[86] Binqing Fu, Zhigang Tian, and Haiming Wei. Subsets of human natural killer cells and their regulatory effects. *Immunology*, 141(4):483–489, April 2014.

[87] Megan A Cooper, Todd A Fehniger, and Michael A Caligiuri. The biology of human natural killer-cell subsets. *Trends in Immunology*, 22(11):633 – 640, 2001.

[88] Eric Vivier, Elena Tomasello, Myriam Baratin, Thierry Walzer, and Sophie Ugolini. Functions of natural killer cells. *Nat Immunol*, 9(5):503–510, May 2008.

[89] Michael J. Robertson. Role of chemokines in the biology of natural killer cells. *Journal of Leukocyte Biology*, 71(2):173–183, February 2002.

[90] Judy Lieberman. The abcs of granule-mediated cytotoxicity: new weapons in the arsenal. *Nat Rev Immunol*, 3(5):361–370, May 2003.

[91] Joseph A. Trapani and Phillip I. Bird. A renaissance in understanding the multiple and diverse functions of granzymes? *Immunity*, 29(5):665–667, 2008.

[92] Kimberly C. Gilmour, Hodaka Fujii, Treena Cranston, E. Graham Davies, Christine Kinnon, and Hubert B. Gaspar. Defective expression of the interleukin-2/interleukin-15 receptor β subunit leads to a natural killer cell–deficient form of severe combined immunodeficiency. *Blood*, 98(3):877–879, 2001.

[93] Jordan S. Orange. Natural killer cell deficiency. *Journal of Allergy and Clinical Immunology*, 132(3):515–525, September 2013.

[94] Christine A. Biron, Kevin S. Byron, and John L. Sullivan. Severe herpesvirus infections in an adolescent without natural killer cells. *N Engl J Med*, 320(26):1731–1735, June 1989.

[95] Akiba H, M Motoki Y FAU Satoh, K Satoh M FAU Iwatsuki, F Iwatsuki K FAU Kaneko, and Kaneko F. Recalcitrant trichophytic granuloma associated with nk-cell deficiency in a sle patient treated with corticosteroid. *European Journal of Dermatology*, 11(1):58–62, February 2001.

[96] ZK Ballas, JM Turner, DA Turner, EA Goetzman, and JD Kemp. A patient with simultaneous absence of "classical" natural killer cells (cd3-, cd16+, and nkh1+) and expansion of cd3+, cd4-, cd8-, nkh1+ subset. *The Journal of allergy and clinical immunology*, 85(2):453–459, February 1990.

[97] Luigi D. Notarangelo and Evelina Mazzolari. Natural killer cell deficiencies and severe varicella infection. *The Journal of Pediatrics*, 148(4):563–564, 2005.

[98] Stuart Min, Linda Monaco-Shawver, Jordan Orange, and Joseph Church. T.36. classical natural killer cell deficiency (cnkd): A new case. *Clinical Immunology*, 131, Supplement:S61–, 2009.

[99] Frédéric Bernard, Capucine Picard, Valérie Cormier-Daire, Céline Eidenschenk, Graziella Pinto, Jacinta-Cecilia Bustamante, Emmanuelle Jouanguy, Dominique Teillac-Hamel, Virginie Colomb, Isabelle Funck-Brentano, Véronique Pascal, Eric Vivier, Alain Fischer, Françoise Le Deist, and Jean-Laurent Casanova. A novel developmental and immunodeficiency syndrome associated with intrauterine growth retardation and a lack of natural killer cells. *Pediatrics*, 113(1):136–141, 2003.

[100] Céline Eidenschenk, Jean Dunne, Emmanuelle Jouanguy, Claire Fourlinnie, Laure Gineau, Delphine Bacq, Corrina McMahon, Owen Smith, Jean-Laurent Casanova, Laurent Abel, and Conleth Feighery. A novel primary immunodeficiency with specific natural-killer cell deficiency maps to the centromeric region of chromosome 8. *The American Journal of Human Genetics*, 78(4):721–727, April 2006.

[101] Amos Etzioni, Celine Eidenschenk, Rina Katz, Rafeal Beck, Jean Laurent Casanova, and Shimon Pollack. Fatal varicella associated with selective natural killer cell deficiency. *The Journal of Pediatrics*, 146(3):423–425, March 2005.

[102] Thomas Wendland, Silvia Herren, Nikhil Yawalkar, Andreas Cerny, and Werner J Pichler. Strong $\alpha\beta$ and $\gamma\delta$ tcr response in a patient with disseminated mycobacterium avium infection and lack of nk cells and monocytopenia. *Immunology Letters*, 72(2):75–82, 2000.

[103] Rachel K. Shaw, Andrew C. Issekutz, Robert Fraser, Pierre Schmit, Barb Morash, Linda Monaco-Shawver, Jordan S. Orange, and Conrad V. Fernandez. Bilateral adrenal ebv-associated smooth muscle tumors in a child with a natural killer cell deficiency. *Blood*, 119(17):4009–4012, 2012.

[104] Emily M. Mace, Amy P. Hsu, Linda Monaco-Shawver, George Makedonas, Joshua B. Rosen, Lesia Dropulic, Jeffrey I. Cohen, Eugene P. Frenkel, John C. Bagwell, John L. Sullivan, Christine A. Biron, Christine Spalding, Christa S. Zerbe, Gulbu Uzel, Steven M. Holland, and Jordan S. Orange. Mutations in gata2 cause human nk cell deficiency with specific loss of the cd56bright subset. *Blood*, 121(14):2669–2677, 2013.

[105] M. Jondal. The human nk cell–a short over-view and an hypothesis on nk recognition. *Clinical and Experimental Immunology*, 70(2):255–262, November 1987.

[106] Franz M. Karlhofer, Randall K. Ribaudo, and Wayne M. Yokoyama. Mhc class i alloantigen specificity of ly-49+ il-2-activated natural killer cells. *Nature*, 358(6381):66–70, July 1992.

[107] A Moretta, M Vitale, C Bottino, A M Orengo, L Morelli, R Augugliaro, M Barbaresi, E Ciccone, and L Moretta. P58 molecules as putative receptors for major histocompatibility complex (mhc) class i molecules in human natural killer (nk) cells. anti-p58 antibodies reconstitute lysis of mhc class i-protected cells in nk clones displaying different specificities. *Journal of Experimental Medicine*, 178(2):597–604, 1993.

[108] Eric Vivier, David H. Raulet, Alessandro Moretta, Michael A. Caligiuri, Laurence Zitvogel, Lewis L. Lanier, Wayne M. Yokoyama, and Sophie Ugolini. Innate or adaptive immunity? the example of natural killer cells. *Science*, 331(6013):44–, January 2011.

[109] Kuldeep Cheent and Salim I. Khakoo. Natural killer cells: integrating diversity with function. *Immunology*, 126(4):449–457, 2009.

[110] Hollie J. Pegram, Daniel M. Andrews, Mark J. Smyth, Phillip K. Darcy, and Michael H. Kershaw. Activating and inhibitory receptors of natural killer cells. *Immunol Cell Biol*, 89(2):216–224, February 2011.

[111] Janice L Abbey and Helen C O'Neill. Expression of t-cell receptor genes during early t-cell development. *Immunol Cell Biol*, 86(2):166–174, October 2007.

[112] B A Garni-Wagner, A Purohit, P A Mathew, M Bennett, and V Kumar. A novel function-associated molecule related to non-mhc-restricted cytotoxicity mediated by activated natural killer cells and t cells. *The Journal of Immunology*, 151(1):60–70, 1993.

[113] Ofer Mandelboim, Niva Lieberman, Marianna Lev, Lada Paul, Tal I. Arnon, Yuri Bushkin, Daniel M. Davis, Jack L. Strominger, Jonathan W. Yewdell, and Angel Porgador. Recognition of haemagglutinins on virus-infected cells by nkp46 activates lysis by human nk cells. *Nature*, 409(6823):1055–1060, February 2001.

[114] Amanda M. Jamieson, Andreas Diefenbach, Christopher W. McMahon, Na Xiong, James R. Carlyle, and David H. Raulet. The role of the nkg2d immunoreceptor in immune cell activation and natural killing. *Immunity*, 17(1):19–29, July 2002.

[115] Stefan Bauer, Veronika Groh, Jun Wu, Alexander Steinle, Joseph H. Phillips, Lewis L. Lanier, and Thomas Spies. Activation of nk cells and t cells by nkg2d, a receptor for stress-inducible mica. *Science*, 285(5428):727–729, 1999.

[116] G. Trinchieri and N. Valiante. Receptors for the fc fragment of igg on natural killer cells. *Natural immunity*, 12:218–34, 1993.

[117] B Perussia, G Trinchieri, A Jackson, N L Warner, J Faust, H Rumpold, D Kraft, and L L Lanier. The fc receptor for igg on human natural killer cells: phenotypic, functional, and comparative studies with monoclonal antibodies. *The Journal of Immunology*, 133(1):180–189, 1984.

[118] Veronique M. Braud, David S. J. Allan, Christopher A. O'Callaghan, Kalle Soderstrom, Annalisa D'Andrea, Graham S. Ogg, Sasha Lazetic, Neil T. Young, John I. Bell, Joseph H. Phillips, Lewis L. Lanier, and Andrew J. McMichael. Hla-e binds to natural killer cell receptors cd94/nkg2a, b and c. *Nature*, 391(6669):795–799, February 1998.

[119] Yili Li, Maike Hofmann, Qian Wang, Leslie Teng, Lukasz K. Chlewicki, Hanspeter Pircher, and Roy A. Mariuzza. Structure of natural killer cell receptor klrg1 bound to e-cadherin reveals basis for mhc-independent missing self recognition. *Immunity*, 31(1):35–46, July 2009.

[120] Masayuki Ito, Takuma Maruyama, Naotoshi Saito, Satoru Koganei, Kazuo Yamamoto, and Naoki Matsumoto. Killer cell lectin-like receptor g1 binds three members of the classical cadherin family to inhibit nk cell cytotoxicity. *Journal of Experimental Medicine*, 203(2):289–295, 2006.

[121] Eric Vivier, Jacques A. Nunès, and Frédéric Vély. Natural killer cell signaling pathways. *Science*, 306(5701):1517–1519, 2004.

[122] Yenan T. Bryceson, Hans-Gustaf Ljunggren, and Eric O. Long. Minimal requirement for induction of natural cytotoxicity and intersection of activation signals by inhibitory receptors. *Blood*, 114(13):2657–2666, 2009.

[123] Lorenzo Moretta and Alessandro Moretta. Unravelling natural killer cell function: triggering and inhibitory human nk receptors. *The EMBO Journal*, 23(2):255–259, 2003.

[124] L. L. Lanier. Nk cell recognition. *Annual Review of Immunology*, 23(1):225–274, 2005. PMID: 15771571.

[125] I Waldhauer and A Steinle. Nk cells and cancer immunosurveillance. *Oncogene*, 27(45):5932–5943, 2008.

[126] Assaf Marcus, Benjamin G. Gowen, Thornton W. Thompson, Alexandre Iannello, Michele Ardolino, Weiwen Deng, Lin Wang, Nataliya Shifrin, and David H. Raulet. Chapter three - recognition of tumors by the innate immune system and natural killer cells. In Frederick W. Alt, editor, *Advances in Immunology*, volume 122 of *Advances in Immunology*, pages 91 – 128. Academic Press, 2014.

[127] Zhang Zhang, Tao Su, Liang He, Hongtao Wang, Gang Ji, Xiaonan Liu, Yun Zhang, and Guanglong Dong. Identification and functional analysis of ligands for natural killer cell activating receptors in colon carcinoma. *The Tohoku Journal of Experimental Medicine*, 226(1):59–68, 2012.

[128] Yenan T. Bryceson, Michael E. March, Hans-Gustaf Ljunggren, and Eric O. Long. Synergy among receptors on resting nk cells for the activation of natural cytotoxicity and cytokine secretion. *Blood*, 107(1):159–166, 2005.

[129] Rizwan Romee, Bree Foley, Todd Lenvik, Yue Wang, Bin Zhang, Dave Ankarlo, Xianghua Luo, Sarah Cooley, Mike Verneris, Bruce Walcheck, and Jeffrey Miller. Nk cell cd16 surface expression and function is regulated by a disintegrin and metalloprotease-17 (adam17). *Blood*, 121(18):3599–3608, 2013.

[130] L L Lanier, G Yu, and J H Phillips. Analysis of fc gamma riii (cd16) membrane expression and association with cd3 zeta and fc epsilon ri-gamma by site-directed mutation. *The Journal of Immunology*, 146(5):1571–1576, 1991.

[131] Antonino Musolino, Nadia Naldi, Beatrice Bortesi, Debora Pezzuolo, Marzia Capelletti, Gabriele Missale, Diletta Laccabue, Alessandro Zerbini, Roberta Camisa, Giancarlo Bisagni, Tauro Maria Neri, and Andrea Ardizzoni. Immunoglobulin g fragment c receptor polymorphisms and clinical efficacy of trastuzumab-based therapy in patients with her-2/neu-positive metastatic breast cancer. *Journal of Clinical Oncology*, 26(11):1789–1796, 2008. PMID: 18347005.

[132] Andrew M. Scott, Jedd D. Wolchok, and Lloyd J. Old. Antibody therapy of cancer. *Nat Rev Cancer*, 12(4):278–287, April 2012.

[133] Andrew C. Chan and Paul J. Carter. Therapeutic antibodies for autoimmunity and inflammation. *Nat Rev Immunol*, 10(5):301–316, May 2010.

[134] Junji Uchida, Yasuhito Hamaguchi, Julie A. Oliver, Jeffrey V. Ravetch, Jonathan C. Poe, Karen M. Haas, and Thomas F. Tedder. The innate mononuclear phagocyte network depletes b lymphocytes through fc receptor–dependent mechanisms during anti-cd20 antibody immunotherapy. *Journal of Experimental Medicine*, 199(12):1659–1669, 2004.

[135] L Arnould, M Gelly, F Penault-Llorca, L Benoit, F Bonnetain, C Migeon, V Cabaret, V Fermeaux, P Bertheau, J Garnier, J-F Jeannin, and B Coudert. Trastuzumab-based treatment of her2-positive breast cancer: an antibody-dependent cellular cytotoxicity mechanism? *Br J Cancer*, 94(2):259–267, January 2006.

[136] Steve Kohl. Role as antibody-dependent cellular cytotoxicity in defense against herpes simplex virus infections. *Reviews of Infectious Diseases*, 13(1):108, 1990.

[137] S. John Curnow, Martin J. Glennie, and George T. Stevenson. The role of apoptosis in antibody-dependent cellular cytotoxicity. *Cancer Immunology, Immunotherapy*, 36(3):149–155, 1993.

[138] ME Reff, K Carner, KS Chambers, PC Chinn, JE Leonard, R Raab, RA Newman, N Hanna, and DR Anderson. Depletion of b cells in vivo by a chimeric mouse human monoclonal antibody to cd20. *Blood*, 83(2):435–445, 1994.

[139] David G. Maloney, Antonio J. Grillo-López, Christine A. White, David Bodkin, Russell J. Schilder, James A. Neidhart, Nalini Janakiraman, Kenneth A. Foon, Tina-Marie Liles, Brian K. Dallaire, Ken Wey, Ivor Royston, Thomas Davis, and Ronald Levy. Idec-c2b8 (rituximab) anti-cd20 monoclonal antibody therapy in patients with relapsed low-grade non-hodgkin's lymphoma. *Blood*, 90(6):2188–2195, 1997.

[140] Wolfgang Merkt, Hanns-Martin Lorenz, and Carsten Watzl. Rituximab induces phenotypical and functional changes of nk cells in a non-malignant experimental setting. *Arthritis Research & Therapy*, 18(1):206, 2016.

[141] William Larry Gluck, Deborah Hurst, Alan Yuen, Alexandra M. Levine, Mark A. Dayton, Jon P. Gockerman, Jennifer Lucas, Kimberly Denis-Mize, Barbara Tong, Dawn Navis, Anita Difrancesco, Sandra Milan, Susan E. Wilson, and Maurice Wolin. Phase i studies of interleukin (il)-2 and rituximab in b-cell non-hodgkin's lymphoma. *Clinical Cancer Research*, 10(7):2253–2264, 2004.

[142] Cyril Fauriat, Eric O. Long, Hans-Gustaf Ljunggren, and Yenan T. Bryceson. Regulation of human nk-cell cytokine and chemokine production by target cell recognition. *Blood*, 115(11):2167–2176, 2010.

[143] S. J. Singer and Garth L. Nicolson. The fluid mosaic model of the structure of cell membranes. *Science*, 175(4023):720–731, 1972.

[144] Garth L. Nicolson. The fluid–mosaic model of membrane structure: Still relevant to understanding the structure, function and dynamics of biological membranes after more than 40 years. *Biochimica et Biophysica Acta (BBA) - Biomembranes*, 1838(6):1451–1466, 2014. Membrane Structure and Function: Relevance in the Cell's Physiology, Pathology and Therapy.

[145] Colin R. F. Monks, Benjamin A. Freiberg, Hannah Kupfer, Noah Sciaky, and Abraham Kupfer. Three-dimensional segregation of supramolecular activation clusters in t cells. *Nature*, 395(6697):82–86, September 1998.

[146] Bozidar Purtic, Lisa A. Pitcher, Nicolai S. C. van Oers, and Christoph Wülfing. T cell receptor (tcr) clustering in the immunological synapse integrates tcr and costimulatory signaling in selected t cells. *Proceedings of the National Academy of Sciences of the United States of America*, 102(8):2904–2909, 2005.

[147] Gabriele Campi, Rajat Varma, and Michael L. Dustin. Actin and agonist mhc–peptide complex–dependent t cell receptor microclusters as scaffolds for signaling. *Journal of Experimental Medicine*, 202(8):1031–1036, 2005.

[148] David Depoil, Sebastian Fleire, Bebhinn L Treanor, Michele Weber, Naomi E Harwood, Kevin L Marchbank, Victor L J Tybulewicz, and Facundo D Batista. Cd19 is essential for b cell activation by promoting b

cell receptor-antigen microcluster formation in response to membrane-bound ligand. *Nat Immunol*, 9(1):63–72, January 2008.

[149] Daniel M Davis, Isaac Chiu, Marlys Fassett, George B Cohen, Ofer Mandelboim, and Jack L Strominger. The human natural killer cell immune synapse. *Proceedings of the National Academy of Sciences of the United States of America*, 96(26):15062–15067, October 1999.

[150] Bebhinn Treanor, Peter M.P. Lanigan, Sunil Kumar, Chris Dunsby, Ian Munro, Egidijus Auksorius, Fiona J. Culley, Marco A. Purbhoo, David Phillips, Mark A.A. Neil, Deborah N. Burshtyn, Paul M.W. French, and Daniel M. Davis. Microclusters of inhibitory killer immunoglobulin–like receptor signaling at natural killer cell immunological synapses. *The Journal of Cell Biology*, 174(1):153–161, 2006.

[151] Jordan S Orange, K Eliza Harris, Milena M Andzelm, Markus M Valter, Raif S Geha, and Jack L Strominger. The mature activating natural killer cell immunologic synapse is formed in distinct stages. *Proceedings of the National Academy of Sciences of the United States of America*, 100(24):14151–14156, November 2003.

[152] CC Snyder. On the history of the suture. *Bulletin of the History of Dentistry*, pages 79–84, Oct 1977.

[153] J. H. Breasted. *The Edwin Smith Surgical Papyrus, Volume 1: Hieroglyphic Transliteration, Translation, and Commentary.* Oriental Institue Publications, 1930.

[154] Véronique Migonney. *Biomaterials*. Wiley, 2014.

[155] Marshall Joseph Becker. Etruscan gold dental appliances: Three newly "discovered" examples. *American Journal of Archaeology*, 103(1):103–111, 1999.

[156] A Bobbio. The first endosseous alloplastic implant in the history of man. *Bulletin of the History of Dentistry*, pages 1–6, Jun 1972.

[157] H. S. Levert. Experiments on the use of metallic ligatures, as applied to arteries. *American Journal of Medical Science*, 7:17–23, 1829.

[158] William Waugh. *John Charnley - The Man and the Hip*. Springer London, 1990.

[159] P. I. Brøanemark, U. Breine, B. Johansson, P. J. Roylance, H. Röckert, and J. M. Yoffey. Regeneration of bone marrow - a clinical and experimental study following removal of bone marrow by curettage. *Acta Anatomica*, 59:1–46, 1964.

[160] R. Langer and J. Folkman. Polymers for the sustained release of proteins and other macromolecules. *Nature*, 263:797–800, October 1976.

[161] G. Nöldge, G. M. Richter, V. Siegerstetter, O. Garcia, and J. C. Palmaz. Tierexperimentelle untersuchungen über den einflußder flußrestriktion auf die thrombogenität des palmaz-stentes mittels ^{111}indiummarkierter thrombozyten. *Fortschr RÃÂÃÂ¶ntgenstr*, 152(03):264–270, 1990.

[162] G. M. Richter, J. C. Palmaz, G. Noeldge, and F. Tio. Relationship between blood flow, thrombus, and neointima in stents. *Journal of vascular and interventional radiology : JVIR*, 10:598–604, May 1999.

[163] Buddy Ratner, Allan Hoffman, Frederick Schoen, and Jack Lemons. *Biomaterials Science*. Elsevier, 3rd edition, Dec 2012.

[164] Thomas J Webster. Ijn's second year is now a part of nanomedicine history! *International Journal of Nanomedicine*, 2(1178-2013 (Electronic)):1–2, Apr 2007.

[165] K. Eric Drexler. Molecular engineering: An approach to the development of general capabilities for molecular manipulation. *Proceedings of the National Academy of Sciences*, 78(9):5275–5278, 1981.

[166] K. E. Drexler. *Engines of Creation: The Coming Era of Nanotechnology*. Doubleday, 1986.

[167] Adarsh Sandhu. Who invented nano? *Nat Nano*, 1(2):87–87, November 2006.

[168] Mikhail I. Katsnelson. Graphene: carbon in two dimensions. *Materials Today*, 10(1–2):20–27, January 2007.

[169] Alexander S. Mayorov, Roman V. Gorbachev, Sergey V. Morozov, Liam Britnell, Rashid Jalil, Leonid A. Ponomarenko, Peter Blake, Kostya S. Novoselov, Kenji Watanabe, Takashi Taniguchi, and A. K. Geim. Micrometer-Scale Ballistic Transport in Encapsulated Graphene at Room Temperature. *Nano Letters*, 11(6):2396–2399, June 2011.

[170] Changgu Lee, Xiaoding Wei, Jeffrey W. Kysar, and James Hone. Measurement of the Elastic Properties and Intrinsic Strength of Monolayer Graphene. *Science*, 321(5887):385–388, July 2008.

[171] Alexander A. Balandin. Thermal properties of graphene and nanostructured carbon materials. *Nature Materials*, 10(8):569–581, August 2011.

[172] R. R. Nair, P. Blake, A. N. Grigorenko, K. S. Novoselov, T. J. Booth, T. Stauber, N. M. R. Peres, and A. K. Geim. Fine Structure Constant Defines Visual Transparency of Graphene. *Science*, 320(5881):1308–1308, June 2008.

[173] K. S. Novoselov, V. I. Fal'ko, L. Colombo, P. R. Gellert, M. G. Schwab, and K. Kim. A roadmap for graphene. *Nature*, 490(7419):192–200, October 2012.

[174] G. Ruess and F. Vogt. Höchstlamellarer Kohlenstoff aus Graphitoxyhydroxyd. *Monatshefte für Chemie und verwandte Teile anderer Wissenschaften*, 78(3-4):222–242, May 1948.

[175] H. P. Boehm, A. Clauss, G. Fischer, and U. Hofmann. The surface properties of extremely thine graphite lamellae. In *Proceedings of the Fifth Conference on Carbon*, 1962.

[176] Alexander E. Karu and Michael Beer. Pyrolytic Formation of Highly Crystalline Graphite Films. *Journal of Applied Physics*, 37(5):2179–2181, April 1966.

[177] Chuhei Oshima and Ayato Nagashima. Ultra-thin epitaxial films of graphite and hexagonal boron nitride on solid surfaces. *Journal of Physics: Condensed Matter*, 9(1):1, 1997.

[178] K. S. Novoselov, A. K. Geim, S. V. Morozov, D. Jiang, Y. Zhang, S. V. Dubonos, I. V. Grigorieva, and A. A. Firsov. Electric Field Effect in Atomically Thin Carbon Films. *Science*, 306(5696):666–669, October 2004.

[179] B. C. Brodie. On the Atomic Weight of Graphite. *Philosophical Transactions of the Royal Society of London*, 149:249–259, January 1859.

[180] L. Staudenmaier. Verfahren zur Darstellung der Graphitsure. *Berichte der deutschen chemischen Gesellschaft*, 31(2):1481–1487, May 1898.

[181] Daniela C. Marcano, Dmitry V. Kosynkin, Jacob M. Berlin, Alexander Sinitskii, Zhengzong Sun, Alexander Slesarev, Lawrence B. Alemany,

Wei Lu, and James M. Tour. Improved Synthesis of Graphene Oxide. *ACS Nano*, 4(8):4806–4814, August 2010.

[182] Ji Chen, Bowen Yao, Chun Li, and Gaoquan Shi. An improved Hummers method for eco-friendly synthesis of graphene oxide. *Carbon*, 64:225–229, November 2013.

[183] Huitao Yu, Bangwen Zhang, Chaoke Bulin, Ruihong Li, and Ruiguang Xing. High-efficient Synthesis of Graphene Oxide Based on Improved Hummers Method. *Scientific Reports*, 6:36143, November 2016.

[184] J. I. Paredes, S. Villar-Rodil, A. MartÃÂnez-Alonso, and J. M. D. TascÃÂn. Graphene oxide dispersions in organic solvents. *Langmuir*, 24(19):10560–10564, 2008. PMID: 18759411.

[185] Sungjin Park and Rodney S. Ruoff. Chemical methods for the production of graphenes. *Nature Nanotechnology*, 4(4):217–224, April 2009.

[186] Anton Lerf, Heyong He, Michael Forster, and Jacek Klinowski. Structure of Graphite Oxide Revisited. *The Journal of Physical Chemistry B*, 102(23):4477–4482, June 1998.

[187] F Perrozzi, S Prezioso, and L Ottaviano. Graphene oxide: from fundamentals to applications. *Journal of Physics: Condensed Matter*, 27(1):013002, 2015.

[188] A. Martín Rodríguez and P. S. Valerga Jimínez. Some new aspects of graphite oxidation at 0°c in a liquid medium. A mechanism proposal for oxidation to graphite oxide. *Carbon*, 24(2):163–167, January 1986.

[189] D. Hadzi and A. Novak. Infra-red spectra of graphitic oxide. *Trans. Faraday Soc.*, 51:1614–1620, 1955.

[190] Shreya H. Dave, Chuncheng Gong, Alex W. Robertson, Jamie H. Warner, and Jeffrey C. Grossman. Chemistry and Structure of Graphene Oxide via Direct Imaging. *ACS Nano*, 10(8):7515–7522, August 2016.

[191] Daniel R. Dreyer, Sungjin Park, Christopher W. Bielawski, and Rodney S. Ruoff. The chemistry of graphene oxide. *Chem. Soc. Rev.*, 39:228–240, 2010.

[192] Jonathan P. Rourke, Priyanka A. Pandey, Joseph J. Moore, Matthew Bates, Ian A. Kinloch, Robert J. Young, and Neil R. Wilson. The Real Graphene Oxide Revealed: Stripping the Oxidative Debris from the Graphene-like Sheets. *Angewandte Chemie International Edition*, 50(14):3173–3177, March 2011.

[193] Helen R. Thomas, Stephen P. Day, William E. Woodruff, Cristina Vallés, Robert J. Young, Ian A. Kinloch, Gavin W. Morley, John V. Hanna, Neil R. Wilson, and Jonathan P. Rourke. Deoxygenation of Graphene Oxide: Reduction or Cleaning? *Chemistry of Materials*, 25(18):3580–3588, September 2013.

[194] Jonathan P. Rourke and Neil R. Wilson. Letter to the Editor: A defence of the two-component model of graphene oxide. *Carbon*, 96:339–341, January 2016.

[195] Ayrat M. Dimiev, Lawrence B. Alemany, and James M. Tour. Graphene Oxide. Origin of Acidity, Its Instability in Water, and a New Dynamic Structural Model. *ACS Nano*, 7(1):576–588, January 2013.

[196] Ayrat M. Dimiev and Thomas A. Polson. Contesting the two-component structural model of graphene oxide and reexamining the chemistry of graphene oxide in basic media. *Carbon*, 93:544–554, November 2015.

[197] A. Nekahi, S. P. H. Marashi, and D. Haghshenas Fatmesari. Modified structure of graphene oxide by investigation of structure evolution. *Bulletin of Materials Science*, 38(7):1717–1722, December 2015.

[198] Wei Gao, Lawrence B. Alemany, Lijie Ci, and Pulickel M. Ajayan. New insights into the structure and reduction of graphite oxide. *Nature Chemistry*, 1(5):403–408, August 2009.

[199] Daniel R. Dreyer, Alexander D. Todd, and Christopher W. Bielawski. Harnessing the chemistry of graphene oxide. *Chem. Soc. Rev.*, 43:5288–5301, 2014.

[200] Sasha Stankovich, Dmitriy A. Dikin, Richard D. Piner, Kevin A. Kohlhaas, Alfred Kleinhammes, Yuanyuan Jia, Yue Wu, SonBinh T. Nguyen, and Rodney S. Ruoff. Synthesis of graphene-based nanosheets via chemical reduction of exfoliated graphite oxide. *Carbon*, 45(7):1558–1565, June 2007.

[201] Sungjin Park, Jinho An, Jeffrey R. Potts, Aruna Velamakanni, Shanthi Murali, and Rodney S. Ruoff. Hydrazine-reduction of graphite- and graphene oxide. *Carbon*, 49(9):3019 – 3023, 2011.

[202] Hyeon-Jin Shin, Ki Kang Kim, Anass Benayad, Seon-Mi Yoon, Hyeon Ki Park, In-Sun Jung, Mei Hua Jin, Hae-Kyung Jeong, Jong Min Kim, Jae-Young Choi, and Young Hee Lee. Efficient Reduction of Graphite Oxide by Sodium Borohydride and Its Effect on Electrical Conductance. *Advanced Functional Materials*, 19(12):1987–1992, June 2009.

[203] Daniel R. Dreyer, Shanthi Murali, Yanwu Zhu, Rodney S. Ruoff, and Christopher W. Bielawski. Reduction of graphite oxide using alcohols. *J. Mater. Chem.*, 21:3443–3447, 2011.

[204] Michael J. McAllister, Je Luen Li, Douglas H. Adamson, Hannes C. Schniepp, Ahmed A. Abdala, Jun Liu, Margarita Herrera-Alonso, David L. Milius, Roberto Car, Robert K. Prud'homme, and Ilhan A. Aksay. Single sheet functionalized graphene by oxidation and thermal expansion of graphite. *Chemistry of Materials*, 19(18):4396–4404, September 2007.

[205] O. Akhavan. The effect of heat treatment on formation of graphene thin films from graphene oxide nanosheets. *Carbon*, 48(2):509 – 519, 2010.

[206] Ming Zhou, Yuling Wang, Yueming Zhai, Junfeng Zhai, Wen Ren, Fuan Wang, and Shaojun Dong. Controlled Synthesis of Large-Area and Patterned Electrochemically Reduced Graphene Oxide Films. *Chemistry A European Journal*, 15(25):6116–6120, June 2009.

[207] Joshua T. Robinson, Scott M. Tabakman, Yongye Liang, Hailiang Wang, Hernan Sanchez Casalongue, Daniel Vinh, and Hongjie Dai. Ultrasmall Reduced Graphene Oxide with High Near-Infrared Absorbance for Photothermal Therapy. *Journal of the American Chemical Society*, 133(17):6825–6831, May 2011.

[208] Jessica M. Rosenholm, Emilia Peuhu, John E. Eriksson, Cecilia Sahlgren, and Mika Lindén. Targeted intracellular delivery of hydrophobic agents using mesoporous hybrid silica nanoparticles as carrier systems. *Nano Letters*, 9(9):3308–3311, 2009. PMID: 19736973.

[209] Rui Hao, Wen Qian, Luhui Zhang, and Yanglong Hou. Aqueous dispersions of tcnq-anion-stabilized graphene sheets. *Chem. Commun.*, pages 6576–6578, 2008.

[210] Yuxi Xu, Hua Bai, Gewu Lu, Chun Li, and Gaoquan Shi. Flexible graphene films via the filtration of water-soluble noncovalent func-

tionalized graphene sheets. *Journal of the American Chemical Society*, 130(18):5856–5857, 2008. PMID: 18399634.

[211] Sasha Stankovich, Richard D. Piner, Xinqi Chen, Nianqiang Wu, Son-Binh T. Nguyen, and Rodney S. Ruoff. Stable aqueous dispersions of graphitic nanoplatelets via the reduction of exfoliated graphite oxide in the presence of poly(sodium 4-styrenesulfonate). *Journal of Materials Chemistry*, 16(2):155–158, 2006.

[212] Sheng-Zhen Zu and Bao-Hang Han. Aqueous Dispersion of Graphene Sheets Stabilized by Pluronic Copolymers: Formation of Supramolecular Hydrogel. *The Journal of Physical Chemistry C*, 113(31):13651–13657, August 2009.

[213] Hua Bai, Yuxi Xu, Lu Zhao, Chun Li, and Gaoquan Shi. Non-covalent functionalization of graphene sheets by sulfonated polyaniline. *Chemical Communications*, 0(13):1667–1669, 2009.

[214] Chun-Hua Lu, Huang-Hao Yang, Chun-Ling Zhu, Xi Chen, and Guo-Nan Chen. A Graphene Platform for Sensing Biomolecules. *Angewandte Chemie International Edition*, 48(26):4785–4787, June 2009.

[215] Xiaoying Yang, Xiaoyan Zhang, Zunfeng Liu, Yanfeng Ma, Yi Huang, and Yongsheng Chen. High-Efficiency Loading and Controlled Release of Doxorubicin Hydrochloride on Graphene Oxide. *The Journal of Physical Chemistry C*, 112(45):17554–17558, November 2008.

[216] Jiang Long, Ming Fang, and Guohua Chen. Microwave-assisted rapid synthesis of water-soluble graphene. *J. Mater. Chem.*, 21:10421–10425, 2011.

[217] Xiaoyong Zhang, Mingsong Han, Shu Chen, Lin Bao, Ling Li, and Weijian Xu. Azo addition to exfoliated graphene: a facile and high yield route to functionalized graphene. *RSC Adv.*, 3:17689–17692, 2013.

[218] Brianna C. Thompson, Eoin Murray, and Gordon G. Wallace. Graphite Oxide to Graphene. Biomaterials to Bionics. *Advanced Materials*, 27(46):7563–7582, December 2015.

[219] Dingshan Yu, Yan Yang, Michael Durstock, Jong-Beom Baek, and Liming Dai. Soluble p3ht-grafted graphene for efficient bilayer-heterojunction photovoltaic devices. *ACS Nano*, 4(10):5633–5640, 2010. PMID: 20831214.

[220] Yanfei Xu, Zhibo Liu, Xiaoliang Zhang, Yan Wang, Jianguo Tian, Yi Huang, Yanfeng Ma, Xiaoyan Zhang, and Yongsheng Chen. A Graphene Hybrid Material Covalently Functionalized with Porphyrin: Synthesis and Optical Limiting Property. *Advanced Materials*, 21(12):1275–1279, March 2009.

[221] Zhi-Bo Liu, Yan-Fei Xu, Xiao-Yan Zhang, Xiao-Liang Zhang, Yong-Sheng Chen, and Jian-Guo Tian. Porphyrin and fullerene covalently functionalized graphene hybrid materials with large nonlinear optical properties. *The Journal of Physical Chemistry B*, 113(29):9681–9686, 2009. PMID: 19569625.

[222] Nihar Mohanty and Vikas Berry. Graphene-based single-bacterium resolution biodevice and dna transistor: Interfacing graphene derivatives with nanoscale and microscale biocomponents. *Nano Letters*, 8(12):4469–4476, 2008. PMID: 18983201.

[223] Hongqian Bao, Yongzheng Pan, Yuan Ping, Nanda Gopal Sahoo, Tongfei Wu, Lin Li, Jun Li, and Leong Huat Gan. Chitosan-

Functionalized Graphene Oxide as a Nanocarrier for Drug and Gene Delivery. *Small*, 7(11):1569–1578, June 2011.

[224] Liangzhu Feng, Xianzhu Yang, Xiaoze Shi, Xiaofang Tan, Rui Peng, Jun Wang, and Zhuang Liu. Polyethylene Glycol and Polyethylenimine Dual-Functionalized Nano-Graphene Oxide for Photothermally Enhanced Gene Delivery. *Small*, 9(11):1989–1997, June 2013.

[225] L. Monica Veca, Fushen Lu, Mohammed J. Meziani, Li Cao, Puyu Zhang, Gang Qi, Liangwei Qu, Mona Shrestha, and Ya-Ping Sun. Polymer functionalization and solubilization of carbon nanosheets. *Chem. Commun.*, pages 2565–2567, 2009.

[226] Bin Zhang, Yu Chen, Liqun Xu, Longjia Zeng, Ying He, En-Tang Kang, and Jinjuan Zhang. Growing poly(N-vinylcarbazole) from the surface of graphene oxide via RAFT polymerization. *Journal of Polymer Science Part A: Polymer Chemistry*, 49(9):2043–2050, May 2011.

[227] Xiaowei Ou, Lang Jiang, Penglei Chen, Mingshan Zhu, Wenping Hu, Minghua Liu, Junfa Zhu, and Huanxin Ju. Highly Stable Graphene-Based Multilayer Films Immobilized via Covalent Bonds and Their Applications in Organic Field-Effect Transistors. *Advanced Functional Materials*, 23(19):2422–2435, May 2013.

[228] Haiqing Yao, Lin Jin, Hung-Jue Sue, Yasuhiro Sumi, and Riichi Nishimura. Facile decoration of au nanoparticles on reduced graphene oxide surfaces via a one-step chemical functionalization approach. *J. Mater. Chem. A*, 1:10783–10789, 2013.

[229] William R. Collins, Wiktor Lewandowski, Ezequiel Schmois, Joseph Walish, and Timothy M. Swager. Claisen Rearrangement of Graphite Oxide: A Route to Covalently Functionalized Graphenes. *Angewandte Chemie International Edition*, 50(38):8848–8852, September 2011.

[230] Huafeng Yang, Fenghua Li, Changsheng Shan, Dongxue Han, Qixian Zhang, Li Niu, and Ari Ivaska. Covalent functionalization of chemically converted graphene sheets via silane and its reinforcement. *J. Mater. Chem.*, 19:4632–4638, 2009.

[231] Shuai Wang, Perq-Jon Chia, Lay-Lay Chua, Li-Hong Zhao, Rui-Qi Png, Sankaran Sivaramakrishnan, Mi Zhou, Roland G.-S. Goh, Richard H. Friend, Andrew T.-S. Wee, and Peter K.-H. Ho. Band-like Transport in Surface-Functionalized Highly Solution-Processable Graphene Nanosheets. *Advanced Materials*, 20(18):3440–3446, September 2008.

[232] Huafeng Yang, Changsheng Shan, Fenghua Li, Dongxue Han, Qixian Zhang, and Li Niu. Covalent functionalization of polydisperse chemically-converted graphene sheets with amine-terminated ionic liquid. *Chem. Commun.*, pages 3880–3882, 2009.

[233] William R. Collins, Ezequiel Schmois, and Timothy M. Swager. Graphene oxide as an electrophile for carbon nucleophiles. *Chem. Commun.*, 47:8790–8792, 2011.

[234] Xiaowei Zhang, Oleg V. Yazyev, Juanjuan Feng, Liming Xie, Chenggang Tao, Yen-Chia Chen, Liying Jiao, Zahra Pedramrazi, Alex Zettl, Steven G. Louie, Hongjie Dai, and Michael F. Crommie. Experimentally Engineering the Edge Termination of Graphene Nanoribbons. *ACS Nano*, 7(1):198–202, January 2013.

[235] Guy Renaud, Robert L. Hamilton, and Richard J. Havel. Hepatic metabolism of colloidal gold-low-density lipoprotein complexes in the rat: Evidence for bulk excretion of lysosomal contents into bile. *Hepatology*, 9(3):380–392, March 1989.

[236] M. J. Hardonk, G. Harms, and J. Koudstaal. Zonal heterogeneity of rat hepatocytes in the in vivo uptake of 17 nm colloidal gold granules. *Histochemistry*, 83(5):473–477, September 1985.

[237] Ravi Singh, Davide Pantarotto, Lara Lacerda, Giorgia Pastorin, Cédric Klumpp, Maurizio Prato, Alberto Bianco, and Kostas Kostarelos. Tissue biodistribution and blood clearance rates of intravenously administered carbon nanotube radiotracers. *Proceedings of the National Academy of Sciences of the United States of America*, 103(9):3357–3362, February 2006.

[238] Haifang Wang, Jing Wang, Xiaoyong Deng, Hongfang Sun, Zujin Shi, Zhennan Gu, Yuanfang Liu, and Yuliang Zhaoc. Biodistribution of Carbon Single-Wall Carbon Nanotubes in Mice. *Journal of Nanoscience and Nanotechnology*, 4(8):1019–1024, November 2004.

[239] Ning Li, Tian Xia, and Andre E. Nel. The role of oxidative stress in ambient particulate matter-induced lung diseases and its implications in the toxicity of engineered nanoparticles. *Free Radical Biology and Medicine*, 44(9):1689–1699, May 2008.

[240] Klaus Unfried, Catrin Albrecht, Lars-Oliver Klotz, Anna Von Mikecz, Susanne Grether-Beck, and Roel P. F. Schins. Cellular responses to nanoparticles: Target structures and mechanisms. *Nanotoxicology*, 1(1):52–71, January 2007.

[241] Andre Nel, Tian Xia, Lutz MÃdler, and Ning Li. Toxic Potential of Materials at the Nanolevel. *Science*, 311(5761):622–627, February 2006.

[242] Zhou J. Deng, Mingtao Liang, Michael Monteiro, Istvan Toth, and Rodney F. Minchin. Nanoparticle-induced unfolding of fibrinogen promotes Mac-1 receptor activation and inflammation. *Nature Nanotechnology*, 6(1):39–44, January 2011.

[243] Shahriar Sharifi, Shahed Behzadi, Sophie Laurent, M. Laird Forrest, Pieter Stroeve, and Morteza Mahmoudi. Toxicity of nanomaterials. *Chemical Society Reviews*, 41(6):2323–2343, 2012.

[244] Cyrill Bussy, Hanene Ali-Boucetta, and Kostas Kostarelos. Safety Considerations for Graphene: Lessons Learnt from Carbon Nanotubes. *Accounts of Chemical Research*, 46(3):692–701, March 2013.

[245] Ying Liu, Yuliang Zhao, Baoyun Sun, and Chunying Chen. Understanding the Toxicity of Carbon Nanotubes. *Accounts of Chemical Research*, 46(3):702–713, March 2013.

[246] Yoshinori Sato, Atsuro Yokoyama, Ken-ichiro Shibata, Yuki Akimoto, Shin-ichi Ogino, Yoshinobu Nodasaka, Takao Kohgo, Kazuchika Tamura, Tsukasa Akasaka, Motohiro Uo, Kenichi Motomiya, Balachandran Jeyadevan, Mikio Ishiguro, Rikizo Hatakeyama, Fumio Watari, and Kazuyuki Tohji. Influence of length on cytotoxicity of multiwalled carbon nanotubes against human acute monocytic leukemia cell line thp-1 in vitro and subcutaneous tissue of rats in vivo. *Mol. BioSyst.*, 1:176–182, 2005.

[247] Bice Fubini, Mara Ghiazza, and Ivana Fenoglio. Physico-chemical features of engineered nanoparticles relevant to their toxicity. *Nanotoxicology*, 4(4):347–363, December 2010.

[248] Ning Li, Xuemin Zhang, Qin Song, Ruigong Su, Qi Zhang, Tao Kong, Liwei Liu, Gang Jin, Mingliang Tang, and Guosheng Cheng. The promotion of neurite sprouting and outgrowth of mouse hippocampal cells in culture by graphene substrates. *Biomaterials*, 32(35):9374–9382, December 2011.

[249] Amel Bendali, Lucas H. Hess, Max Seifert, Valerie Forster, Anne-Fleur Stephan, Jose A. Garrido, and Serge Picaud. Purified Neurons can Sur-

vive on Peptide-Free Graphene Layers. *Advanced Healthcare Materials*, 2(7):929–933, July 2013.

[250] Jifeng Yuan, Hongcai Gao, Jianjun Sui, Hongwei Duan, Wei N. Chen, and Chi B. Ching. Cytotoxicity Evaluation of Oxidized Single-Walled Carbon Nanotubes and Graphene Oxide on Human Hepatoma HepG2 cells: An iTRAQ-Coupled 2d LC-MS/MS Proteome Analysis. *Toxicological Sciences*, 126(1):149–161, March 2012.

[251] Sook Hee Ku and Chan Beum Park. Myoblast differentiation on graphene oxide. *Biomaterials*, 34(8):2017–2023, March 2013.

[252] HN Lim, NM Huang, SS Lim, I Harrison, and CH Chia. Fabrication and characterization of graphene hydrogel via hydrothermal approach as a scaffold for preliminary study of cell growth. *International Journal of Nanomedicine*, 6:1817–1823, August 2011.

[253] Abhilash Sasidharan, L. S. Panchakarla, Parwathy Chandran, Deepthy Menon, Shantikumar Nair, C. N. R. Rao, and Manzoor Koyakutty. Differential nano-bio interactions and toxicity effects of pristine versus functionalized graphene. *Nanoscale*, 3(6):2461–2464, 2011.

[254] Kan Wang, Jing Ruan, Hua Song, Jiali Zhang, Yan Wo, Shouwu Guo, and Daxiang Cui. Biocompatibility of Graphene Oxide. *Nanoscale Res Lett*, 6(1):8, December 2011.

[255] Xiaoyong Zhang, Jilei Yin, Cheng Peng, Weiqing Hu, Zhiyong Zhu, Wenxin Li, Chunhai Fan, and Qing Huang. Distribution and biocompatibility studies of graphene oxide in mice after intravenous administration. *Carbon*, 49(3):986–995, March 2011.

[256] Jia-Hui Liu, Sheng-Tao Yang, Haifang Wang, Yanli Chang, Aoneng Cao, and Yuanfang Liu. Effect of size and dose on the biodistribution of graphene oxide in mice. *Nanomedicine*, 7(12):1801–1812, July 2012.

[257] Hanene Ali-Boucetta, Dimitrios Bitounis, Rahul Raveendran-Nair, Ania Servant, Jeroen Van den Bossche, and Kostas Kostarelos. Purified Graphene Oxide Dispersions Lack In Vitro Cytotoxicity and In Vivo Pathogenicity. *Advanced Healthcare Materials*, 2(3):433–441, March 2013.

[258] Elaine Lay Khim Chng and Martin Pumera. The toxicity of graphene oxides: dependence on the oxidative methods used. *Chemistry (Weinheim an der Bergstrasse, Germany)*, 19(25):8227–35, jun 2013.

[259] Sunil K. Singh, Manoj K. Singh, Manasa K. Nayak, Sharda Kumari, Siddhartha Shrivastava, José J. A. Grácio, and Debabrata Dash. Thrombus Inducing Property of Atomically Thin Graphene Oxide Sheets. *ACS Nano*, 5(6):4987–4996, June 2011.

[260] Chao Sun, DevinÂ L. Wakefield, Yimo Han, DavidÂ A. Muller, DavidÂ A. Holowka, BarbaraÂ A. Baird, and WilliamÂ R. Dichtel. Graphene oxide nanosheets stimulate ruffling and shedding of mammalian cell plasma membranes. *Chem*, 1(2):273–286, 2016.

[261] Cyrill Bussy and Kostas Kostarelos. Culture media critically influence graphene oxide effects on plasma membranes. *Chem*, 2(3):322–323, 2017.

[262] Kai Yang, Jianmei Wan, Shuai Zhang, Youjiu Zhang, Shuit-Tong Lee, and Zhuang Liu. In Vivo Pharmacokinetics, Long-Term Biodistribution, and Toxicology of PEGylated Graphene in Mice. *ACS Nano*, 5(1):516–522, January 2011.

[263] Dhifaf A. Jasim, Herve Boutin, Michael Fairclough, Cécilia Ménard-Moyon, Christian Prenant, Alberto Bianco, and Kostas Kostarelos. Thickness of functionalized graphene oxide sheets plays critical role in tissue accumulation and urinary excretion: A pilot PET/CT study. *Applied Materials Today*, 4:24–30, September 2016.

[264] Dhifaf A. Jasim, Stephanie Murphy, Leon Newman, Aleksandr Mironov, Eric Prestat, James McCaffrey, Cecilia Menard-Moyon, Artur Filipe Rodrigues, Alberto Bianco, Sarah Haigh, Rachel Lennon, and Kostas Kostarelos. The Effects of Extensive Glomerular Filtration of Thin Graphene Oxide Sheets on Kidney Physiology. *ACS Nano*, 10(12):10753–10767, December 2016.

[265] Dan Li, Marc B. Müller, Scott Gilje, Richard B. Kaner, and Gordon G. Wallace. Processable aqueous dispersions of graphene nanosheets. *Nature Nanotechnology*, 3(2):101–105, February 2008.

[266] Douglas H. Everett. *Basic Principles of Colloid Science*. The Royal Society of Chemistry, September 1988.

[267] D. H Napper. Steric stabilization. *Journal of Colloid and Interface Science*, 58(2):390–407, February 1977.

[268] Jun Araki, Masahisa Wada, and Shigenori Kuga. Steric Stabilization of a Cellulose Microcrystal Suspension by Poly(ethylene glycol) Grafting. *Langmuir*, 17(1):21–27, January 2001.

[269] Hyunwoo Kim, Duhwan Lee, Jinhwan Kim, Tae-il Kim, and Won Jong Kim. Photothermally Triggered Cytosolic Drug Delivery via Endosome Disruption Using a Functionalized Reduced Graphene Oxide. *ACS Nano*, 7(8):6735–6746, August 2013.

[270] L. Monica Veca, Fushen Lu, Mohammed J. Meziani, Li Cao, Puyu Zhang, Gang Qi, Liangwei Qu, Mona Shrestha, and Ya-Ping Sun. Polymer functionalization and solubilization of carbon nanosheets. *Chemical Communications*, 0(18):2565–2567, 2009.

[271] Tingjie Yin, Jiyong Liu, Zekai Zhao, Yuanyuan Zhao, Lihui Dong, Meng Yang, Jianping Zhou, and Meirong Huo. Redox Sensitive Hyaluronic Acid-Decorated Graphene Oxide for Photothermally Controlled Tumor-Cytoplasm-Selective Rapid Drug Delivery. *Advanced Functional Materials*, March 2017.

[272] Liming Zhang, Jingguang Xia, Qinghuan Zhao, Liwei Liu, and Zhijun Zhang. Functional Graphene Oxide as a Nanocarrier for Controlled Loading and Targeted Delivery of Mixed Anticancer Drugs. *Small*, 6(4):537–544, February 2010.

[273] Yongchao Si and Edward T. Samulski. Synthesis of Water Soluble Graphene. *Nano Letters*, 8(6):1679–1682, June 2008.

[274] Yong Liu, Dingshan Yu, Chao Zeng, Zongcheng Miao, and Liming Dai. Biocompatible Graphene Oxide-Based Glucose Biosensors, March 2010.

[275] Xinhuang Kang, Jun Wang, Hong Wu, Ilhan A. Aksay, Jun Liu, and Yuehe Lin. Glucose Oxidase-graphene-chitosan modified electrode for direct electrochemistry and glucose sensing. *Biosensors and Bioelectronics*, 25(4):901–905, December 2009.

[276] Z. H. Dai, J. Ni, X. H. Huang, G. F. Lu, and J. C. Bao. Direct electrochemistry of glucose oxidase immobilized on a hexagonal mesoporous silica-MCM-41 matrix. *Bioelectrochemistry*, 70(2):250–256, May 2007.

[277] Adeline Huiling Loo, Alessandra Bonanni, Adriano Ambrosi, Hwee Ling Poh, and Martin Pumera. Impedimetric immunoglobulin G immunosensor based on chemically modified graphenes. *Nanoscale*, 4(3):921–925, 2012.

[278] Guangfeng Wang, Hao Huang, Ge Zhang, Xiaojun Zhang, Bin Fang, and Lun Wang. Gold nanoparticles / l-cysteine / graphene composite based immobilization strategy for an electrochemical immunosensor. *Analytical Methods*, 2(11):1692–1697, 2010.

[279] Dan Du, Limin Wang, Yuyan Shao, Jun Wang, Mark H. Engelhard, and Yuehe Lin. Functionalized Graphene Oxide as a Nanocarrier in a Multienzyme Labeling Amplification Strategy for Ultrasensitive Electrochemical Immunoassay of Phosphorylated p53 (S392). *Analytical Chemistry*, 83(3):746–752, February 2011.

[280] Yujing Guo, Yihong Chen, Qiang Zhao, Shaomin Shuang, and Chuan Dong. Electrochemical Sensor for Ultrasensitive Determination of Doxorubicin and Methotrexate Based on Cyclodextrin-Graphene Hybrid Nanosheets. *Electroanalysis*, 23(10):2400–2407, October 2011.

[281] Peng Qi, Yi Wan, Dun Zhang, and Jiajia Wu. Reduced Graphene Sheets Modified Electrodes for Electrochemical Detection of Sulfide. *Electroanalysis*, 23(12):2796–2801, December 2011.

[282] Bin WANG, Yan-hong CHANG, and Lin-jie ZHI. High yield production of graphene and its improved property in detecting heavy metal ions. *New Carbon Materials*, 26(1):31–35, January 2011.

[283] Yujing Guo, Shaojun Guo, Jing Li, Erkang Wang, and Shaojun Dong. Cyclodextrin-graphene hybrid nanosheets as enhanced sensing platform for ultrasensitive determination of carbendazim. *Talanta*, 84(1):60–64, March 2011.

[284] Da Chen, Hongbin Feng, and Jinghong Li. Graphene Oxide: Preparation, Functionalization, and Electrochemical Applications. *Chemical Reviews*, 112(11):6027–6053, November 2012.

[285] Dimitrios Bitounis, Hanene Ali-Boucetta, Byung Hee Hong, Dal-Hee Min, and Kostas Kostarelos. Prospects and Challenges of Graphene in Biomedical Applications. *Advanced Materials*, 25(16):2258–2268, April 2013.

[286] Vasilios Georgakilas, Jitendra N. Tiwari, K. Christian Kemp, Jason A. Perman, Athanasios B. Bourlinos, Kwang S. Kim, and Radek Zboril. Noncovalent Functionalization of Graphene and Graphene Oxide for Energy Materials, Biosensing, Catalytic, and Biomedical Applications. *Chemical Reviews*, 116(9):5464–5519, May 2016.

[287] Francois Berthiaume, Timothy J. Maguire, and Martin L. Yarmush. Tissue engineering and regenerative medicine: History, progress, and challenges. *Annual Review of Chemical and Biomolecular Engineering*, 2(1):403–430, 2011. PMID: 22432625.

[288] Vivien Marx. Tissue engineering: Organs from the lab. *Nature*, 522(7556):373–377, June 2015.

[289] Ali Khademhosseini and Robert Langer. A decade of progress in tissue engineering. *Nat. Protocols*, 11(10):1775–1781, October 2016.

[290] M P Lutolf and J A Hubbell. Synthetic biomaterials as instructive extracellular microenvironments for morphogenesis in tissue engineering. *Nat Biotech*, 23(1):47–55, January 2005.

[291] Hugo Fernandes, Lorenzo Moroni, Clemens van Blitterswijk, and Jan de Boer. Extracellular matrix and tissue engineering applications. *J. Mater. Chem.*, 19:5474–5484, 2009.

[292] Byung-Soo Kim, In-Kyu Park, Takashi Hoshiba, Hu-Lin Jiang, Yun-Jaie Choi, Toshihiro Akaike, and Chong-Su Cho. Design of artificial extracellular matrices for tissue engineering. *Progress in Polymer Science*, 36(2):238 – 268, 2011.

[293] Matthias P. Lutolf, Franz E. Weber, Hugo G. Schmoekel, Jason C. Schense, Thomas Kohler, Ralph Muller, and Jeffrey A. Hubbell. Repair of bone defects using synthetic mimetics of collagenous extracellular matrices. *Nat Biotech*, 21(5):513–518, May 2003.

[294] Chris S. Hughes, Lynne M. Postovit, and Gilles A. Lajoie. Matrigel: A complex protein mixture required for optimal growth of cell culture. *PROTEOMICS*, 10(9):1886–1890, 2010.

[295] Jeffrey D. Hartgerink, Elia Beniash, and Samuel I. Stupp. Self-assembly and mineralization of peptide-amphiphile nanofibers. *Science*, 294(5547):1684–1688, 2001.

[296] Yuxi Xu, Kaixuan Sheng, Chun Li, and Gaoquan Shi. Self-assembled graphene hydrogel via a one-step hydrothermal process. *ACS Nano*, 4(7):4324–4330, 2010. PMID: 20590149.

[297] D. Depan, B. Girase, J.S. Shah, and R.D.K. Misra. Structure–process–property relationship of the polar graphene oxide-mediated cellular response and stimulated growth of osteoblasts on hybrid chitosan network structure nanocomposite scaffolds. *Acta Biomaterialia*, 7(9):3432 – 3445, 2011.

[298] Han Hu, Zongbin Zhao, Wubo Wan, Yury Gogotsi, and Jieshan Qiu. Ultralight and highly compressible graphene aerogels. *Advanced Materials*, 25(15):2219–2223, 2013.

[299] Ning Li, Qi Zhang, Song Gao, Qin Song, Rong Huang, Long Wang, Liwei Liu, Jianwu Dai, Mingliang Tang, and Guosheng Cheng. Three-dimensional graphene foam as a biocompatible and conductive scaffold for neural stem cells. *Scientific Reports*, 3:1604–, April 2013.

[300] Peter C. Sherrell, Brianna C. Thompson, Jonathan K. Wassei, Amy A. Gelmi, Michael J. Higgins, Richard B. Kaner, and Gordon G. Wallace. Maintaining cytocompatibility of biopolymers through a graphene layer for electrical stimulation of nerve cells. *Advanced Functional Materials*, 24(6):769–776, 2014.

[301] Yi Liu, Jing Huang, and Hua Li. Synthesis of hydroxyapatite-reduced graphite oxide nanocomposites for biomedical applications: oriented nucleation and epitaxial growth of hydroxyapatite. *J. Mater. Chem. B*, 1:1826–1834, 2013.

[302] Hongyan Liu, Pinxian Xi, Guoqiang Xie, Yanjun Shi, Fengping Hou, Liang Huang, Fengjuan Chen, Zhengzhi Zeng, Changwei Shao, and Jun Wang. Simultaneous reduction and surface functionalization of graphene oxide for hydroxyapatite mineralization. *The Journal of Physical Chemistry C*, 116(5):3334–3341, 2012.

[303] Sungjin Kim, Sook Hee Ku, Seong Yoon Lim, Jae Hong Kim, and Chan Beum Park. Graphene–biomineral hybrid materials. *Advanced Materials*, 23(17):2009–2014, 2011.

[304] HaiBin Ma, WenXin Su, ZhiXin Tai, DongFei Sun, XingBin Yan, Bin Liu, and QunJi Xue. Preparation and cytocompatibility of polylactic acid/hydroxyapatite/graphene oxide nanocomposite fibrous membrane. *Chinese Science Bulletin*, 57(23):3051–3058, 2012.

[305] Yingjie Li, Liangzhu Feng, Xiaoze Shi, Xiaojing Wang, Yinlong Yang, Kai Yang, Teng Liu, Guangbao Yang, and Zhuang Liu. Surface coating-

dependent cytotoxicity and degradation of graphene derivatives: Towards the design of non-toxic, degradable nano-graphene. *Small*, 10(8):1544–1554, 2014.

[306] Yang Yang, Ying-Ming Zhang, Yong Chen, Di Zhao, Jia-Tong Chen, and Yu Liu. Construction of a Graphene Oxide Based Noncovalent Multiple Nanosupramolecular Assembly as a Scaffold for Drug Delivery. *Chemistry – A European Journal*, 18(14):4208–4215, April 2012.

[307] Dong Ma, Jiantao Lin, Yuyun Chen, Wei Xue, and Li-Ming Zhang. In situ gelation and sustained release of an antitumor drug by graphene oxide nanosheets. *Carbon*, 50(8):3001–3007, July 2012.

[308] Dennis E. J. G. J. Dolmans, Dai Fukumura, and Rakesh K. Jain. Photodynamic therapy for cancer. *Nature Reviews Cancer*, 3(5):380–387, May 2003.

[309] Jung Jun Bae, Jung Hyun Yoon, Sooyeon Jeong, Byoung Hee Moon, Joong Tark Han, Hee Jin Jeong, Geon-Woong Lee, Ha Ryong Hwang, Young Hee Lee, Seung Yol Jeong, and Seong Chu Lim. Sensitive photo-thermal response of graphene oxide for mid-infrared detection. *Nanoscale*, 7(38):15695–15700, 2015.

[310] Jilian R. Melamed, Rachel S. Edelstein, and Emily S. Day. Elucidating the Fundamental Mechanisms of Cell Death Triggered by Photothermal Therapy. *ACS Nano*, 9(1):6–11, January 2015.

[311] Marta Pérez-Hernández, Pablo del Pino, Scott G. Mitchell, María Moros, Grazyna Stepien, Beatriz Pelaz, Wolfgang J. Parak, Eva M. Gálvez, Julián Pardo, and Jesús M. de la Fuente. Dissecting the Molecular Mechanism of Apoptosis during Photothermal Therapy Using Gold Nanoprisms. *ACS Nano*, 9(1):52–61, January 2015.

[312] H.-U. Simon, A. Haj-Yehia, and F. Levi-Schaffer. Role of reactive oxygen species (ROS) in apoptosis induction. *Apoptosis*, 5(5):415–418, November 2000.

[313] Michael D. Jacobson. Reactive oxygen species and programmed cell death. *Trends in Biochemical Sciences*, 21(3):83–86, March 1996.

[314] Ho Sang Jung, Won Ho Kong, Dong Kyung Sung, Min-Young Lee, Song Eun Beack, Do Hee Keum, Ki Su Kim, Seok Hyun Yun, and Sei Kwang Hahn. Nanographene Oxide–Hyaluronic Acid Conjugate for Photothermal Ablation Therapy of Skin Cancer. *ACS Nano*, 8(1):260–268, January 2014.

[315] Kai Yang, Shuai Zhang, Guoxin Zhang, Xiaoming Sun, Shuit-Tong Lee, and Zhuang Liu. Graphene in Mice: Ultrahigh In Vivo Tumor Uptake and Efficient Photothermal Therapy. *Nano Letters*, 10(9):3318–3323, September 2010.

[316] Xinxing Ma, Huiquan Tao, Kai Yang, Liangzhu Feng, Liang Cheng, Xiaoze Shi, Yonggang Li, Liang Guo, and Zhuang Liu. A functionalized graphene oxide-iron oxide nanocomposite for magnetically targeted drug delivery, photothermal therapy, and magnetic resonance imaging. *Nano Research*, 5(3):199–212, March 2012.

[317] Wan Li, Jean K. Chung, Young Kwang Lee, and Jay T. Groves. Graphene-Templated Supported Lipid Bilayer Nanochannels. *Nano Letters*, 16(8):5022–5026, August 2016.

[318] Eun-Kyung Lim, Taekhoon Kim, Soonmyung Paik, Seungjoo Haam, Yong-Min Huh, and Kwangyeol Lee. Nanomaterials for theranostics: Recent advances and future challenges. *Chemical Reviews*, 115(1):327–394, 2015. PMID: 25423180.

[319] N. Vigneswaran, Fahmi Samsuri, Balu Ranganathan, and Padmapriya. Recent advances in nano patterning and nano imprint lithography for biological applications. *Procedia Engineering*, 97:1387 – 1398, 2014.

[320] Alexandros Besinis, Tracy De Peralta, Christopher J. Tredwin, and Richard D. Handy. Review of nanomaterials in dentistry: Interactions with the oral microenvironment, clinical applications, hazards, and benefits. *ACS Nano*, 9(3):2255–2289, 2015. PMID: 25625290.

[321] Wayne M. Moreau. *Semiconductor Lithography: Principles, Practices, and Materials*. Springer US, 1988.

[322] G.K. Bennig. Atomic force microscope and method for imaging surfaces with atomic resolution, February 9 1988. US Patent 4,724,318.

[323] G. Binnig, C. F. Quate, and Ch. Gerber. Atomic force microscope. *Phys. Rev. Lett.*, 56:930–933, Mar 1986.

[324] Ricardo Garcia, Armin W. Knoll, and Elisa Riedo. Advanced scanning probe lithography. *Nat Nano*, 9(8):577–587, August 2014.

[325] Byron D. Gates, Qiaobing Xu, Michael Stewart, Declan Ryan, C. Grant Willson, and George M. Whitesides. New approaches to nanofabrication: Molding, printing, and other techniques. *Chemical Reviews*, 105(4):1171–1196, 2005. PMID: 15826012.

[326] M Feldman. *Nanolithography: The Art of Fabricating Nanoelectronic and Nanophotonic Devices and Systems*. Woodhead Publishing, 1st edition, 2013.

[327] Christian Wagner and Noreen Harned. Euv lithography: Lithography gets extreme. *Nat Photon*, 4(1):24–26, January 2010.

[328] R. L. Seliger, J. W. Ward, V. Wang, and R. L. Kubena. A high intensity scanning ion probe with submicrometer spot size. *Applied Physics Letters*, 34(5):310–312, 1979.

[329] W H Escovitz, T R Fox, and R Levi-Setti. Scanning transmission ion microscope with a field ion source. *Proceedings of the National Academy of Sciences*, 72(5):1826–1828, 1975.

[330] J. H. Orloff and L. W. Swanson. Study of a field-ionization source for microprobe applications. *Journal of Vacuum Science and Technology*, 12(6):1209–1213, 1975.

[331] Kenji Gamo. Focused ion beam lithography. *Nuclear Instruments and Methods in Physics Research Section B: Beam Interactions with Materials and Atoms*, 65(1):40 – 49, 1992.

[332] G M Shedd and P Russell. The scanning tunneling microscope as a tool for nanofabrication. *Nanotechnology*, 1(1):67, 1990.

[333] M. F. Crommie, C. P. Lutz, and D. M. Eigler. Confinement of electrons to quantum corrals on a metal surface. *Science*, 262(5131):218–220, 1993.

[334] E. J. Heller, M. F. Crommie, C. P. Lutz, and D. M. Eigler. Scattering and absorption of surface electron waves in quantum corrals. *Nature*, 369(6480):464–466, June 1994.

[335] R. Guckenberger, C. Kösslinger, R. Gatz, H. Breu, N. Levai, and W. Baumeister. A scanning tunneling microscope (stm) for biological applications: design and performance. *Ultramicroscopy*, 25(2):111 – 121, 1988.

[336] Richard D. Piner, Jin Zhu, Feng Xu, Seunghun Hong, and Chad A. Mirkin. "dip-pen" nanolithography. *Science*, 283(5402):661–663, 1999.

[337] Kee Suk Ryu, Xuefeng Wang, Kashan Shaikh, David Bullen, Edgar Goluch, Jun Zou, Chang Liu, and Chad A. Mirkin. Integrated microfluidic linking chip for scanning probe nanolithography. *Applied Physics Letters*, 85(1):136–138, 2004.

[338] Seunghun Hong and Chad A. Mirkin. A nanoplotter with both parallel and serial writing capabilities. *Science*, 288(5472):1808–1811, 2000.

[339] Seunghun Hong, Jin Zhu, and Chad A. Mirkin. Multiple ink nanolithography: Toward a multiple-pen nano-plotter. *Science*, 286(5439):523–525, 1999.

[340] Gang-yu Liu and Song Xu. *Nanometer Scale Fabrication of Self-Assembled Monolayers: Nanoshaving and Nanografting*, chapter 15, pages 199–208. ACS, 1999.

[341] Jeremy R. Kenseth, Jennifer A. Harnisch, Vivian W. Jones, and Marc D. Porter. Investigation of approaches for the fabrication of protein patterns by scanning probe lithography. *Langmuir*, 17(13):4105–4112, 2001.

[342] Jianhua Gu, Chi Ming Yam, Sha Li, and Chengzhi Cai. Nanometric protein arrays on protein-resistant monolayers on silicon surfaces. *Journal of the American Chemical Society*, 126(26):8098–8099, 2004. PMID: 15225034.

[343] Guoting Qin, Jianhua Gu, Kai Liu, Zhongdang Xiao, Chi Ming Yam, and Chengzhi. Cai. Conductive afm patterning on oligo(ethylene glycol)-terminated alkyl monolayers on silicon substrates: Proposed mechanism and fabrication of avidin patterns. *Langmuir*, 27(11):6987–6994, 2011.

[344] Guo Ting Qin and Cheng Zhi. Cai. Oligo(ethylene glycol)-terminated monolayers on silicon surfaces and their nanopatterning with a con-

ductive atomic force microscope. *Science China: Chemistry*, 53(1):36–44, 2010.

[345] Pia Eduardo Antonio Della, Jeppe V. Holm, Noemie Lloret, Bon Christel Le, Jean-Luc Popot, Manuela Zoonens, Jesper Nygard, and Karen Laurence Martinez. A step closer to membrane protein multiplexed nanoarrays using biotin-doped polypyrrole. *ACS nano*, 8(2):1844–53, 2014.

[346] Zhikun Zheng, Menglong Yang, and Bailin. Zhang. Constructive nanolithography by chemically modified tips: Nanoelectrochemical patterning on sams/au. *Journal of Physical Chemistry C*, 114(45):19220–19226, 2010.

[347] Weifu Sun. Interaction forces between a spherical nanoparticle and a flat surface. *Phys. Chem. Chem. Phys.*, 16:5846–5854, 2014.

[348] J. Christopher Love, Lara A. Estroff, Jennah K. Kriebel, Ralph G. Nuzzo, and George M. Whitesides. Self-assembled monolayers of thiolates on metals as a form of nanotechnology. *Chemical Reviews*, 105(4):1103–1170, 2005. PMID: 15826011.

[349] Stoyan K. Smoukov, Sumit Gangwal, Manuel Marquez, and Orlin D. Velev. Reconfigurable responsive structures assembled from magnetic janus particles. *Soft Matter*, 5:1285–1292, 2009.

[350] Harold E Gaubert and Wolfgang Frey. Highly parallel fabrication of nanopatterned surfaces with nanoscale orthogonal biofunctionalization imprint lithography. *Nanotechnology*, 18(13):135101, 2007.

[351] Sang Ouk Kim, Harun H. Solak, Mark P. Stoykovich, Nicola J. Ferrier, Juan J. de Pablo, and Paul F. Nealey. Epitaxial self-assembly of block

copolymers on lithographically defined nanopatterned substrates. *Nature*, 424(6947):411–414, July 2003.

[352] Christopher M. Bates, Michael J. Maher, Dustin W. Janes, Christopher J. Ellison, and C. Grant Willson. Block copolymer lithography. *Macromolecules*, 47(1):2–12, 2014.

[353] Paschalis Alexandridis and Björn Lindman, editors. *Amphiphilic Block Copolymers: Self-Assembly and Applications*. Elsevier Science B.V., Amsterdam, 2000.

[354] Lifeng Zhang and Adi Eisenberg. Multiple morphologies of "crew-cut" aggregates of polystyrene-b-poly(acrylic acid) block copolymers. *Science*, 268(5218):1728–1731, 1995.

[355] Stephan Forster and Thomas Plantenberg. From self-organizing polymers to nanohybrid and biomaterials. *Angewandte Chemie (International ed. in English)*, 41:689–714, Mar 2002.

[356] Frank S. Bates and Glenn H. Fredrickson. Block copolymers–designer soft materials. *Physics Today*, 1999.

[357] Neil S Cameron, Muriel K Corbierre, and Adi Eisenberg. 1998 e.w.r. steacie award lecture asymmetric amphiphilic block copolymers in solution: a morphological wonderland. *Canadian Journal of Chemistry*, 77(8):1311–1326, 1999.

[358] Yiyong Mai and Adi Eisenberg. Self-assembly of block copolymers. *Chem. Soc. Rev.*, 41:5969–5985, 2012.

[359] Christophe Sinturel, Marylène Vayer, Michael Morris, and Marc A. Hillmyer. Solvent vapor annealing of block polymer thin films. *Macromolecules*, 46(14):5399–5415, 2013.

[360] Xiaodan Gu, Ilja Gunkel, and Thomas P. Russell. Pattern transfer using block copolymers. *Philosophical Transactions of the Royal Society of London A: Mathematical, Physical and Engineering Sciences*, 371(2000), 2013.

[361] S. H. Kim, M. J. Misner, T. Xu, M. Kimura, and T. P. Russell. Highly oriented and ordered arrays from block copolymers via solvent evaporation. *Advanced Materials*, 16(3):226–231, 2004.

[362] Jonathan W. Choi, Myungwoong Kim, Nathaniel S. Safron, Michael S. Arnold, and Padma Gopalan. Transfer of pre-assembled block copolymer thin film to nanopattern unconventional substrates. *ACS Applied Materials & Interfaces*, 6(12):9442–9448, 2014. PMID: 24869477.

[363] Lifeng Zhang and Adi Eisenberg. Formation of crew-cut aggregates of various morphologies from amphiphilic block copolymers in solution. *Polymers for Advanced Technologies*, October 1998.

[364] Sumeet Jain and Frank S. Bates. On the origins of morphological complexity in block copolymer surfactants. *Science*, 300(5618):460–464, 2003.

[365] Dennis E. Discher and Fariyal Ahmed. Polymersomes. *Annual Review of Biomedical Engineering*, 8(1):323–341, 2006. PMID: 16834559.

[366] Giuseppe Battaglia and Anthony J. Ryan. Effect of amphiphile size on the transformation from a lyotropic gel to a vesicular dispersion. *Macromolecules*, 39(2):798–805, 2006.

[367] Hua Chen and Jun Li. *Nanotechnology*, pages 411–436. Humana Press, Totowa, NJ, 2007.

[368] J F Mooney, A J Hunt, J R McIntosh, C A Liberko, D M Walba, and C T Rogers. Patterning of functional antibodies and other proteins

by photolithography of silane monolayers. *Proceedings of the National Academy of Sciences*, 93(22):12287–12291, 1996.

[369] Kook-Nyung Lee, Dong-Sik Shin, Yoon-Sik Lee, and Yong-Kweon Kim. Protein patterning by virtual mask photolithography using a micromirror array. *Journal of Micromechanics and Microengineering*, 13(1):18, 2003.

[370] Ji Youn Lee and Alexander Revzin. *Merging Photolithography and Robotic Protein Printing to Create Cellular Microarrays*, pages 195–206. Humana Press, Totowa, NJ, 2011.

[371] Eliedonna E. Cacao, Azeem Nasrullah, Tim Sherlock, Steven Kemper, Katerina Kourentzi, Paul Ruchhoeft, Gila E. Stein, and Richard C. Willson. High-resolution, high-throughput, positive-tone patterning of poly(ethylene glycol) by helium beam exposure through stencil masks. *PLOS ONE*, 8(5):1–8, 05 2013.

[372] M. Holgado, C.A. Barrios, F.J. Ortega, F.J. Sanza, R. Casquel, M.F. Laguna, M.J. Ba nuls, D. López-Romero, R. Puchades, and A. Maquieira. Label-free biosensing by means of periodic lattices of high aspect ratio su-8 nano-pillars. *Biosensors and Bioelectronics*, 25(12):2553 – 2558, 2010.

[373] F.J. Sanza, M. Holgado, F.J. Ortega, R. Casquel, D. López-Romero, M.J. Ba nuls, M.F. Laguna, C.A. Barrios, R. Puchades, and A. Maquieira. Bio-photonic sensing cells over transparent substrates for anti-gestrinone antibodies biosensing. *Biosensors and Bioelectronics*, 26(12):4842 – 4847, 2011.

[374] C. K. Harnett, K. M. Satyalakshmi, and H. G. Craighead. Bioactive templates fabricated by low-energy electron beam lithography of self-assembled monolayers. *Langmuir*, 17(1):178–182, 2001.

[375] Jonas Rundqvist, Beatriz Mendoza, Jeffrey L. Werbin, William F. Heinz, Christopher Lemmon, Lewis H. Romer, David B. Haviland, and Jan H. Hoh. High fidelity functional patterns of an extracellular matrix protein by electron beam-based inactivation. *Journal of the American Chemical Society*, 129(1):59–67, 2007. PMID: 17199283.

[376] Ye Hong, Peter Krsko, and Matthew Libera. Protein surface patterning using nanoscale peg hydrogels. *Langmuir*, 20(25):11123–11126, 2004. PMID: 15568866.

[377] Karen L. Christman, Eric Schopf, Rebecca M. Broyer, Ronald C. Li, Yong Chen, and Heather D. Maynard. Positioning multiple proteins at the nanoscale with electron beam cross-linked functional polymers. *Journal of the American Chemical Society*, 131(2):521–527, 2009. PMID: 19160460.

[378] Peter Krsko, Thomas E. McCann, Thu-Trang Thach, Tracy L. Laabs, Herbert M. Geller, and Matthew R. Libera. Length-scale mediated adhesion and directed growth of neural cells by surface-patterned poly(ethylene glycol) hydrogels. *Biomaterials*, 30(5):721 – 729, 2009.

[379] Christopher M. Kolodziej and Heather D. Maynard. Electron-beam lithography for patterning biomolecules at the micron and nanometer scale. *Chemistry of Materials*, 24(5):774–780, 2012.

[380] H K Edwards, S C Coe, M W Fay, C A Scotchford, D M Grant, and P D Brown. Site-specific, cross-sectional imaging of biomaterials and the cell/biomaterial interface using focused ion beam/scanning electron microscopy. *Journal of Physics: Conference Series*, 126(1):012097, 2008.

[381] Kathryn Grandfield and Håkan Engqvist. Focused ion beam in the study of biomaterials and biological matter. *Advances in Materials Science and Engineering*, 2012:6, 2012.

[382] R. A. Vega, D. Maspoch, K. Salaita, and C. A. Mirkin. Nanoarrays of single virus particles. *Angew. Chem. Int. Edn*, 44:6013–6015, 2005.

[383] S. Lenhert, P. Sun, Y. Wang, C. A. Mirkin, and H. Fuchs. Massively parallel dip-pen nanolithography of heterogeneous supported phospholipid multilayer patterns. *Small*, 3:71–75, 2007.

[384] K. Salaita. Massively parallel dip-pen nanolithography with 55,000-pen two-dimensional arrays. *Angew. Chem. Int. Edn*, 45, 2006.

[385] Sean R. Coyer, Andrés J. García, and Emmanuel Delamarche. Facile preparation of complex protein architectures with sub-100-nm resolution on surfaces. *Angewandte Chemie International Edition*, 46(36):6837–6840, 2007.

[386] Paula M. Mendes, Chun L. Yeung, and Jon A. Preece. Bio-nanopatterning of surfaces. *Nanoscale Research Letters*, 2(8):373, 2007.

[387] Van N. Truskett and Michael P.C. Watts. Trends in imprint lithography for biological applications. *Trends in Biotechnology*, 24(7):312 – 317, 2006.

[388] Ray C. Schmidt and Kevin E. Healy. Controlling biological interfaces on the nanometer length scale. *Journal of Biomedical Materials Research Part A*, 90A(4):1252–1261, 2009.

[389] Tamar Shahal, Benjamin Geiger, Iain Dunlop, and Joachim Spatz. Regulation of integrin adhesions by varying the density of substrate-bound epidermal growth factor. *Biointerphases*, 7:1–11, 2012. 10.1007/s13758-012-0023-0.

[390] Judith Guasch, Jennifer Diemer, Hossein Riahinezhad, Stefanie Neubauer, Horst Kessler, and Joachim P. Spatz. Synthesis of binary

nanopatterns on hydrogels for initiating cellular responses. *Chemistry of Materials*, 28(6):1806–1815, 2016.

[391] Sarah Jahn, Sebastian J. Lechner, Helene Freichels, Martin Möller, and Joachim P. Spatz. Precise auxpt1-x alloy nanoparticle array of tunable composition for catalytic applications. *Scientific Reports*, 6:20536, February 2016.

[392] Alexandra M. Greiner, Adria Sales, Hao Chen, Sarah A. Biela, Dieter Kaufmann, and Ralf Kemkemer. Nano- and microstructured materials for in vitro studies of the physiology of vascular cells. *Beilstein Journal of Nanotechnology*, 7:1620–1641, 2016.

[393] G. B. Airy. On the Diffraction of an Object-glass with Circular Aperture. *Transactions of the Cambridge Philosophical Society*, 5:283, 1835.

[394] Ernst Abbe. Beiträge zur Theorie des Mikroskops und der mikroskopischen Wahrnehmung. *Universitätsbibliothek Johann Christian Senckenberg*, 1873.

[395] Joseph von Gerlach. *Mikroskopische Studien aus dem Gebeite der menschlichen Morphologie*. Ferdinand Enke, Erlangen, 1858.

[396] P Mayer. Ueber das farben mit hamatoxylin. *Mitt Zool Stat Neapel*, 10:170–186, 1891.

[397] G Giemsa. Eine vereinfachung und vervollkommnung meiner methylenblau-eosin-farbemethode zur erzielung der romanowsky-nocht'schen chromatinfa rbung. *Centralblatt fur Bakteriologie*, 32:307–313, 1904.

[398] R Feulgen and H Rossenbeck. Mikroskopisch-chemischer nachweis einer nucleisäure vom typus der thymonucleinsäure und die da-

rauf beruhende elektive färbung von zellkernen in mikroskopischen präparaten. *Hoppe Seyler Z Physiol Chem*, 135:203–248, 1924.

[399] F. Das Zernike. Phasenkontrastverfahren bei der mikroskopischen beobachtung. *Z. technische Physik*, 16:454—-457, 1935.

[400] W. J. Schmidt. Doppelbrechung der kernspindel und zugfasertheorie der chromosomenbewegung. *Chromosoma 1*, pages 253—-264, 1939.

[401] A. G. E. Pearse. History of staining (third edition). *The Journal of Pathology*, 143(2):139–139, June 1984.

[402] O. Heimstädt. Das fluoreszenzmikroskop. *Z. Wiss. Mikrosk.*, 28:330—-337, 1911.

[403] P Ellinger and A Hirt. Mikroskopische beobachtungen an lebenden organen mit demonstrationen (intravitalmikroskopie). *Arch. Exp. Pathol. Phar.*, 147:63, 1929.

[404] A. H. Coons, H. J. Creech, and R. N. Jones. Immunological properties of an antibody containing a fluorescent group. *Proc. Soc. Expt. Biol. Med.*, 47:200–202, 1941.

[405] A. H. Coons, H. J. Creech, R. N. Jones, and E. Berliner. The Demonstration of Pneumococcal Antigen in Tissues by the Use of Fluorescent Antibody. *The Journal of Immunology*, 45(3):159–170, November 1942.

[406] J. S. Ploem. Die möglichkeit der auflichtfluoreszenzmethoden bei untersuchungen von zellen in durchströmungskammern und leightonröhren. *Acta Histochem*, 7:339–343, 1965.

[407] M. Minsky. Microscopy apparatus, December 19 1961. US Patent 3,013,467.

[408] M. David Egger and Mojmir Petran. New Reflected-Light Microscope for Viewing Unstained Brain and Ganglion Cells. *Science*, 157(3786):305–307, July 1967.

[409] J. G. White, W. B. Amos, and M. Fordham. An evaluation of confocal versus conventional imaging of biological structures by fluorescence light microscopy. *The Journal of Cell Biology*, 105(1):41–48, July 1987.

[410] D. Axelrod. Cell-substrate contacts illuminated by total internal reflection fluorescence. *The Journal of Cell Biology*, 89(1):141–145, April 1981.

[411] Takashi Funatsu, Yoshie Harada, Makio Tokunaga, Kiwamu Saito, and Toshio Yanagida. Imaging of single fluorescent molecules and individual ATP turnovers by single myosin molecules in aqueous solution. *Nature*, 374(6522):555–559, April 1995.

[412] Stefan W. Hell and Jan Wichmann. Breaking the diffraction resolution limit by stimulated emission: stimulated-emission-depletion fluorescence microscopy. *Optics Letters*, 19(11):780–782, June 1994.

[413] Mats G. L. Gustafsson. Nonlinear structured-illumination microscopy: Wide-field fluorescence imaging with theoretically unlimited resolution. *Proceedings of the National Academy of Sciences of the United States of America*, 102(37):13081–13086, September 2005.

[414] Michael J. Rust, Mark Bates, and Xiaowei Zhuang. Sub-diffraction-limit imaging by stochastic optical reconstruction microscopy (STORM). *Nature Methods*, 3(10):793–796, October 2006.

[415] Javad N. Farahani, Matthew J. Schibler, and Laurent A. Bentolila. *Stimulated Emission Depletion (STED) Microscopy: from Theory to Practice*.

[416] Manish Saxena, Gangadhar Eluru, and Sai Siva Gorthi. Structured illumination microscopy. *Adv. Opt. Photon.*, 7(2):241–275, Jun 2015.

[417] Markus Sauer and Mike Heilemann. Single-molecule localization microscopy in eukaryotes. *Chemical Reviews*, 117(11):7478–7509, 2017. PMID: 28287710.

[418] Graham T. Dempsey, Joshua C. Vaughan, Kok Hao Chen, Mark Bates, and Xiaowei Zhuang. Evaluation of fluorophores for optimal performance in localization-based super-resolution imaging. *Nature Methods*, 8(12):1027–1036, December 2011.

[419] Jennifer Lippincott-Schwartz and George H. Patterson. Photoactivatable fluorescent proteins for diffraction-limited and super-resolution imaging. *Trends in Cell Biology*, 19(11):555–565, November 2009.

[420] Justin Demmerle, Eva Wegel, Lothar Schermelleh, and Ian M. Dobbie. Assessing resolution in super-resolution imaging. *Methods*, 88:3 – 10, 2015. Super-resolution Light Microscopy.

[421] Hari Shroff, Catherine G. Galbraith, James A. Galbraith, Helen White, Jennifer Gillette, Scott Olenych, Michael W. Davidson, and Eric Betzig. Dual-color superresolution imaging of genetically expressed probes within individual adhesion complexes. *Proceedings of the National Academy of Sciences*, 104(51):20308–20313, December 2007.

[422] Adish Dani, Bo Huang, Joseph Bergan, Catherine Dulac, and Xiaowei Zhuang. Superresolution Imaging of Chemical Synapses in the Brain. *Neuron*, 68(5):843–856, December 2010.

[423] Sang-Hee Shim, Chenglong Xia, Guisheng Zhong, Hazen P. Babcock, Joshua C. Vaughan, Bo Huang, Xun Wang, Cheng Xu, Guo-Qiang Bi,

and Xiaowei Zhuang. Super-resolution fluorescence imaging of organelles in live cells with photoswitchable membrane probes. *Proceedings of the National Academy of Sciences*, 109(35):13978–13983, August 2012.

[424] Jennifer Lippincott-Schwartz and Suliana Manley. Putting super-resolution fluorescence microscopy to work. *Nature Methods*, 6(1):21–23, January 2009.

[425] Chaitanya K. Ullal, Roman Schmidt, Stefan W. Hell, and Alexander Egner. Block Copolymer Nanostructures Mapped by Far-Field Optics. *Nano Letters*, 9(6):2497–2500, June 2009.

[426] Jason J. Han, Andrew P. Shreve, and James H. Werner. Super-Resolution Optical Microscopy. In *Characterization of Materials*. John Wiley & Sons, Inc., 2002. DOI: 10.1002/0471266965.com128.

[427] Theobald Lohmüller, Sara Triffo, Geoff P. O'Donoghue, Qian Xu, Michael P. Coyle, and Jay T. Groves. Supported Membranes Embedded with Fixed Arrays of Gold Nanoparticles. *Nano Letters*, 11(11):4912–4918, November 2011.

[428] Zunfeng Liu, Linhua Jiang, Federica Galli, Igor Nederlof, René C. L. Olsthoorn, Gerda E. M. Lamers, Tjerk. H. Oosterkamp, and Jan Pieter Abrahams. A graphene oxidestreptavidin complex for biorecognition – towards affinity purification. *Advanced Functional Materials*, 20(17):2857–2865, 2010.

[429] Christa M. Stoscheck and Murray P. Deutscher. *Quantitation of protein*, volume Volume 182, pages 50–68. Academic Press, 1990.

[430] Yih Horng Tan, Maozi Liu, Birte Nolting, Joan G. Go, Jacquelyn Gervay-Hague, and Gang-yu Liu. A nanoengineering approach for

investigation and regulation of protein immobilization. *ACS Nano*, 2(11):2374–2384, 2008.

[431] Calum S Neish, Ian L Martin, Robert M Henderson, and J Michael Edwardson. Direct visualization of ligand-protein interactions using atomic force microscopy. *British Journal of Pharmacology*, 135(8):1943–1950, 2002.

[432] Yong Chen, Jiye Cai, Qingcai Xu, and Zheng W. Chen. Atomic force bio-analytics of polymerization and aggregation of phycoerythrin-conjugated immunoglobulin g molecules. *Molecular Immunology*, 41(12):1247–1252, 11 2004.

[433] Nana Luo, Jeffrey K. Weber, Shuang Wang, Binquan Luan, Hua Yue, Xiaobo Xi, Jing Du, Zaixing Yang, Wei Wei, Ruhong Zhou, and Guanghui Ma. Pegylated graphene oxide elicits strong immunological responses despite surface passivation. 8:14537, February 2017.

[434] Galit Alter, Jessica M. Malenfant, and Marcus Altfeld. Cd107a as a functional marker for the identification of natural killer cell activity. *Journal of Immunological Methods*, 294(1–2):15–22, 11 2004.

[435] Kate Schroder, Paul J. Hertzog, Timothy Ravasi, and David A. Hume. Interferon-: an overview of signals, mechanisms and functions. *Journal of Leukocyte Biology*, 75(2):163–189, 2004.

[436] A Snijders, P Kalinski, C M Hilkens, and M L Kapsenberg. High-level il-12 production by human dendritic cells requires two signals. *International Immunology*, 10(11):1593–1598, 1998.

[437] Guido Valente, Laurence Ozmen, Francesco Novelli, Massimo Geuna, Giorgio Palestro, Guido Forni, and Gianni Garotta. Distribution of

interferon- receptor in human tissues. *European Journal of Immunology*, 22(9):2403–2412, 1992.

[438] Nicole A de Weerd and Thao Nguyen. The interferons and their receptors[mdash]distribution and regulation. *Immunol Cell Biol*, 90(5):483–491, 05 2012.

[439] Carlos Tassa, Jay L. Duffner, Timothy A. Lewis, Ralph Weissleder, Stuart L. Schreiber, Angela N. Koehler, and Stanley Y. Shaw. Binding affinity and kinetic analysis of targeted small molecule-modified nanoparticles. *Bioconjugate Chemistry*, 21(1):14–19, 01 2010.

[440] Mauro Acchione, Hyewon Kwon, Claudia M. Jochheim, and William M. Atkins. Impact of linker and conjugation chemistry on antigen binding, fc receptor binding and thermal stability of model antibody-drug conjugates. *mAbs*, 4(3):362–372, 2012. PMID: 22531451.

[441] JH Gong, G Maki, and HG Klingemann. Characterization of a human cell line (nk-92) with phenotypical and functional characteristics of activated natural killer cells. *Leukemia*, 8(4):652—658, April 1994.

[442] Borrego, Robertson, Ritz, Pena, and Solana. Cd69 is a stimulatory receptor for natural killer cell and its cytotoxic effect is blocked by cd94 inhibitory receptor. *Immunology*, 97(1):159–165, 1999.

[443] S H Chan, B Perussia, J W Gupta, M Kobayashi, M Pospísil, H A Young, S F Wolf, D Young, S C Clark, and G Trinchieri. Induction of interferon gamma production by natural killer cell stimulatory factor: characterization of the responder cells and synergy with other inducers. *Journal of Experimental Medicine*, 173(4):869–879, 1991.

[444] Leslie A. Fogel, Michel M. Sun, Theresa L. Geurs, Leonidas N. Carayannopoulos, and Anthony R. French. Markers of nonselective

and specific nk cell activation. *The Journal of Immunology*, 190(12):6269–6276, 2013.

[445] Hortensia de la Fuente, Aranzazu Cruz-Adalia, Gloria Martinez del Hoyo, Danay Cibrián-Vera, Pedro Bonay, Daniel Pérez-Hernández, Jesús Vázquez, Pilar Navarro, Ricardo Gutierrez-Gallego, Marta Ramirez-Huesca, Pilar Martín, and Francisco Sánchez-Madrid. The leukocyte activation receptor cd69 controls t cell differentiation through its interaction with galectin-1. *Molecular and Cellular Biology*, 34(13):2479–2487, 2014.

[446] L L Lanier, D W Buck, L Rhodes, A Ding, E Evans, C Barney, and J H Phillips. Interleukin 2 activation of natural killer cells rapidly induces the expression and phosphorylation of the leu-23 activation antigen. *Journal of Experimental Medicine*, 167(5):1572–1585, 1988.

[447] Francisco Borrego, José Peña, and Rafael Solana. Regulation of cd69 expression on human natural killer cells: differential involvement of protein kinase c and protein tyrosine kinases. *European Journal of Immunology*, 23(5):1039–1043, 1993.

[448] Steven F. Ziegler, Fred Ramsdell, Kathryn A. Hjerrild, Richard J. Armitage, Kenneth H. Grabstein, Kathryn B. Hennen, Terry Farrah, William C. Fanslow, Ethan M. Shevach, and Mark R. Alderson. Molecular characterization of the early activation antigen cd69: A type ii membrane glycoprotein related to a family of natural killer cell activation antigens. *European Journal of Immunology*, 23(7):1643–1648, 1993.

[449] M Fukuda. Lysosomal membrane glycoproteins. structure, biosynthesis, and intracellular trafficking. *Journal of Biological Chemistry*, 266(32):21327–21330, 1991.

[450] Bryan G. Winchester. Lysosomal membrane proteins. *European Journal of Paediatric Neurology*, 5:11 – 19, 2001.

[451] Jamie R. Schoenborn and Christopher B. Wilson. Regulation of interferon-gamma during innate and adaptive immune responses. *Advances in immunology*, 96:41–101, 2007.

[452] A Nagler, L L Lanier, S Cwirla, and J H Phillips. Comparative studies of human fcriii-positive and negative natural killer cells. *The Journal of Immunology*, 143(10):3183–3191, 1989.

[453] Todd A. Fehniger, Megan A. Cooper, Gerard J. Nuovo, Marina Cella, Fabio Facchetti, Marco Colonna, and Michael A. Caligiuri. Cd56bright natural killer cells are present in human lymph nodes and are activated by t cell–derived il-2: a potential new link between adaptive and innate immunity. *Blood*, 101(8):3052–3057, 2003.

[454] Todd A. Fehniger, Eric M. Bluman, Michelle M. Porter, Ewa Mrózek, Megan A. Cooper, Jeffrey B. VanDeusen, Stanley R. Frankel, Wendy Stock, and Michael A. Caligiuri. Potential mechanisms of human natural killer cell expansion in vivo during low-dose il-2 therapy. *The Journal of Clinical Investigation*, 106(1):117–124, 1 2000.

[455] Bruno Vanherberghen, Per E. Olofsson, Elin Forslund, Michal Sternberg-Simon, Mohammad Ali Khorshidi, Simon Pacouret, Karolin Guldevall, Monika Enqvist, Karl-Johan Malmberg, Ramit Mehr, and Björn Önfelt. Classification of human natural killer cells based on migration behavior and cytotoxic response. *Blood*, 121(8):1326–1334, 2013.

[456] Li Du, Shaoling Wu, Yanhui Li, Xindong Zhao, Xiaoyan Ju, and Yuzhen Wang. Cytotoxicity of pegylated graphene oxide on lymphoma cells. *Bio-medical materials and engineering*, 24:2135–41, 2014.

[457] S Syama, C P Aby, Toru Maekawa, D Sakthikumar, and P V Mohanan. Nano-bio compatibility of pegylated reduced graphene oxide on mesenchymal stem cells. *2D Materials*, 4(2):025066, 2017.

[458] Yan Bao, Xingguang Liu, Chaofeng Han, Sheng Xu, Bin Xie, Qian Zhang, Yan Gu, Jin Hou, Li Qian, Cheng Qian, Huanxing Han, and Xuetao Cao. Identification of ifn-[gamma]-producing innate b cells. *Cell Res*, 24(2):161–176, 02 2014.

[459] A. Dinter and E. G. Berger. Golgi-disturbing agents. *Histochemistry and cell biology*, 109:571–90, May-Jun 1998.

[460] Hilton H. Mollenhauer, D. James Morré, and Loyd D. Rowe. Alteration of intracellular traffic by monensin; mechanism, specificity and relationship to toxicity. *Biochimica et Biophysica Acta (BBA) - Reviews on Biomembranes*, 1031(2):225 – 246, 1990.

[461] Laurie Lamoreaux, Mario Roederer, and Richard Koup. Intracellular cytokine optimization and standard operating procedure. *Nat. Protocols*, 1(3):1507–1516, 10 2006.

[462] Nancy J. O'Neil-Andersen and David A. Lawrence. Differential modulation of surface and intracellular protein expression by t cells after stimulation in the presence of monensin or brefeldin a. *Clinical and Diagnostic Laboratory Immunology*, 9(2):243–250, 03 2002.

[463] Dongfang Liu, Liang Xu, Fan Yang, Dongdong Li, Feili Gong, and Tao Xu. Rapid biogenesis and sensitization of secretory lysosomes in nk cells mediated by target-cell recognition. *Proceedings of the National Academy of Sciences of the United States of America*, 102(1):123–127, 01 2005.

[464] Deborah L. Hodge, Alfredo Martinez, John G. Julias, Lynn S. Taylor, and Howard A. Young. Regulation of nuclear gamma interferon gene expression by interleukin 12 (il-12) and il-2 represents a novel form of posttranscriptional control. *Molecular and Cellular Biology*, 22(6):1742–1753, 03 2002.

[465] Ruipeng Wang, Jessica J. Jaw, Nicole C. Stutzman, Zhongcheng Zou, and Peter D. Sun. Natural killer cell-produced ifn- and tnf- induce target cell cytolysis through up-regulation of icam-1. *Journal of Leukocyte Biology*, 91(2):299–309, 2012.

[466] Kerstin Juelke, Monica Killig, Merlin Luetke-Eversloh, Eliana Parente, Joachim Gruen, Barbara Morandi, Guido Ferlazzo, Andreas Thiel, Isabela Schmitt-Knosalla, and Chiara Romagnani. Cd62l expression identifies a unique subset of polyfunctional cd56dim nk cells. *Blood*, 116(8):1299–1307, 2010.

[467] C. Une, J. Andersson, M-L. Eloranta, D. Sunnemark, R. A. Harris, and A. Örn. Enhancement of natural killer (nk) cell cytotoxicity and induction of nk cell-derived interferon-gamma (ifn-γ) display different kinetics during experimental infection with trypanosoma cruzi. *Clinical & Experimental Immunology*, 121(3):499–505, 2000.

[468] Emily L. Ho, Leonidas N. Carayannopoulos, Jennifer Poursine-Laurent, Jeremy Kinder, Beatrice Plougastel, Hamish R. C. Smith, and Wayne M. Yokoyama. Costimulation of multiple nk cell activation receptors by nkg2d. *The Journal of Immunology*, 169(7):3667–3675, 2002.

[469] Yenan T. Bryceson, Michael E. March, Domingo F. Barber, Hans-Gustaf Ljunggren, and Eric O. Long. Cytolytic granule polarization and degranulation controlled by different receptors in resting nk cells. *The Journal of Cell Biology*, 171(1):i1–i1, 2005.

[470] Jennifer R Cochran, Thomas O Cameron, and Lawrence J Stern. The relationship of mhc-peptide binding and t cell activation probed using chemically defined mhc class ii oligomers. *Immunity*, 12(3):241 – 250, 2000.

[471] Caroline A. Schneider, Wayne S. Rasband, and Kevin W. Eliceiri. Nih image to imagej: 25 years of image analysis. *Nature Methods*, 9:671, June 2012.

[472] Johannes Schindelin, Ignacio Arganda-Carreras, Erwin Frise, Verena Kaynig, Mark Longair, Tobias Pietzsch, Stephan Preibisch, Curtis Rueden, Stephan Saalfeld, Benjamin Schmid, Jean-Yves Tinevez, Daniel James White, Volker Hartenstein, Kevin Eliceiri, Pavel Tomancak, and Albert Cardona. Fiji: an open-source platform for biological-image analysis. *Nature Methods*, 9:676, June 2012.

[473] Martin Ovesný, Pavel Křížek, Josef Borkovec, Zdeněk Švindrych, and Guy M. Hagen. Thunderstorm: a comprehensive imagej plug-in for palm and storm data analysis and super-resolution imaging. *Bioinformatics*, 30(16):2389, 2014.

[474] Evangelina Pensa, Emiliano Cortés, Gastón Corthey, Pilar Carro, Carolina Vericat, Mariano H. Fonticelli, Guillermo Benítez, Aldo A. Rubert, and Roberto C. Salvarezza. The chemistry of the sulfur–gold interface: In search of a unified model. *Accounts of Chemical Research*, 45(8):1183–1192, 2012. PMID: 22444437.

[475] Hannu Hakkinen. The gold-sulfur interface at the nanoscale. *Nat Chem*, 4(6):443–455, June 2012.

[476] Che-Ming Jack Hu, Sharmeela Kaushal, Hop S. Tran Cao, Santosh Aryal, Marta Sartor, Sadik Esener, Michael Bouvet, and Liangfang

Zhang. Half-antibody functionalized lipidpolymer hybrid nanoparticles for targeted drug delivery to carcinoembryonic antigen presenting pancreatic cancer cells. *Molecular Pharmaceutics*, 7(3):914–920, 2010. PMID: 20394436.

[477] Linda C. Knight, Jan E. Romano, Barbara Krynska, Scott Faro, Feroze B. Mohamed, and Jennifer Gordon. Binding and internalization of iron oxide nanoparticles targeted to nuclear oncoprotein. *Journal of Molecular Biomarkers & Diagnosis*, 1(1):2–6, November 2010.

[478] Julija Baniukevic, Justina Kirlyte, Arunas Ramanavicius, and Almira Ramanaviciene. Application of oriented and random antibody immobilization methods in immunosensor design. *Sensors and Actuators B: Chemical*, 189:217 – 223, 2013. Selected Papers from the 26th European Conference on Solid-State Transducers.

[479] Sean Lowe, Neil M. O'Brien-Simpson, and Luke A. Connal. Antibiofouling polymer interfaces: poly(ethylene glycol) and other promising candidates. *Polym. Chem.*, 6:198–212, 2015.

[480] Gregory L. Kenausis, Janos Vörös, Donald L. Elbert, Ningping Huang, Rolf Hofer, Laurence Ruiz-Taylor, Marcus Textor, Jeffrey A. Hubbell, and Nicholas D. Spencer. Poly(l-lysine)-g-poly(ethylene glycol) layers on metal oxide surfaces: attachment mechanism and effects of polymer architecture on resistance to protein adsorption. *The Journal of Physical Chemistry B*, 104(14):3298–3309, 2000.

[481] Sina Saxer, Cyril Portmann, Samuele Tosatti, Karl Gademann, Stefan Zürcher, and Marcus Textor. Surface assembly of catechol-functionalized poly(l-lysine)-graft-poly(ethylene glycol) copolymer on titanium exploiting combined electrostatically driven self-organization

and biomimetic strong adhesion. *Macromolecules*, 43(2):1050–1060, 2010.

[482] Laszlo Barna, Barna Dudok, Vivien Miczan, Andras Horvath, Zsofia I. Laszlo, and Istvan Katona. Correlated confocal and super-resolution imaging by vividstorm. *Nat. Protocols*, 11(1):163–183, January 2016.

[483] Bassam Hajj, Jan Wisniewski, Mohamed El Beheiry, Jiji Chen, Andrey Revyakin, Carl Wu, and Maxime Dahan. Whole-cell, multicolor super-resolution imaging using volumetric multifocus microscopy. *Proceedings of the National Academy of Sciences*, 111(49):17480–17485, 2014.

[484] David W. Scott. *Averaged Shifted Histograms*, pages 125–136. John Wiley & Sons, Inc, 2015.

[485] David W. Scott. Averaged shifted histograms: Effective nonparametric density estimators in several dimensions. *The Annals of Statistics*, 13(3):1024–1040, 1985.

[486] Natalia Ziebacz, Stefan A. Wieczorek, Tomasz Kalwarczyk, Marcin Fialkowski, and Robert Holyst. Crossover regime for the diffusion of nanoparticles in polyethylene glycol solutions: influence of the depletion layer. *Soft Matter*, 7:7181–7186, 2011.

[487] Paula Malo de Molina, Sahger Lad, and Matthew E. Helgeson. Heterogeneity and its influence on the properties of difunctional poly(ethylene glycol) hydrogels: Structure and mechanics. *Macromolecules*, 48(15):5402–5411, 2015.

[488] J. K. Armstrong, R. B. Wenby, H. J. Meiselman, and T. C. Fisher. The hydrodynamic radii of macromolecules and their effect on red blood cell aggregation. *Biophysical Journal*, 87(6):4259–4270, 2004.

[489] Cornelius Cilliers, Ian Nessler, Nikolas Christodolu, and Greg M. Thurber. Tracking antibody distribution with near-infrared fluorescent dyes: Impact of dye structure and degree of labeling on plasma clearance. *Molecular Pharmaceutics*, 14(5):1623–1633, 2017. PMID: 28294622.

[490] Michael T. Kim, Yan Chen, Joseph Marhoul, and Fred Jacobson. Statistical modeling of the drug load distribution on trastuzumab emtansine (kadcyla), a lysine-linked antibody drug conjugate. *Bioconjugate Chemistry*, 25(7):1223–1232, 2014. PMID: 24873191.

[491] Victor S. Goldmacher, Godfrey Amphlett, Lintao Wang, and Alexandru C. Lazar. Statistics of the distribution of the abundance of molecules with various drug loads in maytansinoid antibody–drug conjugates. *Molecular Pharmaceutics*, 12(6):1738–1744, 2015. PMID: 25635630.

[492] Sergiy Mayilo, Meike A. Kloster, Michael Wunderlich, Andrey Lutich, Thomas A. Klar, Alfons Nichtl, Konrad Kürzinger, Fernando D. Stefani, and Jochen Feldmann. Long-range fluorescence quenching by gold nanoparticles in a sandwich immunoassay for cardiac troponin t. *Nano Letters*, 9(12):4558–4563, 2009. PMID: 19921780.

[493] Lisa Maus, Joachim P. Spatz, and Roberto Fiammengo. Quantification and reactivity of functional groups in the ligand shell of pegylated gold nanoparticles via a fluorescence-based assay. *Langmuir*, 25(14):7910–7917, 2009. PMID: 19419188.

[494] Guillermo P. Acuna, Martina Bucher, Ingo H. Stein, Christian Steinhauer, Anton Kuzyk, Phil Holzmeister, Robert Schreiber, Alexander Moroz, Fernando D. Stefani, Tim Liedl, Friedrich C. Simmel, and Philip Tinnefeld. Distance dependence of single-fluorophore

quenching by gold nanoparticles studied on dna origami. *ACS Nano*, 6(4):3189–3195, 2012. PMID: 22439823.

[495] Alex Small and Shane Stahlheber. Fluorophore localization algorithms for super-resolution microscopy. *Nat Meth*, 11(3):267–279, March 2014.

[496] Pavel Křížek, Ivan Raška, and Guy M. Hagen. Minimizing detection errors in single molecule localization microscopy. *Opt. Express*, 19(4):3226–3235, Feb 2011.

[497] Carla Coltharp, Xinxing Yang, and Jie Xiao. Quantitative analysis of single-molecule superresolution images. *Current Opinion in Structural Biology*, 28:112 – 121, 2014.

[498] P. J Diggle. *Statistical Analysis of Spatial and Spatio-Temporal Point Patterns*. Chapman and Hall/CRC, 2013.

[499] B. D. Ripley. Modelling spatial patterns. *Journal of the Royal Statistical Society. Series B (Methodological)*, 39(2):172–212, 1977.

[500] Dylan M. Owen, Carles Rentero, Jérémie Rossy, Astrid Magenau, David Williamson, Macarena Rodriguez, and Katharina Gaus. Palm imaging and cluster analysis of protein heterogeneity at the cell surface. *Journal of Biophotonics*, 3(7):446–454, 2010.